



FACULTÉ
DES SCIENCES

UNIVERSITÉ LIBRE DE BRUXELLES



北航物理学院
SCHOOL OF PHYSICS, BUAA

**Measurements of the Higgs boson
properties from off-shell production in the
 $ZZ \rightarrow 2l2\nu$ final state with the CMS detector**

Thesis presented by Hanwen WANG

in fulfilment of the requirements of the PhD Degree in Science (ULB -
“Docteur en Sciences”) and in Science (BUAA)
Année académique 2022-2023

Supervisors : Professor Pascal VANLAER (Université libre de Bruxelles)
Service de Physique des particules élémentaires
Interuniversity Institute for High Energies
and Professor Chengping SHEN (Fudan University)
Department of Physics
and Professor Li YUAN (Beihang University)
School of Physics

Thesis jury :

Prof. Laurent FAVART (Université libre de Bruxelles, Chair)
Prof. Li YUAN (Beihang University, Secretary)
Prof. Pascal VANLAER (Université libre de Bruxelles, Supervisor)
Prof. Chengping SHEN (Fudan University, Co-Supervisor)
Prof. Haijun YANG (Shanghai Jiao Tong University)

Abstract

Following the discovery of a new boson, consistent with the standard model (SM) Higgs boson, by the ATLAS and CMS collaborations in proton-proton collisions at the LHC, numerous Higgs boson properties have been measured, including mass, spin, parity, width, coupling strengths, decay rates, and fiducial differential cross sections. The width measurement of the Higgs boson, however, remains challenging. The SM-predicted Higgs width is approximately 4.1 MeV, while the invariant mass resolution of the Higgs boson reconstructed from the four charged leptons or di-photon channels is around 1 GeV—far from the required measurement resolution using the reconstructed mass peak. This study aims to refine the Higgs width measurement by relating off-shell production strength to on-shell production strength in the ZZ channels, using data recorded by the CMS experiment at a center-of-mass energy of 13 TeV from 2015 to 2018.

The $ZZ \rightarrow 4\ell$ final state presents minimal background, enabling the clear observation of the on-shell Higgs boson peak. In the meanwhile, the $ZZ \rightarrow 2\ell 2\nu$ final state offers an approximately six-fold larger branching ratio than the $ZZ \rightarrow 4\ell$ state, allowing for the measurement of off-shell Higgs productions, albeit with larger background contributions and reduced sensitivity in the on-shell region. Both final states are observed to have similar sensitivities to off-shell H boson production. To extract the Higgs width, data from both channels are combined. This thesis presents a detailed analysis based on the $ZZ \rightarrow 2\ell 2\nu$ final state, focusing on the charged-lepton identification efficiency, event level trigger efficiency, and background estimation of non-resonant processes.

By combining the on-shell and off-shell analyses from both $ZZ \rightarrow 4\ell$ and $ZZ \rightarrow 2\ell 2\nu$ channels, this study observes the first evidence of off-shell ZZ production (3.6σ) and significantly improves the precision of the Higgs width measurement. The final measured value is $3.2_{-1.7}^{+2.4}$ MeV, consistent with the SM prediction.

Résumé

Suite à la découverte d'un nouveau boson, compatible avec le boson de Brout-Englert-Higgs du modèle standard (SM), par les collaborations ATLAS et CMS dans les collisions proton-proton au LHC, de nombreuses propriétés du boson H ont été mesurées, notamment la masse, le spin, la parité, les couplages, les taux de décroissance et les sections efficaces différentielles fiducielles. La mesure de la largeur du boson H reste cependant difficile. La largeur prédite par SM est d'environ 4,1 MeV, tandis que la résolution en masse invariante du boson H reconstruit à partir du canal en quatre leptons chargés ou du canal di-photons est d'environ 1 GeV, loin de la résolution requise. Cette thèse de doctorat vise à affiner la mesure de la largeur du boson H en reliant la force du signal de production de bosons H fortement virtuels (> 200 GeV) à la force du signal de production de bosons H de masse nominale (125 GeV) dans les canaux ZZ , en utilisant les données enregistrées par l'expérience CMS de 2015 à 2018 à une énergie dans le centre de masse de 13 TeV.

L'état final $\rightarrow ZZ \rightarrow 4\ell$ présente un bruit de fond minimal, permettant l'observation claire du pic du boson H. L'état final $ZZ \rightarrow 2\ell 2\nu$, sur lequel porte cette thèse, offre un rapport d'embranchement environ six fois supérieur à celui de l'état $\rightarrow ZZ \rightarrow 4\ell$, ce qui permet de mesurer les productions de bosons H fortement virtuels, mais avec des bruits de fond plus importants et sans être sensible au pic correspondant à la masse nominale. Nous observons que les deux états finaux ont des sensibilités comparables à la contribution de bosons H fortement virtuels. Pour extraire la largeur du boson H, les données des deux canaux sont combinées. Cette thèse présente une analyse détaillée basée sur l'état final $ZZ \rightarrow 2\ell 2\nu$, en se concentrant sur l'efficacité d'identification des leptons chargés, l'efficacité du système de déclenchement de CMS pour les événements $ZZ \rightarrow 2\ell 2\nu$, et l'estimation du bruit de fond causé par les processus non résonnants.

En combinant les analyses on-shell et off-shell des canaux $\rightarrow ZZ \rightarrow 4\ell$ et $ZZ \rightarrow 2\ell 2\nu$, nous établissons la première évidence de bosons H fortement virtuels, à un niveau de signification de 3.6 sigma, et nous améliorons considérablement la précision de la mesure de la largeur du boson H. La valeur mesurée finale est de $3, 2^{+2,4}_{-1,7}$ MeV, compatible avec la prédiction du modèle standard.

摘要

继ATLAS 和 CMS 合作组在大型强子对撞机 (LHC) 的质子-质子对撞实验中发现希格斯粒子之后, 科学家对其性质也进行了详细的测量, 其中包括质量、自旋、宇称、宽度、耦合强度、衰变率、基准微分截面等。在这些测量中, 希格斯粒子的宽度测量颇具挑战性。标准模型中预言的希格斯粒子的宽度约为 4.1 MeV , 而由四个带电轻子或双光子衰变末态重建的希格斯粒子在实验中的质量分辨率约为 1 GeV , 远远超过利用其不变质量谱共振峰测量宽度的分辨率要求。本文利用2015-2018 年LHC上CMS 实验记录的质心能量为 13 TeV 的质子-质子对撞数据, 通过 ZZ 衰变末态将希格斯粒子的离壳信号强度与在壳信号强度相关联的方法, 对希格斯粒子宽度进行了更精确的测量。

$ZZ \rightarrow 4\ell$ 末态的本底背景贡献较低, 使我们能够清晰地观察到在壳的希格斯粒子共振峰。同时, $ZZ \rightarrow 2\ell 2\nu$ 末态的分支比约为 $ZZ \rightarrow 4\ell$ 末态的六倍, 我们可以从中得到更多的离壳希格斯事例, 但此衰变末态也伴随着显著的本底背景干扰从而损失了在壳区域的灵敏度。在实验中, 我们发现两种末态在离壳区域贡献的灵敏度大致相当。此项工作对 $ZZ \rightarrow 2\ell 2\nu$ 末态的分析进行了详细描述, 并将重点放在轻子鉴别效率研究、事例级触发效率研究以及非共振态过程的本底背景估计上。

在分析中, 结合希格斯粒子衰变到 $ZZ \rightarrow 4\ell$ 末态和 $ZZ \rightarrow 2\ell 2\nu$ 末态的在壳和离壳事例, 我们首次观测到希格斯粒子离壳事例存在的证据 (3.6倍标准偏差), 并且使得希格斯粒子宽度的测量精度显著提高, 最终测量值为 $3.2^{+2.4}_{-1.7} \text{ MeV}$, 与标准模型的预言一致。

Acknowledgements

Time runs so fast that finally it brings us here, the end of the journey, a journey that is too short, sealed only with some words and papers. It's also long, full of adventures, accompanying people and many memorable moments. Chengping Shen is my supervisor, or, the mentor that brings me in the field of particle physics. His meaningful research and enthusiasm in his work inspired me, at a time when I felt lost and couldn't find a destination in my life or even any directions. He has shown me his research work that I one day wish to be doing, and more important, his efforts, with which he could achieve the goal. He told me that I can manage it, too. It's a simple but most contagious word that I've ever heard, a word of great comfort as well as stimulation. As people in the field of particle physics know, it is not an area that people can easily step in. It requires great knowledge and experience in physics and management of a lot of skills. Chengping is the person who helps me start from scratch, from zero to one, and then accelerate in this field until near speed of light. Li Yuan is my second supervisor and she was the only researcher working on the project of LHC experiments at that time. I was fascinated by the ideas and discoveries from the LHC and she is the one who brought me from my dreams into reality. We have practical research to do. It's around that time I started to understand an physical analysis of CMS in real. The topics that we chose together finally becomes the one of my thesis. After that, I began to learn about the data analysis, the detector, programming and every relative aspect. She is always kind, skillful and full of patience. I've grown up fast since the time we met. Pascal Vanlaer, my supervisor at ULB, takes me to a new level in particle physics. He is an experienced expert from whom I can always find an answer. He is also a mentor helping me start my journey in Belgium. It's the first time that I study and live a life abroad, in a totally different place. We shared many wonderful moments during that time, attending workshops and lectures, riding in his car, having good meals at local restaurants and enjoying coffee in the office during break time, chatting about varieties of topics. This reminds me of all the people in IIHE. Laurent Favart, who always smiles when I came to see him. Hugo Delannoy, Hugues Brun and Andrey Popov, who helped me a lot with their expertise in particle physics and the experiment. Audrey Terrier, the secretary who helps me deal with many problems in my life at ULB. The IT team, who maintains the IIHE cluster and solves every IT problem you ask, even including how to replace the battery of a Macbook.

Many thanks should go to my $2\ell 2\nu$ working group, especially to Mostafa Mahdavi and Nicolas Postiau, my two colleagues at ULB. We used to work in the same office. I really miss the time we can solve bugs or just simply say good morning to each other everyday. I should also thank Ulascan Sarica, an expert and a man of action in our group, who has been pushing the work forward and sharing his experience in every aspect of the experiment.

I would also thank the whole CMS collaboration, thousands of people working on every part of the experiment. Though email is the only way we communicate and know each other, we still achieve a lot by solving problems and exchanging our ideas and knowledge.

In particular, I would like to thank my family and friends, who have been continuously supporting me during the Ph.D life, without whose help I can never reach this point.

Contents

Abstract	i
Table of contents	v
Introduction	xix
I Theory fundamentals	1
1 The Standard Model and the Higgs boson	2
1.1 Elementary particles and fundamental interactions	2
1.2 The Standard Model description	4
1.2.1 The standard model Lagrangian	4
1.2.2 More on the Higgs sector	9
1.3 Properties of the Higgs boson	11
1.3.1 Higgs boson production and decay	11
1.3.2 Off-shell Higgs production and Higgs interference	11
1.3.3 Measurement of the Higgs boson width	12
1.4 Phenomenology of anomalous HVV interactions	15
II Experimental point of view	17
2 The Large Hadron Collider and The Compact Muon Solenoid	18
2.1 The Large Hadron Collider	18
2.1.1 Accelerator and Particle beams	19
2.1.2 Luminosity accumulation	20
2.2 The Compact Muon Solenoid	22
2.2.1 Overview	22
2.2.2 Inner tracking system	25
2.2.3 The electromagnetic calorimeter	26

2.2.4	The hadronic calorimeter	27
2.2.5	The muon system	29
3	The CMS trigger system and physics object reconstruction	32
3.1	The CMS trigger system	32
3.1.1	The Level-1 Trigger	32
3.1.2	The High Level Trigger	34
3.2	Physics objects reconstruction	36
3.2.1	Tracks, vertices and beam spot	36
3.2.2	Muons	38
3.2.3	Electrons and photons	41
3.2.4	Jets	43
3.2.5	Missing transverse momentum	45
III	Measurements of the Higgs boson properties from off-shell production in the ZZ final state	46
4	Data and Simulations	47
4.1	Datasets	47
4.1.1	Datasets for the analysis	47
4.2	Simulations	49
4.2.1	Simulations of the non-interfering backgrounds	50
4.2.2	Simulation of the signal and interfering background processes	53
5	Analysis strategy	55
5.1	Triggers	55
5.1.1	Measurement of trigger efficiencies for dilepton events	59
5.1.2	Measurement of muon trigger efficiencies	71
5.2	Physics object selections	75
5.2.1	Measurement of lepton efficiencies	77
5.2.2	Investigations on the photon additional selections	88
5.3	Event selection and categorization	89
5.4	Observables and Discriminants	89
5.5	Likelihood parameterization	91
5.6	Systematic uncertainties	93
6	Data-driven background estimations	95
6.1	Non-resonant Backgrounds	96
6.1.1	Estimation with reweighted $e\mu$ events	96
6.1.2	Alpha method	97
6.2	Single-photon control region	115
6.3	WZ control region	118
7	Results and Intepretations	120
	Conclusion	132
	Bibliography	133

List of Figures

1.1	Particle family of the Standard Model [1]	3
1.2	Matter particles (fermions) and interaction particles (gauge bosons and the Higgs). Gluons (g) couple to colour charge, which only quarks, antiquarks, and gluons themselves, have. Photons (γ) couple to electric charge, which is found in (anti)quarks and electrically charged (anti)leptons. The weak bosons (W^- , W^+ , Z^0) couple to the weak charge, which all matter particles have. Weak bosons can also interact with the photon (but this is a pure weak interaction, not an electromagnetic one). And finally, the BEH field interacts with particles that have mass (all particles except the massless gluon and photon) [2].	4
1.3	The best-fit estimates for the reduced coupling modifiers extracted for fermions and weak bosons compared to their corresponding prediction from the SM. The associated error bars represent 68% CL intervals for the measured parameters [3]. In the SM, the Yukawa coupling between the Higgs boson and the fermions (λ_F) is proportional to the fermion mass (m_F), while the coupling to weak bosons (g_V) is proportional to the square of the vector boson masses (m_V). The results from the κ -framework fit can therefore be translated in terms of reduced coupling strength modifiers, defined as $y_V = \sqrt{\kappa_V} m_V / V$ for weak bosons and $y_F = \kappa_F m_F / V$ for fermions, where v is the vacuum expectation value of the Higgs field of 246.22 GeV.	7
1.4	Lowest order Feynman diagrams of 4 major scalar boson production modes at the LHC: gluon-gluon fusion(top, left), vector boson fusion(top, right), associated production with a vector boson(bottom, left) and top quark fusion(bottom, right).	11
1.5	Higgs boson production cross sections as a function of its mass (SM-like coupling, narrow-width approximation, no electroweak corrections) at $\sqrt{s} = 13$ TeV [4].	12
1.6	Standard Model Higgs boson decay branching ratios as a function of the invariant mass [4]	13
1.7	The distributions of $m_{2\ell 2\nu}$ in the gluon fusion(left panel) and $m_{4\ell}$ in the electro-weak(right panel) production modes. Different processes including the H ($ H ^2$), interfering continuum ($ C ^2$), their direct sum without the interference ($ H ^2 + C ^2$) and the sum with interference included ($ H + C ^2$). The integrated luminosity is taken to be 1fb^{-1}	14
2.1	The LHC accelerator complex and experiments[5]	19

2.2	The measured luminosity delivered by the LHC to CMS (yellow) and recorded by CMS (red) during stable beams and for proton-proton collisions at a 13 TeV center-of-mass energy in the year of 2015 (left, top), 2016 (right, top), 2017 (left, bottom), 2018 (right, bottom) [6]	21
2.3	A perspective view of the CMS detector	22
2.4	A schematic view of the CMS detector [7]	23
2.5	An illustration of the conventional 3D coordinate system at the CMS detector	24
2.6	Distribution of the average number of interactions per crossing (pileup) for pp collisions during Run-2 [6]	25
2.7	Cross section of the current CMS tracker, showing the nomenclature used to identify different sections. Each line represents a detector module. Double lines indicate back-to-back modules which deliver stereo hits in the strip tracker [8].	26
2.8	A 3-D view of the electromagnetic calorimeter [8]	27
2.9	A schematic view of one quarter of the CMS HCAL, showing the positions of its four major components: the hadron barrel (HB), the hadron endcap (HE), the hadron outer (HO), and the hadron forward (HF) calorimeters [8]	28
2.10	Module components of different layers (left) and sketch of a cassette with modules mounted on either side of the copper cooling plate (right)	29
2.11	An $R - z$ cross-section of one quadrant of the CMS detector with the axis parallel to the beam (z) running horizontally and radius (r) increasing upward. The interaction region is at the lower left. Shown are the locations of the various muon stations and the steel disks [9].	30
2.12	Layout of the CMS barrel muon DT chambers in one of the 5 wheels [10]	31
3.1	Architecture of the Level-1 Trigger after LS1 upgrade. Details are given in the text [11]	33
3.2	Illustration of electron trajectories and bremsstrahlung effects in the detector.	41
4.1	Feynman diagrams for important contributions to ZZ production. Diagrams can be distinguished as those involving the H (top), and those that give rise to continuum ZZ production (bottom). The interaction displayed at tree level in each diagram is meant to progress from left to right. Each straight, curvy, or curly line refers to the different set of particles denoted. Straight, solid lines with no arrows indicate the line could refer to either a particle or an antiparticle, whereas those with forward (backward) arrows refer to a particle (an antiparticle).	53
5.1	Comparisons of the p_T^{miss} distribution and efficiencies in bins of p_T^{miss} from data and simulation of 2016. Total in the legend refers to all events passing MET orthogonal triggers and the offline event preselection. Pass refers to events passing both orthogonal triggers and di-lepton triggers, in addition to the offline event preselection. From top to bottom are ee , $\mu\mu$ and $e\mu$ with data on the left and simulation on the right.	62
5.2	Comparisons of the p_T^{miss} distribution and efficiencies in bins of p_T^{miss} from data and simulation of 2017. Total in the legend refers to all events passing MET orthogonal triggers and the offline event preselection. Pass refers to events passing both orthogonal triggers and di-lepton triggers, in addition to the offline event preselection. From top to bottom are ee , $\mu\mu$ and $e\mu$ with data on the left and simulation on the right.	63
5.3	Comparisons of the p_T^{miss} distribution and efficiencies in bins of p_T^{miss} from data and simulation of 2018. Total in the legend refers to all events passing MET orthogonal triggers and the offline event preselection. Pass refers to events passing both orthogonal triggers and di-lepton triggers, in addition to the offline event preselection. From top to bottom are ee , $\mu\mu$ and $e\mu$ with data on the left and simulation on the right.	64

5.4	The efficiencies of the combined SR/CR dilepton event triggers measured from the observed data in the 2016 data period are shown for the ee , $\mu\mu$, and $e\mu$ decay channels from left to right. The first or second lepton in the pair are required to be both in the barrel region, the first lepton to be in the barrel and the second to be in the endcap, the first lepton to be in the endcap and the second to be in the barrel, and both to be in the endcap region, in order from top to bottom panels. The order of leptons is defined by which one has higher p_T^ℓ in the ee and $\mu\mu$ channels, and the muon is chosen to be the first lepton in the $e\mu$ case.	65
5.5	The efficiencies of the combined SR/CR dilepton event triggers measured from the observed data in the 2017 data period are shown for the ee , $\mu\mu$, and $e\mu$ decay channels from left to right. The first or second lepton in the pair are required to be both in the barrel region, the first lepton to be in the barrel and the second to be in the endcap, the first lepton to be in the endcap and the second to be in the barrel, and both to be in the endcap region, in order from top to bottom panels. The order of leptons is defined by which one has higher p_T^ℓ in the ee and $\mu\mu$ channels, and the muon is chosen to be the first lepton in the $e\mu$ case.	66
5.6	The efficiencies of the combined SR/CR dilepton event triggers measured from the observed data in the 2018 data period are shown for the ee , $\mu\mu$, and $e\mu$ decay channels from left to right. The first or second lepton in the pair are required to be both in the barrel region, the first lepton to be in the barrel and the second to be in the endcap, the first lepton to be in the endcap and the second to be in the barrel, and both to be in the endcap region, in order from top to bottom panels. The order of leptons is defined by which one has higher p_T^ℓ in the ee and $\mu\mu$ channels, and the muon is chosen to be the first lepton in the $e\mu$ case.	67
5.7	The efficiencies of the combined SR/CR dilepton event triggers measured from the simulation in the 2016 data period. The order of the panels is the same as those shown for the efficiencies observed in real data.	68
5.8	The efficiencies of the combined SR/CR dilepton event triggers measured from the simulation in the 2017 data period. The order of the panels is the same as those shown for the efficiencies observed in real data.	69
5.9	The efficiencies of the combined SR/CR dilepton event triggers measured from the simulation in the 2018 data period. The order of the panels is the same as those shown for the efficiencies observed in real data.	70
5.10	Fitting results in p_T (Unit is GeV) bins of [25, 50](top, left), (50, 75](top, right), (75, 100] (bottom, left) and (100, 150] (bottom, right) from 2018 data.	72
5.11	Mu17 efficiencies measured in bins of η (top) and p_T (bottom) for 2017	73
5.12	Mu17 efficiencies measured in bins of η (top) and p_T (bottom) for 2018	73
5.13	MC closure test shows the efficiency difference between two sets of results in η bins. Results are derived from Drell-Yan simulation in 2018 condition.	74
5.14	Shown are the results of the muon mass fit for testing the medium isolation selection for 2016 as an example, with top three figures for data and bottom three for Drell-Yan simulation. The functions used for fitting the shape of background are RooCMSShape, Chebyshev and Exponential from left to right respectively, in the bin of $ \eta < 1.2$ and a combined p_T bin of $25 < p_T < 55$. Black dots represents for observed data, green line for the fit of the events passing iso. test, red for the failing and blue for the total (passing plus failing).	79

5.15	The lepton identification and isolation efficiencies measured from observed data in 2016 for muons (first row), non-gap and gap electrons combined (second row), non-gap electrons only (third row) and gap electrons only (fourth row). The panels show the nominal variations of the conditional efficiencies to pass lepton identification (first column), pass loose isolation for event veto (second column), and pass tight isolation for analysis (third column).	82
5.16	The lepton identification and isolation efficiencies measured from observed data in 2017 for muons (first row), non-gap and gap electrons combined (second row), non-gap electrons only (third row) and gap electrons only (fourth row). The panels show the nominal variations of the conditional efficiencies to pass lepton identification (first column), pass loose isolation for event veto (second column), and pass tight isolation for analysis (third column).	83
5.17	The lepton identification and isolation efficiencies measured from observed data in 2018 for muons (first row), non-gap and gap electrons combined (second row), non-gap electrons only (third row) and gap electrons only (fourth row). The panels show the nominal variations of the conditional efficiencies to pass lepton identification (first column), pass loose isolation for event veto (second column), and pass tight isolation for analysis (third column).	84
5.18	The lepton identification and isolation efficiencies measured from the simulation for the 2016 data period for muons (first row), non-gap and gap electrons combined (second row), non-gap electrons only (third row) and gap electrons only (fourth row). The panels show the nominal variations of the conditional efficiencies to pass lepton identification (first column), pass loose isolation for event veto (second column), and pass tight isolation for analysis (third column).	85
5.19	The lepton identification and isolation efficiencies measured from the simulation for the 2017 data period for muons (first row), non-gap and gap electrons combined (second row), non-gap electrons only (third row) and gap electrons only (fourth row). The panels show the nominal variations of the conditional efficiencies to pass lepton identification (first column), pass loose isolation for event veto (second column), and pass tight isolation for analysis (third column).	86
5.20	The lepton identification and isolation efficiencies measured from the simulation for the 2018 data period for muons (first row), non-gap and gap electrons combined (second row), non-gap electrons only (third row) and gap electrons only (fourth row). The panels show the nominal variations of the conditional efficiencies to pass lepton identification (first column), pass loose isolation for event veto (second column), and pass tight isolation for analysis (third column).	87
5.21	Photon seedtime distributions for 2016 (left), 2017 (middle) and 2018 (right), for a selection of 1 good photon, 0 jet, $p_T^\gamma \geq 55\text{GeV}$ and $\phi_{\text{miss}}^{\text{boson}} \geq 2.5$. Signs of non-gaussian tails can be seen in data after $ t_{\text{seed}} > 2\text{ns}$, and in 2018, the tail starts at $t_{\text{seed}} > 1\text{ns}$	88
5.22	Comparison of photon p_T distribution before and after applying the particle-flow ID on the photons , in the $ll\gamma$ CR for data (left), MC (middle) and the comparison between their ratios (right). The $ll\gamma$ CR is believed to be enriched with real, prompt photons.	88
5.23	Comparison of photon p_T distribution before and after applying the pixel seed veto and conversion safe ID on the photons , in the $ll\gamma$ CR for data (left), MC (middle) and the comparison between their ratios (right). The $ll\gamma$ CR is believed to be enriched with real, prompt photons.	89
6.1	Illustration of a common ABCD method [12]	95

6.2	Distributions of the VBF discriminants for nonresonant background. The distributions of the SM $\mathcal{D}_{2\text{jet}}^{\text{VBF}}$ (left) and $\mathcal{D}_{2\text{jet}}^{\text{VBF},a2}$ (right) kinematic VBF discriminants are shown in the $2\ell 2\nu$ signal region, $N_j \geq 2$ category. The stacked histogram shows the predictions from simulation, which consists of nonresonant contributions from WW (green) and $t\bar{t}$ (gray) production, or other small components (orange). The black points with error bars as uncertainties at 68% CL show the prediction from the $e\mu$ CR data. While only the data is used in the final estimate of the nonresonant background, we note that predictions from simulation already agree well with the data estimate.	97
6.3	Distributions of $m_{\ell\ell}$ in NRB control region from data and all related MC simulation of 2016. At least one b-tagged jet with loose WP is required. From top to bottom are ee , $\mu\mu$ and $e\mu$ with $p_T^{\text{miss}} > 50$ GeV on the left and $p_T^{\text{miss}} > 80$ GeV on the right. A pre-selection of $m_{\ell\ell} \geq 50$ GeV is applied, which accounts for the cutoff around the threshold.	99
6.4	Distributions of $m_{\ell\ell}$ in NRB control region from data and all related MC simulation of 2016. Events containing one or more b-tagged jets with loose WP are rejected. From top to bottom are ee , $\mu\mu$ and $e\mu$ with $p_T^{\text{miss}} > 50$ GeV on the left and $p_T^{\text{miss}} > 80$ GeV on the right. A pre-selection of $m_{\ell\ell} \geq 50$ GeV is applied, which accounts for the cutoff around the threshold.	100
6.5	Distributions of $m_{\ell\ell}$ in NRB control region from data and all related MC simulation of 2017. At least one b-tagged jet with Loose WP is required. From top to bottom are ee , $\mu\mu$ and $e\mu$ with $p_T^{\text{miss}} > 50$ GeV on the left and $p_T^{\text{miss}} > 80$ GeV on the right. A pre-selection of $m_{\ell\ell} \geq 50$ GeV is applied, which accounts for the cutoff around the threshold.	101
6.6	Distributions of $m_{\ell\ell}$ in NRB control region from data and all related MC simulation of 2017. Events containing one or more b-tagged jets with loose WP are rejected. From top to bottom are ee , $\mu\mu$ and $e\mu$ with $p_T^{\text{miss}} > 50$ GeV on the left and $p_T^{\text{miss}} > 80$ GeV on the right. A pre-selection of $m_{\ell\ell} \geq 50$ GeV is applied, which accounts for the cutoff around the threshold.	102
6.7	Distributions of $m_{\ell\ell}$ in NRB control region from data and all related MC simulation of 2018. At least one b-tagged jet with Loose WP is required. From top to bottom are ee , $\mu\mu$ and $e\mu$ with $p_T^{\text{miss}} > 50$ GeV on the left and $p_T^{\text{miss}} > 80$ GeV on the right. A pre-selection of $m_{\ell\ell} \geq 50$ GeV is applied, which accounts for the cutoff around the threshold.	103
6.8	Distributions of $m_{\ell\ell}$ in NRB control region from data and all related MC simulation of 2018. Events containing one or more b-tagged jets with loose WP are rejected. From top to bottom are ee , $\mu\mu$ and $e\mu$ with $p_T^{\text{miss}} > 50$ GeV on the left and $p_T^{\text{miss}} > 80$ GeV on the right. A pre-selection of $m_{\ell\ell} \geq 50$ GeV is applied, which accounts for the cutoff around the threshold.	104
6.9	α value as a function of the met cut computed from all side bands ($40 < m_{\ell\ell} < 70$ GeV and $110 < m_{\ell\ell} < 200$ GeV) with b-tagged jet required in the events using both data (left) and MC simulations (right) in di-electron (red) and di-muon (blue) channel of year 2016 (top), 2017 (middle), 2018 (bottom).	105
6.10	α value as a function of the met cut computed from all side bands ($40 < m_{\ell\ell} < 70$ GeV and $110 < m_{\ell\ell} < 200$ GeV) with events containing b-tagged jet rejected using both data (left) and MC simulations (right) in di-electron (red) and di-muon (blue) channel of year 2016 (top), 2017 (middle), 2018 (bottom).	106

6.11	Distributions of p_T^{miss} from non-resonant contribution in the signal region for 2016. The stacked histograms are MC simulations of nonresonant contribution in the signal region and the color legend for them is given in the plots. Reweighted $e\mu$ events from data are shown as black points with error bars. The solid line in magenta shows the shape derived from reweighted $e\mu$ events of simulations. Bottom panels represent for the bias that is calculated in a similar way as Eq. 6.4 in each p_T^{miss} bin.	107
6.12	Distributions of m_T^{ZZ} from non-resonant contribution in the signal region for 2016. The stacked histograms are MC simulations of nonresonant contribution in the signal region and the color legend for them is given in the plots. Reweighted $e\mu$ events from data are shown as black points with error bars. The solid line in magenta shows the shape derived from reweighted $e\mu$ events of simulations. Bottom panels represent for the bias that is calculated in a similar way as Eq. 6.4 in each m_T^{ZZ} bin.	108
6.13	Distributions of p_T^{miss} from non-resonant contribution in the signal region for 2017. The stacked histograms are MC simulations of nonresonant contribution in the signal region and the color legend for them is given in the plots. Reweighted $e\mu$ events from data are shown as black points with error bars. The solid line in magenta shows the shape derived from reweighted $e\mu$ events of simulations. Bottom panels represent for the bias that is calculated in a similar way as Eq. 6.4 in each p_T^{miss} bin.	109
6.14	Distributions of m_T^{ZZ} from non-resonant contribution in the signal region for 2017. The stacked histograms are MC simulations of nonresonant contribution in the signal region and the color legend for them is given in the plots. Reweighted $e\mu$ events from data are shown as black points with error bars. The solid line in magenta shows the shape derived from reweighted $e\mu$ events of simulations. Bottom panels represent for the bias that is calculated in a similar way as Eq. 6.4 in each m_T^{ZZ} bin.	110
6.15	Distributions of p_T^{miss} from non-resonant contribution in the signal region for 2018. The stacked histograms are MC simulations of nonresonant contribution in the signal region and the color legend for them is given in the plots. Reweighted $e\mu$ events from data are shown as black points with error bars. The solid line in magenta shows the shape derived from reweighted $e\mu$ events of simulations. Bottom panels represent for the bias that is calculated in a similar way as Eq. 6.4 in each p_T^{miss} bin.	111
6.16	Distributions of m_T^{ZZ} from non-resonant contribution in the signal region for 2018. The stacked histograms are MC simulations of nonresonant contribution in the signal region and the color legend for them is given in the plots. Reweighted $e\mu$ events from data are shown as black points with error bars. The solid line in magenta shows the shape derived from reweighted $e\mu$ events of simulations. Bottom panels represent for the bias that is calculated in a similar way as Eq. 6.4 in each m_T^{ZZ} bin.	112
6.17	Computed bias as a function of the met cut computed from all side bands ($40 < m_{\ell\ell} < 70$ GeV and $110 < m_{\ell\ell} < 200$ GeV) with b-tagged jet required in the events using both data (left) and MC simulations (right) in di-electron (red) and di-muon (blue) channel of year 2016 (top), 2017 (middle), 2018 (bottom).	113
6.18	Computed bias as a function of the met cut computed from all side bands ($40 < m_{\ell\ell} < 70$ GeV and $110 < m_{\ell\ell} < 200$ GeV) with events containing b-tagged jet rejected using both data (left) and MC simulations (right) in di-electron (red) and di-muon (blue) channel of year 2016 (top), 2017 (middle), 2018 (bottom).	114
6.19	Feynman diagram of the Drell-Yan process	115

6.20	The data vs MC distributions of p_T^{miss} distribution in 0 jet (left), 1 jet (middle) and ≥ 2 jets (right) categories, collected over an data taking period correspond to an integrated luminosity of 138fb^{-1} . In these distributions, some discrepancy between data and MC are expected as the γ +jets process come from simulations are not expected to be fully reliable. The gray error bands only correspond to the statistical uncertainty in the simulation.	115
6.21	The data vs MC distributions of m_T^{ZZ} distribution in 0 jet (top left), 1 jet (top right), ≥ 2 jets with $140 \leq p_T^{\text{miss}} < 200\text{GeV}$ (bottom left) and ≥ 2 jets with $p_T^{\text{miss}} \geq 200\text{GeV}$ (bottom right) categories, collected over an data taking period correspond to an integrated luminosity of 138fb^{-1} . In these distributions, some discrepancy between data and MC are expected as the γ +jets process come from simulations are not expected to be fully reliable.	116
6.22	Distributions of m_T^{WZ} in different N_j categories of the WZ control region. The postfit distributions of the transverse WZ invariant mass are displayed for the $N_j = 0$, $N_j = 1$, and $N_j \geq 2$ jet multiplicity categories of the $WZ \rightarrow 3\ell 1\nu$ control region from left to right. Postfit refers to a combined $2\ell 2\nu + 4\ell$ fit, together with this control region, assuming SM H parameters. The stacked histogram is shown with the hashed band as the total postfit uncertainty at 68% CL. The color legend is given above the plots, with the different contributions referring to the WZ (light green), ZZ (blue), Z+jets (dark green), $Z\gamma$ (yellow), $t\bar{t}$ (gray), and $tV+X$ (brown, with X being any other particle) production processes, as well as the small EW ZZ production component (dark pink). The black points with error bars as uncertainties at 68% CL show the observed data. The middle panels along the vertical show the ratio of the data to the total prediction, and the lower panels show the predicted relative contributions of each process. The rightmost bins contain the overflow.	119
7.1	Distributions of m_T^{ZZ} in the different N_j categories of the $2\ell 2\nu$ signal region. Shown are the transverse ZZ invariant mass distributions in the jet multiplicity categories of $N_j=0$ (left), $=1$ (middle), and ≥ 2 (right) with a requirement of $p_T^{\text{miss}} > 200\text{GeV}$ to enrich H contributions. The color legend for the stacked or dot-dashed histograms is given above the plots. Observed data are shown as black points with error bars as uncertainties at 68% CL. SM backgrounds including the estimations from data-driven are shown in stacked histogram with the hashed band as the total postfit uncertainty at 68% CL. No off-shell H boson production after the fit is shown in dot-dashed gold line. The middle panels along the vertical show the ratio of the data or dashed histograms to the stacked histogram, and the lower panels show the predicted relative contributions of each process.	121
7.2	Shown are the top 30 nuisance parameters affecting the constraints on $\mu^{\text{off-shell}}$ when $R_{V,F}^{\text{off-shell}}$ and on-shell μ_V are unconstrained. The impacts are shown for the expected result only.	122
7.3	Shown are the top 30 nuisance parameters affecting the constraints on $\mu^{\text{off-shell}}$ when $R_{V,F}^{\text{off-shell}}$ and on-shell μ_V are fixed to the SM expectation. The impacts are shown for the expected result only.	123

7.4 **Distributions of ZZ invariant mass observables in the off-shell signal regions.**

The distributions of transverse ZZ invariant mass, m_T^{ZZ} from the $2\ell 2\nu$ off-shell signal region are displayed on the left panel, and those of the 4ℓ invariant mass, $m_{4\ell}$, from the 4ℓ off-shell signal region are displayed on the right. The stacked histogram displays the distribution after a fit to the data with SM couplings, with the blue filled area corresponding to the SM processes that do not include H interactions, and the pink filled area adding processes that include H and interference contributions. The gold dot-dashed line shows the fit to the no off-shell hypothesis. The black points with error bars as uncertainties at 68% CL show the observed data, which is consistent with the prediction with SM couplings within one standard deviation. The last bins contain the overflow. The requirements on the missing transverse momentum p_T^{miss} in $2\ell 2\nu$ events, and the \mathcal{D}_{bkg} -type kinematic background discriminants (see Table II of Ref. [13]) in 4ℓ events are applied in order to enhance the H signal contribution. The values of integrated luminosity displayed correspond to those included in the off-shell analyses of each final state. The bottom panels show the ratio of the data or dashed histograms to the SM prediction (stacked histogram). The black horizontal line in these panels marks unit ratio.

126

7.5 **Log-likelihood scans of $\mu_F^{\text{off-shell}}$ and $\mu_V^{\text{off-shell}}$, and Γ_H .** Left panel: Two-parameter likelihood scan of the off-shell gg and EW production signal strength parameters, $\mu_F^{\text{off-shell}}$ and $\mu_V^{\text{off-shell}}$, respectively. The dot-dashed and dashed contours enclose the 68% ($-\Delta \ln \mathcal{L}=2.30$) and 95% ($-\Delta \ln \mathcal{L}=5.99$) CL regions. The cross marks the minimum, and the blue diamond marks the SM expectation. The integrated luminosity reaches only up to 138 fb^{-1} as on-shell 4ℓ events are not included in performing this scan. Right panel: The observed (solid) and expected (dashed) one-parameter likelihood scans over Γ_H . Scans are shown for the combination of 4ℓ on-shell data with 4ℓ off-shell (magenta) or $2\ell 2\nu$ off-shell data (green) alone, or with both data sets (black). The horizontal lines indicate the 68% $-\Delta \ln \mathcal{L}=1.0$ and 95% ($-\Delta \ln \mathcal{L}=3.84$) CL regions. The integrated luminosity reaches up to 140 fb^{-1} as on-shell 4ℓ events are included in performing these scans. The exclusion of the no off-shell hypothesis is consistent with 3.6 standard deviations on both panels.

127

7.6 **Log-likelihood scans of the off-shell signal strengths, Γ_H , and \bar{f}_{ai} .** Top panels: The likelihood scans are shown for $\mu_F^{\text{off-shell}}$ or $\mu_V^{\text{off-shell}}$ (left), $\mu^{\text{off-shell}}$ (middle), and Γ_H (right). Scans for $\mu_F^{\text{off-shell}}$ (blue) and $\mu_V^{\text{off-shell}}$ (magenta) are obtained with the other parameter unconstrained. Those for $\mu^{\text{off-shell}}$ are shown with (blue) and without (magenta) the constraint $R_{V,F}^{\text{off-shell}} (= \mu_V^{\text{off-shell}} / \mu_F^{\text{off-shell}}) = 1$. Constraints on Γ_H are shown with and without anomalous HVV couplings. Bottom panels: The likelihood scans of the anomalous HVV coupling parameters \bar{f}_{a2} (left), \bar{f}_{a3} (middle), and $\bar{f}_{\Lambda 1}$ (right) are shown with the constraint $\Gamma_H = \Gamma_H^{\text{SM}} = 4.1 \text{ MeV}$ (blue), Γ_H unconstrained (magenta), or based on on-shell 4ℓ data only (green). Observed (expected) scans are shown with solid (dashed) curves. The horizontal lines indicate the 68% ($-\Delta \ln \mathcal{L}=1.0$) and 95% $-\Delta \ln \mathcal{L}=3.84$) CL regions. The integrated luminosity reaches up to 138 fb^{-1} when only off-shell information is used, and up to 140 fb^{-1} when on-shell 4ℓ events are included.

128

7.7 **Distributions of ratios of the numbers of events in each off-shell signal region bin.** The ratios are taken after separate fits to the no off-shell hypothesis ($N_{\text{no off-shell}}$) and the best overall fit ($N_{\text{best fit}}$) with the observed Γ_H value of 3.2MeV in the SM-like HVV couplings scenario. The stacked histogram displays the predicted contributions (pink from the 4ℓ off-shell and green from the $2\ell 2\nu$ off-shell signal regions) after the best fit, with the hashed band representing the total postfit uncertainty at 68% CL, and the gold dot-dashed line shows the predicted distribution of these ratios for a fit to the no off-shell hypothesis. The black solid (hollow) points, with error bars as uncertainties at 68% CL, represent the observed $2\ell 2\nu$ and 4ℓ (4ℓ -only) data. The first and last bins contain the underflow and the overflow, respectively. The bottom panel displays the ratio of the various displayed hypotheses or observed data to the prediction from the best fit. The integrated luminosity reaches only up to 138fb^{-1} since on-shell 4ℓ events are not displayed. 129

List of Tables

1.1	The anomalous HVV couplings considered in the measurement assuming a spin-0 Higgs boson. The definition of the effective fractions f_{ai} is discussed in the text, and the translation constants are the cross section ratios corresponding to the process $H \rightarrow 2\ell 2\nu$ (or equivalently, $H \rightarrow 2e2\mu$) with the Higgs mass $m_H = 125\text{GeV}$. These calculations are performed using the JHUGEN program [14–18].	16
2.1	Important parameters of the LHC for Run-2	18
3.1	The observables used in the training of the BDT in order to identify prompt electrons. The training is done using the 2017 simulation, and this same training is used for 2016 and 2018.	42
3.2	The working points of the electron identification BDT, defined as a function of the p_T^e before any residual energy scale and smear corrections. The same working points are used in all three years.	42
3.3	The effective area A_{eff}^e values used in each η_{SC} range to mitigate the dependence of the isolation requirement on pileup. The same values are used in all three years.	43
3.4	The baseline selection requirements on the photons. The requirements are kept the same among the three data taking periods.	43
3.5	The values of the effective areas $A_{\text{eff,ch}}^\gamma$, $A_{\text{eff,nh}}^\gamma$, and $A_{\text{eff},\gamma}^\gamma$ used in each η_{SC} range to mitigate the dependence of the isolation requirement on pileup. The same values are used in all three years.	44
4.1	The luminosities for 2016, 2017 and 2018 during LHC Run-II data taking [19]	47
4.2	The primary datasets used in the analysis for all three years	48
4.3	Datasets and global tags used in the analysis	49
4.4	Non-interfering background samples, generators and their cross sections used in the analysis of dilepton signal or control regions. The cross sections are obtained with NNPDF 3.1 PDF set. Since WZ or ZZ background contributes to the signal region, the events are reweighted to the NNPDF 3.0 condition to have a uniform cross section predictions across the data periods.	51
4.5	Non-interfering background samples, generators and their cross sections used in the analysis of single photon control region. The cross sections are obtained with NNPDF 3.1 PDF set.	52

4.6	The cross section values for the different Higgs boson production modes are listed for the samples produced at different values of the Higgs boson pole mass m_H using the POWHEG 2 event generator. TheMINLO HVJ add-on is used in the VH modes. The cross sections are obtained with the NNPDF 3.0 NLO nominal PDF set. The cross sections are reported in units of pb.	54
5.1	List of the HLT paths used in the analysis for the Run-2 data	56
5.2	List of the HLT paths used in the analysis for the Run-2 data	57
5.3	The p_T^γ thresholds applied to the single-photon triggers in 2016. These thresholds on the reconstructed p_T^γ are approximately 10% above the HLT-level threshold values.	58
5.4	The p_T^γ thresholds applied to the single-photon triggers in 2017 or 2018. The thresholds are approximately 10% above the turn-on value.	58
5.5	Summary of tag and probe selection requirements for the lepton efficiency measurements. The requirements on the probe leptons for loose and tight isolation measurements add lepton identification or loose isolation as appropriate. The SR/CR triggers mentioned are listed in Sec. 5.1.	80
5.6	Fit functions of dilepton resonance peak in the observed data and simulated Drell-Yan sample	81
5.7	Fit functions of the background in the observed data	81
5.8	The binning used in each of the observables examined in the analysis. Binning for m_T^{ZZ} is identical in each N_j category, and the binning for p_T^{miss} is different between $N_j < 2$ and ≥ 2	91
5.9	The set of observables used in each interpretation are summarized for the $2\ell 2\nu$ final state. The interpretations are grouped by the parameters constrained. The observables for $N_j < 2$ are identical in any interpretation scenario, and the BSM $\mathcal{D}_{2\text{jet}}^{\text{VBF}}$ discriminant in the $N_j \geq 2$ category changes based on the anomalous HVV coupling constrained. The BSM discriminant $\mathcal{D}_{2\text{jet}}^{\text{VBF},a2}$ is added to the SM-like HVV coupling scenarios as well in order to gain equivalent signal separation strength. Only two bins in p_T^{miss} , $<$ and $\geq 200\text{GeV}$, are considered for $N_j \geq 2$ as outlined in Tab. 5.8.	91
6.1	α_ℓ with ℓ being e or μ computation from all side bands and only right side band	98
7.1	Results on the off-shell signal strengths and Γ_H. The various fit conditions are indicated in the column labeled ‘‘Cond.’’: Results on $\mu^{\text{off-shell}}$ are presented with $R_{V,F}^{\text{off-shell}} = \mu_V^{\text{off-shell}}/\mu_F^{\text{off-shell}}$ either unconstrained (u) or = 1, and constraints on $\mu_F^{\text{off-shell}}$ and $\mu_V^{\text{off-shell}}$ are shown with the other signal strength unconstrained. Results on Γ_H (in units of MeV) are obtained with the on-shell signal strengths unconstrained, and the different conditions listed for this quantity reflect which off-shell final states are combined with on-shell 4ℓ data. The expected central values, not quoted explicitly in this table, are either unity for $\mu^{\text{off-shell}}$, $\mu_F^{\text{off-shell}}$, and $\mu_V^{\text{off-shell}}$, or $\Gamma_H = 4.1\text{MeV}$	124
7.2	Results on Γ_H and the different anomalous HVV couplings. The results on Γ_H are displayed in units of MeV, and those on the anomalous HVV couplings are summarized in terms of the corresponding on-shell cross section fractions f_{a2} , f_{a3} , and $f_{\Lambda 1}$ (\bar{f}_{ai} in short, and scaled by 10^5). For the results on Γ_H , the tests with the anomalous HVV couplings are distinguished by the denoted \bar{f}_{ai} , and the expected best-fit values, not quoted explicitly in the table, are always $\Gamma_H = 4.1\text{MeV}$. The SM-like result is the same as that from the combination of all 4ℓ and $2\ell 2\nu$ data sets in Tab. 7.1. For the results on \bar{f}_{ai} , the constraints are shown with either $\Gamma_H = \Gamma_H^{\text{SM}} = 4.1\text{MeV}$ required, or Γ_H left unconstrained, and the expected best-fit values, also not quoted explicitly, are always null. The various fit conditions are indicated in the column labeled ‘‘Condition’’, where the abbreviation ‘‘(u)’’ indicates which parameter is unconstrained.	125

Introduction

The standard model of particle physics, developed in the 1960s and 1970s, has been tested for 50-60 years as the theory of particle physics. While some facts show and also people believe that the standard model is not a complete description of basic physical rules governing from tiny elementary particles to the whole universe, it still has stood for such many years, successfully explaining most of the experimental facts.

Many topics are waiting to be explored: What is mass? What is the Higgs boson like? What is the dark matter and the dark energy? Is there a theory explaining everything? To answer those questions, scientists and engineers have built many large scale scientific facilities performing experiments with high energy, high luminosity and high precision. Among them stands the Large Hadron Collider (LHC), the world's largest and most powerful particle accelerator [20]. Inside the accelerator, two high-energy particle beams travel at close to the speed of light before they are made to collide at four locations around its ring. The Compact Muon Solenoid (or CMS) detector sits at one of these four collision points [21]. It is a general-purpose detector; that is, it is designed to observe any new physics phenomena that the LHC might reveal.

Many physical analyses in terms of the Higgs boson are performed by collecting and analyzing the proton-proton collision data recorded by the CMS. After the discovery of this particle, many people believe that measurement of the properties of the Higgs is a key to examine the SM and is likely to open the door of new physics. During writing this thesis, the most recent results of the Higgs width measurement were published [22], using data from the CMS experiment at the LHC that correspond to an integrated luminosity of 138fb^{-1} (140fb^{-1} with 4ℓ on-shell included) at a center-of-mass energy of 13TeV . We found the evidence of off-shell Higgs contribution in the $ZZ \rightarrow 2\ell 2\nu$ final state combining with $ZZ \rightarrow 4\ell$ final state and the no off-shell scenario is excluded at a p -value of 0.0003 (3.6 standard deviations). The $ZZ \rightarrow 4\ell$ final state has very little background and allows to see the on-shell H boson peak. The $ZZ \rightarrow 2\ell 2\nu$ final state has approximately 6 times larger branching fraction than the $ZZ \rightarrow 4\ell$ final state, which makes it possible to measure the small off-shell cross-section. It however suffers from large backgrounds and is not sensitive in the on-shell region. In terms of the statistical analysis, the $ZZ \rightarrow 4\ell$ final states has greater sensitivity on limiting the upper bound of the Higgs boson width while the $ZZ \rightarrow 2\ell 2\nu$ is sensitive when constraining the lower bound and is the major contribution of finding evidence of the off-shell production of the Higgs boson. Therefore, to extract the H boson width, the data from both channels are combined.

The $ZZ \rightarrow 2\ell 2\nu$ analysis faces several most important challenges, which are modeling of the signal, the continuum background and their interference; estimation of major background in a data-driven way; constraining the uncertainties introduced by the irreducible background; the measurement of trigger efficiencies. Other tasks, such as physics objects reconstructions and corrections, measurement of the lepton offline selection efficiencies, precise estimation of uncertainties and statistical interpretations are crucial studies to make, following the CMS standards. I have made various important contributions to this publication. In particular, I made measurements of the lepton and trigger efficiencies, which are crucial ingredients of the analysis as described in Sec. 5.1 and Sec. 5.2. Furthermore, I contributed to the estimation of the flavour-symmetric di-lepton background from $t\bar{t}$ and WW processes as described in Sec. 6.1. I attended hardware research on the topics of high-granularity calorimeter for the future HL-LHC in the very beginning of my research journey, introduced in Sec. 2.2.4. I also contributed to the CMS service work on the topic of Level-1 trigger data quality monitoring, which is introduced briefly in Sec. 3.1.1.

This thesis is divided into three parts, with part I giving an overview of theory and phenomenology, part II describing the accelerator and the detector of the experiment, and part III presenting the analysis of measurements of the Higgs boson properties from off-shell production in the ZZ final

state. Part I contain only one chapter 1 describing the standard model, the Higgs mechanism and the Higgs boson properties. Part II includes chapter 2, giving some details about the LHC and the CMS detector, and chapter 3, which describes the CMS trigger system and how we reconstruct physics objects in the CMS experiment. Part III contains four chapters related to the analysis, with chapter 4 summarizing how we use the data and simulations in the analysis, chapter 5 describing the analysis strategy in details, and chapter 6 describing the data-driven background estimation techniques and several control regions, and then the last chapter 7 showing final distributions, likelihood scans and data interpretations.

“Dear friend, I feel the silence of your great thoughts of many a deepening eventide on this beach when I listen to these waves.”

“The world puts off its mask of vastness to its lover. It becomes small as one song, as one kiss of the eternal.”

Rabindranath Tagore
Stray Birds

Part I

Theory fundamentals

The Standard Model and the Higgs boson

The standard model provides the modern understanding of all of the interactions of subatomic particles, except those due to gravity. Though it is not perfect, the theory has emerged as the best distillation of decades of research. In this chapter, Sec. 1.1 presents some basic information about elementary particles and fundamental interactions; Sec. 1.2 describes the standard model in a mathematical way by introducing the Lagrangian; Sec. 1.3 discusses about the Higgs production and decay modes, the off-shell production and how we can measure the Higgs width; Sec. 1.4 introduces the phenomenology of the Higgs anomalous couplings, which could potentially affect the width measurement.

1.1 Elementary particles and fundamental interactions

Elementary particles in particle physics are subatomic particles that have no internal structure. They are the smallest building blocks of the universe. The Standard Model (SM) of physics, a theory that describes the interactions of particles and forces, indicates several kinds of elementary particles shown Fig. 1.1. They can be divided into spin-one particles (gauge bosons), spin-half particles (fermions) and the spin-zero scalar boson (the Higgs). Fermions include three generations of leptons and anti-leptons (e^\pm, μ^\pm, τ^\pm) and their neutrinos ($\nu^e, \bar{\nu}^e, \nu^\mu, \bar{\nu}^\mu, \nu^\tau, \bar{\nu}^\tau$) as well as quarks and anti-quarks ($u, \bar{u}, d, \bar{d}, c, \bar{c}, s, \bar{s}, b, \bar{b}, t, \bar{t}$). Bosons include gauge bosons that act as interaction mediators (W^\pm, Z^0, γ, g) and the Higgs boson. However, the gravitons, which are thought to carry the force of gravity, are not accommodated by the SM. The strong, weak, and electromagnetic interactions are understood as arising due to the exchange of various spin-one bosons amongst the spin-half particles that make up matter. Furthermore, an elementary particle can be influenced by more than one fundamental interaction, in which case it has several charges. For example, gluons carry color charge and experience the strong interaction between themselves. Another case is that a muon can be influenced both by the electromagnetic interaction and the weak interaction due to its electric and weak charges.

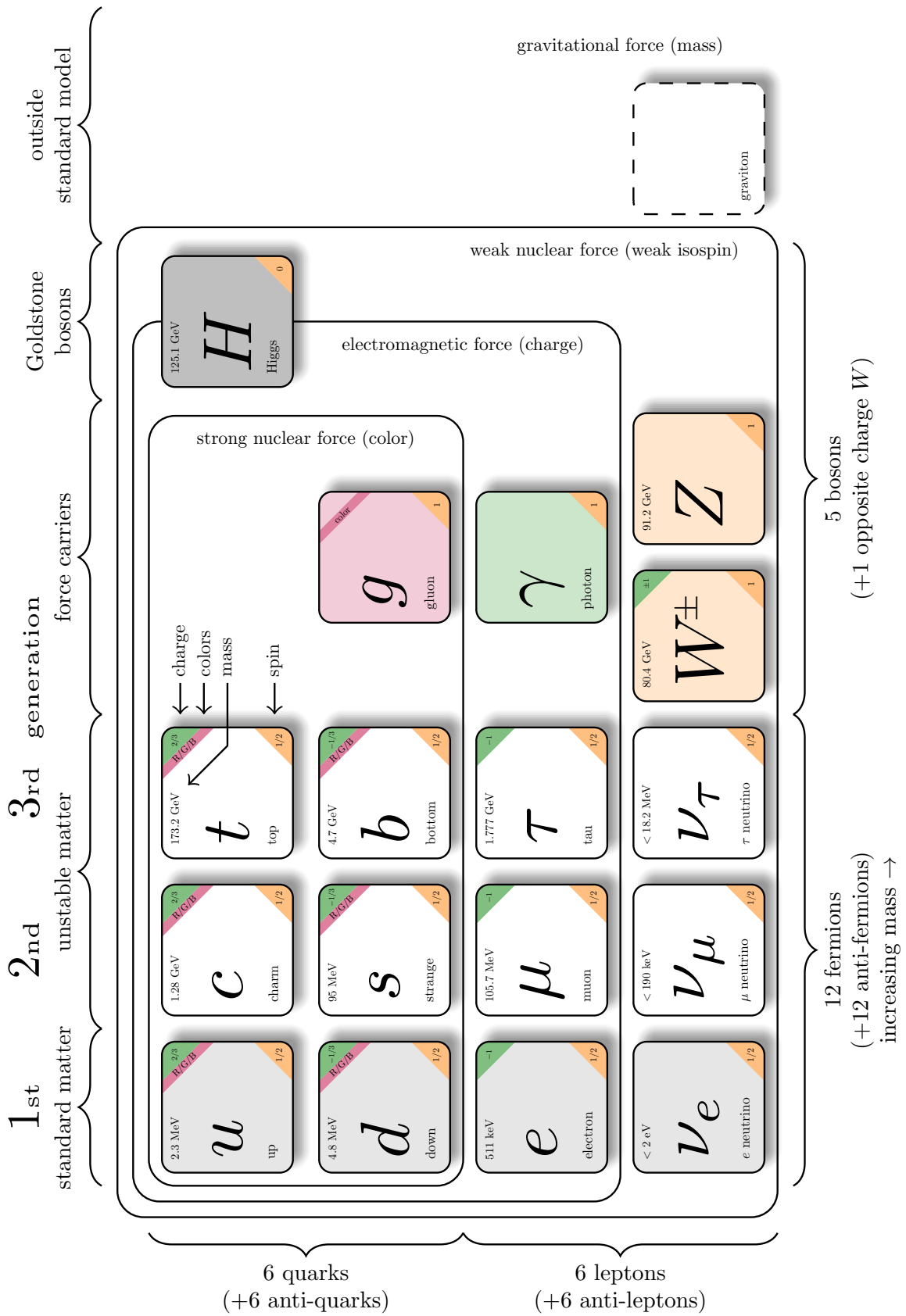


Figure 1.1: Particle family of the Standard Model [1]

1.2 The Standard Model description

1.2.1 The standard model Lagrangian

The Standard Model of particle physics is a quantum field theory. When handling quantum fields, the Lagrangian density describes the kinematics and dynamics of the quantum system. We can use the Lagrangian \mathcal{L} to depict SM in a very elegant way, following closely the way as it is explained in [2, 23, 24]:

$$\mathcal{L}_{\text{SM}} = \mathcal{L}_{\text{gauge}} + \mathcal{L}_{\text{f}} + \mathcal{L}_{\text{Yukawa}} + \mathcal{L}_{\text{Higgs}} \quad (1.1)$$

Where we group all the terms of SM Lagrangian into four sectors, $\mathcal{L}_{\text{gauge}}$, \mathcal{L}_{f} , $\mathcal{L}_{\text{Yukawa}}$ and $\mathcal{L}_{\text{Higgs}}$. Each sector describes certain kind of fundamental processes:

- $\mathcal{L}_{\text{gauge}} = -\frac{1}{4}F_{\mu\nu}F^{\mu\nu}$: The gauge Lagrangian density is a scalar product of the field strength tensor $F_{\mu\nu}$, where μ and ν are Lorentz indices representing the spacetime components. It contains the information of all gauge bosons, or vector bosons, and how they interact with each other.
- $\mathcal{L}_{\text{f}} = i\bar{\psi}\not{D}\psi$: This fermionic sector describes how gauge bosons interact with matter particles, or fermions (see Fig. 1.2). The field ψ and $\bar{\psi}$ describe quarks, leptons and their anti-counterparts. \not{D} is the covariant derivative characterizing all gauge bosons but without their self-interactions.
- $\mathcal{L}_{\text{Yukawa}} = \psi_i y_{ij} \psi_j \phi + \text{h.c.}$: The Yukawa Lagrangian density describes how fermions gain mass by coupling to the Brout–Englert–Higgs (BEH) field (or the Higgs field hereinafter) ϕ . y_{ij} is the element of the Yukawa matrix representing the coupling parameters to the ϕ , which is directly related to the mass of the fermions. The last term h.c. represents the hermitian conjugate of the former terms.
- $\mathcal{L}_{\text{Higgs}} = |D_\mu\phi|^2 - V(\phi)$: In the Higgs sector, $|D_\mu\phi|^2$ describes how the gauge bosons (only those of weak interactions) couple to the Higgs field and thereby obtain their mass. $V(\phi)$ describes the potential of the Higgs field as well as how Higgs bosons couple to each other.

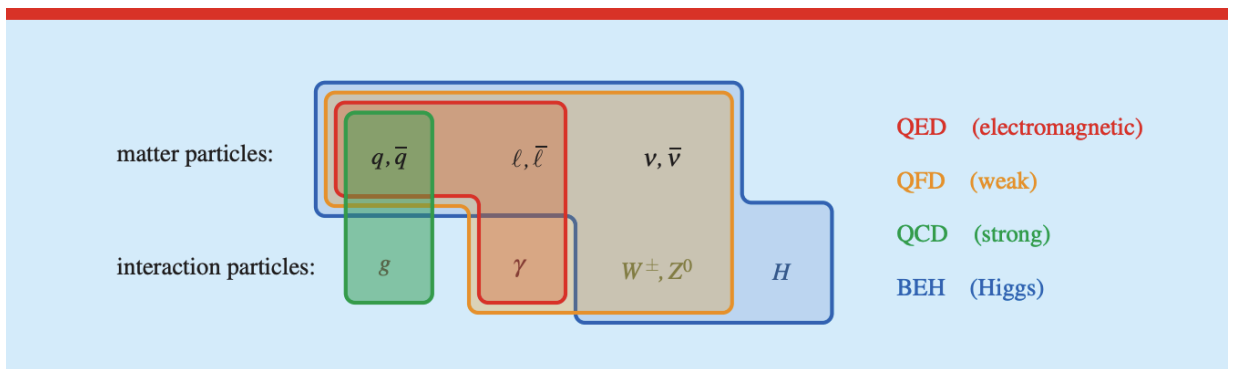


Figure 1.2: **Matter particles (fermions) and interaction particles (gauge bosons and the Higgs).** Gluons (g) couple to colour charge, which only quarks, antiquarks, and gluons themselves, have. Photons (γ) couple to electric charge, which is found in (anti)quarks and electrically charged (anti)leptons. The weak bosons (W^-, W^+, Z^0) couple to the weak charge, which all matter particles have. Weak bosons can also interact with the photon (but this is a pure weak interaction, not an electromagnetic one). And finally, the BEH field interacts with particles that have mass (all particles except the massless gluon and photon) [2].

Gauge sector The gauge Langrangian density sector can be rewritten in the format:

$$\mathcal{L}_{\text{gauge}} = -\frac{1}{4}G_{\mu\nu}^\alpha G^{\alpha\mu\nu} - \frac{1}{4}W^{a\mu\nu}W_{\mu\nu}^a - \frac{1}{4}B_{\mu\nu}B^{\mu\nu} \quad (1.2)$$

where

$$G_{\mu\nu}^\alpha = \partial_\mu G_\nu^\alpha - \partial_\nu G_\mu^\alpha + g_3 f_{\beta\gamma}^\alpha G_\mu^\beta G_\nu^\gamma \quad (1.3)$$

$$W_{\mu\nu}^a = \partial_\mu W_\nu^a - \partial_\nu W_\mu^a + g_2 \epsilon_{abc} W_\mu^b W_\nu^c \quad (1.4)$$

$$B_{\mu\nu} = \partial_\mu B_\nu - \partial_\nu B_\mu \quad (1.5)$$

$\alpha, \beta, \gamma = 1, 2, \dots, 8$ denote the 3×3 Gell-Mann matrices of $SU_c(3)$ and $a, b, c = 1, 2, 3$ denote the 2×2 Pauli matrices that act on the the $SU_L(2)$ -indices. The gauge couplings, $g_i, i = 1, 2, 3$ are associated with their symmetry groups $U_Y(1)$, $SU_L(2)$ and $SU_c(3)$. The eight spin-one particles, $G_\mu^\alpha(x)$, associated with the factor $SU_c(3)$ are called gluons and the associated subscript "c" is meant to denote "color". Three spin-one particles, $W_\mu^a(x)$, are associated with the factor $SU_L(2)$, and one, $B_\mu(x)$, with the factor $U_Y(1)$. The four spin-one bosons associated with the factors $SU_L(2) \times U_Y(1)$ are related to the physical bosons that mediate the weak interactions, W^\pm and Z^0 , and the familiar photon from Quantum Electrodynamics (QED). The term $g_3 f_{\beta\gamma}^\alpha G_\mu^\beta G_\nu^\gamma$ in Eq. 1.3 and the term $g_2 \epsilon_{abc} W_\mu^b W_\nu^c$ in Eq. 1.4 indicates self-interaction of the gauge fields G^α and W^α from the non-Abelian nature of $SU_c(3)$ and $SU_L(2)$. As for the $U_Y(1)$, which is Abelian in nature, the structure constants are zero and hence photons have no electric charge to interact with each other. Therefore, the electromagnetic interaction contribution in a form of Eq. 1.5 consists only of a kinetic term, the basis for the existence of free photons.

Fermionic sector The fermionic part of Langrangian density $\mathcal{L}_f = i\bar{\psi}\not{D}\psi$ is a simple version of a more complex one with

$$\mathcal{L}_f = -\frac{1}{2}\bar{L}_m\not{D}L_m - \frac{1}{2}\bar{E}_m\not{D}E_m - \frac{1}{2}\bar{Q}_m\not{D}Q_m - \frac{1}{2}\bar{U}_m\not{D}U_m - \frac{1}{2}\bar{D}_m\not{D}D_m \quad (1.6)$$

Spinors written in capital letters L, E, D, U, Q , or script letters $\mathcal{E}, \mathcal{U}, \mathcal{D}$, and neutrinos ν_i are taken as Majorana spinors. The left- and right-handed components of these spinors are denoted by subscripts L, R. Spinors written in lower case Roman letters $l_i, u_i, d_i, e, \mu, \tau, u, c, t, d, s, b$ are Dirac spinors. The electron field is represented in quantum electrodynamics by the Dirac spinor:

$$e = \begin{pmatrix} e_L \\ e_R \end{pmatrix} \quad (1.7)$$

In the standard model, however, the electron is represented by two Majorana fields, E and \mathcal{E} :

$$\mathcal{E} = \begin{pmatrix} e_L \\ \epsilon e_L^* \end{pmatrix}, \quad E = \begin{pmatrix} -\epsilon e_R^* \\ e_R \end{pmatrix} \quad (1.8)$$

where $\epsilon \equiv i\sigma_2 = \begin{bmatrix} 0 & 1 \\ -1 & 0 \end{bmatrix}$. Therefore, the Dirac spinor, e , is related to the Majorana fields, E and \mathcal{E} , by projecting onto the left- or right-handed part:

$$e = P_L \mathcal{E} + P_R E \quad (1.9)$$

The "left-handed" electron field \mathcal{E} appears within an $SU_L(2)$ -doublet with the neutrino field ν . This doublet is denoted L

$$P_L L = \begin{pmatrix} P_L \nu \\ P_L \mathcal{E} \end{pmatrix} \quad (1.10)$$

Similarly we denote another doublet with Q :

$$P_L Q_m = \begin{pmatrix} P_L \mathcal{U}_m \\ P_L \mathcal{D}_m \end{pmatrix} \quad (1.11)$$

where m is the number in increasing order of the fermion generation from 1 to 3.

We use the Feynman slash notation $\not{D} = \gamma_\mu D^\mu$ and now we can write the gauge-covariant derivatives \not{D} as following terms:

$$\begin{aligned} D_\mu L_m &= \partial_\mu L_m + \left[\frac{i}{2} g_1 B_\mu - \frac{i}{2} g_2 W_\mu^a \tau_a \right] P_L L_m \\ &\quad + \left[-\frac{i}{2} g_1 B_\mu + \frac{i}{2} g_2 W_\mu^a \tau_a^* \right] P_R L_m \\ D_\mu E_m &= \partial_\mu E_m + i g_1 B_\mu (P_R E_m) - i g_1 B_\mu (P_L E_m) \\ D_\mu Q_m &= \partial_\mu Q_m + \left[-\frac{i}{2} g_3 G_\mu^\alpha \lambda_\alpha - \frac{i}{2} g_2 W_\mu^a \tau_a - \frac{i}{6} g_1 B_\mu \right] P_L Q_m \\ &\quad + \left[\frac{i}{2} g_3 G_\mu^\alpha \lambda_\alpha^* + \frac{i}{2} g_2 W_\mu^a \tau_a^* + \frac{i}{6} g_1 B_\mu \right] P_R Q_m \\ D_\mu U_m &= \partial_\mu U_m + \left[-\frac{i}{2} g_3 G_\mu^\alpha \lambda_\alpha - \frac{2i}{3} g_1 B_\mu \right] P_R U_m \\ &\quad + \left[\frac{i}{2} g_3 G_\mu^\alpha \lambda_\alpha^* + \frac{2i}{3} g_1 B_\mu \right] P_L U_m \\ D_\mu D_m &= \partial_\mu D_m + \left[-\frac{i}{2} g_3 G_\mu^\alpha \lambda_\alpha + \frac{i}{3} g_1 B_\mu \right] P_R D_m \\ &\quad + \left[+\frac{i}{2} g_3 G_\mu^\alpha \lambda_\alpha^* - \frac{i}{3} g_1 B_\mu \right] P_L D_m \end{aligned} \quad (1.12)$$

Where λ_α denotes the Gell-Mann matrices. The electric charge Q of a field is defined in terms of the hypercharge Y and the $SU_L(2)$ charge's T_3 ($= \frac{1}{2} \lambda_3$) component by the relation of $Q = T_3 + Y$.

At this point, it is worth emphasizing that only terms of singlets under $SU_c(3) \times SU_L(2) \times U_Y(1)$ can appear in $\mathcal{L}_{\text{gauge}}$ and \mathcal{L}_f , otherwise it will break gauge invariance. This explains why mass terms do not appear in $\mathcal{L}_{\text{gauge}}$ and \mathcal{L}_f . However, as the results from experiments have shown, fermions and the W and Z bosons are not massless particles. The way those particles acquiring mass is introduced by the BEH mechanism, which preserves unitarity in the SM and will be explained in the next.

Yukawa sector The Yukawa sector $\mathcal{L}_{\text{Yukawa}} = \psi_i y_{ij} \psi_j \phi + \text{h.c.}$ can be rewritten as

$$\mathcal{L}_{\text{Yukawa}} = -f_{mn} \bar{L}_m P_R E_n \phi - h_{mn} \bar{Q}_m P_R D_n \phi - g_{mn} \bar{Q}_m P_R U_n \tilde{\phi} + \text{h.c.} \quad (1.13)$$

where ϕ denotes the scalar doublet, the so-called Higgs field $\phi = \begin{pmatrix} \phi^+ \\ \phi^0 \end{pmatrix}$. Its complex conjugate is

denoted $\tilde{\phi} \equiv \begin{pmatrix} \phi^{0*} \\ -\phi^{+*} \end{pmatrix}$. f_{mn} , h_{mn} and g_{mn} are 3×3 complex matrices determining the couplings of the fermions to the Higgs field, which are directly related to the mass of the particle. These parameters are not predicted by the SM, but have been determined experimentally. A particle with strong coupling to the Higgs field also couples strongly to the Higgs boson. Fig. 1.3 shows the latest results from the CMS experiment of coupling strengths of these massive particles to the Higgs boson. The term "h.c.", the hermitian conjugate of former term describing the antimatter particles, is necessary in this sector since the former term is not self-adjoint.

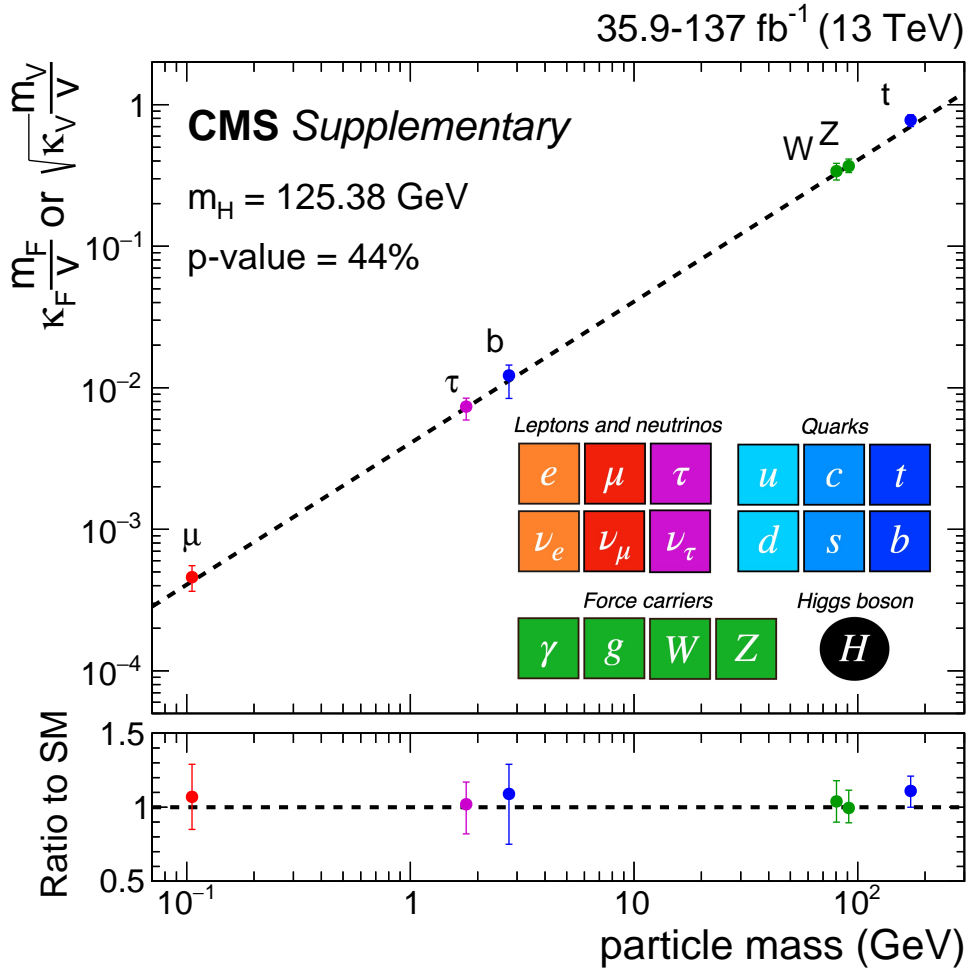


Figure 1.3: **The best-fit estimates for the reduced coupling modifiers extracted for fermions and weak bosons compared to their corresponding prediction from the SM.** The associated error bars represent 68% CL intervals for the measured parameters [3]. In the SM, the Yukawa coupling between the Higgs boson and the fermions (λ_F) is proportional to the fermion mass (m_F), while the coupling to weak bosons (g_V) is proportional to the square of the vector boson masses (m_V). The results from the κ -framework fit can therefore be translated in terms of reduced coupling strength modifiers, defined as $y_V = \sqrt{\kappa_V} m_V / V$ for weak bosons and $y_F = \kappa_F m_F / V$ for fermions, where ν is the vacuum expectation value of the Higgs field of 246.22 GeV.

Higgs sector The Higgs sector of the Langrangian density is composed of a kinetic and a potential term

$$\mathcal{L}_{\text{Higgs}} = - (D_\mu \phi)^\dagger (D^\mu \phi) - V(\phi^\dagger \phi) \quad (1.14)$$

in which

$$\begin{aligned} V(\phi^\dagger \phi) &= \lambda [\phi^\dagger \phi - \mu^2/2\lambda]^2 \\ &= \lambda (\phi^\dagger \phi)^2 - \mu^2 \phi^\dagger \phi + \mu^4/4\lambda \end{aligned} \quad (1.15)$$

and its covariant derivative be

$$D_\mu \phi = \partial_\mu \phi - \frac{i}{2} g_2 W_\mu^a \tau_a \phi - \frac{i}{2} g_1 B_\mu \phi \quad (1.16)$$

Where unitarity requires the constants λ and μ^2 to be real and stability demands that λ be positive. We further require that μ^2 be positive to ensure the ground state is not $SU_L(2) \times U_Y(1)$ invariant.

1.2.2 More on the Higgs sector

As mentioned in the previous section, mass terms cannot appear in $\mathcal{L}_{\text{gauge}}$ and \mathcal{L}_f due to the respectation of gauge invariance. Bosons are then expected to obtain mass in a special way, the Brout-Englert-Higgs (BEH) mechanism, which was developed simultaneously by R. Brout, F. Englert [25] and P. Higgs [26] in 1960s. The BEH mechanism implies the existence of a scalar boson as the excitation of the scalar field that was observed on July 2012 at the LHC by both CMS and ATLAS collaborations [27, 28]. The CMS [13, 29–35] and ATLAS [36–41] experiments have also set constraints on the spin-parity properties and anomalous couplings of the Higgs boson, finding results that favor the hypothesis of the Higgs being a scalar boson with $J^{PC} = 0^{++}$, but allowing small anomalous couplings to two electroweak(EW) gauge bosons (anomalous HVV couplings with VV denoting ZZ, WW, Z γ , $\gamma\gamma$), which will be introduced in the next Sec. 1.4.

Now let us go further into the details of the Higgs sector to demystify this mechanism. We can use the gauge freedom to transform ϕ to unitary gauge, defined as

$$\phi = \begin{pmatrix} 0 \\ \frac{1}{\sqrt{2}}(v + H) \end{pmatrix} \quad (1.17)$$

where H is a real field and v is determined by minimizing the potential in Eq. 1.15 that satisfies $v^2 = \mu^2/\lambda$, which indicates that the scalar field has a vacuum expectation value. This non-zero value underlies the Brout-Englert-Higgs mechanism describing electroweak symmetry breaking.

When we go back to the Langrangian using

$$D_\mu\phi = \frac{1}{\sqrt{2}} \begin{pmatrix} 0 \\ \partial_\mu H \end{pmatrix} - \frac{i}{2\sqrt{2}} \begin{pmatrix} g_2 W_\mu^3 + g_1 B_\mu & g_2 W_\mu^1 - i g_2 W_\mu^2 \\ g_2 W_\mu^1 + i g_2 W_\mu^2 & -g_2 W_\mu^3 + g_1 B_\mu \end{pmatrix} \begin{pmatrix} 0 \\ v + H \end{pmatrix} \quad (1.18)$$

the kinetic term of the scalar field becomes

$$\begin{aligned} -(D_\mu\phi)^\dagger (D^\mu\phi) &= -\frac{1}{2}\partial_\mu H\partial^\mu H - \frac{1}{8}(v + H)^2 g_2^2 (W_\mu^1 - iW_\mu^2) (W^{1\mu} + iW^{2\mu}) \\ &\quad - \frac{1}{8}(v + H)^2 (-g_2 W^{3\mu} + g_1 B^\mu) (-g_2 W_{3\mu} + g_1 B_\mu) \end{aligned} \quad (1.19)$$

The scalar potential term remains

$$\begin{aligned} V &= \frac{\lambda}{4} [(v + H)^2 - \mu^2/\lambda]^2 \\ &= \frac{\lambda}{4} (2vH + H^2)^2 \\ &= \lambda v^2 H^2 + \lambda v H^3 + \frac{\lambda}{4} H^4 \end{aligned} \quad (1.20)$$

Considering a constant gauge transformation, we write W_1 and W_2 as the real and imaginary parts of a complex, charged field:

$$W_\mu^\pm \equiv \frac{1}{\sqrt{2}} (W_\mu^1 \mp iW_\mu^2) \quad (1.21)$$

Normalizing the factors of another mass term, we define the mass eigenstate:

$$\begin{aligned} Z_\mu &\equiv \frac{-g_1 B_\mu + g_2 W_\mu^3}{\sqrt{g_1^2 + g_2^2}} \\ &\equiv W_\mu^3 \cos \theta_W - B_\mu \sin \theta_W \end{aligned} \quad (1.22)$$

where the last line defines the weak-mixing angle or Weinberg angle, θ_W , given by

$$\begin{aligned}\cos \theta_W &= \frac{g_2}{\sqrt{g_1^2 + g_2^2}} \\ \sin \theta_W &= \frac{g_1}{\sqrt{g_1^2 + g_2^2}}\end{aligned}\tag{1.23}$$

Another mass eigenstate is the combination of W_μ^3 and B_μ that is orthogonal to Z_μ :

$$A_\mu = W_\mu^3 \sin \theta_W + B_\mu \cos \theta_W = \frac{g_1 W_\mu^3 + g_2 B_\mu}{\sqrt{g_1^2 + g_2^2}}\tag{1.24}$$

At this point, we find the terms related to boson mass appear in $\mathcal{L}_{\text{Higgs}}$ in the form of

$$\mathcal{L}_{\text{Higgs}} = -\lambda v^2 H^2 - \frac{g_2^2 v^2}{4} W_\mu^+ W^{-\mu} - \frac{1}{2} \frac{(g_1^2 + g_2^2) v^2}{4} Z_\mu Z^\mu + \text{others}.\tag{1.25}$$

Comparing these terms with the standard form $-\frac{1}{2} M_\Phi^2 \Phi^2$ with Φ denoting the fields W_1, W_2, Z and H , we derive boson masses

$$\begin{aligned}m_H^2 &= 2\lambda v^2 = 2\mu^2, \\ M_W &= M_1 = M_2 = \frac{g_2 v}{2}, \\ M_Z^2 &= \frac{1}{4} (g_1^2 + g_2^2) v^2\end{aligned}\tag{1.26}$$

The masslessness of A_μ corresponds to the fact that the linear combination $Q = T_3 + Y$ is unbroken even when $v \neq 0$. A_μ is the corresponding massless gauge boson required for this unbroken symmetry. Since Q is the electric charge, we expect A_μ to have the couplings of the usual photon.

As for the mass terms for fermions, we can follow similar procedures replacing ϕ with the gauge transformation in $\mathcal{L}_{\text{Yukawa}}$. Since it is irrelevant to the topics, details of the fermion couplings to the scalar field will not expand in the text.

1.3 Properties of the Higgs boson

1.3.1 Higgs boson production and decay

Higgs bosons are produced in mostly four major modes in proton-proton collisions at LHC. They are

- Gluon-gluon fusion (ggF or ggH)
- Vector boson fusion (VBF or qqH)
- Associated production with a vector boson (VH)
- Associated production with top quarks ($t\bar{t}H$)

and corresponding Feynman diagrams are shown in Fig. 1.4.

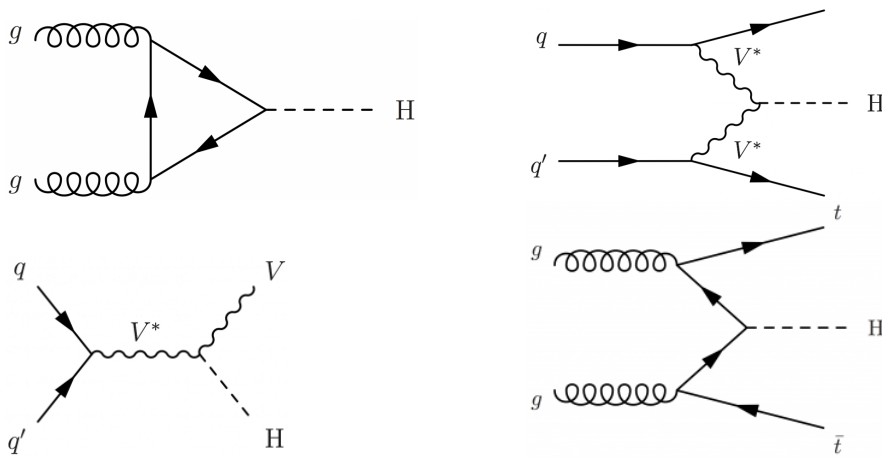


Figure 1.4: **Lowest order Feynman diagrams of 4 major scalar boson production modes at the LHC:** gluon-gluon fusion(top, left), vector boson fusion(top, right), associated production with a vector boson(bottom, left) and top quark fusion(bottom, right).

For a relatively low Higgs invariant mass region, the loop-induced ggF production mode dominates [42]. Secondly comes the VBF production mode in an order of cross-section magnitude. Its cross-section branching ratio over the one of ggF becomes larger as the mass increases. The VH production mode, also the so-called *Higgsstrahlung*, has a cross-section lower than the VBF one. The last in order comes the $t\bar{t}H$ production mode. (see Fig. 1.5)

In the SM, the Higgs boson can potentially decay into fermions and gauge bosons. The couplings of fermions to the scalar field are proportional to their masses. Fig. 1.6 shows the branching ratios of the Higgs decay in different channels. As for the Higgs decaying into weak bosons, the branching fractions become larger when the mass increases, which is especially obvious when the mass reaches certain threshold. Though massless gauge bosons do not couple to the scalar field, Higgs can still decay into those bosons (γ and g) in the processes associated with intermediate loop of virtual heavy quarks (t or b) or massive gauge bosons.

1.3.2 Off-shell Higgs production and Higgs interference

The Higgs boson produced on-shell with a mass around 125 GeV decays into a pair of massive gauge bosons V (with V representing for vector boson Z or W^\pm). The mass of the on-shell Higgs is between $[m_V, 2m_V]$. In order to satisfy four-momentum conservation, one of the vector bosons must

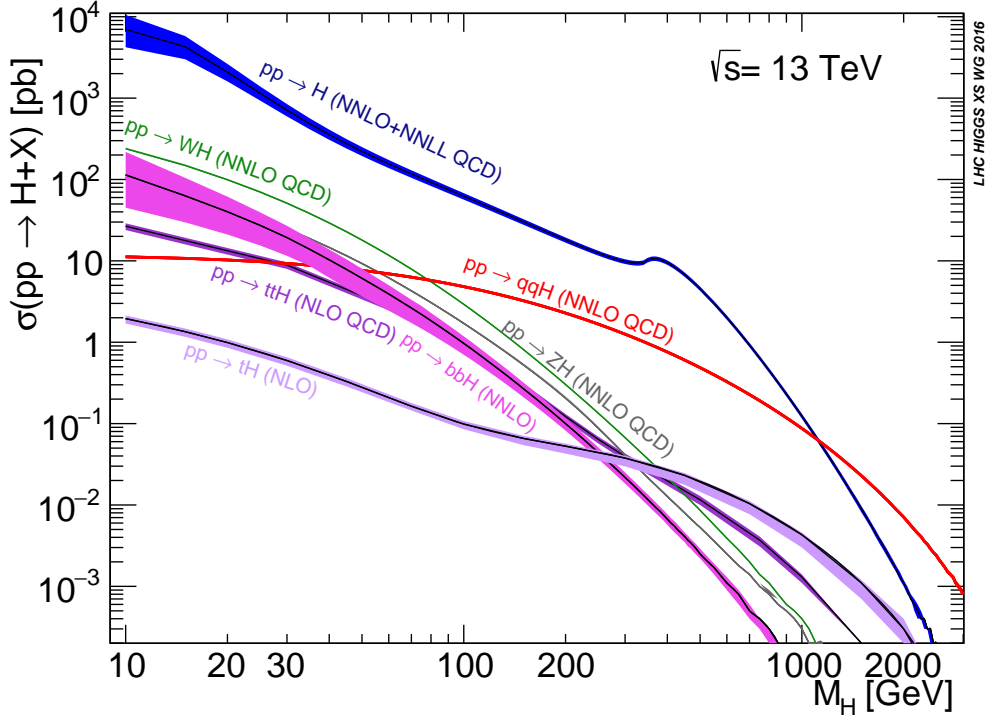


Figure 1.5: **Higgs boson production cross sections as a function of its mass** (SM-like coupling, narrow-width approximation, no electroweak corrections) at $\sqrt{s} = 13$ TeV [4].

be off-shell. When the Higgs boson is produced off-shell with a large invariant mass $m_{VV} > 2m_V$, the vector bosons themselves are produced on-shell. Due to this reason, the Higgs boson decay rate is enhanced when the mass reaches the vicinity of the Z boson pair production threshold. A further enhancement comes, in gluon fusion production, from the top-quark pair production threshold.

Destructive interference between the Higgs boson signal amplitude and the background continuum VV production occurs in this region, reaching a magnitude as large as twice the size of the signal production rate itself [43, 44] and growing as m_{VV} increases. This interference is important as it is predicted by the SM to preserve the unitarity of the scattering of massive gauge bosons, keeping the computation of the cross section for processes $gg \rightarrow VV$ and $VV \rightarrow VV$ finite [45–47].

Off-shell Higgs boson production can also be used to constrain the Higgs boson total width Γ_H [48, 49], which will be explained in details in the next.

1.3.3 Measurement of the Higgs boson width

The SM has a prediction of the Higgs boson width $\Gamma_H^{\text{SM}} = 4.1\text{MeV}$ but experimentally it is too small to be resolved by the detector. We could directly measure its width by the resonance peak using invariant mass distributions of the Higgs boson decaying into final state particles. $H \rightarrow ZZ$ and $H \rightarrow \gamma\gamma$ are the two best choices for this measurement. Several studies from the CMS and ATLAS experiment have reached the precisions of approximately 1GeV [50–52].

Another way constraining the Higgs boson width is using its off-shell production and decay to two Z bosons away from the resonance peak (the off-shell region), as it is well described and adopted for the width measurement in Ref. [13, 32, 53–55].

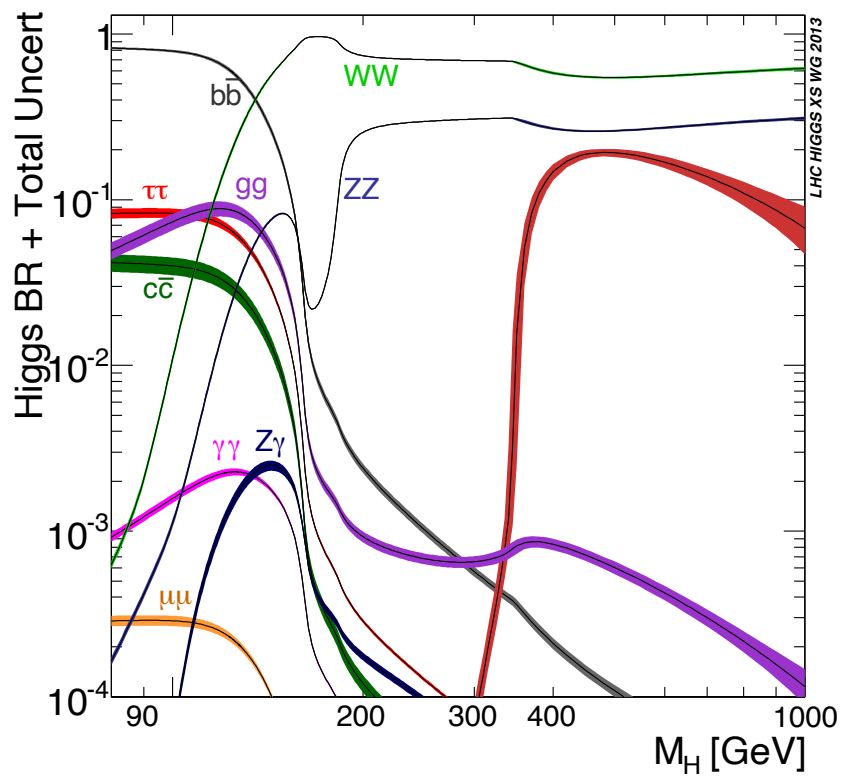


Figure 1.6: Standard Model Higgs boson decay branching ratios as a function of the invariant mass [4]

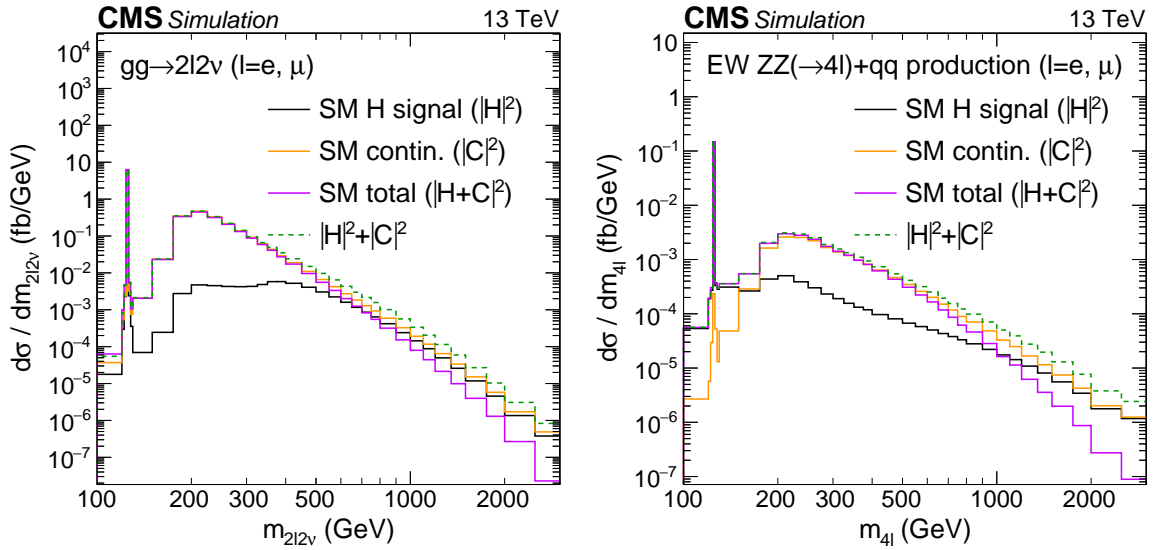


Figure 1.7: **The distributions of $m_{2\ell 2\nu}$ in the gluon fusion(left panel) and $m_{4\ell}$ in the electro-weak(right panel) production modes.** Different processes including the H ($|H|^2$), interfering continuum ($|C|^2$), their direct sum without the interference ($|H|^2 + |C|^2$) and the sum with interference included ($|H + C|^2$). The integrated luminosity is taken to be 1fb^{-1} .

The cross-section of the ggH production mode depends on Γ_H through the Higgs boson propagator

$$\frac{d\sigma_{gg \rightarrow H \rightarrow ZZ}}{dm_{ZZ}^2} \sim \frac{g_{ggH}^2 g_{HZZ}^2}{(m_{ZZ}^2 - m_H^2)^2 + m_H^2 \Gamma_H^2} \quad (1.27)$$

in which g_{ggH} and g_{HZZ} denote the couplings of the Higgs boson to gluons and Z bosons. m_H is the nominal value of the on-shell resonance peak around 125 GeV.

When we integrate the differential cross section in a small range around m_H , we derive the on-shell cross section

$$\sigma_{gg \rightarrow H \rightarrow ZZ}^{\text{on-shell}} \sim \frac{g_{ggH}^2 g_{HZZ}^2}{m_H \Gamma_H} \quad (1.28)$$

As mentioned in previous Sec. 1.3.2, the off-shell production cross section sizable especially in the dominant ggF production mode. The off-shell cross section is derived by integrating in a region above the mass threshold $2m_Z$, the off-shell region where $m_{ZZ} - m_H \gg \Gamma_H$

$$\sigma_{gg \rightarrow H^* \rightarrow ZZ}^{\text{off-shell}} \sim \frac{g_{ggH}^2 g_{HZZ}^2}{(2m_Z)^2} \quad (1.29)$$

By Eq. 1.28 and 1.29, measurement of the Higgs boson width Γ_H becomes a measurement of the relative off-shell and on-shell production in the $H \rightarrow ZZ$ channel, under the conditions that the coupling ratios remain consistent as predicted by the SM, which means the ggH production mode is always dominated by the top-quark loop and there are no new particles contributing. In the SM, the running of the Higgs couplings to elementary particles within the off-shell range is negligible at the LHC and at all currently planned experiments [56].

The measurement uses a ratio to denote off-shell event yield from ggF production normalised to the SM prediction, the signal strength $\mu_{\text{off-shell}}$

$$\mu_{\text{off-shell}} = \frac{\sigma_{gg \rightarrow H^* \rightarrow ZZ}^{\text{off-shell}}}{\sigma_{gg \rightarrow H^* \rightarrow ZZ}^{\text{off-shell, SM}}} = \kappa_{g, \text{off-shell}}^2 \cdot \kappa_{Z, \text{off-shell}}^2 \quad (1.30)$$

where $\kappa_{g, \text{off-shell}}$ and $\kappa_{Z, \text{off-shell}}$ are the off-shell coupling modifiers relative to the SM predictions associated with the $gg \rightarrow H$ production and the $H \rightarrow ZZ$ decay, respectively. Similarly, $\mu_{\text{on-shell}}$ for the on-shell Higgs boson production via ggF is given by:

$$\mu_{\text{on-shell}} = \frac{\sigma_{gg \rightarrow H \rightarrow ZZ^*}^{\text{on-shell}}}{\sigma_{gg \rightarrow H \rightarrow ZZ^*}^{\text{on-shell, SM}}} = \frac{\kappa_{g, \text{on-shell}}^2 \cdot \kappa_{Z, \text{on-shell}}^2}{\Gamma_H / \Gamma_H^{\text{SM}}} \quad (1.31)$$

which depends on the Higgs boson total width Γ_H . This also applies to the VBF production mode.

The CMS and ATLAS experiments have used this method to set constraints as tight as $0.08 \text{ MeV} < \Gamma_H < 9.16 \text{ MeV}$ at 95% confidence level (CL) on the Higgs boson total width in previous studies [13, 32, 53–55, 57]. By the works described in the present thesis, we reach the precision of $\Gamma_H = 3.2^{+2.4}_{-1.7} \text{ MeV}$ at 68% confidence level (CL) and $\Gamma_H = 3.2^{+5.3}_{-2.7} \text{ MeV}$ at 95% CL and for the first time find the evidence of the off-shell Higgs contributions to ZZ production. By the time writing this text, ATLAS presents its results of the width measurement with LHC Run-2 data, finding $\Gamma_H = 4.6^{+2.6}_{-2.5} \text{ MeV}$ at 68% CL [58].

1.4 Phenomenology of anomalous HVV interactions

The size and kinematic properties of off-shell Higgs production may also be affected by potential beyond the standard model (BSM) contributions to the couplings of the Higgs boson [18, 32, 59]. Previous studies have taken into account those effects and discussed about the parametrization in a very detailed way as it is shown in Ref. [13]. The signal scattering amplitude describing the interaction between a spin-0 Higgs boson and two spin-1 gauge bosons $VV(ZZ, WW, Z\gamma, \gamma\gamma)$ can be written as [16]

$$\begin{aligned} A \sim & \left[a_1^{\text{VV}} - \frac{\kappa_1^{\text{VV}} q_1^2 + \kappa_2^{\text{VV}} q_2^2}{(\Lambda_1^{\text{VV}})^2} - \frac{\kappa_3^{\text{VV}} (q_1 + q_2)^2}{(\Lambda_Q^{\text{VV}})^2} \right] m_{V_1}^2 \epsilon_{V_1}^* \epsilon_{V_2}^* \\ & + a_2^{\text{VV}} f_{\mu\nu}^{*(1)} f^{*(2)\mu\nu} \\ & + a_3^{\text{VV}} f_{\mu\nu}^{*(1)} \tilde{f}^{*(2)\mu\nu} \end{aligned} \quad (1.32)$$

where ϵ_i is the polarization vector of gauge boson V_i , $f^{(i)\mu\nu} = \epsilon_i^\mu q_i^\nu - \epsilon_i^\nu q_i^\mu$ is a scalar tensor constructed from the polarization vector and the momentum of the gauge boson, and $\tilde{f}_{\mu\nu}^{(i)} = \frac{1}{2} \epsilon_{\mu\nu\rho\sigma} f^{(i)\rho\sigma}$ is its pseudoscalar counterpart. When at least one of the gauge bosons V is massive, m_{V_1} is the pole mass of that gauge boson. We denote the scales of BSM physics with Λ_1 and Λ_Q . Therefore, a_i^{VV} , $1/\Lambda_1$ and $1/\Lambda_Q$ denote the coupling-strength modifiers of the corresponding HVV amplitudes, where a_i^{VV} can be any complex number, and κ_i^{VV} with $|\kappa_i^{\text{VV}}| = 0$ or 1 are also complex. If we assume that those couplings are constant and real, the Eq. 1.32 of the scattering amplitude is equivalent to an effective Lagrangian notation.

We assume the custodial symmetry $a_1^{\text{ZZ}} = a_1^{\text{WW}}$ when considering the only leading tree-level contributions $a_1^{\text{ZZ}} \neq 0$ and $a_1^{\text{WW}} \neq 0$. The terms with the rest modifiers (a_2, a_3, Λ_1 and Λ_Q) are considered anomalous contributions arising from either loop effects in the SM or BSM physics. Symmetry and gauge invariance require $\kappa_1^{\text{ZZ}} = \kappa_2^{\text{ZZ}} = -\exp(i\phi_{\Lambda_1}^{\text{ZZ}})$, $\kappa_1^{\gamma\gamma} = \kappa_2^{\gamma\gamma} = 0$, $\kappa_1^{\text{gg}} = \kappa_2^{\text{gg}} = 0$, $\kappa_1^{Z\gamma} = 0$, and $\kappa_2^{Z\gamma} = -\exp(i\phi_{\Lambda_1}^{Z\gamma})$. While not strictly required, the same symmetry is considered in the WW case $\kappa_1^{\text{WW}} = \kappa_2^{\text{WW}} = -\exp(i\phi_{\Lambda_1}^{\text{WW}})$.

In this analysis, we only consider a_i^{VV} with VV denoting ZZ or WW and ignore $Z\gamma$ and $\gamma\gamma$ terms, since no sizable off-shell enhancement and no obvious off-shell threshold are found in $H \rightarrow Z\gamma$ or $H \rightarrow \gamma\gamma$. While the $a_{2,3}^{Z\gamma}$ and $a_{2,3}^{\gamma\gamma}$ are measured under off-shell scenario in the study using LHC

Run-I data [31], the precision is not competitive with the on-shell measurements. On the other hand, because we are only able to test the $\Lambda_1^{Z\gamma}$ with off-shell photon decaying into a pair of fermions, it is preferable performing the test in the on-shell analysis. The Λ_Q term depends only on the invariant mass of the Higgs boson and is only measurable through the off-shell region. Previous study already set constraints on this parameter with Run-I data [32] and it is not considered in our analysis.

Therefore, the ZZ labels for the ZZ interactions are omitted since other terms are not considered and we also assume $a_i^{ZZ} = a_i^{WW}$ to have WW integrated into the test. This assumption does not affect analyzing the kinematics of the events since the difference between kinematic distributions in events initiated by WW and ZZ fusion can be ignored. We use a generic notation a_i to denote a_2 , a_3 , and $1/\Lambda_1$, the three couplings parameters tested in this analysis as listed in Tab. 1.1.

By taking the ratios of each term to the total cross section, most systematic uncertainties can be canceled. Therefore, measurement of a_i relative to the dominant SM-like contribution a_1 is a preferable approach. For this purpose, the effective fractional ZZ cross sections f_{ai} and phases ϕ_{ai} are defined as

$$f_{ai} = \frac{|a_i|^2 \sigma_i}{\sum_{j=1,2,3\dots} |a_j|^2 \sigma_j},$$

$$\phi_{ai} = \arg\left(\frac{a_i}{a_1}\right),$$
(1.33)

where σ_i is the cross section for the process corresponding to $a_i = 1$ and $a_{j \neq i} = 0$, while $\tilde{\sigma}_{\Lambda_1}$ is the effective cross section for the process corresponding to $\Lambda_1 = 1\text{TeV}$, given in units of fb TeV^4 . The cross-section ratios are quoted in Tab. 1.1. The a_i/a_1 ratios can be obtained from the ratio f_{ai}/f_{a1} , the cross-section ratios, and the phase ϕ_{ai} as

$$\frac{a_i}{a_1} = \sqrt{\frac{f_{ai}}{f_{a1}} \frac{\sigma_1}{\sigma_i}} e^{i\phi_{ai}}.$$
(1.34)

The effective fractions f_{ai} are bounded between 0 and 1 and do not depend on the coupling convention. In most cases, uncertainties on these measurements scale with integrated luminosity as $1/\sqrt{\mathcal{L}}$ until effects of interference become important. Furthermore, the values of f_{ai} have a simple interpretation as the fractional size of the BSM contribution for the $H \rightarrow 2\ell 2\nu$ or $H \rightarrow 2e2\mu$ decay. For example, $f_{ai} = 0$ indicates a pure SM-like H, $f_{ai} = 1$ gives a pure BSM particle, and $f_{ai} = 0.5$ means that the two couplings contribute equally to the $H \rightarrow 2\ell 2\nu$ process. Because real couplings are tested, we will use the signed fraction $\bar{f}_{ai} = f_{ai} \cos(\phi_{ai})$ to parametrize the results interpreted in this context.

Table 1.1: The anomalous HVV couplings considered in the measurement assuming a spin-0 Higgs boson. The definition of the effective fractions f_{ai} is discussed in the text, and the translation constants are the cross section ratios corresponding to the process $H \rightarrow 2\ell 2\nu$ (or equivalently, $H \rightarrow 2e2\mu$) with the Higgs mass $m_H = 125\text{GeV}$. These calculations are performed using the JHUGEN program [14–18].

Anomalous Coupling	Coupling Phase	Effective Fraction	Translation Constant
a_2	ϕ_{a2}	f_{a2}	$\sigma_1/\sigma_2 = 2.77$
a_3	ϕ_{a3}	f_{a3}	$\sigma_1/\sigma_3 = 6.53$
Λ_1	ϕ_{Λ_1}	f_{Λ_1}	$\sigma_1/\tilde{\sigma}_{\Lambda_1} = 1.47 \times 10^4 \text{TeV}^{-4}$

Part II

Experimental point of view

The Large Hadron Collider and The Compact Muon Solenoid

Studying the properties of the Higgs boson, a subatomic particle with very high mass (about 125 GeV), is not an easy task without first-class experimental equipment. Fortunately, we have the world's largest and most powerful particle accelerator, the Large Hadron Collider (LHC), and a general-purpose detector, the Compact Muon Solenoid (CMS) at the LHC. The LHC is described in Sec. 2.1 and the CMS detector and sub-detectors are described in Sec. 2.2.

2.1 The Large Hadron Collider

The Large Hadron Collider (LHC) is the world's largest and most powerful particle accelerator [60]. It was built by the European Organization for Nuclear Research (CERN) between 1998 and 2008. The LHC consists of a 27-kilometre ring of superconducting magnets with a number of accelerating structures beneath the France–Switzerland border near Geneva.

Table 2.1: **Important parameters of the LHC for Run-2**

Quantity	Number
Circumference	26 659 m
Dipole operating temperature	1.9 K (-271.3°C)
Number of magnets	9593
Number of main dipoles	1232
Number of main quadrupoles	392
Number of RF cavities	8 per beam
Nominal energy, protons	6.5 TeV
Nominal energy, ions	2.56 TeV/u (energy per nucleon)
Nominal energy, protons collisions	13 TeV
No. of bunches per proton beam	2808
No. of protons per bunch (at start)	1.2×10^{11}
Number of turns per second	11245
Number of collisions per second	1 billion

CERN's Accelerator Complex

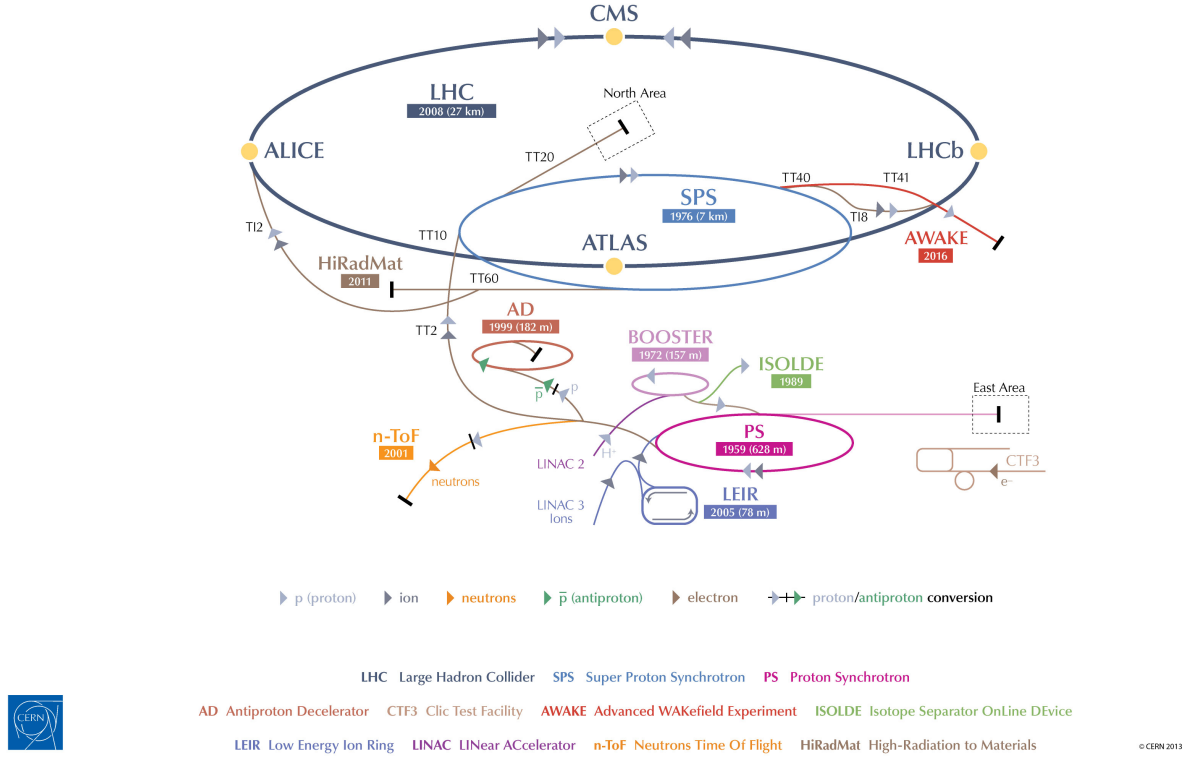


Figure 2.1: The LHC accelerator complex and experiments[5]

2.1.1 Accelerator and Particle beams

Inside the LHC, two particle beams travel at close to the speed of light before they are made to collide. The beams travel in separate beam pipes at ultrahigh vacuum. Their trajectories are bent by a strong magnetic field provided by superconducting electromagnets working at a temperature of $1.9K$. The number of events per second generated in the LHC collisions is given by [61]

$$N_{\text{event}} = \mathcal{L}\sigma_{\text{process}} \quad (2.1)$$

where σ_{process} is the cross section for the process under study and \mathcal{L} is the machine instantaneous luminosity. The machine instantaneous luminosity is determined by the beam parameters whose typical values in Run 2 data taking period are listed in Tab. 2.1 and can be written for a Gaussian beam distribution as:

$$\mathcal{L} = \frac{N_b^2 n_b f_{\text{rev}} \gamma_r}{4\pi \epsilon_n \beta^*} F \quad (2.2)$$

where $N_b = 2808$ is the number of bunches per beam, $n_b = 1.15 \times 10^{11}$ the number of particles per bunch, $f_{\text{rev}} = 11.2\text{kHz}$ the revolution frequency, γ_r the relativistic gamma factor, $\epsilon_n = 3.75\mu\text{m}$ the normalized transverse beam emittance, $\beta^* \approx 0.55\text{m}$ the beta function at the collision point and F the geometric luminosity reduction factor due to the crossing angle at the interaction point (IP):

$$F = 1/\sqrt{1 + \left(\frac{\theta_c \sigma_z}{2\sigma^*}\right)^2} \quad (2.3)$$

where θ_c is the full crossing angle at the IP, σ_z the RMS bunch length and σ^* the transverse RMS beam size at the IP. (The above expression assumes equal beam parameters for both circulating

beams). The exploration of rare events in the LHC collisions therefore requires both high beam energies and high beam intensities. The two high luminosity experiments at the LHC, ATLAS and CMS, aim at a peak luminosity of $10^{34} \text{ cm}^{-2} \text{ s}^{-1}$ (upgraded to $1.9 \times 10^{34} \text{ cm}^{-2} \text{ s}^{-1}$ in the year of 2017, mostly by reducing the factors in denominator, ϵ_n and β^*)

The orbit of the LHC has to be a closed loop, and so the main dipole magnets in the ring have to define a bending angle of exactly 2π overall. If α denotes the bending angle of a single magnet, then

$$\alpha = \frac{ds}{\rho} = \frac{B ds}{B \cdot \rho} \quad (2.4)$$

We therefore require that

$$\frac{\int B dl}{B \cdot \rho} = 2\pi \quad (2.5)$$

In the case of the LHC, the dipole field has been pushed to the highest achievable values; 1232 superconducting dipole magnets, each of length 15 m, define the geometry of the ring and the maximum momentum for the stored proton beam. Using the equation given above, for a maximum momentum of $p = 7 \text{ TeV}$ we obtain a required magnetic field of

$$B = \frac{2\pi \cdot 7000 \cdot 10^9 \text{ eV}}{1232 \cdot 15 \text{ m} \cdot 2.99792 \cdot 10^8 \text{ ms}^{-1}} = 8.33 \text{ T} \quad (2.6)$$

The power loss due to synchrotron radiation depends on the bending radius and the energy of the particle beam:

$$P_s = \frac{2}{3} \alpha \hbar c^2 \frac{\gamma^4}{\rho^2} \quad (2.7)$$

2.1.2 Luminosity accumulation

In CMS, the online luminosity measurements are provided by the Pixel Luminosity Telescope (PLT), the Hadronic Forward (HF) calorimeter, the Beam Conditions Monitor-Fast (BCM1F), and the Drift Tubes (DT). Offline, in addition to the preceding, the Pixel Cluster Counting (PCC) algorithm is used with the main CMS pixel detector, and vertex counting is also available. The luminosity calibration is derived from the analysis using separation scans, the so called "van der Meer scans". As shown in Fig. 2.2, the recorded integrated luminosities for each year during Run 2 data taking are: 3.86 fb^{-1} for 2015, 38.25 fb^{-1} for 2016, 44.98 fb^{-1} for 2017 and 63.67 fb^{-1} for 2018.

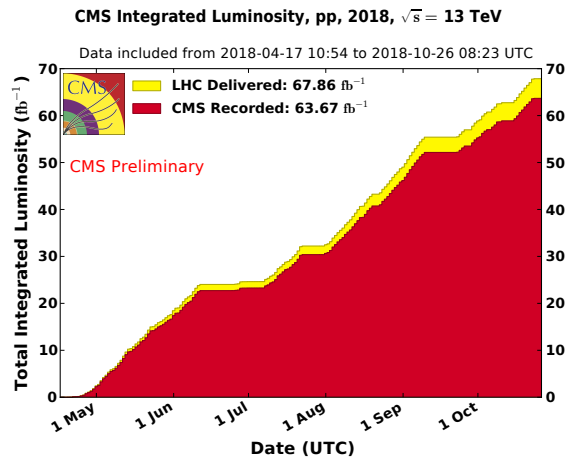
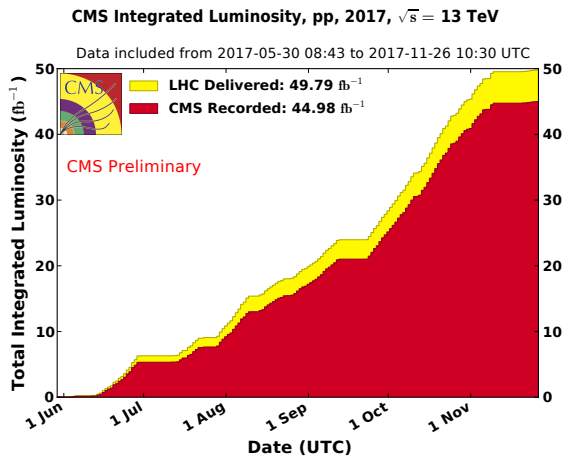
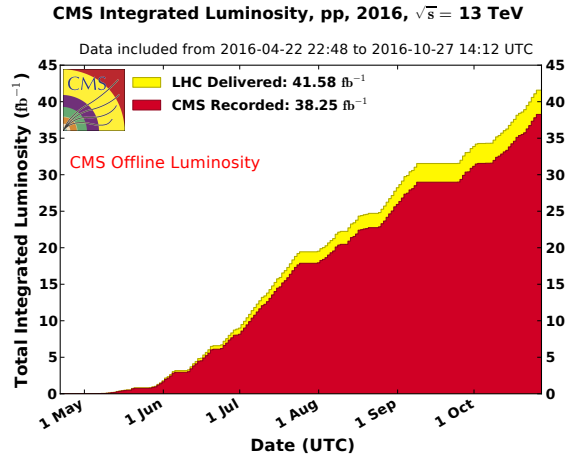
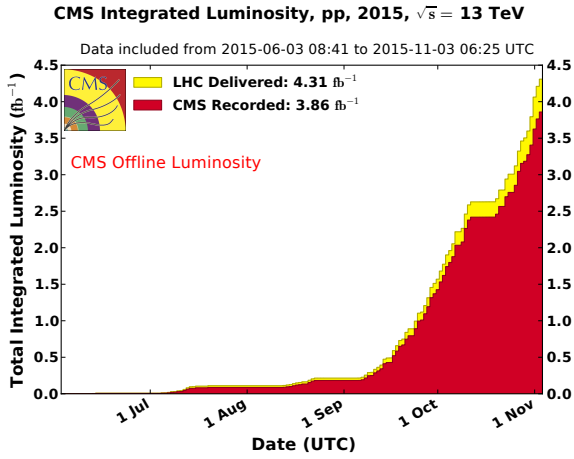


Figure 2.2: The measured luminosity delivered by the LHC to CMS (yellow) and recorded by CMS (red) during stable beams and for proton-proton collisions at a 13 TeV center-of-mass energy in the year of 2015 (left, top), 2016 (right, top), 2017 (left, bottom), 2018 (right, bottom) [6]

2.2 The Compact Muon Solenoid

The Compact Muon Solenoid (CMS) detector is a multi-purpose apparatus due to operate at the LHC for proton-proton and heavy ion collisions. This section will introduce designs and functions of the CMS detector and its subdetectors.

2.2.1 Overview

CMS detector as a whole is cylindrical in shape. Its overall length is about 29 meters and its overall diameter is about 15 meters. In the inner part, there is a 13-m-long, 6-m-inner-diameter, 3.8-T superconducting solenoid providing a large bending power (12 Tm) as shown in Fig. 2.3. It is pretty compact compared with another general-purpose detector on the LHC, i.e the ATLAS detector, which is with 25 m in height and 44 m in length, and immersed in a 2 T solenoidal field. Large

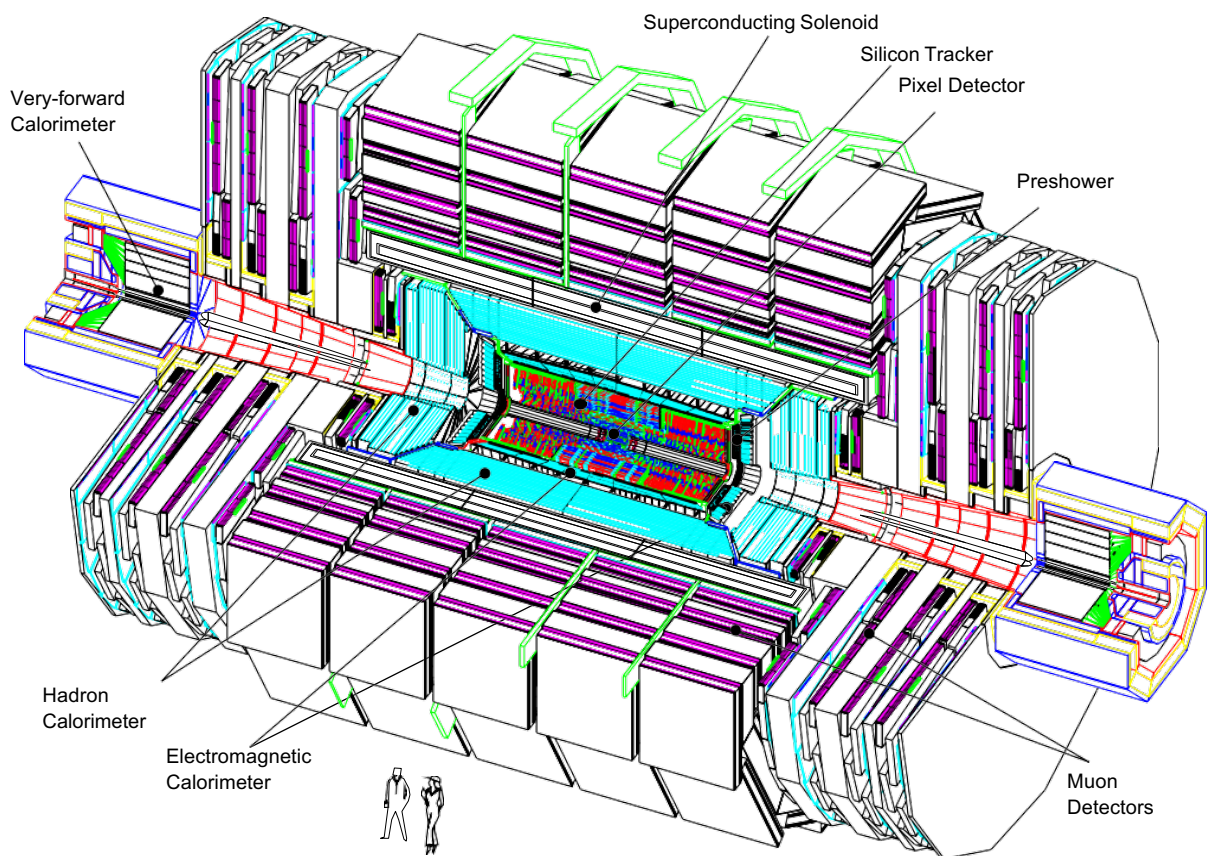


Figure 2.3: A perspective view of the CMS detector

bending power is needed to measure precisely the momentum of high-energy charged particles such as muons. A magnetic field of 3.8-T guarantees good momentum resolution for high momentum ($= 1$ TeV) muons up to pseudo-rapidity (shown in Fig. 2.5) of 2.5, without intense demands on the chamber space resolution.

Components of the CMS detector CMS detector (Fig. 2.4) [8] consists of layers of material that exploit the different properties of particles to catch and measure the energy and momentum of each one:

- **Inner tracker:** a high quality central tracking system to give accurate momentum measurements

CMS DETECTOR

Total weight : 14,000 tonnes
 Overall diameter : 15.0 m
 Overall length : 28.7 m
 Magnetic field : 3.8 T

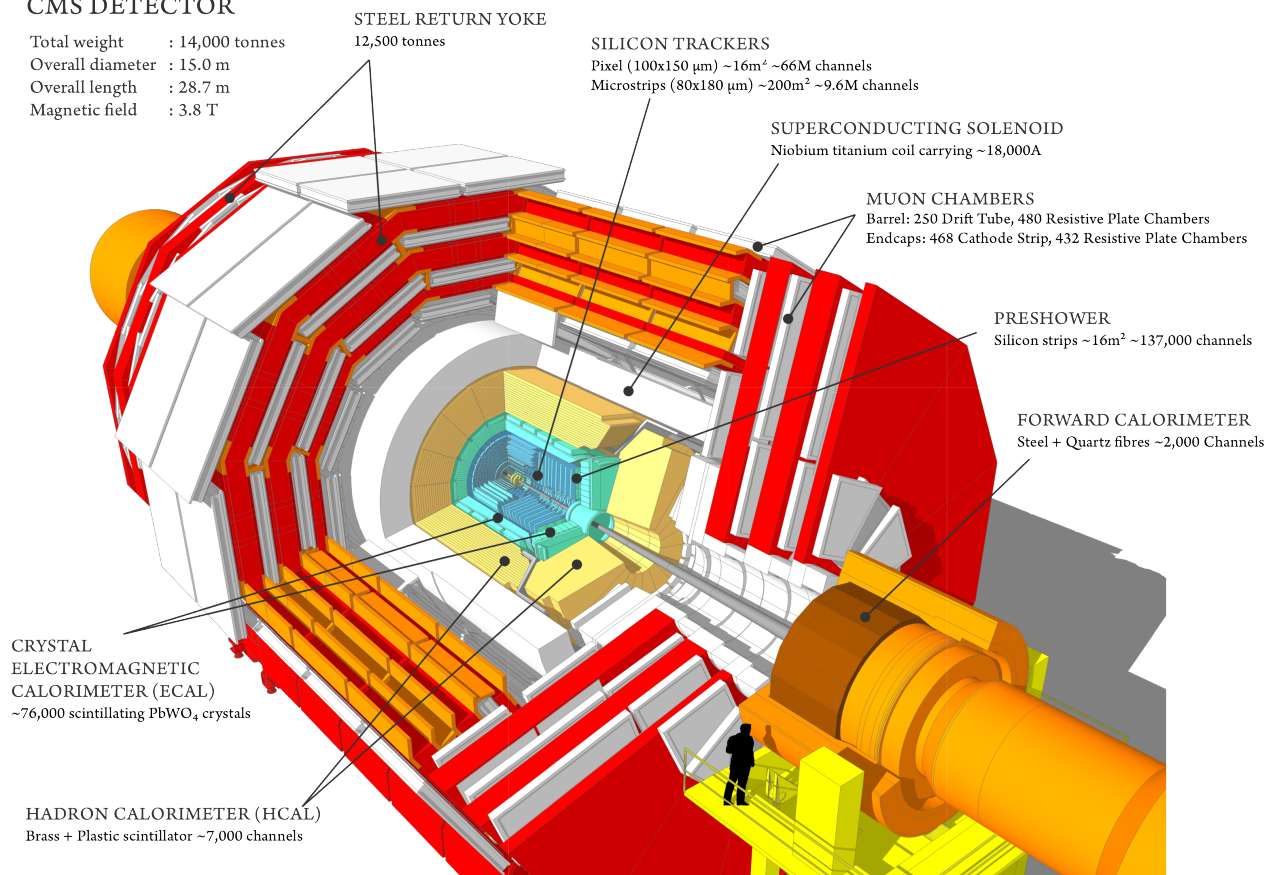


Figure 2.4: A schematic view of the CMS detector [7]

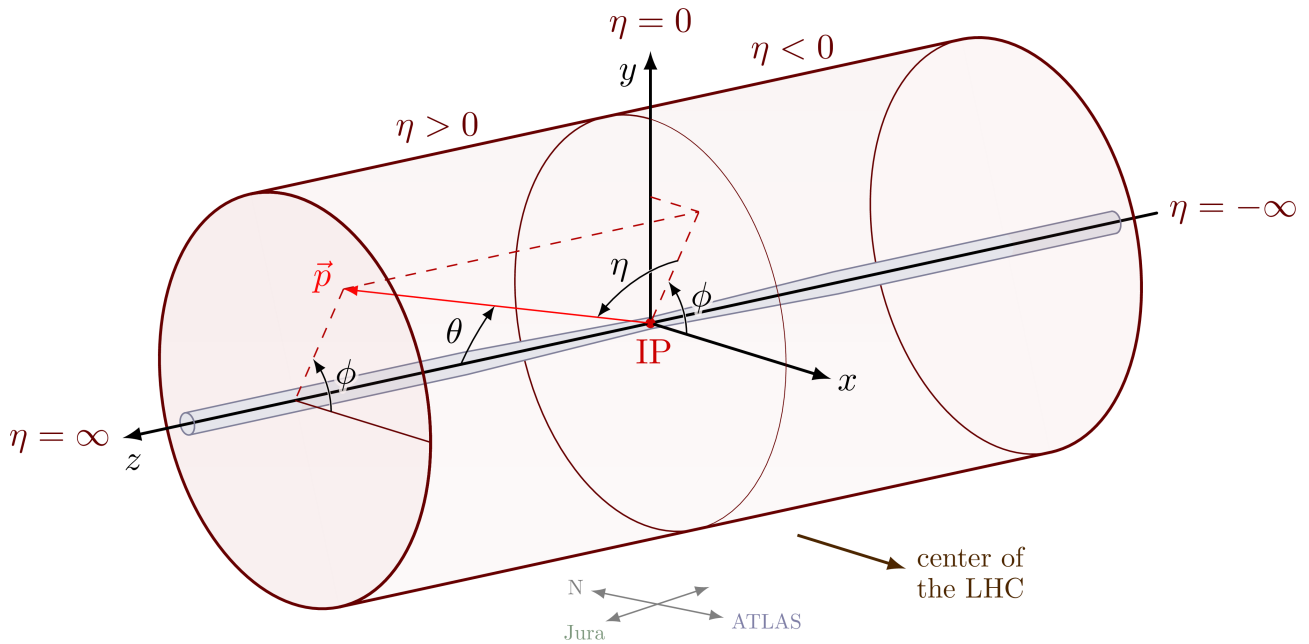


Figure 2.5: An illustration of the conventional 3D coordinate system at the CMS detector

- **ECAL:** a high resolution electro-magnetic calorimeter to detect and measure electrons and photons
- **HCAL:** a “hermetic” hadron calorimeter, designed to surround almost entirely the collision and prevent most particles from being undetected
- **Muon system:** a high performance system to detect and measure muons

CMS coordinate system See Fig. 2.5

- IP is the interaction point of proton-proton collision
- x-axis points to the center of the LHC
- z-axis is along the beampipe and points in the anti-clockwise direction of the LHC
- y-axis points upwards to form a right-handed coordinate system
- θ is the polar angle with respect to the z-axis
- Pseudo-rapidity η describes the angle of a particle relative to the beam axis and is defined as

$$\eta \equiv -\ln \left[\tan \left(\frac{\theta}{2} \right) \right] \quad (2.8)$$

- Azimuthal angle ϕ is the signed angle measured from the azimuth reference direction (x-axis) to the orthogonal projection of \vec{p} on $x - y$ plane.

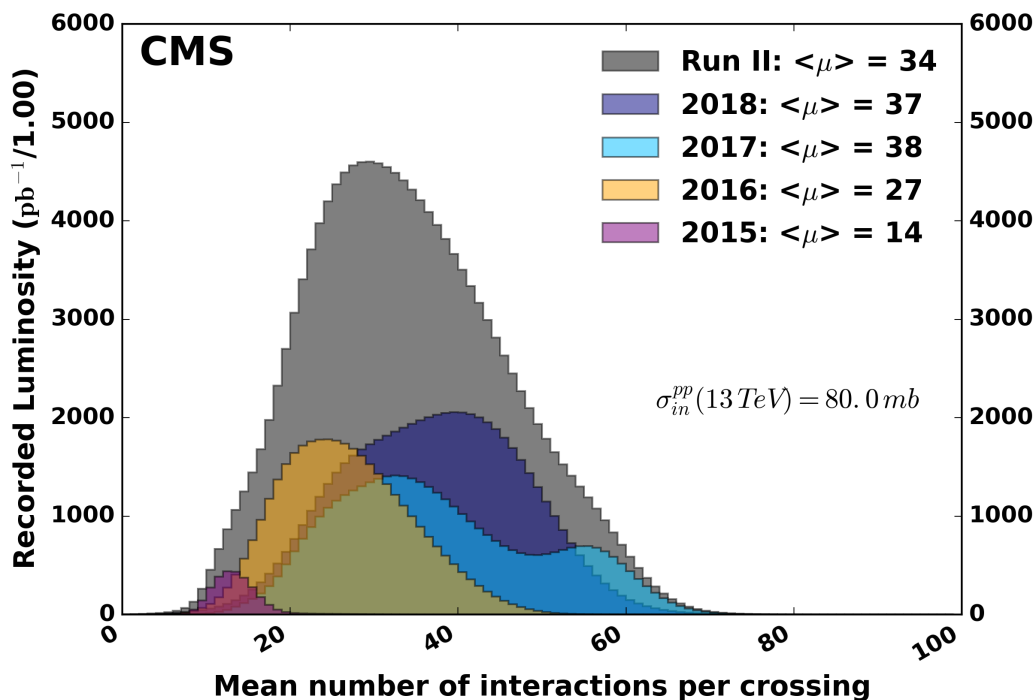


Figure 2.6: Distribution of the average number of interactions per crossing (pileup) for pp collisions during Run-2 [6]

2.2.2 Inner tracking system

The CMS tracker is an all-silicon detector closest to the interaction point (IP). The sensors are placed in concentric cylinders around the LHC beampipes in the barrel part, and in disks perpendicular to the beams direction in the endcaps. The function of the tracker is to measure space-points along the trajectories of charged particles with high precision and and reconstruct the secondary vertexes efficiently, for charged particles emitted within $|\eta| < 2.5$.

The CMS detector will experience dozens inelastic interactions per bunch crossing (referred to as event pile-up) during Run-2 as shown in Fig. 2.6. Therefore the tracker should feature high granularity and fast time response to ensure that the trajectories are reliably measured and attributed to the corresponding bench crossing. Another requirement is to use less material to limit multiple scattering, bremsstrahlung, photon conversion, and nuclear interactions. The tracker also suffers from severe radiation damage from intense particle flux from the very near of the IP. The design of the tracking system is challenging. These requirements above lead to a tracker design entirely using silicon detectors.

A schematic view of the current CMS tracker, including the pixel detector, is shown in Fig. 2.7. Before 2016-2017 upgrade, the pixel detector consist of 3 layers in the barrel and 2 disks in the endcap with 66 million $100 \times 150\mu\text{m}^2$ pixel cells at distance of 4 to 11 cm from the beamline. During the 2016-2017 year-end shutdown of the LHC, the 3-layer barrel (BPIX), 2-disk endcap (FPIX) system is replaced with a 4-layer barrel, 3-disk endcap system for four hit coverage [62]. The upgraded pixel detector covers radii from 29 mm to 160 mm, and counts about 124 million channels. The fourth barrel layer at a radius of 16 cm provides redundancy in pattern recognition and reduces fake rates with high pile-up. It also provides a safety margin if the first silicon strip layer degrades more rapidly in radiation exposure than expected.

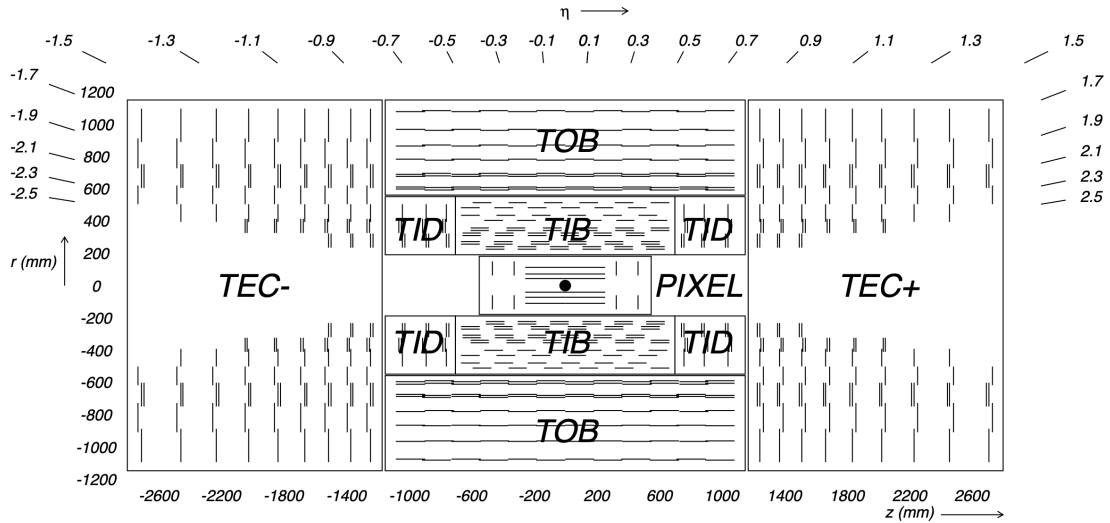


Figure 2.7: **Cross section of the current CMS tracker**, showing the nomenclature used to identify different sections. Each line represents a detector module. Double lines indicate back-to-back modules which deliver stereo hits in the strip tracker [8].

As we go further away from the beamline, it is not economically wise covering larger areas with pixel cells. Instead, we use silicon strips in the outer layers of the tracker. The silicon strip detectors are divided in the tracker inner barrel part (TIB), the tracker inner disks (TID), the tracker outer barrel (TOB) and tracker end-caps (TEC). The layout of the Tracker substructures is sketched in Fig. 2.7 Stereo modules are spaced in four layers in the barrel and multiple layers in the endcap to allow for two-dimension measurement. Some layers consist of two back-to-back silicon strip sensor modules aligned at a 100 mrad relative angle to provide a measurement of the third coordinate.

2.2.3 The electromagnetic calorimeter

The primary function of the electromagnetic calorimeter (ECAL) is to identify and measure precisely the energy of photons and electrons. A 3D view of the ECAL system can be found in Fig. 2.8 The ECAL is a hermetic, homogeneous calorimeter comprising 61200 lead tungstate (PbWO_4) crystals in the ECAL Barrel (EB), from $0 < |\eta| < 1.48$, and 14648 crystals in the ECAL Endcaps (EE) from $1.48 < |\eta| < 3$ [63]. The choice of using PbWO_4 crystals was based on the following considerations: PbWO_4 has a short radiation length (shorter radiation length means shorter distance over which the electron loses all but $1/e$ of its energy by bremsstrahlung.) and a small Molière radius (2.2 cm, the radius of a cylinder containing 90% deposited energy of the shower); it is a fast scintillator; it is relatively easy to produce from readily available raw materials, and substantial experience and production capacity already exists in some countries. With PbWO_4 crystals, we get a compact calorimeter, as indicated in the first word of CMS, also with fine granularity. The scintillation decay time of PbWO_4 crystals also meets the requirement considering bunch crossing time 25ns at the LHC.

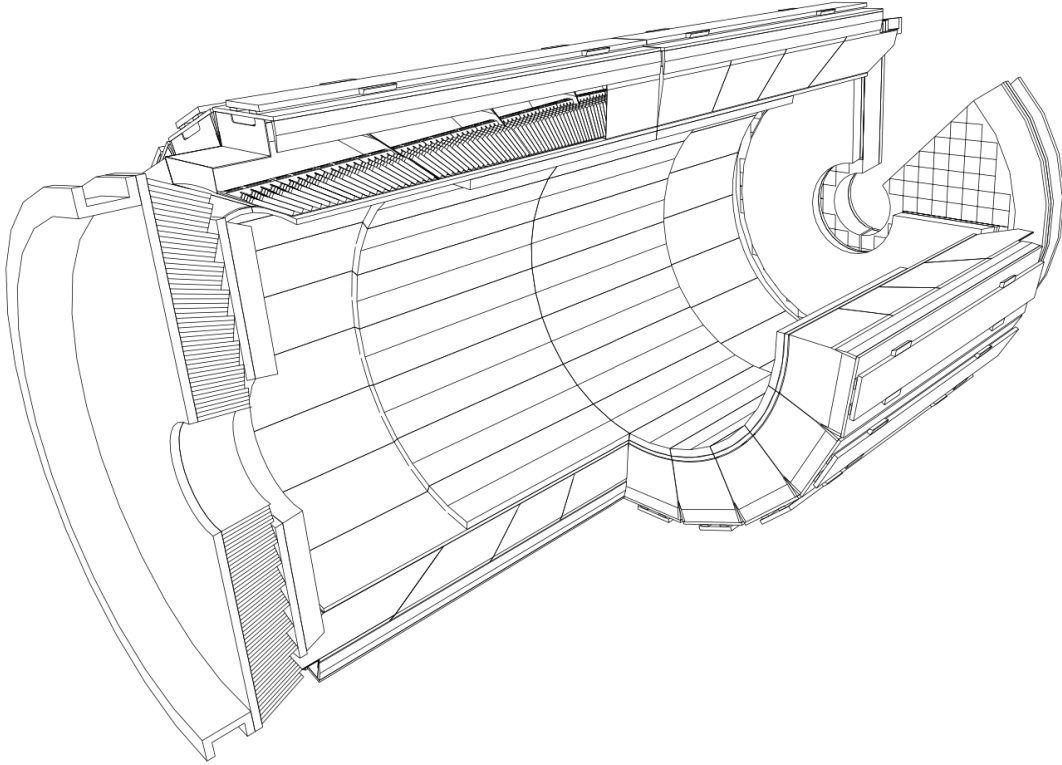


Figure 2.8: A 3-D view of the electromagnetic calorimeter [8]

2.2.4 The hadronic calorimeter

The Hadron Calorimeter (HCAL) consists of four major components: the barrel (HB), the endcap (HE), the outer calorimeter (HO), and the forward calorimeter (HF). Fig. 2.9 shows the positions of four components in a schematic view of the CMS detector. The HCAL is important for measuring the energies of hadron jets and missing transverse energies resulting from particles like neutrinos.

The central pseudorapidity range $|\eta| < 3.0$ is covered by the barrel and endcap calorimeter system consisting of ECAL followed by the HB and HE. Both the HB calorimeter and the HE calorimeter experience the 4 T magnetic field of the CMS solenoid and hence are made of non-magnetic material (copper alloy and stainless steel) [64]. The central hadron calorimeter (including the HB and the HE) is a sampling calorimeter with plastic scintillator tiles with wavelength shifting fibers inserted between copper absorber plates. To ensure adequate sampling depth for the entire barrel region, the HB calorimeter is complemented with an outer calorimeter (HO) located outside the cryostat and inside the magnetic flux return yoke.

To extend the hermeticity of the central hadron calorimeter system to $|\eta|$ of 5.2 (as required for a good missing transverse energy measurement), CMS employs a forward calorimeter (HF) located 6m downstream of the HE endcaps. The HF calorimeter covers the region $3.0 < |\eta| < 5.0$ [65]. It uses quartz fibers as the active medium, embedded in a copper absorber matrix. The HF is placed in very high radiation and a very high rate environment. Because of the quartz fiber active element, it is predominantly sensitive to Cerenkov light from neutral pions. This effect leads to its unique and desirable feature of a localized response to hadronic showers.

The CMS HCAL group developed a drop-in replacement for the current front-end based on silicon photo multipliers (SiPMs) as photo-sensors. SiPMs are pixel arrays of Avalanche Photodiodes operating in Geiger mode. SiPMs are insensitive to the magnetic field and efficient in photon-detection.

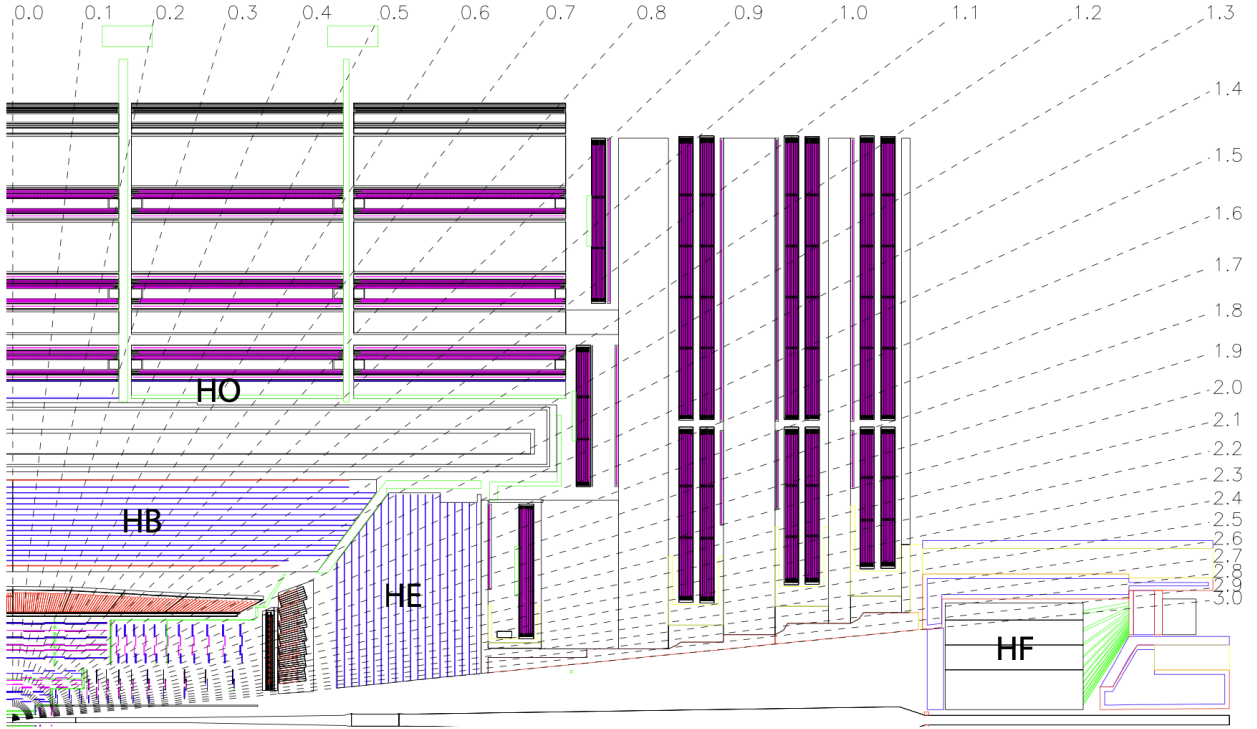


Figure 2.9: A schematic view of one quarter of the CMS HCAL, showing the positions of its four major components: the hadron barrel (HB), the hadron endcap (HE), the hadron outer (HO), and the hadron forward (HF) calorimeters [8]

Also SiPM boards could be easily placed in the limited space of present readout systems. The HO was already upgraded with SiPMs before Run-2 [66], the HE was in the 17-18 technical shutdown, and the HB after the end of Run-2 [67].

The initial calibration of the calorimeters was based on results from test beams, augmented with the use of radioactive sources and lasers. It was improved substantially using proton-proton collision data collected at $\sqrt{s} = 7, 8, \text{ and } 13 \text{ TeV}$, as well as cosmic ray muon data collected during the periods when the LHC beams were not present. The present calibration is performed using the 13 TeV data collected during 2016 corresponding to an integrated luminosity of 35.9 fb^{-1} [68]. The initial energy resolution of HCAL was measured using HCAL TB02 data in year of 2002 with test beams, and could be denoted as [69]:

$$\left(\frac{\sigma_E}{E}\right)^2 = \left(\frac{115\%}{\sqrt{E(\text{GeV})}}\right)^2 + (5.5\%)^2 \quad (2.9)$$

High-Granularity Calorimeter for the future HL-LHC When we move to the HL-LHC, the end-cap calorimeter has to be radiation-tolerant and has capability to cope with the very high pile-up. For this purpose, CMS proposes the replacement of the endcap calorimeters with a new high-granularity sampling calorimeter, covering the range, referred as HGCAL [70]. It features a 4-D measurement capability with high resolution and fast timing response (3 dimensions of shower topologies, adding ultra fast timing capabilities).

Active elements in HGCAL are 8 inches (or pairs of 6 inches) hexagonal $320 \mu\text{m}$ -thick silicon sensors. Sensors are mounted on printed circuit boards (PCB), and glued on the other face to a copper-tungsten baseplate to form a module. Modules will be mounted on a cooler plate made by 6mm-thick copper with embedded stainless steel pipes, making a “cassette” (Fig. 2.10)

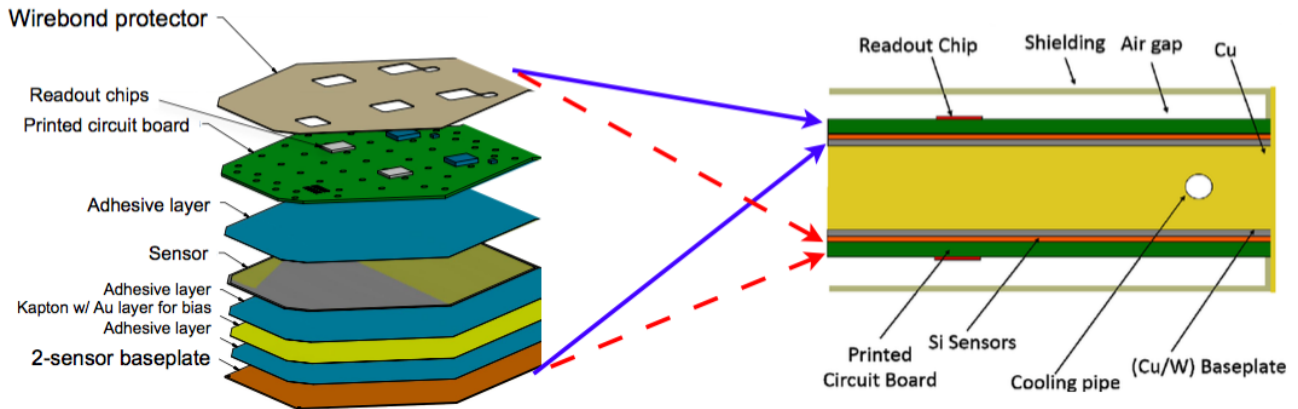


Figure 2.10: **Module components of different layers (left) and sketch of a cassette with modules mounted on either side of the copper cooling plate (right)**

2.2.5 The muon system

The muon system has three functions: muon identification, momentum measurement, and triggering. It uses three different technologies to detect and measure the muons; drift tubes (DT) in the barrel region, cathode strip chambers (CSC) in the endcap region, and resistive plate chambers (RPC) in both the barrel and endcap.

Fig. 2.11 and Fig. 2.12 show the architecture of the muon detector in two planes separately. All the muon chambers are aligned roughly perpendicular to the muon trajectories and distributed to provide hermetic coverage over the η range from 0 to 2.4. The barrel DTs cover roughly in the region $|\eta| < 1.2$ while the endcap CSCs cover the region $0.9 < |\eta| < 2.4$. The RPCs cover the region $|\eta| < 1.6$. The high $|\eta|$ part of the RPC system ($1.6 < |\eta| < 2.4$) has been staged until the LHC is scheduled to deliver its design luminosity of $10^{34} \text{ cm}^{-2}\text{s}^{-1}$.

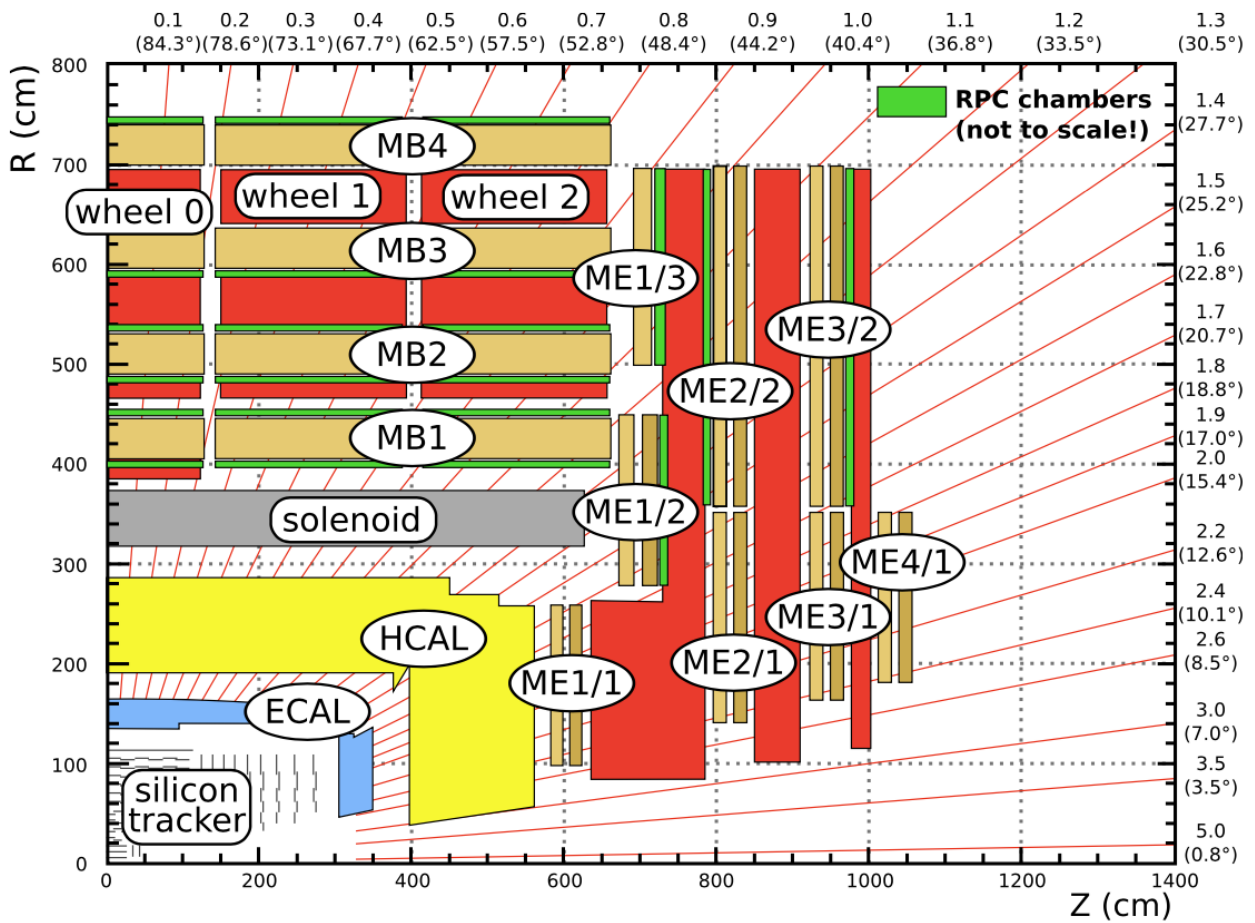


Figure 2.11: An $R - z$ cross-section of one quadrant of the CMS detector with the axis parallel to the beam (z) running horizontally and radius (r) increasing upward. The interaction region is at the lower left. Shown are the locations of the various muon stations and the steel disks [9].

The CMS trigger system and physics object reconstruction

3.1 The CMS trigger system

The CMS trigger system utilizes two levels to select events of potential physics interest, the first level hardware trigger (Level-1 trigger, L1 trigger) and the second level (high level trigger, HLT). The L1 trigger is implemented in custom hardware. Its thresholds are adjusted during data taking in response to the value of the LHC instantaneous luminosity, restricting the output rate to 100 kHz [71]. The HLT is implemented in software and selects an average rate of 1 kHz for offline storage.

3.1.1 The Level-1 Trigger

For flexibility, the L1 Trigger hardware is implemented in field-programmable gate arrays (FPGAs) where possible, but application-specific integrated circuits (ASICs) and programmable memory lookup tables (LUT) are also utilized where speed, density and radiation resistance are needed [8]. There was also a major upgrade of Level-1 trigger during Long Shutdown 1 (LS1, 2013-2015). A key feature of this upgrade is that it significantly increases flexibility beyond that provided by the current trigger system. This feature is accomplished by using high bandwidth optical links for most of the data communication between trigger cards and by adopting modern, large FPGAs and large memory resources for the trigger logic [72]. The architecture of the L1 Trigger after LS1 upgrade is shown in Fig. 3.1 .

The L1 trigger has a fixed latency, $4\mu s$, of one collision. The trigger decision must be made within $4\mu s$ if an event should be tentatively accepted or rejected using information from the calorimeter and muon detectors. A final L1 decision is made by the global trigger (GT) after processing trigger primitives (TP) from calorimeters (ECAL and HCAL) and from the muon detectors in several steps.

Calorimeter Trigger

The ECAL L1 trigger comprises a barrel region (EB) and two endcap regions (EE). In the barrel, the trigger primitive is computed from the transverse energy in each trigger tower (TT) in the form

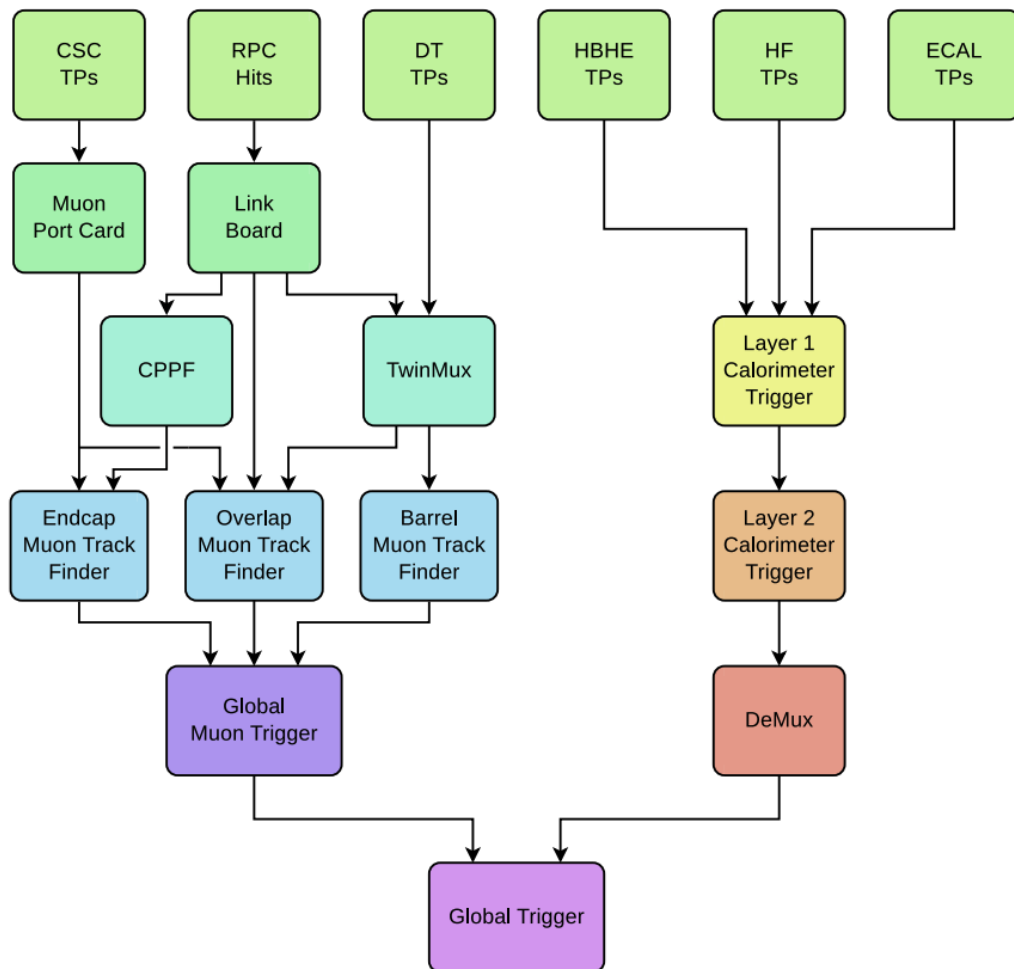


Figure 3.1: **Architecture of the Level-1 Trigger after LS1 upgrade.** Details are given in the text [11]

of a 5×5 array of lead tungstate (PbWO₄) crystals. In endcaps, trigger primitives are also computed from the transverse energy in trigger towers (TTs), but the topology is more complicated by grouping varying numbers of crystals. The ECAL PbWO₄ crystals lose some of the transparency during radiation exposure. Part of them recovers when the radiation stops. Due to this effect, the response of the ECAL changes over time. A laser system is implemented to mitigate this effect by monitoring the transparency of each crystal. The HCAL trigger primitives are computed similarly as ECAL by the deposited transverse energy. One TP corresponds to one HCAL readout in the barrel, whereas two depth-segmented detector readout elements are combined in the endcap. For the forward hadron calorimeter (HF), 12 readouts are combined to form one TP.

The upgrade Calorimeter Trigger used in run 2 has two layers, Layer-1 and Layer-2. Layer-1 receives Trigger Primitives (TPs) consisting of 8-bit of non-linear E_T information accompanied by a data quality bit for each calorimeter tower ($0.087\eta \times 0.087\phi$) from the HCAL and ECAL Trigger Primitive Generators (TPGs). Layer-1 uses the TPs to find e/γ candidates and calculate tower cluster sums that are sent to Layer-2 for sorting, jet finding, and calculating global quantities such as missing E_T . Layer-2 performs the jet finding and sorting, e/γ candidate sorting, and calculates all transverse energy quantities.

Muon Trigger

After 2016 the L1 muon trigger underwent major upgrades in order to cope with the increasing instantaneous luminosity. The CMS Muon Trigger is based on three kind of detectors: Drift Tubes in the barrel, Cathode Strip Chambers in the endcaps, and Resistive Plate Chambers placed both in the barrel and the endcaps. In the CMS muon system, a muon trigger in the barrel region is generated using a mean-timer to identify patterns. In the endcap the trigger is generated from the cathode readout patterns and the wire timing. For both barrel and endcap the RPCs provide an additional trigger signal which has a different sensitivity to backgrounds [73]. The Drift Tube Track Finder (DTTF) identifies muon candidates in the barrel muon detector and determines their transverse momenta, position and quality. The candidates are then sorted by rank (based on p_T and number of hits) by dedicated cards and the highest four are sent to the Global Muon Trigger.

RPC chambers cover roughly the same area as the DTs and CSCs but provide a faster timing signal and have a different sensitivity to background. Trigger signals coming from three muon subdetectors proceed in parallel until reaching the level of the global trigger logic. This provides redundancy for evaluating efficiencies, and results in a higher efficiency and greater rate capability.

Global trigger

The global trigger (GT) is the final step of the L1 trigger system. The GT decides to accept a physics event or not for subsequent evaluation by the high level trigger. This decision is made by combining information of trigger objects from the L1 muon and calorimeter systems. The trigger algorithm calculations are performed at the global trigger logic (GTL) module, after receiving trigger objects from former layers and synchronizing input data from all subsystems to the LHC orbit clock. The GT system records all trigger rates and deadtimes to allow for the extraction of absolute trigger cross sections from data.

3.1.2 The High Level Trigger

The High Level Trigger takes events with L1 trigger acceptance. Those events are processed in an offline way: for each event, objects are reconstructed and certain identification criteria are applied to favor possible physics interest for data analysis. It is a CPU intensive approach and performed by a collection of about 600 algorithms, usually called HLT paths. During this step, event rate is reduced

from about 100 kHz to the level of 1 kHz. If the event rate after the HLT is still very high for an HLT path, a prescale value is applied to that HLT path to reduce the event rate.

3.2 Physics objects reconstruction

3.2.1 Tracks, vertices and beam spot

The CMS tracker has already been introduced in Sec. 2.2.2 To reconstruct the track, we first need to construct valid hits in detectors. The first step of the reconstruction process is referred to as *local reconstruction* [74]. In this step, we cluster signals above certain thresholds in pixels and strips into hits, estimating their positions and uncertainties by defining a local coordinate system in each sensor. In that next step, for the track reconstruction, we use the hits to estimate the momentum and position parameters of the charged particles responsible for those hits. The local coordinate system is translated into the global coordinate system of the track in this step.

It is computationally challenging to reconstruct the trajectories of charged particles. Some difficulties regarding the reconstruction algorithms and solutions are reviewed in some articles [75–77]. The software for track reconstruction used by CMS is Combinatorial Track Finder (CTF). The reconstruction is done by several iterations:

- Iteration 0, find prompt tracks (original hit near the IP) with $p_T \geq 0.8\text{GeV}$ that have three pixel hits.
- Iteration 1, recover prompt tracks that have only two pixel hits.
- Iteration 2, find low- p_T prompt tracks.
- Iteration 3-5, find non-prompt tracks and recover tracks that are not found in above iterations

Before each iteration, hits associated with good tracks found in previous iterations are masked and not skimmed in this iteration. In each iteration, there are several steps:

- Seed trajectories are generated to obtain an initial estimate of the tracks parameters and their uncertainties using only 2-3 hits.
- Searching for extra hits that are associated to the seeds based on a Kalman filter.
- Perform the track-fitting to get best estimates by means of a Kalman filter and smoother.
- Discard tracks failing specified criteria.

Iterations only differ from different configurations of the seed generation and the track selection. A review of track reconstruction efficiency and track parameter resolution can be found in Ref. [74].

To reconstruct the primary-vertex, we need to find a way locating all p-p interaction vertices using reconstructed tracks. Firstly, tracks are selected by imposing some requirements (transverse impact parameter, the number of strip and pixel hits, and the normalized χ^2 from a fit to the trajectory) In the second step, the selected tracks are clustered based on their distance to the beam spot along z -axis. An previous example of clustering algorithm is described in this article [78]. Currently CMS is using an algorithm named *deterministic annealing* (DA) [79], finding the global minimum with many degrees of freedom, in a similar way to finding the minimal energy of a system by gradually reducing its temperature.

CMS has in independent reconstruction of tracks and primary vertices with only the pixel detector. This way of reconstruction is speedy and is a useful tool for many algorithms in the high level

trigger (HLT). Pixel tracks are reconstructed in the same way as describes above by iterations. Vertex finding by pixel tracks is also efficient for primary-vertex reconstruction, based on the same clustering algorithm describe in Ref. [79].

3.2.2 Muons

Hit and segment reconstruction Muons and other charged particles that go through a muon detector ionize the gas in the chambers, producing electric signals on the sensors. These signals are derived by the readout system and are clustered with already defined locations that are the so-called “hits”.

In the drift tubes (DTs), hits are reconstructed in a unit of DT drift cell. The drift cell measures the transverse distance between the wire and the intersection of the muon trajectory with the plane containing the wires in the layer. Gas ionization by the muon produces electrons, which are collected at the anode wire. A time-to-digital converter (TDC) records the time T_{TDC} when electrons arrive. Corrected by a time pedestal T_{ped} , the reconstructed position can be described as [80]:

$$\text{position} = (T_{\text{TDC}} - T_{\text{ped}}) \times v. \quad (3.1)$$

where v is the electron drift velocity. The drift velocity is assumed to be mostly constant with a uniform electric field provided by the DT drift cell design. The time pedestal accounts for several time factors and its calibration is described in detail in Ref. [81]. This T_{ped} implicitly assumes that all muons take the same time to get to the hit position from the interaction region. However, this assumption is not always true since hitting muons can originate from other bunch crossings or be produced by heavy particles traveling at a reduced speed. Therefore, an additional time parameter is added into the reconstruction before Run-2.

Hit reconstruction in a CSC layer utilizes information from the cathode strips and anode wires to measure the position of the passing muon. As described in Sec. 2.2.5, the CSC strips are radial, each subtending an angle of about 3 mrad and therefore can measure the azimuthal angle ϕ . The wires are divided into groups of around 1-2 cm width, which gives a measurement of relatively low granularity in the radial direction. A hit in CSC is then reconstructed at the intersection points of hit strips and wire groups.

Hits in the RPC are reconstructed by clustering strips. As described in Sec. 2.2.5, RPC works in avalanche mode with the electric signals picked up by strips when a charged particle passing through. The strips are aligned along η with up to 2 cm strip pitch, providing a few cm spatial resolution in the ϕ direction. Adjacent strips are clustered considering ionization charge can be shared by more than one strip. The hit is reconstructed with the centroid of the strip cluster.

Muon track reconstruction Tracks are reconstructed independently in the inner tracking system (tracker track) and the muon system (standalone-muon track in a standard CMS reconstruction approach and taken as an input for muon track reconstruction. There are several definitions in the muon track reconstruction procedure [80]:

- *Tracker tracks* are reconstructed using the iterative approach as described in Sec. 3.2.1.
- *Standalone-muon tracks* are reconstructed from seeds of muon segments only.
- *Tracker muon tracks* are reconstructed by taking all tracks from the inner tracker with $p_T > 0.5\text{GeV}$ and $p > 2.5\text{GeV}$ and extrapolating them to the muon system. A track-to-segment matching is performed by specially defined coordinate systems.
- *Global muon tracks* are build by matching above two types of tracks based on the Kalman filter (KF) technique [82].

Tracker muon reconstruction is efficient for muons with low p_T while global muon reconstruction is designed to have high efficiency for high p_T muons (especially for $p_T > 200\text{GeV}$). Muons reconstructed only as standalone-muon tracks have worse momentum resolution and a higher probability coming from cosmic muons.

Muon identification A set of variables based on the muon reconstruction (for examples, the number of hits per track, track fit χ^2 , matching results between tracker tracks and standalone-muon tracks) are used to define the main identification types of muons used in CMS physics analyses include:

- *Loose muon identification (ID)*
- *Medium muon ID*
- *Tight muon ID*
- *Soft muon ID*
- *High momentum muon ID*

The basic muon identification criteria used in this analysis correspond to the cut-based 'medium' identification requirements, with additional longitudinal and transverse distance of closest approach requirements to increase selection purity of prompt muons. The muon momentum is also corrected in both real and simulated data based on the Rochester calibration method using $Z \rightarrow \mu\mu$ events [83]. The identification criteria are as follows:

- The muon is a PF muon, and should be either a tracker or global muon.
- The fraction of valid inner tracker hits should be greater than 0.8.
- When the muon is a global muon, and the global fit has a χ^2 per degree of freedom less than 3, and the position match between the tracker muon and standalone muon has $\chi^2 < 12$, and the maximum χ^2 computed by the kink-finding algorithm is less than 20, the muon segment compatibility should be greater than 0.303. Otherwise, segment compatibility should be greater than 0.451.
- The best track of the muon should satisfy the longitudinal closest approach requirement $|d_z| < 0.1$, and the transverse closest approach requirement $|d_{xy}| < 0.02$. The distance values are computed with respect to the primary vertex of the event.

Muon isolation To distinguish between prompt muons and those from weak decays within jets, the isolation of a muon is derived by summing up the energy in geometrical cones, $\Delta R = \sqrt{(\Delta\phi)^2 + (\Delta\eta)^2}$, surrounding the muon. This method uses charged hadrons and neutral particles coming from particle-flow (PF isolation). The isolation of the muon candidates used in this analysis is computed from the flux of particle flow candidates found within a cone of $\Delta R < 0.3$ built around the lepton direction. The flux of particles is computed independently for the charged hadrons (\mathcal{I}_{ch}), neutral hadrons (\mathcal{I}_{nh}), and photon candidates (\mathcal{I}_{γ}). The neutral hadron flux \mathcal{I}_{nh} is corrected for pileup using the 'delta-beta' method by subtracting half of the scalar p_T sum over the charged particles within the cone of interest but not originating from the primary vertex ($\mathcal{I}_{\text{ch}}^{\text{PU}}$). The muon isolation is therefore defined as

$$\mathcal{I}_{\text{rel}}^{\mu} = \frac{\mathcal{I}_{\text{ch}} + \max(\mathcal{I}_{\text{nh}} + \mathcal{I}_{\gamma} - 0.5 \times \mathcal{I}_{\text{ch}}^{\text{PU}}, 0)}{p_T^{\mu}}, \quad (3.2)$$

with p_T^μ in the denominator after momentum corrections. The muons used in this analysis are required to satisfy $\mathcal{I}_{\text{rel}}^\mu < 0.15$, $p_T^\mu \geq 5\text{GeV}$, and $|\eta| < 2.4$. Events are vetoed if there are excess muons with $\mathcal{I}_{\text{rel}}^\mu < 0.4$.

3.2.3 Electrons and photons

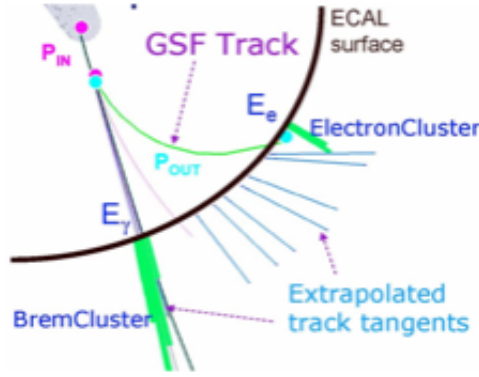


Figure 3.2: **Illustration of electron trajectories and bremsstrahlung effects in the detector.**

Electron and photon reconstruction The presence in CMS of material in front of the ECAL results in bremsstrahlung and photon conversions. In such case, we have a shower of multiple electrons and photons reaching the ECAL, spreading in ϕ direction (see Fig. 3.2). A dedicated algorithm is used to derive the energy of the original electron or photon from the clusters of multiple particles. The curvature of an electron trajectory changes when the electron loses momentum by emitting bremsstrahlung photons. To estimate the track parameters in such case, a tracking algorithm based on the Gaussian sum filter (GSF) is used.

Electrons and photons deposit almost all of their energy in the ECAL. Energy deposits collected by several ECAL channels are clustered and considered to correspond to a particle when reaching a certain energy threshold. The energy reaching the ECAL is spread in ϕ . The spread energy is clustered by building a cluster of clusters, a supercluster, which is extended in ϕ . Two dedicated algorithms [84] are used for this superclustering step, the “mustache” algorithm measuring low energy deposits and the “refined” algorithm combining information from detector subsystems other than ECAL.

Electron identification Reconstructed electrons are identified using an XGBoost [85] boosted decision tree algorithm, exploiting observables from the electromagnetic clusters, electron tracking, and track-cluster matching to distinguish prompt electrons. The full list of used observables in the training of this BDT can be found in the Tab. 3.1. The working points on the output BDT score is adjusted for 6 categories of p_T^e and electron supercluster pseudorapidity (η_{SC}) ranges, summarized in Tab. 3.2. This analysis uses identification BDT score working points corresponding to the ‘Fall17 (no iso.) WP90’ criteria provided by the Egamma POG for all three years.

Electron isolation Electron isolation is defined in a similar way to Eq. 3.2, with the cone radius also being the same. In this case, the neutral hadron flux \mathcal{I}_{nh} is corrected by using the average energy density (ρ) due to pileup and underlying event in the central region of the detector, and an effective area correction (A_{eff}^e) to normalize this estimator in such a way that the isolation is independent of the number of pileup interactions. The values of A_{eff}^e vary between the $|\eta_{SC}|$ range and are listed in Tab. 3.3. With these quantities, the electron isolation is therefore defined as

$$\mathcal{I}_{rel}^e = \frac{\mathcal{I}_{ch} + \max(\mathcal{I}_{nh} + \mathcal{I}_{\gamma} - A_{eff}^e \times \rho, 0)}{p_T^e}, \quad (3.3)$$

Table 3.1: **The observables used in the training of the BDT in order to identify prompt electrons.** The training is done using the 2017 simulation, and this same training is used for 2016 and 2018.

Cluster variables
RMS of the energy-crystal numbering along η and ϕ , $\sigma_{i\eta i\eta}$ and $\sigma_{i\phi i\phi}$
Supercluster width along η and ϕ
Ratio of the hadronic energy behind the electron supercluster to the supercluster energy, H/E
Circularity, $(E_{5\times 5} - E_{5\times 1})/E_{5\times 5}$
Sum of the seed and adjacent crystal over the supercluster energy, R_9
For endcap electrons: Energy fraction in preshower, E_{PS}/E_{raw}
Tracking variables
Fractional momentum loss, $f_{brem} = 1 - p_{out}/p_{in}$
Number of hits of the KF and GSF tracks
Reduced χ^2 of the KF and GSF tracks
Number of expected but missing inner hits
Probability transform of conversion vertex fit χ^2
Track-cluster matching variables
Energy-momentum agreement: E_{tot}/p_{in} , E_e/p_{out} , $1/E_{tot} - 1/p_{in}$
Position matching: $\Delta\eta_{in}$, $\Delta\varphi_{in}$, $\Delta\eta_{seed}$

Table 3.2: **The working points of the electron identification BDT**, defined as a function of the p_T^e before any residual energy scale and smear corrections. The same working points are used in all three years.

p_T^e range (GeV)	$ \eta_{SC} $ range	Working point definition
< 10	< 0.800	$2.771 - \exp(-p_T^e/3.815) \times 8.163$
	[0.800, 1.479)	$1.856 - \exp(-p_T^e/2.187) \times 11.856$
	≥ 1.479	$1.735 - \exp(-p_T^e/2.016) \times 17.014$
≥ 10	< 0.800	$5.918 - \exp(-p_T^e/13.481) \times 9.320$
	[0.800, 1.479)	$5.016 - \exp(-p_T^e/13.128) \times 8.794$
	≥ 1.479	$4.169 - \exp(-p_T^e/13.202) \times 9.007$

with p_T^e in the denominator after electron energy corrections. The electrons used in this analysis are required to satisfy $\mathcal{I}_{\text{rel}}^e < 0.1$, $p_T^e \geq 5\text{GeV}$, and $|\eta_{\text{SC}}| < 2.5$. Events are vetoed if there are excess electrons with $\mathcal{I}_{\text{rel}}^e < 0.4$.

Table 3.3: **The effective area A_{eff}^e values used in each $|\eta_{\text{SC}}|$ range to mitigate the dependence of the isolation requirement on pileup.** The same values are used in all three years.

$ \eta_{\text{SC}} $ range	A_{eff}^e
< 1	0.1440
$[1, 1.479)$	0.1562
$[1.479, 2)$	0.1032
$[2, 2.2)$	0.0859
$[2.2, 2.3)$	0.1116
$[2.3, 2.4)$	0.1321
≥ 2.4	0.1654

Photon identification Reconstructed photons are identified using a cut-based selection flow. The baseline requirements are listed in Tab. 3.4 and are kept the same for all three years. The requirements feature independent requirements on the charged and neutral particle-flow hadron, or the particle-flow photon fluxes within a cone of $\Delta R < 0.3$. Independent effective area corrections $A_{\text{eff,ch}}^\gamma$, $A_{\text{eff,nh}}^\gamma$, and $A_{\text{eff},\gamma}^\gamma$, respectively, are applied to mitigate the dependence of the selection efficiency on pileup. These effective area values are listed in Tab. 3.5 and are also kept the same for the three years.

Table 3.4: **The baseline selection requirements on the photons.** The requirements are kept the same among the three data taking periods.

Requirement	Value for $ \eta_{\text{SC}} < 1.479$	Value for $ \eta_{\text{SC}} \geq 1.479$
$H/E <$	0.02148	0.0321
$\sigma_{\text{in}\eta} <$	0.00996	0.0271
$\mathcal{I}_{\text{ch}} <$	0.65	0.517
$\mathcal{I}_{\text{nh}} <$	$0.317 + 0.01512 \times p_T^\gamma$ $+ 2.259 \cdot 10^{-5} \times p_T^{\gamma 2}$	$2.716 + 0.0117 \times p_T^\gamma$ $+ 2.3 \cdot 10^{-5} \times p_T^{\gamma 2}$
$\mathcal{I}_\gamma <$	$2.044 + 0.004017 \times p_T^\gamma$	$3.032 + 0.0037 \times p_T^\gamma$

3.2.4 Jets

Jets in the CMS experiment are reconstructed using the anti- k_T clustering algorithm [86]. In this algorithm, distances d_{ij} are calculated iteratively between entities i and j and d_{iB} between entity i and the beam (B). In each step, the smallest of the distances and if it is a d_{ij} recombining entities i and j , while if it is d_{iB} calling i a pseudo-jet and removing it from the list of entities. This procedure will be repeated until no entities are left.

$$d_{ij} = \min(k_{ti}^{-2}, k_{tj}^{-2}) \frac{(y_i - y_j)^2 + (\phi_i - \phi_j)^2}{R^2}$$

$$d_{iB} = k_{ti}^{2p}$$

Table 3.5: **The values of the effective areas $A_{\text{eff,ch}}^\gamma$, $A_{\text{eff,nh}}^\gamma$, and $A_{\text{eff},\gamma}^\gamma$ used in each $|\eta_{\text{SC}}|$ range to mitigate the dependence of the isolation requirement on pileup.** The same values are used in all three years.

$ \eta_{\text{SC}} $ range	$A_{\text{eff,ch}}^\gamma$	$A_{\text{eff,nh}}^\gamma$	$A_{\text{eff},\gamma}^\gamma$
< 1	0.0112	0.0668	0.1113
$[1, 1.479)$	0.0108	0.1054	0.0953
$[1.479, 2)$	0.0106	0.0786	0.0619
$[2, 2.2)$	0.01002	0.0233	0.0837
$[2.2, 2.3)$	0.0098	0.0078	0.1070
$[2.3, 2.4)$	0.0089	0.0028	0.1212
≥ 2.4	0.0087	0.0137	0.1466

where k_{ti} , y_i and ϕ_i are respectively the transverse momentum, rapidity and azimuthal angle of particle i . R is a usual radius parameter determining the size of the jets. In CMS, jets with $R = 0.4$ are called AK4 jets and $R = 0.8$ for AK8 jets.

Jets reconstructed often group low p_T particles and are easily contaminated by the particles from pileup collisions. A correction technique “the charged hadron subtraction” (CHS) is used to remove particles not associated with the primary vertex [87]. The technique also helps reduce detector noise.

Jet energy calibration and measurement of jet energy resolution use techniques described in Ref. [88].

Jets are tagged as b-tagged jets using the DeepJet algorithm [89], which provides performance improvements over the DeepCSV algorithm [90, 91] by using approximately 650 input variables related to PF candidates, vertexing and jet constituents, and improved neural network training. b-tagging can be considered for all jets with $p_T \geq 20\text{GeV}$ and $|\eta| < 2.5$ ($|\eta| < 2.4$ in 2016 due to different tracker geometry). The loose (tight) working point is defined in this analysis based on the ‘loose’ (‘medium’) working point prescription of the CMS b-Tag & Vertexing Physics Object Group (BTV POG)

3.2.5 Missing transverse momentum

In proton-proton collision process, the initial momentum in particles traveling transverse to the beam axis is negligible. the total momentum in the transverse plane after the collision should also be zero due to the conservation of momentum. In general, missing transverse energy is the negative of the vector sum of the transverse momenta of all final-state particles reconstructed in the detector. There are three dedicated algorithms of p_T^{miss} reconstruction. In this paper, the symbol $\mathbf{p}_T^{\text{miss}}$ with \mathbf{p} in bold font represents for the vector form and MET for the absolute value of missing transverse momentum. The MET used in this analysis is the PF MET, which is calculated using a complete particle-flow technique. The missing transverse momentum is formulated as

$$\mathbf{p}_T^{\text{miss}} = - \sum_{i \in \text{all}} \mathbf{p}_T \quad (3.4)$$

where $i \in \text{all}$ indicates all reconstructed particles. The MET derived from this formula is called raw MET, which is systematically different from true MET. The raw MET also includes the non-compensating nature of the calorimeters and detector misalignment besides invisible particles. For this reason, application of MET corrections is necessary.

Type-I correction This correction is a propagation of the jet energy corrections (JEC) to MET. The Type-I correction replaces the vector sum of transverse momenta of particles which can be clustered as jets with the vector sum of the transverse momenta of the jets to which JEC is applied. Eq. 3.4 can also be expressed as

$$\mathbf{p}_T^{\text{missRaw}} = - \sum_{i \in \text{jets}} \mathbf{p}_T - \sum_{i \in \text{uncl.}} \mathbf{p}_T \quad (3.5)$$

where $i \in \text{uncl.}$ indicates particles that are not clustered with respect to any jet. The Type-I correction replaces the raw jet \mathbf{p}_T with the corrected jet \mathbf{p}_T and can be written as

$$\mathbf{C}_T^{\text{Type-I}} = \sum_{i \in \text{jets}} \mathbf{p}_T - \sum_{\text{jet}} \mathbf{p}_{T\text{jet}}^{\text{JEC}} \quad (3.6)$$

The Type-I corrected MET can be written as

$$\mathbf{p}_T^{\text{missType-I}} = - \sum_{\text{jet}} \vec{p}_{T\text{jet}}^{\text{JEC}} - \sum_{i \in \text{uncl.}} \vec{p}_{Ti} \quad (3.7)$$

The relation between raw MET and Type-I corrected MET

$$\mathbf{p}_T^{\text{missType-I}} = \mathbf{p}_T^{\text{missRaw}} + \mathbf{C}_T^{\text{Type-I}} \quad (3.8)$$

Part III

Measurements of the Higgs boson properties from off-shell production in the ZZ final state

Data and Simulations

The data used in this analysis consists of proton-proton collision events that correspond to an integrated luminosity of 138 fb^{-1} at a center-of-mass energy of 13 TeV, collected by the CMS experiment at LHC in 2016, 2017 and 2018 during Run-II. The luminosities for different years are given in the Tab. 4.1. When the two channels $ZZ \rightarrow 4\ell$ and $ZZ \rightarrow 2\ell 2\nu$ are combined, data from 2015 is used and therefore some results are shown with a luminosity label of 140 fb^{-1} .

Table 4.1: The luminosities for 2016, 2017 and 2018 during LHC Run-II data taking [19]

Data taking period	Preliminary luminosity (fb^{-1})	Recommended luminosity (fb^{-1})
2015	-	2.26
2016	35.92	36.31
2017	41.48	41.48
2018	59.83	59.83

4.1 Datasets

To enable an effective way of getting access to the data, they are split into physics datasets (PDs), which are based on trigger decisions. After the trigger selections, the amount of data collected is still too large for people to deal with. The main strategy in dealing with such a large number of events is to filter them, and do that in layers of ever-tighter event selection. Event information is filtered step by step and in each step it is logically grouped into what we call a data tier. For example, data tiers include RAW and RECO for real data, and GEN, SIM and DIGI for MC simulations. Reconstructed (RECO) data contain information of objects from all steps of reconstruction. Analysis object data (AOD) are derived from the RECO and contain information of objects in a more compact format for physics analysis.

4.1.1 Datasets for the analysis

The analysis is performed using miniAOD and nanoAOD data formats, which are slimmed versions from skimming of AOD. Tab. 4.2 outlines the names of datasets that are used for different

purposes. By other purposes, we means that some key information should be measured from data with certain datasets. For example, `JetHT`, `MET` and `HTMHT` are for trigger efficiency measurement of di-lepton events; `SinglePhoton` for the trigger efficiency measurement of single photon events; `SingleMuon` and `SingleElectron` (or `EGamma` for 2018) for the lepton selection efficiency measurement and also a supplement for the trigger study. Sometimes a single dataset can be used for several different purposes. For example, with `SinglePhoton` dataset we also derive reweighting factors for a $\gamma \rightarrow Z$ translation and define a single photon control region for the instrumental p_T^{miss} background estimation.

Table 4.2: **The primary datasets used in the analysis for all three years**

Primary Datasets	Years			Signal Region	Control Region	Other purposes
	2016	2017	2018			
SingleMuon	✓	✓	✓	✓		✓
DoubleMuon	✓	✓	✓	✓		
SingleElectron	✓	✓		✓	✓	✓
DoubleElectron	✓	✓		✓		
SinglePhoton	✓	✓			✓	✓
MuonEG	✓	✓	✓		✓	
EGamma			✓	✓	✓	
JetHT	✓	✓	✓			✓
HTMHT	✓	✓				✓
MET	✓	✓	✓			✓

Since several skimming compaigns exist with respect to each year, and conditions may change over different compaigns, we use global tags to indicate different settings which are unique to a particular set of data/MC. Tab. 4.3 presents the `miniAOD` tags corresponding to each data set from each year, and also the reconstruction conditions used in analyzing the simulation. For each of the data and simulation samples, the latest corresponding `nanoAOD` tags (v7) are used when the `nanoAOD` format is used.

Table 4.3: **Datasets and global tags used in the analysis**

Datasets	Global tag
2016 data sets	
/JetHT/Run2016B-17Jul2018_ver2-v2/MINIAOD	94X_dataRun2_v10
*/Run2016B-17Jul2018_ver2-v1/MINIAOD	94X_dataRun2_v10
*/Run2016[C-H]-17Jul2018_v1/MINIAOD	94X_dataRun2_v10
Simulation	94X_mcRun2_asymptotic_v3
2017 data sets	
*/Run2017[B-F]-31Mar2018-v1/MINIAOD	94X_dataRun2_v11
Simulation	94X_mc2017_realistic_v17
2018 data sets	
/DoubleMuon/Run2018A-17Sep2018-v2/MINIAOD	102X_dataRun2_v13
/SingleMuon/Run2018A-17Sep2018-v2/MINIAOD	102X_dataRun2_v13
/EGamma/Run2018A-17Sep2018-v2/MINIAOD	102X_dataRun2_v13
*/Run2018[A-C]-17Sep2018-v1/MINIAOD	102X_dataRun2_v13
/SingleMuon/Run2018D-22Jan2019-v2/MINIAOD	102X_dataRun2_v13
/EGamma/Run2018D-22Jan2019-v2/MINIAOD	102X_dataRun2_Prompt_v16
*/Run2018D-PromptReco-v2/MINIAOD	102X_dataRun2_Prompt_v16
Simulation	102X_upgrade2018_realistic_v21

4.2 Simulations

Before we start data analysis, there are certain theory models and processes of interests that we like to examine and simulate. We use Monte Carlo generators to produce events and reconstruct those events in the experimental environment setup. We usually call this procedure the Monte Carlo simulation. Simulation of proton-proton collision events at the LHC is a complicated program involving a series of tasks [92].

It usually starts with a generation of **hard process**, a process in which heavy objects are created or a large momentum transfer occurs. For example, in this analysis, the production of Higgs boson which subsequently decay into 2 vector bosons (Z bosons) with each Z boson further decaying into 2 fermions (electrons, muons or neutrinos), is the result of an interaction between two partons from the colliding protons. The simulation of the hard process describes this interaction at a certain order in perturbative QCD. It is followed by a parton shower, that simulates additional emission of colored particles in a parametrized way, and calculate the momentum transfer as showers progress down from the high scales to the low scales, where QCD interactions can no longer be calculated by perturbation theory. At low energy scales, usually of order of 1 GeV, non-perturbative models are needed for the description of **hadronization**, the transition from the partonic “final” state to a complete representation of the actual hadronic final state. We also need to allow for **underlying event** where interactions other than the hard process produce extra partons, which are typically soft and usually result in modifications of final state observables. The last step is to mimic **the interaction with the detector**. The Monte Carlo generated events are further processed through a dedicated GEANT4 [93] simulation of the CMS detector with geometries and material budget adjusted in each data period based on important changes in the detector conditions. Finally, the response of detector electronic readouts is simulated in a way as described and partially covered in Sec. 2.2. We call this step **digitalization**. The last step is **reconstruction** as discussed in Sec. 3.2.

4.2.1 Simulations of the non-interfering backgrounds

Various simulation samples are used in the analysis to understand the different background components in each of the signal or control regions. They are grouped in different tables based on whether they are used in the analysis of the signal region or dilepton control regions (see Tab. 4.4), or the analysis of the single photon control region (see Tab. 4.5).

The nominal PDF set used in generating these samples are from NNPDF 3.0 [94, 95] for the 2016 data set samples or NNPDF 3.1 [96] for the 2017 and 2018 data set samples with various LO, NLO, or NNLO QCD choices. However, in the determination of the $q\bar{q} \rightarrow VV$ ($VV = WZ$ or ZZ) background contributions to the signal region, the events are reweighted to the NNPDF 3.0 NLO QCD PDF, suitable also to the QCD order of the simulation itself, in order to have a uniform cross section predictions across the data periods. This detail also applies to the simulation of the signal samples, discussed in Sec. 4.2.2. The simulated events for the $q\bar{q} \rightarrow ZZ$ contribution are further reweighted for the NLO EW virtual correction (corresponding to loop diagrams) for two on-shell Z bosons as a function of the Mandelstam variables \hat{s} and \hat{t} for each quark flavor contribution in the initial states [97–99]. For $q\bar{q} \rightarrow WZ$, two contributions exist to the NLO EW corrections: there is a negative correction due to virtual effects, applied in the same way as for $q\bar{q} \rightarrow ZZ$, and a positive contribution due to photon-induced processes, parametrized as a function of \hat{s} . These two contributions are found to nearly cancel each other [100]. Both $q\bar{q} \rightarrow ZZ$ and $q\bar{q} \rightarrow WZ$ are reweighted for NNLO QCD effects as a function of m_{VV} [52, 101, 102]. The NLO EW correction reaches a value up to -15% at $m_{VV} = 1$ TeV with a comparable uncertainty driven by cross-contamination with NLO QCD corrections, and the NNLO QCD correction is an approximately uniform $+15\%$ correction at high m_{ZZ} values in the ZZ case. The methods of application of these corrections are the same as those described in Ref. [13, 34, 52, 99].

Table 4.4: **Non-interfering background samples, generators and their cross sections used in the analysis of dilepton signal or control regions.** The cross sections are obtained with NNPDF 3.1 PDF set. Since WZ or ZZ background contributes to the signal region, the events are reweighted to the NNPDF 3.0 condition to have a uniform cross section predictions across the data periods.

Process	bins/channels	Generator	Cross section (pb)
DY ($Z \rightarrow ll$)+ jets	$10\text{GeV} < m_{ll} < 50\text{GeV}$	aMC@NLO	15800
	$m_{ll} > 50\text{GeV}$	aMC@NLO	6225.4
$t\bar{t} \rightarrow 2l2\nu$	inclusive	powheg	87.3348
single top(top)	s-channel	powheg	5.756
single top(antitop)	s-channel	powheg	3.58
single top(top)	t-channel	powheg	138
single top(antitop)	t-channel	powheg	82.5
tW(top)		powheg	20.248
tW(antitop)		powheg	18.502
$t\bar{t}Z \rightarrow 2q$		aMC@NLO	0.2432
$t\bar{t}W \rightarrow l\nu$		aMC@NLO	0.2181
$tZq(Z \rightarrow ll)$		aMC@NLO	0.0758
$ZZ \rightarrow 2l2\nu$		powheg	0.6008
$ZZ \rightarrow 2l2q$		powheg	3.691
$ZZ \rightarrow 4l$		powheg	1.325
$ZZ \rightarrow 2q2\nu$		aMC@NLO	4.325
WZ $\rightarrow 3l\nu$		powheg	4.658
WZ $\rightarrow 3l\nu$		aMC@NL	5.087
WZ $\rightarrow l\nu2q$		aMC@NLO	11.74
WZ $\rightarrow 2l2q$		aMC@NLO	6.284
WZ $\rightarrow l3\nu$		aMC@NLO	3.325
WW $\rightarrow 2l2\nu$		powheg	11.08
WW $\rightarrow l\nu2q$		powheg	45.99
WWW		aMC@NLO	0.2154
WWZ		aMC@NLO	0.1676
WZZ		aMC@NLO	0.0571
ZZZ		aMC@NLO	0.1473

Table 4.5: **Non-interfering background samples, generators and their cross sections used in the analysis of single photon control region.** The cross sections are obtained with NNPDF 3.1 PDF set.

Process	bins/channels	Generator	Cross section (pb)
W ($\rightarrow l\nu$) + jets	0-jet	aMC@NLO	49141
	1-jet	aMC@NLO	8045.1
	2-jet	aMC@NLO	3159.9
γ + jets	40GeV < HT < 100GeV	madgraph	20790
	100GeV < HT < 200GeV	madgraph	9238
	200GeV < HT < 400GeV	madgraph	2305
	400GeV < HT < 600GeV	madgraph	274.4
	HT > 600GeV	madgraph	93.46
QCD	50GeV < HT < 100GeV	madgraph	185800000
	100GeV < HT < 200GeV	madgraph	23660000
	200GeV < HT < 300GeV	madgraph	1559000
	300GeV < HT < 500GeV	madgraph	323300
	500GeV < HT < 700GeV	madgraph	30000
	700GeV < HT < 1000GeV	madgraph	6330
	1000GeV < HT < 1500GeV	madgraph	1098
	1500GeV < HT < 2000GeV	madgraph	99.8
HT > 2000GeV	madgraph	20.35	
Z ($\rightarrow \nu\nu$) + jets	100GeV < HT < 200GeV	madgraph	303.9
	200GeV < HT < 400GeV	madgraph	91.03
	400GeV < HT < 600GeV	madgraph	13.07
	600GeV < HT < 800GeV	madgraph	3.26
	800GeV < HT < 1200GeV	madgraph	1.509
	1200GeV < HT < 2500GeV	madgraph	0.3401
	HT > 2500GeV	madgraph	0.00527
$t\bar{t}$ + jets		aMC@NLO	748.8
$t\gamma$ + jets		madgraph	2.872
$t\bar{t}\gamma$ + jets		aMC@NLO	3.746
W($\rightarrow l\nu$) γ	0,1-jet	aMC@NLO	191.4
W($\rightarrow l\nu$) γ		madgraph	444.6
W ⁺ ($\rightarrow l\nu$) γ		powheg	34220
W ⁻ ($\rightarrow l\nu$) γ		powheg	25350
WZ γ		aMC@NLO	0.04123
Z($\rightarrow \nu\nu$) γ	inclusive	aMC@NLO	30.05
Z($\rightarrow \nu\nu$) γ	40GeV < p_γ^T < 130GeV	madgraph	3.003
Z($\rightarrow \nu\nu$) γ	p_γ^T > 130GeV	madgraph	0.1926
Z($\rightarrow \nu\nu$) γ	p_γ^T > 130GeV	aMC@NLO	0.2828
Z($\rightarrow ll$) γ	40GeV < p_γ^T < 130GeV	madgraph	5.485
Z($\rightarrow ll$) γ	p_γ^T > 130GeV	madgraph	0.1472
Z($\rightarrow ll$) γ	p_γ^T > 130GeV	aMC@NLO	0.1595

4.2.2 Simulation of the signal and interfering background processes

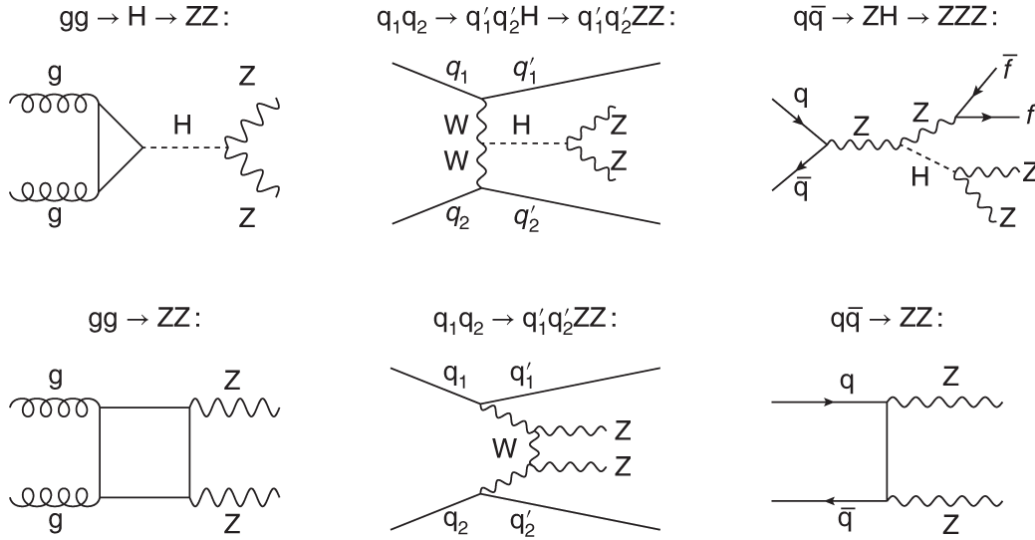


Figure 4.1: **Feynman diagrams for important contributions to ZZ production.** Diagrams can be distinguished as those involving the H (top), and those that give rise to continuum ZZ production (bottom). The interaction displayed at tree level in each diagram is meant to progress from left to right. Each straight, curvy, or curly line refers to the different set of particles denoted. Straight, solid lines with no arrows indicate the line could refer to either a particle or an antiparticle, whereas those with forward (backward) arrows refer to a particle (an antiparticle).

The feynman diagrams of signal and continuum background processes to be simulated are shown in Fig. 4.1. The destructive interference between the H boson signal amplitude and the background continuum ZZ production is also well considered in the simulation procedure.

All events are simulated in two steps. The first step involves producing the events with a stable H in gg , VBF, ZH, or W^+H and W^-H production modes using the POWHEG 2 [103–107] event generator at next-to-leading order (NLO) in QCD. The simulation of VH events is generated using the MINLO HVJ program [108, 109], which brings the precision of the simulation up to NNLO in QCD. In each production mode, the samples are produced at H pole masses $m_H = 125, 160, 170, 180, 190, 200, 210, 230, 250, 270, 300, 350, 400, 450, 500, 550, 600, 700, 800, 900, 1000, 1500, 2000, 2500,$ and 3000 GeV. The H propagator is defined using the Complex-Pole scheme (CPS) [110] mode in these samples in order to give stable generation at higher m_H values, and it is used consistently even at low values to uniformize the reweighting procedure described later in this section. Tab. 4.6 lists the raw cross sections of these samples for the different production modes, where the two different cross section values correspond to the nominal PDF choice of NNPDF 3.0 NLO in QCD for the 2016 data period simulation, and that of NNPDF 3.1 NNLO in QCD for the 2017 and 2018 periods. The final distributions used in the analysis are always reweighted to use the PDF set NNPDF 3.0 NLO in QCD in the hard process in order to have a uniform line shape baseline and because the different variations of the NNLO QCD k-factor correction on the gg process [59], which are applied as a function of m_{VV} inclusively in jet bins, are computed relative to this PDF set. As also done in Reference [13], a uniform k-factor of 1.10 [111] is applied on the gg process in order to scale this contribution to N³LO at $m_{VV} = 125\text{GeV}$ [59], which is where this k-factor is calculated, but the relative uncertainties on the NNLO k-factor are left unscaled in order to avoid overestimating the related uncertainties in the wider mass spectrum. We also see in the baseline cross section calculations between the different generators used in the analysis that these uncertainties cover for the differences.

Table 4.6: **The cross section values for the different Higgs boson production modes are listed for the samples produced at different values of the Higgs boson pole mass m_H using the POWHEG 2 event generator.** TheMINLO HVJ add-on is used in the VH modes. The cross sections are obtained with the NNPDF 3.0 NLO nominal PDF set. The cross sections are reported in units of pb.

m_H	σ_{ggH}	σ_{VBF}	σ_{W+H}	σ_{W-H}	σ_{ZH}
125	30.0	3.77	8.50×10^{-1}	5.34×10^{-1}	7.53×10^{-1}
160	20.0	3.00	3.89×10^{-1}	2.37×10^{-1}	3.47×10^{-1}
170	17.9	2.79	3.15×10^{-1}	1.90×10^{-1}	2.80×10^{-1}
180	16.3	2.62	2.61×10^{-1}	1.56×10^{-1}	2.31×10^{-1}
190	14.8	2.44	2.15×10^{-1}	1.28×10^{-1}	1.90×10^{-1}
200	13.6	2.29	1.80×10^{-1}	1.06×10^{-1}	1.59×10^{-1}
210	12.7	2.18	1.55×10^{-1}	9.00×10^{-2}	1.36×10^{-1}
230	11.2	1.97	1.14×10^{-1}	6.56×10^{-2}	1.01×10^{-1}
250	9.88	1.75	8.49×10^{-2}	4.77×10^{-2}	7.37×10^{-2}
270	8.86	1.56	6.36×10^{-2}	3.51×10^{-2}	5.49×10^{-2}
300	7.89	1.33	4.29×10^{-2}	2.32×10^{-2}	3.66×10^{-2}
350	8.03	1.04	2.39×10^{-2}	1.24×10^{-2}	2.02×10^{-2}
400	7.14	8.47×10^{-1}	1.47×10^{-2}	7.33×10^{-3}	1.21×10^{-2}
450	5.06	6.90×10^{-1}	9.31×10^{-3}	4.51×10^{-3}	7.60×10^{-3}
500	3.36	5.61×10^{-1}	6.07×10^{-3}	2.90×10^{-3}	4.90×10^{-3}
550	2.21	4.59×10^{-1}	5.11×10^{-3}	1.89×10^{-3}	3.23×10^{-3}
600	1.47	3.80×10^{-1}	2.82×10^{-3}	1.27×10^{-3}	2.21×10^{-3}
700	6.87×10^{-1}	2.71×10^{-1}	1.46×10^{-3}	6.31×10^{-4}	1.12×10^{-3}
800	3.49×10^{-1}	2.02×10^{-1}	8.24×10^{-4}	3.48×10^{-4}	6.22×10^{-4}
900	1.92×10^{-1}	1.56×10^{-1}	5.01×10^{-4}	2.01×10^{-4}	3.72×10^{-4}
1000	1.13×10^{-1}	1.24×10^{-1}	3.18×10^{-4}	1.27×10^{-4}	2.36×10^{-4}
1500	1.46×10^{-2}	4.42×10^{-2}	5.49×10^{-5}	2.04×10^{-5}	3.92×10^{-5}
2000	6.23×10^{-3}	3.45×10^{-2}	2.76×10^{-5}	1.00×10^{-5}	2.00×10^{-5}
2500	2.51×10^{-3}	2.14×10^{-2}	1.18×10^{-5}	4.35×10^{-6}	7.95×10^{-6}
3000	1.19×10^{-3}	1.41×10^{-2}	5.56×10^{-6}	2.12×10^{-6}	4.24×10^{-6}

Analysis strategy

This chapter includes details of how we measure the Higgs boson width from off-shell production in the ZZ final state. Sec. 5.1 describes the HLT trigger paths used in the analysis and also gives a review of the trigger efficiency measurement. Sec. 5.2 lists physics selections that are not covered in Sec. 3.2 and also includes details about how we measure the lepton selection efficiencies. Sec. 5.3 presents criteria for event selection and event categorization. Sec. 5.4 discusses about the observables and discriminants used in this analysis as the most important indicators to distinguish the signal from the background. Sec. 5.5 explains how we extract the results and make meaningful interpretations by a likelihood parameterization. Sec. 5.6 summarizes the systematic uncertainties of the measurement introduced by different sources.

5.1 Triggers

As mentioned in previous Sec. 3.1.2, the HLT triggers are software based triggers and run on CPU+GPU based farm. Technically speaking, an HLT trigger is a set of configurations in the sample skimming procedure to help us further refine the events towards physics analysis. Each HLT trigger corresponds to a path named HLT path. An HLT path usually includes the information of number of objects in the event, their momentum threshold as well as some others filters. The HLT paths used in this analysis are listed in Tab. 5.1 and Tab. 5.2. These HLT paths can be categorized into several groups in a similar way as we do with data sets: SingleMuon, DoubleMuon, SingleElectron, DoubleElectron, MuonEG, SinglePhoton, DoublePhoton, etc. In the signal region (SR), target triggers or trigger groups are SingleMuon, DoubleMuon, SingleElectron, DoubleElectron. We also add double photon trigger (DoublePhoton60 in 2016, or DoublePhoton70 in 2017 and 2018) and unrescaled high p_T single photon trigger (Photon175 in 2016, or Photon200 in 2017 and 2018) to the SR because in practice the photon trigger increases efficiency at high $m_{\ell\ell}$, by selecting electrons missed by the electron triggers.

Matching between reconstructed leptons or photons, and the corresponding HLT objects are made with a $\Delta R < 0.2$ requirement whenever needed. No matching to HLT-level jets is performed because some of these jets overlap with reconstructed muons; kinematic requirements on jet kinematics or related observables are placed instead in order to avoid the firing of these jet-associated triggers by a reconstructed physics object other than a reconstructed jet.

Table 5.1: List of the HLT paths used in the analysis for the Run-2 data

Group	HLT path	Year		
		2016	2017	2018
SingleMuon	IsoMu24	✓		✓
	IsoMu27		✓	
	IsoTkMu24	✓		
	TkMu50	✓		
	Mu50	✓	✓	✓
	TkMu100		✓	✓
	OldMu10		✓	✓
DoubleMuon	Mu17_TrkIsoVVL_Mu8_TrkIsoVVL	✓		
	Mu17_TrkIsoVVL_Mu8_TrkIsoVVL_DZ	✓		
	Mu17_TrkIsoVVL_TkMu8_TrkIsoVVL	✓		
	Mu17_TrkIsoVVL_TkMu8_TrkIsoVVL_DZ	✓		
	Mu17_TrkIsoVVL_Mu8_TrkIsoVVL_DZ_Mass8		✓	
	Mu17_TrkIsoVVL_Mu8_TrkIsoVVL_DZ_Mass3p8			✓
SingleElectron	Ele25_eta2p1_WPTight_Gsf	✓		
	Ele27_eta2p1_WPLoose_Gsf	✓		
	Ele27_WPTight_Gsf	✓		
	Ele32_WPTight_Gsf			✓
	Ele35_WPTight_Gsf		✓	
DoubleElectron	Ele23_Ele12_CaloIdL_TrackIdL_IsoVL_DZ	✓		
	Ele23_Ele12_CaloIdL_TrackIdL_IsoVL		✓	✓
	DoubleEle33_CaloIdL_MW	✓	✓	
	DoubleEle33_CaloIdL_GsfTrkIdVL	✓		
MuonEG	Mu8_TrkIsoVVL_Ele23_CaloIdL_TrackIdL_IsoVL	✓		
	Mu8_TrkIsoVVL_Ele23_CaloIdL_TrackIdL_IsoVL_DZ	✓	✓	✓
	Mu23_TrkIsoVVL_Ele8_CaloIdL_TrackIdL_IsoVL	✓		
	Mu23_TrkIsoVVL_Ele8_CaloIdL_TrackIdL_IsoVL_DZ	✓		
	Mu23_TrkIsoVVL_Ele12_CaloIdL_TrackIdL_IsoVL		✓	✓
	Mu23_TrkIsoVVL_Ele12_CaloIdL_TrackIdL_IsoVL_DZ		✓	✓
SinglePhoton	Photon[50,75,90,120,165]_R9Id90_HE10_IsoM	✓	✓	✓
	Photon175	✓		
	Photon200		✓	✓
DoublePhoton	DoublePhoton60	✓		
	DoublePhoton70		✓	✓

Table 5.2: List of the HLT paths used in the analysis for the Run-2 data

Group	HLT path	Year		
		2016	2017	2018
CR-A	AK8PFJet360_TrimMass30	✓		✓
CR-B	DiPFJet40_DEta3p5_MJJ600_PFMETNoMu140 DiJet110_35_Mjj650_PFMET[110-130]	✓	✓	✓
CR-C	PFHT[125-900, excl. 800] PFHT[180-1050]	✓	✓	✓
CR-D	MET[200-600]	✓		
CR-E	PFMET170_HBHECleaned PFMET[300-600] PFMET200_HBHE_BeamHaloCleaned PFMET[250,300]_HBHECleaned	✓ ✓	✓ ✓	✓ ✓
CR-F	PFHT300_PFMET110	✓		
CR-G	PFMET120_PFMHT120_IDTight PFMETNoMu12_PFMHTNoMu120_IDTight PFMET120_PFMHT120_IDTight_PFHT60 PFMETNoMu120_PFMHTNoMu120_IDTight_PFHT60	✓ ✓	✓ ✓ ✓ ✓	✓ ✓ ✓ ✓
CR-H	PFHT[500-800]_PFMET[100-75]_PFMHT[100-75]_IDTight		✓	✓
CR-a	Mu17_TrkIsoVVL Mu17 Mu8_TrkIsoVVL Mu8	✓ ✓ ✓ ✓	✓ ✓ ✓ ✓	✓ ✓ ✓ ✓
CR-b	Ele17_CaloIdM_TrackIdM_PFJet30 Ele17_CaloIdL_TrackIdL_IsoVL_PFJet30 Ele12_CaloIdL_TrackIdL_IsoVL_PFJet30 Ele8_CaloIdM_TrackIdM_PFJet30 Ele8_CaloId_TrackIdL_IsoVL_PFJet30	✓ ✓ ✓ ✓ ✓	✓ ✓ ✓ ✓ ✓	✓ ✓ ✓ ✓ ✓

Some of the photon trigger paths listed in Tab. 5.1 need special treatment. Those single photon HLT triggers are used specifically in the single photon control region toward the estimation of the Drell-Yan background. With the exception of Photon165_R9Id90_HE10_IsoM and Photon175 in 2016, or Photon200 in 2017 and 2018, these triggers are prescaled. In order to avoid trigger turn on effects, and also reduce the overlap between these imperfectly-randomized trigger paths, the single-photon events are selected only when the photon p_T^γ falls into a range defined at the plateau of the trigger efficiency. These thresholds are listed in Tab. 5.3 for 2016 and Tab. 5.4 for 2017 and 2018.

Table 5.3: **The p_T^γ thresholds applied to the single-photon triggers in 2016.** These thresholds on the reconstructed p_T^γ are approximately 10% above the HLT-level threshold values.

HLT path	p_T^γ range (GeV)
HLT_Photon50_R9Id90_HE10_IsoM	[55, 82.5)
HLT_Photon75_R9Id90_HE10_IsoM	[82.5, 99)
HLT_Photon90_R9Id90_HE10_IsoM	[99, 135)
HLT_Photon120_R9Id90_HE10_IsoM	[135, 200)
HLT_Photon165_R9Id90_HE10_IsoM	[200, 220)
HLT_Photon175	≥ 220

Table 5.4: **The p_T^γ thresholds applied to the single-photon triggers in 2017 or 2018.** The thresholds are approximately 10% above the turn-on value.

HLT path	p_T^γ range (GeV)
Photon50_R9Id90_HE10_IsoM	[55, 82.5)
Photon75_R9Id90_HE10_IsoM	[82.5, 99)
Photon90_R9Id90_HE10_IsoM	[99, 132)
Photon120_R9Id90_HE10_IsoM	[132, 181.5)
Photon165_R9Id90_HE10_IsoM	[181.5, 230)
Photon200	≥ 230

HLT paths of classes CR-[A-H] in Tab. 5.2 are used in the estimation of the combined dilepton and single lepton trigger efficiencies for the dilepton events based on their orthogonality with these target triggers. A set of event selection conditions, separately for each of the HLT path classes [A-H], are applied in order to ensure that the efficiencies of these triggers are constant as a function of either p_T^{miss} , H_T , or H_T^{miss} , depending on which HLT-level quantities are employed in order to fire the trigger. As long as it is maintained that efficiencies are constant in the relevant subset of these variables, the kinematics of the leptons should not introduce a bias to the computation of the efficiency. The HLT paths designated CR-a and CR-b are also used in the estimation of the combined dilepton and single lepton trigger efficiencies using a third object in the event, separated by both leptons by $\Delta R > 0.4$. In this case, since some of the triggers feature variations of lepton identification or isolation, splitting in a reconstructed quantity, as done for the CR- γ triggers, is a less precise procedure. Instead, these triggers are prioritized based on the highest p_T threshold and the tightest identification or isolation criteria, which ensures most of the time that if the event is accepted by two or more of these triggers, the lowest prescale value is used as the weight of this event. The order of tabulation for these triggers from top to bottom follows the prioritization of these triggers.

5.1.1 Measurement of trigger efficiencies for dilepton events

The measurements of the trigger efficiencies for dilepton events are done by utilizing orthogonal triggers or a third object in $\ell\ell + X$ events. These efficiencies are used when reweighting simulation for residual scale factors, or the leptons in data, when estimating the nonresonant background using different-flavour lepton pairs, described in Sec. 6.1. The measurements are done for the combination of the SR/CR single-lepton, single-photon and dilepton triggers in Tab. 5.1. The measurement sample is limited in number of events, so all events with $m_{\ell\ell} > 50\text{GeV}$ are included, and the results from orthogonal triggers and third-object triggers are combined. When the measurement of efficiencies is done on the simulation, a combination of Drell-Yan, $t\bar{t}$ and $q\bar{q} \rightarrow WW$ simulations are used, and uncertainties in simulation due to pile-up are taken into account separately.

The method with orthogonal triggers follows similar strategy as in [112]. When events are acquired for this method, the triggers used are the MET/HT/MHT and jet triggers of types CR-A–H in the aforementioned tables. Events selected by requiring those triggers are mainly $t\bar{t}$ events from which the efficiencies of the combination of single-lepton and dilepton triggers can be measured. The data sets used for these events are the J_{etHT} , MET, or HTMHT data sets, depending on the data-taking period. These triggers are orthogonal to the signal triggers only when high-enough MET/MHT/HT requirements are placed. Otherwise, leptons could contribute to MET (e.g. muons could also get clustered into jets at HLT). We investigate on the importance of this bias by temporarily removing the orthogonal trigger thresholds, showing in Fig. 5.1, 5.2 and 5.3, where only baseline selections are applied. The results show that any potential bias is within 1-3% from low MET/MHT/HT region, and it is reduced substantially after high MET/MHT/HT thresholds are applied. Therefore, the following event selection requirements are applied on each of the different trigger types to ensure that turn-on effects are avoided:

- CR-A, B: Contribution of events from these triggers is small, so the requirements on the offline reconstructed jets with a $\Delta R = 0.8$ separation parameter are applied.
- CR-C: Only the highest- H_T trigger is unrescaled, so a binning in H_T needs to be considered. In ascending order for the HLT H_T requirements, the thresholds for each of this type of trigger are assigned to be 350, 440, 480, 500, 520, 550, 600, 690, 740, 1000GeV for the 2016 data period, and 500, 550, 580, 600, 680, 700, 750, 800, 900, 1000, 1150GeV for the 2017 and 2018 data periods.
- CR-D: This trigger type only exists in the 2016 data period. A threshold of $p_T^{\text{miss}} \geq 220\text{GeV}$ is applied.
- CR-E: A threshold of $p_T^{\text{miss}} \geq 190$ (220)GeV is applied for the 2016 (2017 and 2018) data period.
- CR-F: This trigger type only exists in the 2016 data period. The thresholds $H_T \geq 330\text{GeV}$ and $p_T^{\text{miss}} \geq 120\text{GeV}$ are applied.
- CR-G: The thresholds $\text{MHT} \geq 130\text{GeV}$ and $p_T^{\text{miss}} \geq 130\text{GeV}$ are applied without an H_T requirement.
- CR-H: This trigger type only exists in the 2017 and 2018 data periods. The thresholds are $\text{MHT} \geq 83\text{GeV}$ and $p_T^{\text{miss}} \geq 83\text{GeV}$ if $H_T \geq 880\text{GeV}$, $\text{MHT} \geq 94\text{GeV}$ and $p_T^{\text{miss}} \geq 94\text{GeV}$ if $H_T \geq 770\text{GeV}$, or $\text{MHT} \geq 110\text{GeV}$ $p_T^{\text{miss}} \geq 110\text{GeV}$ and $H_T \geq 550\text{GeV}$ otherwise.

When $\ell\ell + X$ events are acquired, the triggers used in triggering the third object X are the SR/CR

single lepton or photon triggers, or the CR-a,b prescaled control triggers in the aforementioned tables. The latter set of triggers contain looser selection or p_T thresholds requirements but are prescaled, so they are included only to gain more statistics. The combination of single lepton and single photon data sets is used. The object X can be any baseline lepton as defined in Sec. 5.2, a photon object based on the all of the single photon control region identification requirements except isolation, or a jet passing the identification and pile-up criteria. The additional objects are required to be matched to at least one of the HLT objects that fired the single lepton or photon reference trigger within $\Delta R < 0.2$ and have to be separated from each of the leptons of the dilepton pair that could fire any of the SR/CR dilepton event triggers, including the single lepton or photon triggers, by $\Delta R > 0.4$. If the object X is a lepton that passes the analysis selection requirements, each dilepton pair in the event is considered separately, provided the remaining leptons in other pairing combinations all satisfy the selection requirements on such additional object.

The events in the selection are required to fail a set of conditions for orthogonality to other signal or control regions in this analysis or related analyses:

- If there are exactly 2 leptons passing analysis requirements, the event is required to fail the combination of the $\Delta\phi$ and b-tagging requirements listed in Sec. 5.3 and $p_T^{\text{miss}} \geq 20\text{GeV}$.
- If there are more than 2 leptons passing analysis requirements, the event is required to fail to satisfy $p_T^{\text{miss}} \geq 20\text{GeV}$, having no b-tagged jets and isolated tracks, $\min_{\text{any}\ell\ell}(m_{\ell\ell}) > 4\text{GeV}$, having at least one dilepton pair with same flavor and opposite charge (OSSF pair), and $\max|m_{\ell\ell}^{\text{OSSF}} - m_Z| < 30\text{GeV}$. The last requirement is to ensure that a WZ region can be combined with this analysis later.

The efficiency for the combined trigger on dilepton events is measured as

$$\epsilon_{\text{trigger}} = \frac{[\text{Event selection} \cap (\text{trigger on } X \cup \text{orthogonal trigger})] \cap \text{dilepton trigger}}{\text{Event selection} \cap (\text{trigger on } X \cup \text{orthogonal trigger})}, \quad (5.1)$$

which combines the events that trigger on the additional object X and those that trigger on orthogonal triggers. The event selection requirements and the denominator in Eq. 5.1 is designed such that it does not depend on the measured dilepton system.

Because statistics is limited, the $|\eta|$ bins are combined into 2 categories, barrel and endcap. For muons, $|\eta| < 1.2$ goes to the barrel and $|\eta| \geq 1.2$ to the endcap. For electrons, $|\eta_{\text{SC}}| < 1.479$ goes to the barrel and $|\eta| \geq 1.479$ to the endcap. Therefore, efficiencies of p_T bins are divided into 4 categories of dilepton combinations, barrel-barrel (BB), barrel-endcap (BE), endcap-barrel (EB), endcap-endcap (EE). Technically, $1.479 < |\eta_{\text{SC}}| < 1.566$ is in a barrel-endcap overlap region and this should be avoided when selecting the electrons in the analysis. For the trigger efficiency measurement, it is not necessary to exclude this region since trigger results show little dependence on the η_{SC} . However, for the lepton ID/Isolation efficiency measurement, the overlap region must be well handled with because those selections introduce many cluster variables related to the ECAL. The p_T bins are defined as follows

- muon p_T^μ bins : [18, 25, 55, 100, overflow]
- electron p_T^e
 - 2016 : [19, 25, 35, 65, overflow]
 - 2017 : [13, 25, 38, 75, overflow]
 - 2018 : [13, 25, 35, 75, overflow]

We note that the efficiencies are also measured in the p_T bin below 25 GeV but in the analysis we require a minimum p_T threshold of 25 GeV. Results are shown in Fig. 5.4, 5.5 and 5.6 for dilepton trigger efficiencies measured in data for all the three years and Fig. 5.7, 5.8 and 5.9 for those in MC.

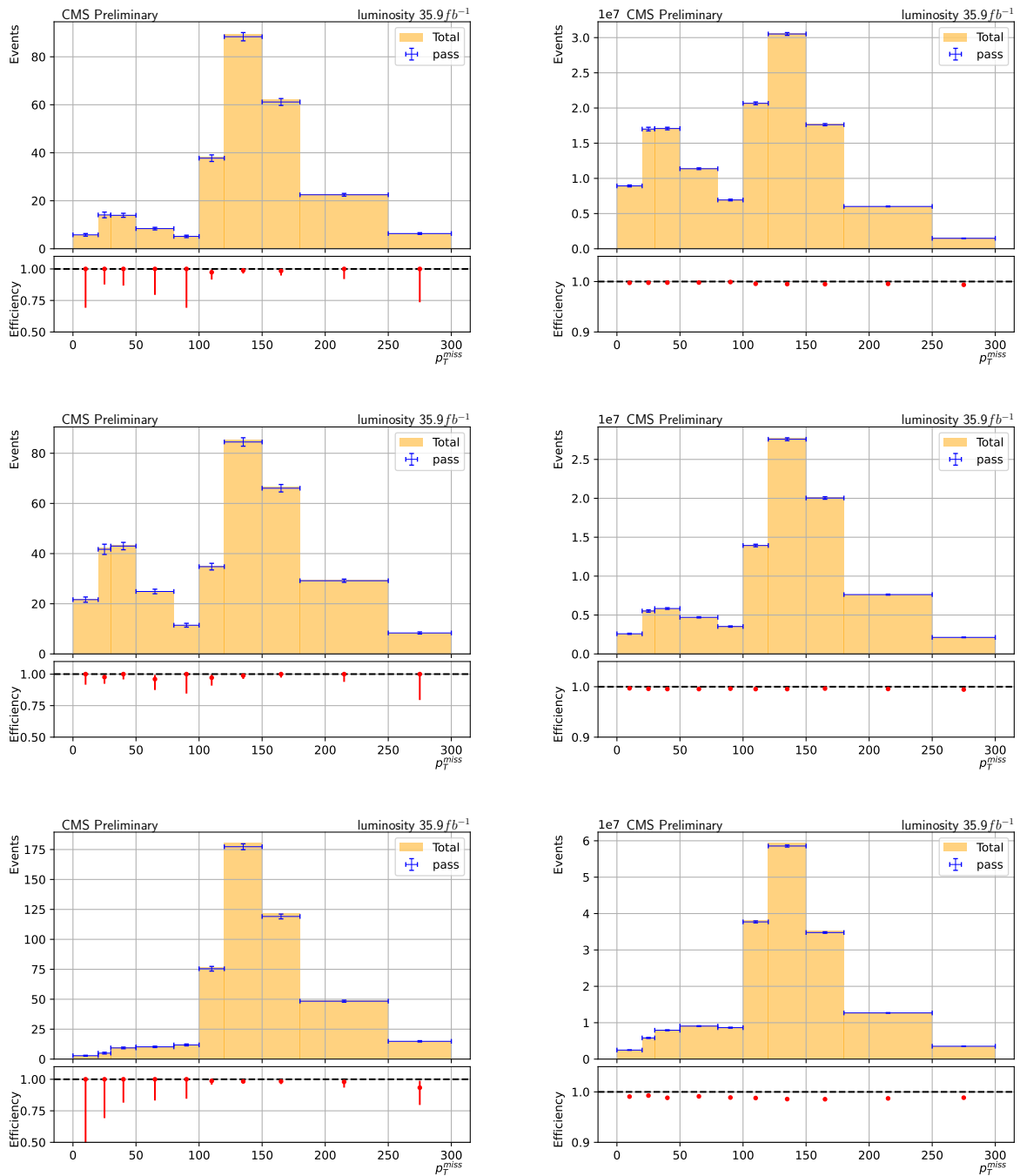


Figure 5.1: Comparisons of the p_T^{miss} distribution and efficiencies in bins of p_T^{miss} from data and simulation of 2016. Total in the legend refers to all events passing MET orthogonal triggers and the offline event preselection. Pass refers to events passing both orthogonal triggers and di-lepton triggers, in addition to the offline event preselection. From top to bottom are ee , $\mu\mu$ and $e\mu$ with data on the left and simulation on the right.

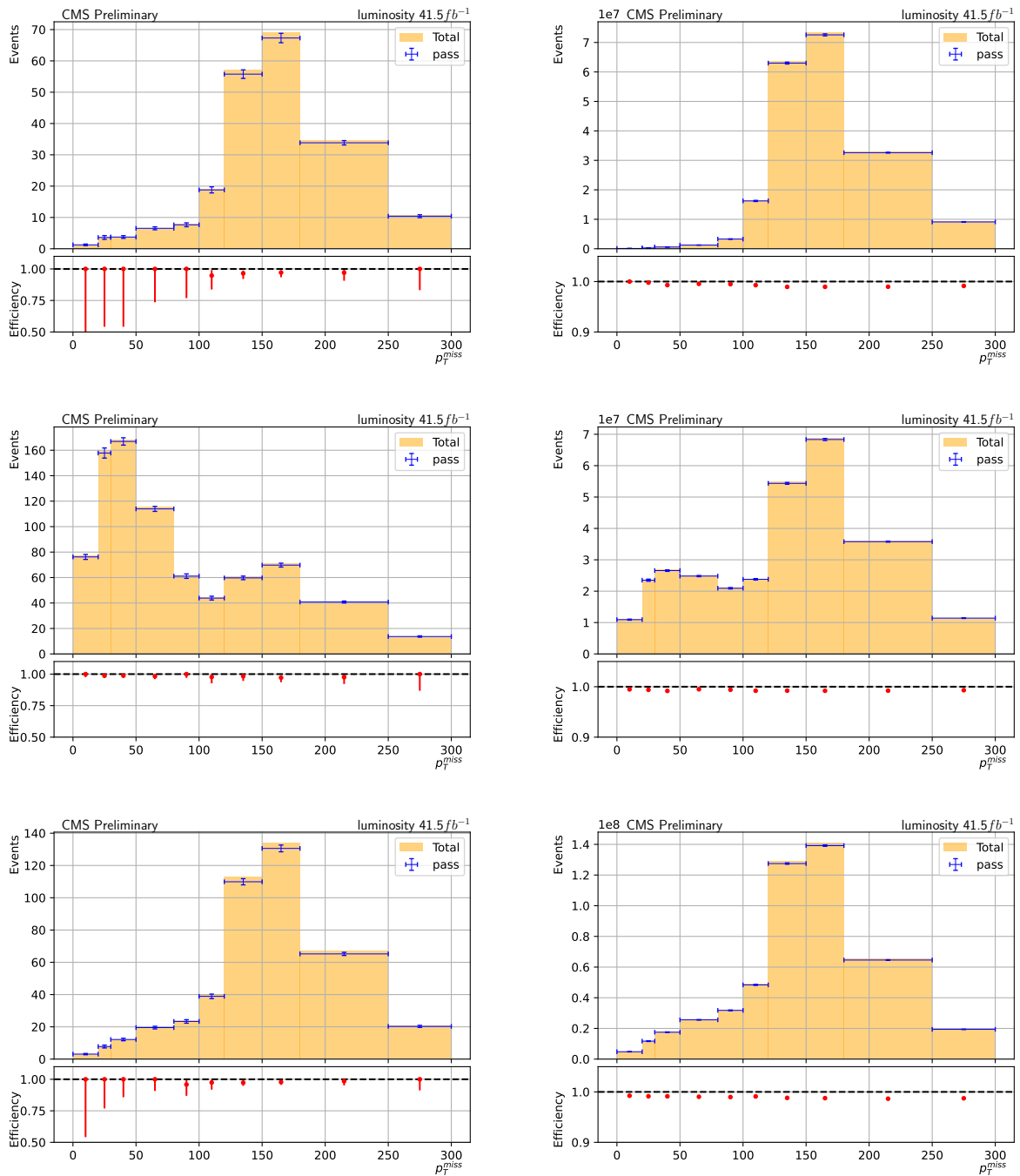


Figure 5.2: Comparisons of the p_T^{miss} distribution and efficiencies in bins of p_T^{miss} from data and simulation of 2017. Total in the legend refers to all events passing MET orthogonal triggers and the offline event preselection. Pass refers to events passing both orthogonal triggers and di-lepton triggers, in addition to the offline event preselection. From top to bottom are ee , $\mu\mu$ and $e\mu$ with data on the left and simulation on the right.

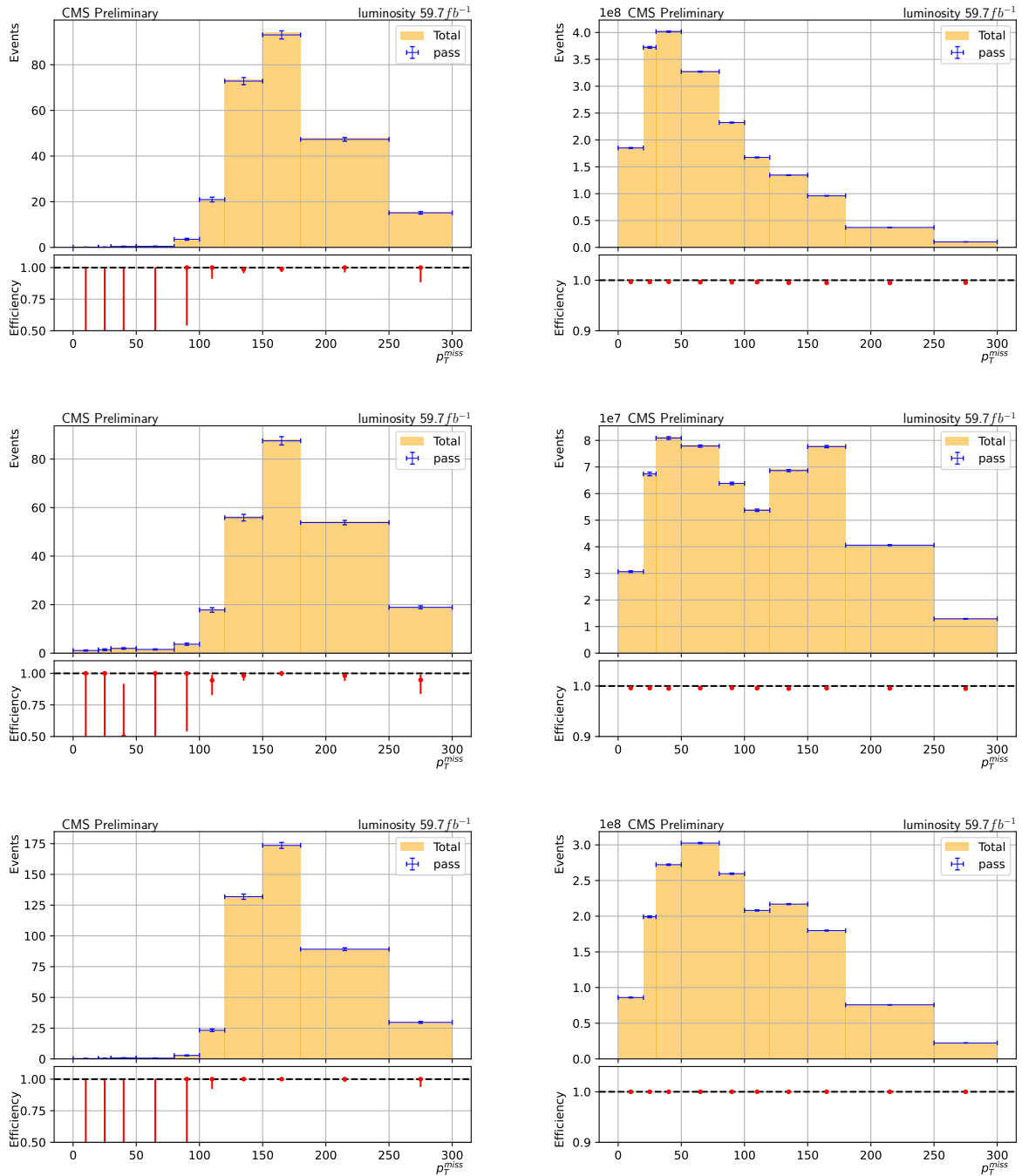


Figure 5.3: Comparisons of the p_T^{miss} distribution and efficiencies in bins of p_T^{miss} from data and simulation of 2018. Total in the legend refers to all events passing MET orthogonal triggers and the offline event preselection. Pass refers to events passing both orthogonal triggers and di-lepton triggers, in addition to the offline event preselection. From top to bottom are ee , $\mu\mu$ and $e\mu$ with data on the left and simulation on the right.

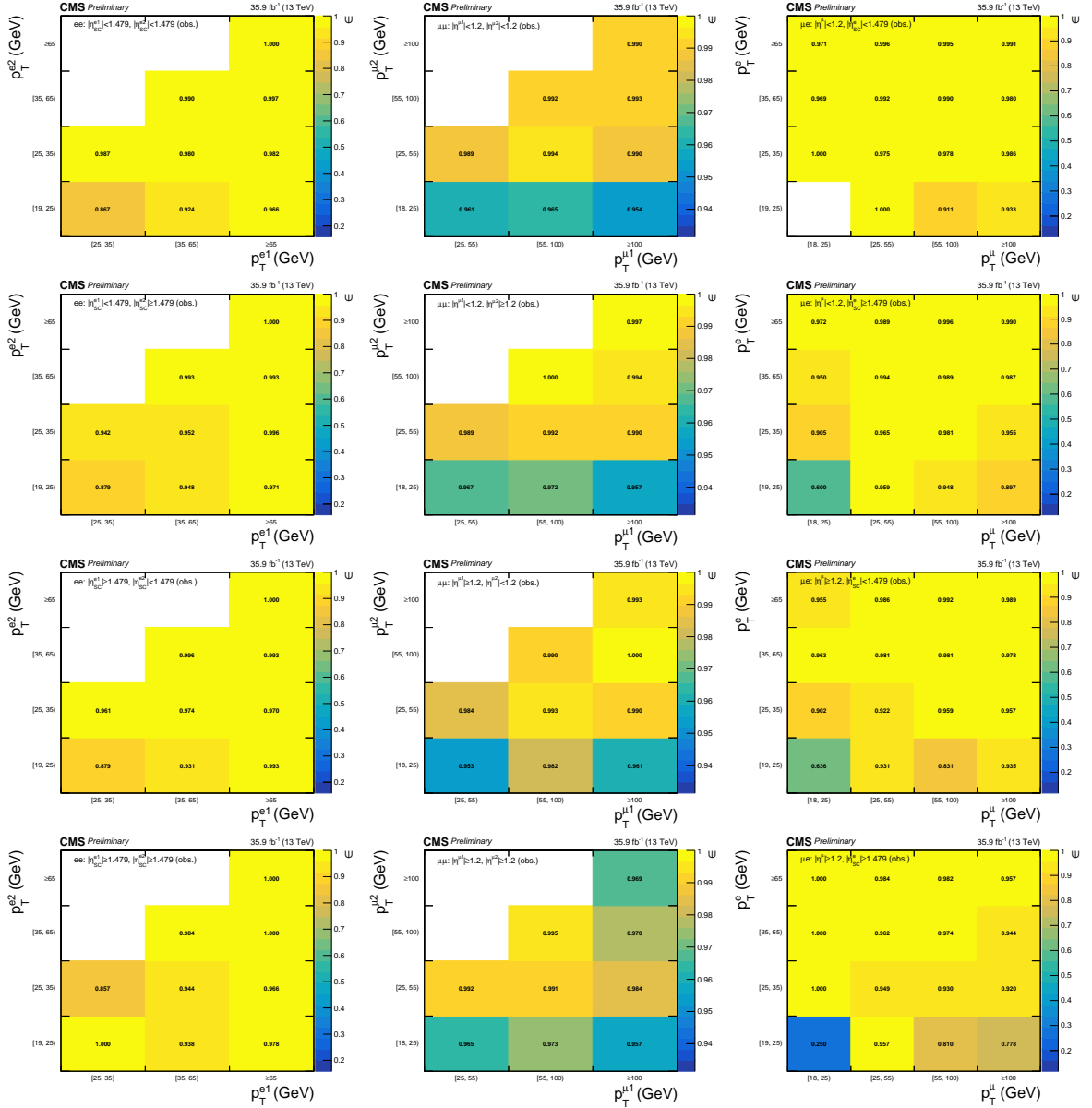


Figure 5.4: The efficiencies of the combined SR/CR dilepton event triggers measured from the observed data in the 2016 data period are shown for the ee , $\mu\mu$, and $e\mu$ decay channels from left to right. The first or second lepton in the pair are required to be both in the barrel region, the first lepton to be in the barrel and the second to be in the endcap, the first lepton to be in the endcap and the second to be in the barrel, and both to be in the endcap region, in order from top to bottom panels. The order of leptons is defined by which one has higher p_T^ℓ in the ee and $\mu\mu$ channels, and the muon is chosen to be the first lepton in the $e\mu$ case.

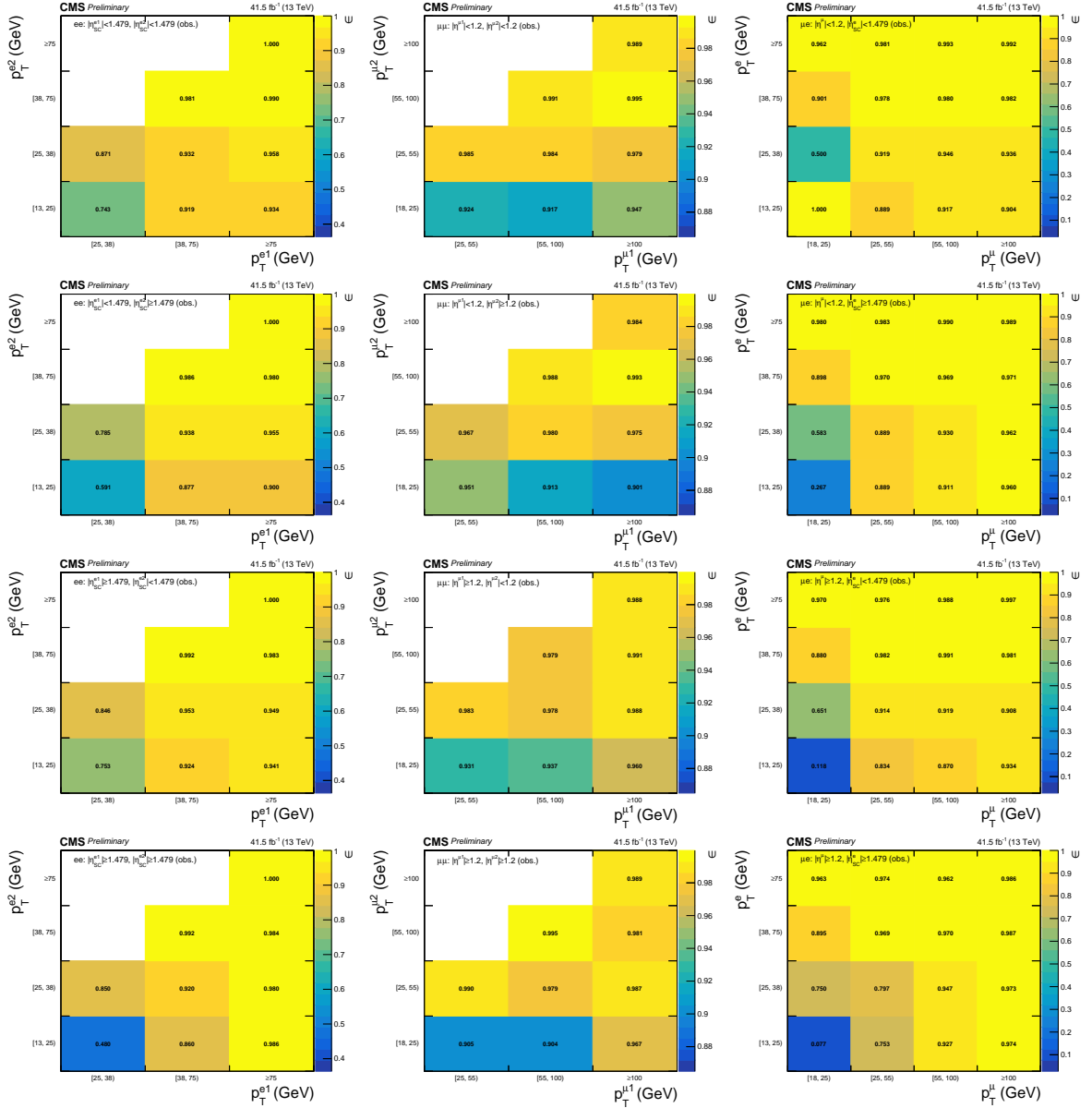


Figure 5.5: The efficiencies of the combined SR/CR dilepton event triggers measured from the observed data in the 2017 data period are shown for the ee , $\mu\mu$, and $e\mu$ decay channels from left to right. The first or second lepton in the pair are required to be both in the barrel region, the first lepton to be in the barrel and the second to be in the endcap, the first lepton to be in the endcap and the second to be in the barrel, and both to be in the endcap region, in order from top to bottom panels. The order of leptons is defined by which one has higher p_T^ℓ in the ee and $\mu\mu$ channels, and the muon is chosen to be the first lepton in the $e\mu$ case.

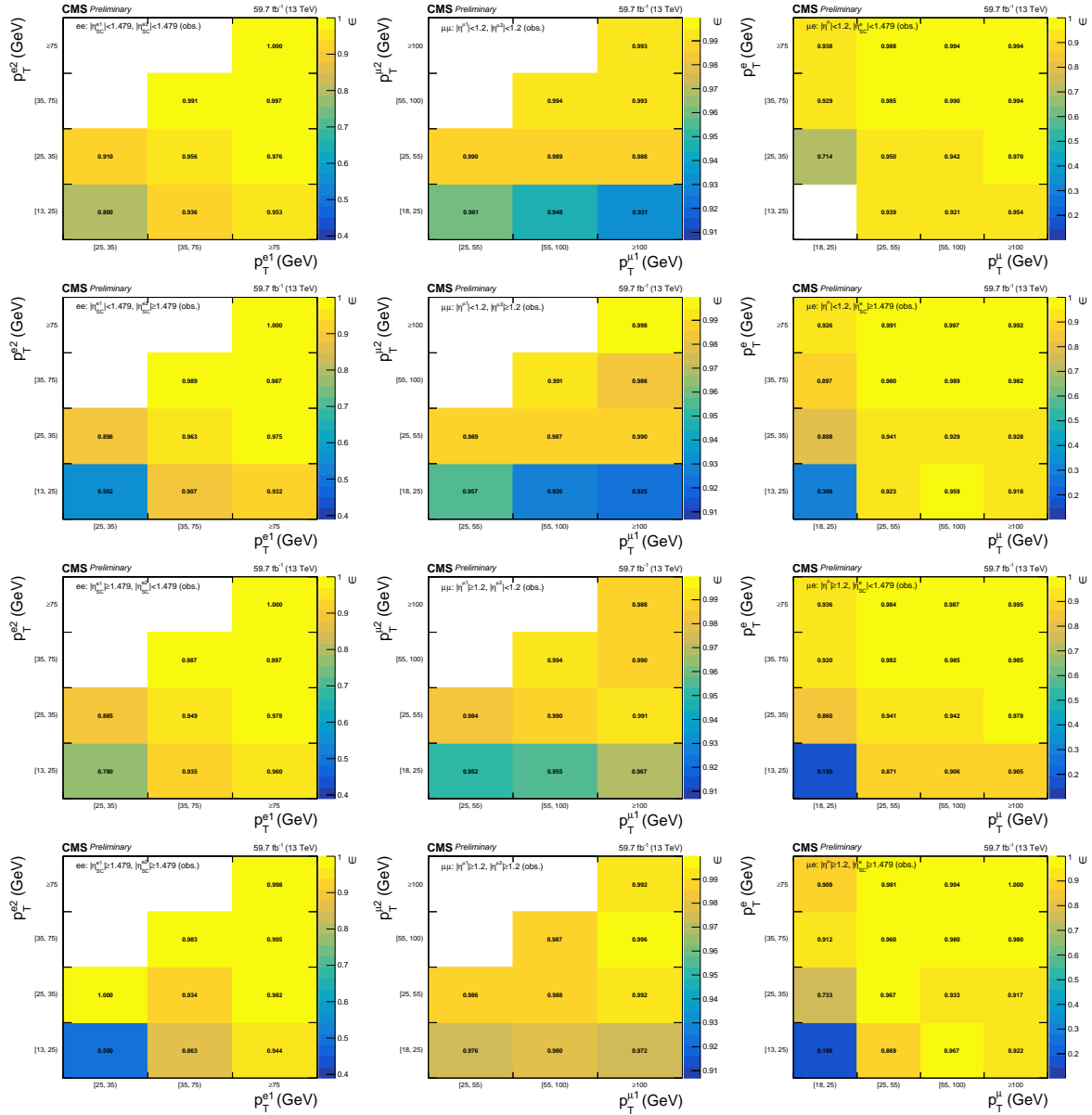


Figure 5.6: The efficiencies of the combined SR/CR dilepton event triggers measured from the observed data in the 2018 data period are shown for the ee , $\mu\mu$, and $e\mu$ decay channels from left to right. The first or second lepton in the pair are required to be both in the barrel region, the first lepton to be in the barrel and the second to be in the endcap, the first lepton to be in the endcap and the second to be in the barrel, and both to be in the endcap region, in order from top to bottom panels. The order of leptons is defined by which one has higher p_T^ℓ in the ee and $\mu\mu$ channels, and the muon is chosen to be the first lepton in the $e\mu$ case.

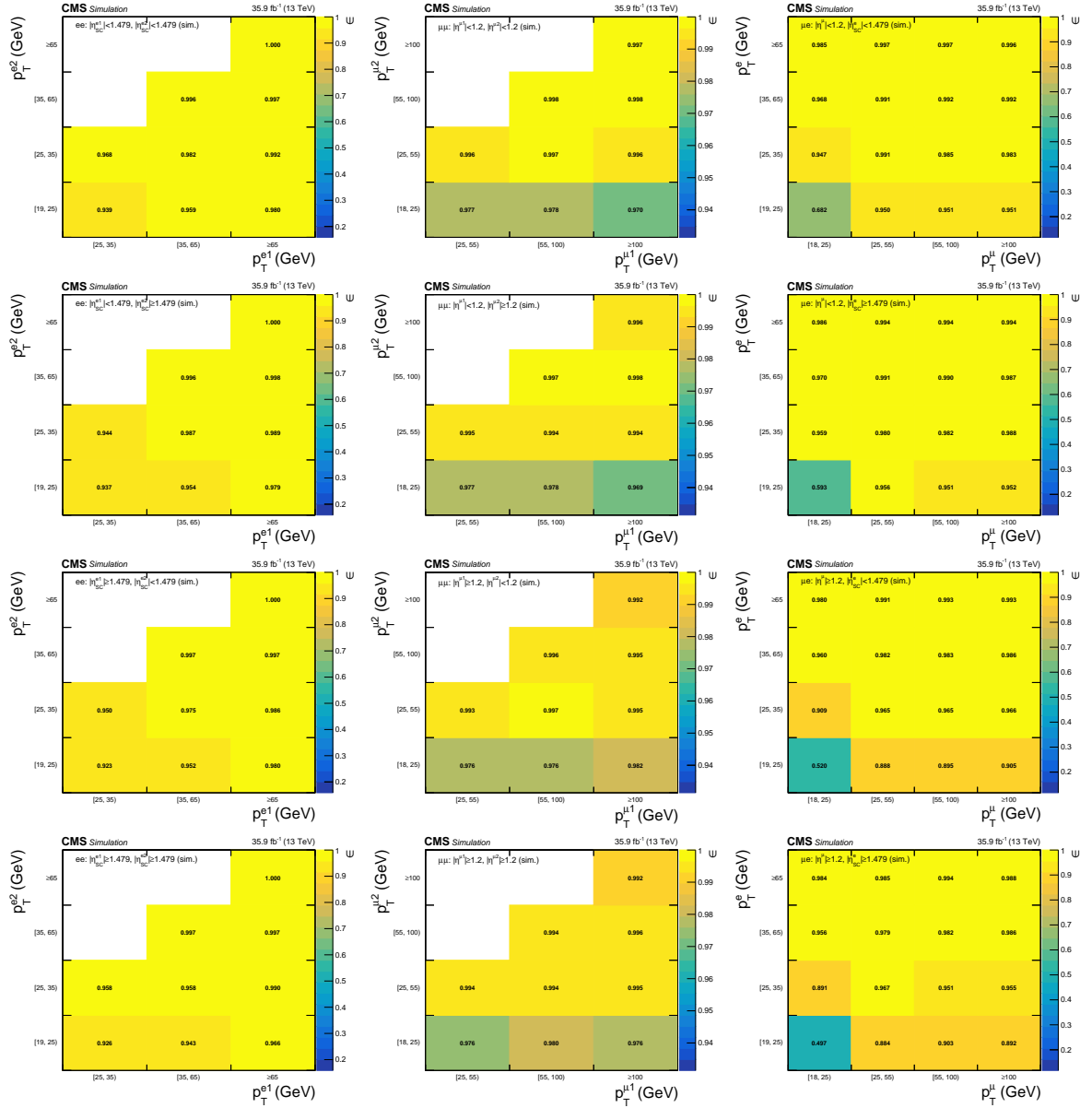


Figure 5.7: The efficiencies of the combined SR/CR dilepton event triggers measured from the simulation in the 2016 data period. The order of the panels is the same as those shown for the efficiencies observed in real data.

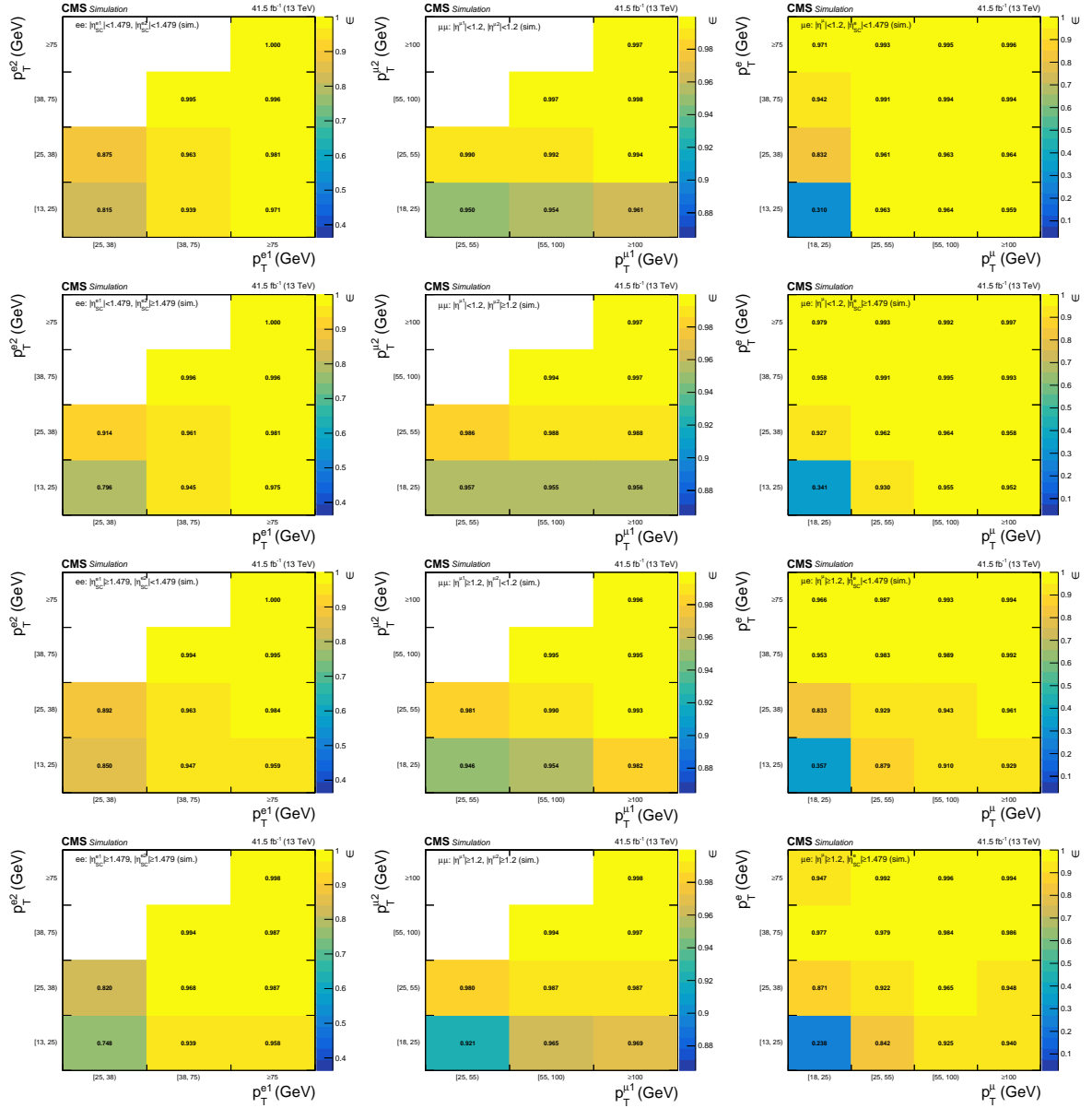


Figure 5.8: The efficiencies of the combined SR/CR dilepton event triggers measured from the simulation in the 2017 data period. The order of the panels is the same as those shown for the efficiencies observed in real data.

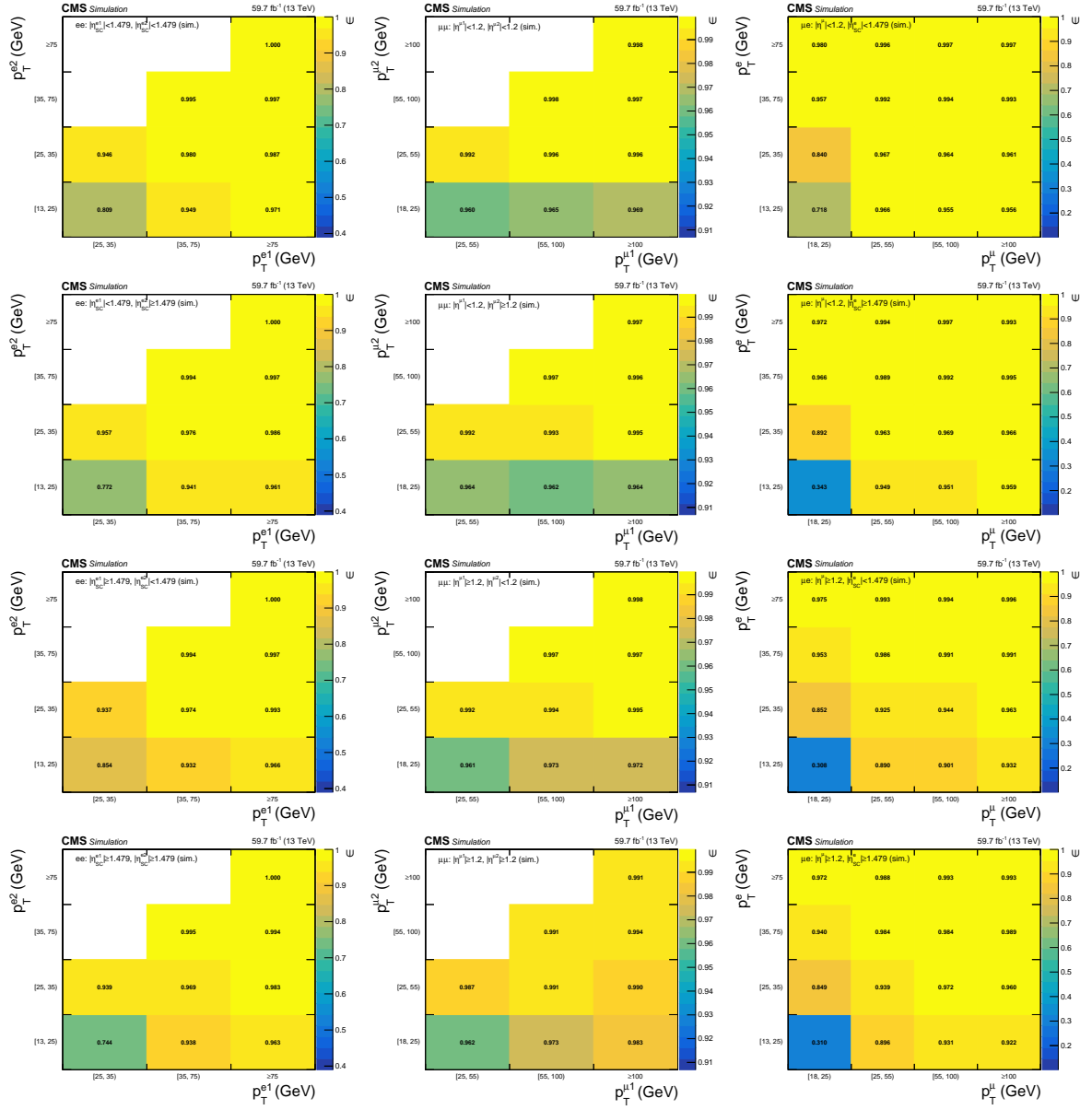


Figure 5.9: The efficiencies of the combined SR/CR dilepton event triggers measured from the simulation in the 2018 data period. The order of the panels is the same as those shown for the efficiencies observed in real data.

5.1.2 Measurement of muon trigger efficiencies

Before we adopted the method described in Sec. 5.1.1 for final results, some different methods for trigger efficiency measurement have been explored. One of them is the reference trigger method, especially used for the muon trigger study.

Reference trigger method The reference trigger method is very useful to measure the efficiency of complex trigger paths, such as single muon triggers with higher threshold, double muon triggers, combination of triggers, etc. Trigger efficiency on di-muon events can be written as

$$\epsilon_{\text{di-muon}} = \epsilon_{\text{ref}} \times \epsilon_{\text{di-muon}|\text{ref}} \quad (5.2)$$

where ϵ_{ref} is the efficiency of reference trigger on di-muon events. For example, we use Mu17 as the reference and it is a single-muon trigger. We derive the efficiency of di-muon events by this formula:

$$\epsilon_{\text{ref on } \mu\mu} = 1 - (1 - \epsilon_{\text{ref on } \mu_1}) \times (1 - \epsilon_{\text{ref on } \mu_2}) \quad (5.3)$$

And di-muon trigger efficiency on the condition of firing reference trigger

$$\epsilon_{\text{di-muon}|\text{ref}} = \frac{\text{Event selection} \cap \text{reference trigger} \cap \text{di-muon trigger}}{\text{Event selection} \cap \text{reference trigger}} \quad (5.4)$$

Choice of the reference trigger The measurement is based on the computation of the complex trigger efficiency on the condition that events pass a reference trigger. For this reason, the reference trigger should have a high efficiency on the events passing the complex trigger. On the other hand, the reference trigger should not bias the result. In this study, Mu17 is the best choice as a reference trigger for complex muon triggers like Mu17_TrkIsoVVL_Mu8_TrkIsoVVL.

Measurement of Mu17 efficiency Efficiency of Mu17 is measured with tag-and-probe method. Tag-and-probe is a method widely used in efficiencies measurement by selecting a lepton pair (with one being tag and another being probe) from the Z resonance. After applying a relatively tight selection on the tag, we have a large chance to get a real lepton pair coming from a real Z. This ensures us the purity of the selected events. To derive the efficiency of a certain flag (IDs, Isolation, etc.), we do it with the probes:

$$\epsilon = \frac{\text{passing probes}}{\text{passing probes} + \text{failing probes}} \quad (5.5)$$

where the total probes sample is split considering whether the leptons pass (Passing probes) or do not pass (Failing probes) the flag that we want to measure.

In practice, Mu17 is a prescaled trigger. Therefore, it is needed to reweight each event to compensate the prescale and the tag muon needs to be matched with the Mu17 trigger object. We require a loose ID for the tag muon with $p_T > 20\text{GeV}$. The tag muon should also be a Particle-flow (PF) muon. As the tag-and-probe is designed to compute efficiency by a single muon, a tag and probe pair can be counted twice in an event with their roles being inverted (the tag being the probe and the probe being the tag). However, as the complex trigger efficiency is computed by muon pair, we need to remove double counting by randomly choosing one of the 2 pairs.

SingleMuon dataset and Drell-Yan ($Z \rightarrow \ell\ell$) simulation sample is used for this study. Di-muon mass range for the fit is set to be [60, 120] (GeV) as no obvious turn-on effects are observed. Since contamination from the background after the selections is small, the model used for fitting the Z resonance is simple:

- Signal : Relativistic Breit-Wigner \otimes Gaussian
- Background : Exponential

Choice of the binning is also flexible for this study. The measurement can be done in a single bin or in several bins depending on the use. The bins are only required to be large enough to ensure enough statistics for the efficiency computation. In this study, we use:

- p_T bins: [25, 50, 75, 100, 150, 200] (GeV)
- $|\eta|$ bins: [0, 0.6, 1.2, 1.8, 2.4]

Fig. 5.10 shows fit results of the first 4 p_T bins from 2018 data.

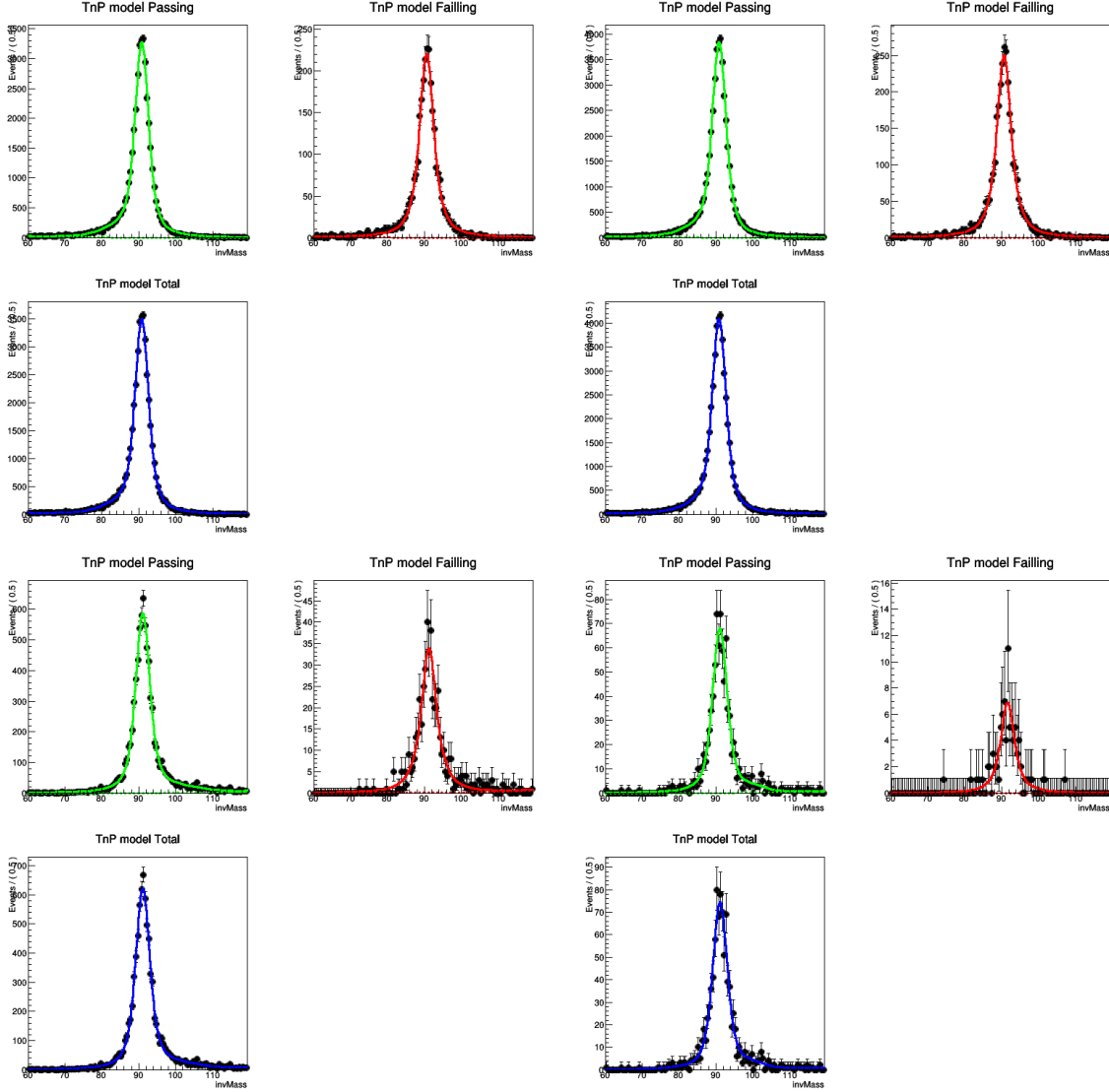


Figure 5.10: **Fitting results in p_T (Unit is GeV) bins of [25, 50](top, left), (50, 75](top, right), (75, 100] (bottom, left) and (100, 150] (bottom, right) from 2018 data.**

Measurement of complex trigger efficiency We first measure the efficiency of the complex trigger on di-muon events triggered by the reference trigger Mu17. In this step, background contamination is further suppressed after applying event selections. To derive the efficiency, we can still fit the Z mass or simply count the events via Formula 5.4. We then compute the reference trigger efficiency in 2-dimension by Formula 5.3 for di-muon events and multiply by the efficiencies derived in the first step bin by bin.

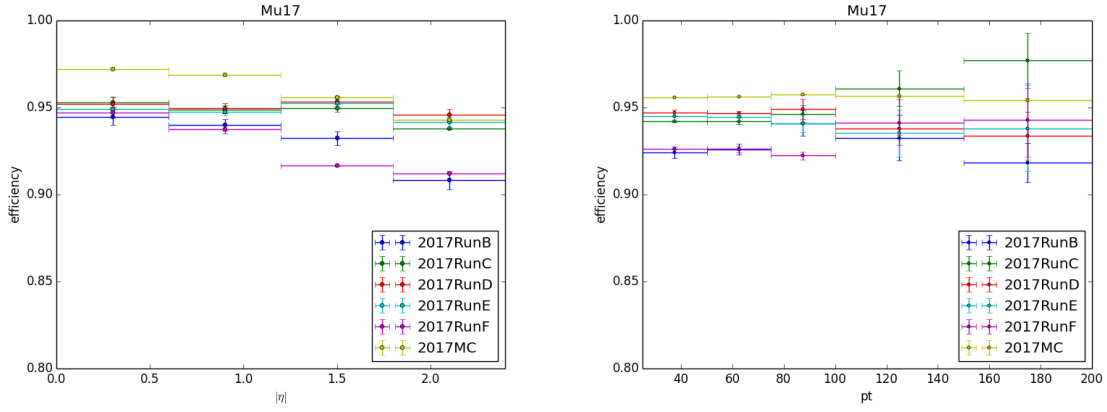


Figure 5.11: Mu17 efficiencies measured in bins of $|\eta|$ (top) and p_T (bottom) for 2017

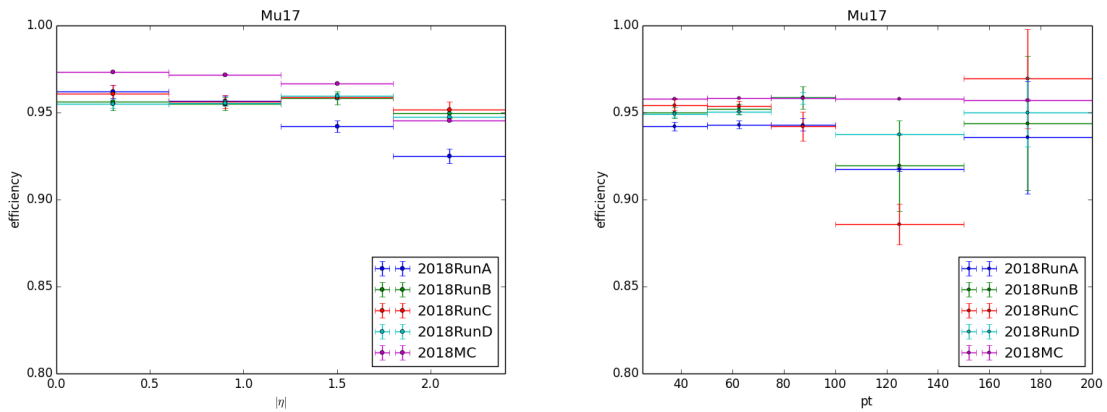


Figure 5.12: Mu17 efficiencies measured in bins of $|\eta|$ (top) and p_T (bottom) for 2018

Bias from the method There are several factors that could potentially bias the results:

- Difference of L1 seed: For example, the quality criterion on muon legs was tighter in single muon L1 seed than in double muon seed during Run-1. It led to a bias reaching 4% at high η . For run-2 the quality cuts of the L1 double muon seed is the same as for L1 single muon seed.
- Additional cut on the tag muon: Requiring muon being matched with a L3 object could introduce an overestimation of the efficiencies. This should be taken into account in the systematic uncertainties.
- Binning: Choice of the binning may introduce bias.

For MC simulation, we can either compute the efficiencies using the reference method by Formula 5.2, or derive the efficiencies directly by counting since they are $Z \rightarrow \ell\ell$ events with high purity

$$\epsilon_{\text{MC truth}} = \frac{\text{Event selection} \cap \text{di-muon trigger}}{\text{Event selection}} \quad (5.6)$$

The difference of the results between this two methods

$$\epsilon_{\text{diff}} = \epsilon_{\text{ref method}} - \epsilon_{\text{MC truth}} \quad (5.7)$$

is shown in Fig. 5.13 with 4 $|\eta|$ bins, taking 2018 result as an example. The effect is within a permille scale and always smaller than the statistical uncertainties

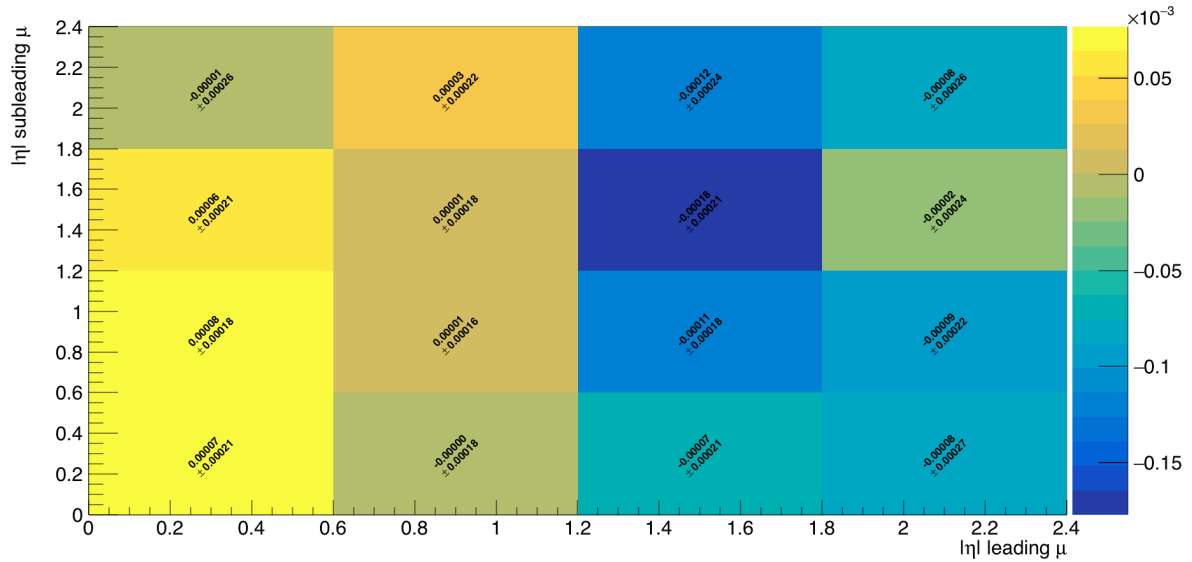


Figure 5.13: MC closure test shows the efficiency difference between two sets of results in $|\eta|$ bins. Results are derived from Drell-Yan simulation in 2018 condition.

Potential use in $ee/e\mu$ cases This method should be usable in $ee/e\mu$ cases as well. However, we need to deal with some difficulties in practice. For example, low p_T electrons often sit on large background. Finding a reference trigger for electron is not always easy since the p_T threshold and selections on L1 seed are tighter than the legs of double electron trigger or MuEG trigger, which has a large chance to bias the results. For $e\mu$ channel, simulation of $t\bar{t}$ events must be selected with high purity. Pre-scale need to be carefully monitored so that running conditions are properly taken into account.

Unlike the case of muon trigger, measuring efficiencies in $ee/e\mu$ using this method requires additional efforts and may still fail at the end.

5.2 Physics object selections

This section lists selection criteria of all the physics objects use in the analysis. Some details of Muon/Electron/Photon identification and isolation standard are already introduced in Sec. 3.2.

Muon

- Cut-based medium prompt ID
- momentum corrected based on the Rochester calibration method using $Z \rightarrow \mu\mu$ events
- Isolation

$$\mathcal{I}_{\text{rel}}^{\mu} = \frac{\mathcal{I}_{\text{ch}} + \max(\mathcal{I}_{\text{nh}} + \mathcal{I}_{\gamma} - 0.5 \times \mathcal{I}_{\text{ch}}^{\text{PU}}, 0)}{p_{\text{T}}^{\mu}}$$

with p_{T}^{μ} in the denominator after momentum corrections.

The muons used in this analysis are required to satisfy $\mathcal{I}_{\text{rel}}^{\mu} < 0.15$, $p_{\text{T}}^{\mu} \geq 5\text{GeV}$, and $|\eta| < 2.4$. Events are vetoed if there are excess muons with $\mathcal{I}_{\text{rel}}^{\mu} < 0.4$.

- $p_{\text{T}} \geq 25\text{ GeV}$ for event selection, $p_{\text{T}} \geq 5\text{ GeV}$ for event veto

Electron

- Identification: Fall17 (no iso.) WP90
- Isolation

$$\mathcal{I}_{\text{rel}}^{\text{e}} = \frac{\mathcal{I}_{\text{ch}} + \max(\mathcal{I}_{\text{nh}} + \mathcal{I}_{\gamma} - A_{\text{eff}}^{\text{e}} \times \rho, 0)}{p_{\text{T}}^{\text{e}}}$$

with p_{T}^{e} in the denominator after electron energy corrections. The electrons used in this analysis are required to satisfy $\mathcal{I}_{\text{rel}}^{\text{e}} < 0.1$, $p_{\text{T}}^{\text{e}} \geq 5\text{GeV}$, and $|\eta| < 2.5$. Events are vetoed if there are excess electrons with $\mathcal{I}_{\text{rel}}^{\text{e}} < 0.4$.

- $p_{\text{T}} \geq 25\text{ GeV}$ for event selection, $p_{\text{T}} \geq 5\text{ GeV}$ for event veto
- not counted if $\Delta R < 0.05$ away from a muon

Photon

- ‘Fall17 tight’ cut-based selection criteria
- $p_{\text{T}} \geq 20\text{GeV}$ & $|\eta| < 2.5$ for event veto
- $p_{\text{T}} \geq 55\text{GeV}$ (barrel-only when $N_j = 0, 1$. N_j represents for number of jets in an event) for the single-photon CR Additional photon selections are applied in order to enrich the purity of photons in the single photon CR as follows:
 - Particle-flow photon requirement: to ensure one reconstructed photon being matched with exactly on particle-flow photon in order to derive a correct $p_{\text{T}}^{\text{miss}}$ calculation from particle-flow candidates
 - pixel seed & electron veto: These two vetoes reduce contamination from $e \rightarrow \gamma$ fake photons.
 - $\sigma_{i\eta i\eta} > 0.001$, $\sigma_{i\phi i\phi} > 0.001$: These requirements remove the ECAL noise in real data characterized as a single-cell spike.

- $E_{\text{MIP}} < 4.9\text{GeV}$: This represents for the total minimum-ionizing particle energy in the photon cluster. We set an upper value of E_{MIP} in order to avoid charged beam halo particles that might deposit energy in ECAL through leaving a trail of clusters.
- $|t_{\text{seed}}| < 2\text{ns}$, $-2\text{ns} < t_{\text{seed}} < 1\text{ns}$ in 2018 : This is the timing difference between the readout of the ECAL seed and the estimated collision time. By setting range of the timing, we further reject beam halo muon contamination with slightly earlier hits than the prompt collision products.

MET(or $p_{\text{T}}^{\text{miss}}$)

- Estimated from PF candidates
- ‘Type-1’ corrections from jets reconstruction
- MET recipe v2 for EE noise mitigation is applied in 2017 run period E and F

MET filters

- 2016:
goodVertices, HBHENoiseFilter, HBHENoiseIsoFilter, EcalDeadCellTriggerPrimitiveFilter, globalSuperTightHalo2016Filter, BadPFMuonFilter (common); eeBadScFilter (real data only)
- 2017 and 2018:
goodVertices, HBHENoiseFilter, HBHENoiseIsoFilter, EcalDeadCellTriggerPrimitiveFilter, globalSuperTightHalo2016Filter, BadPFMuonFilter, ecalBadCalibFilter (common); eeBadScFilter (real data only).
- All dedicated MET filters above are developed by the CMS Jet/MET POG

Isolated track

- Isolated tracks in this analysis are used to clean out extra leptons and most of taus.
- veto event if an isotrack is found satisfying
 - PF candidates
 - $|d_z| < 0.1\text{cm}$
 - $p_T \geq 5(10)\text{GeV}$ for electrons or muons (charged hadrons)
 - $\Delta R > 0.3$ away from each tight charged lepton
 - Track Isolation $< \min(5\text{GeV}, 0.1 \times p_{\text{T}}^{\text{track}})$

Primary vertex Each event must contain at least one reconstructed pp interaction vertex. The primary vertex is supposed to satisfy

- $|z| < 24\text{ cm}$ and $|\rho| < 2\text{ cm}$ in cylindrical geometry,
- Degrees of freedom > 4 ,
- 2 associated tracks.
- Valid and not fake vertex fits by the vertex reconstruction algorithm.

Jet

- ak4 PF-CHS jets
- $p_T \geq 30\text{GeV}$
- $|\eta| < 4.7$
- $\Delta R(\text{jet}, \text{obj}) > 0.4$, obj = any charged lepton, photon

Btagger

- Jets are tagged as b-tagged jets using the DeepJet algorithm [113]
- The loose (tight) working point is defined based on the ‘loose’ (‘medium’) working point in order to veto (accept) events with b-tagged jets in the signal region (the control region for the non-resonant background estimation).

5.2.1 Measurement of lepton efficiencies

The lepton efficiencies are measured with a tag-and-probe method using $Z \rightarrow \ell\ell$ events. In this analysis, lepton efficiencies are measured with selection requirements that are orthogonal to the event preselection, described in Sec. 5.3. All the selection requirements on the events, the tags, and the probes are summarized in Tab. 5.5 and described in detail below.

Baseline requirements For any tag or probe muon described in this section, it’s required to have a track in the tracker, and for any electron described in this section is to satisfy $E_{\text{corr}}^{\text{ECAL}} \sin(\theta_{\text{SC}}^{\text{pos}}) \geq 5\text{GeV}$. Events are required to contain exactly 2 such lepton pairs separated by $\Delta R > 0.4$ and no good isolated tracks or baseline photons separated from the leptons also by $\Delta R > 0.4$, and satisfy all event veto requirements described in Sec. 3.2. The transverse missing momentum is required to satisfy $p_T^{\text{miss}} < 70\text{GeV}$ to ensure total orthogonality of the efficiency measurement regions to the signal region.

Muon selection requirements The tag muon is required to satisfy the same analysis identification and tight isolation criteria in Sec. 3.2 in addition to the baseline selection. The tagging requirement is varied by adding the cut-based tight identification requirements together with a tight charge requirement, $\delta p_T/p_T < 0.2$ for the best track fit, when systematic variations are considered. The combination of the unrescaled single-muon triggers listed in Tab. 5.1 in Sec. 5.1 are used to trigger on the tag muon, with a $\Delta R < 0.2$ matching between the tag and the HLT muon object firing any of these triggers. Only the `SingleMuon` data set is used. The minimum p_T values of the tag muon are 27GeV for the 2016 and 2018 data sets, and 30GeV for the 2017 data set, and a variation with +2GeV is considered to account for any variations due to trigger turn-on. The selection requirements on the probe muons also start with the baseline requirement and progressively apply the analysis muon identification requirement, $\mathcal{I}_{\text{rel}}^\mu < 0.4$, and $\mathcal{I}_{\text{rel}}^\mu < 0.15$, based on the efficiency of the progressively tighter criteria being measured.

Electron selection requirements The tag electron is required to satisfy the same analysis identification and tight isolation criteria in Sec. 3.2 in addition to the baseline selection. The tagging requirement is varied by tightening the BDT score working point to ‘WP80’ and adding a three-charge consistency requirement when systematic variations are considered. The combination of the unrescaled SR/CR single-electron and single-photon triggers listed in Tab. 5.1 in Sec. 5.1 are used to trigger on the tag electron, with a $\Delta R < 0.2$ matching between the tag and the HLT e/γ object firing any of these triggers. Only the `SingleElectron` and `SinglePhoton` (EGamma in the 2018 data period) data sets are used. The minimum p_T values of the tag electron are 28, 38, and 35 GeV for the 2016, 2017 and 2018 data sets respectively, and a variation with +2 GeV is considered to account for any variations due to trigger turn-on. The selection requirements on the probe electrons also start with the baseline requirement and progressively apply the analysis electron identification requirement, $\mathcal{I}_{\text{rel}}^e < 0.4$, and $\mathcal{I}_{\text{rel}}^e < 0.1$, based on the efficiency of the progressively tighter criteria being measured. Efficiencies are measured separately for the gap and non-gap electrons, and their combination.

Statistical model In order to extract the efficiencies in the observed data, the signal $m_{\ell\ell}$ shape is fitted from the simulated Drell-Yan samples in each bin of p_T and η , or η_{SC} , of the probe lepton, matched to generator-level prompt leptons within $\Delta R < 0.2$. The matching requirement is observed to clean non-prompt leptons with no loss in efficiency for events at the resonance peak even in bins where final-state radiation (FSR) could shift the dilepton resonance peak. The fit functions, summarized in Tab. 5.6, use a convolution of a relativistic Breit-Wigner with a resolution function. The resolution function is chosen to be the product of a double-sided Crystal Ball (DCB) with a product of the exponential function and the complementary error function, both shifted separately to center around $\Delta m_{\ell\ell} \sim 0$ GeV just like the DCB in the resolution model and with the shift parameters unconstrained in the fit but kept the same between the observed and simulated data sets. When probe leptons pass identification but fail isolation (loose or tight), non-collinear FSR may shift the mass peak substantially, and the slow rise or fall corrections on the DCB function no longer become adequate. We parametrize those cases by summing the full convolution of a relativistic Breit-Wigner with a DCB with either another DCB or a Gaussian distribution, shifted toward the second peak at lower $m_{\ell\ell}$ values with a varying fractional contribution. When the fits are performed, the $m_{\ell\ell}$ region is varied between [60, 120] GeV, [65, 115] GeV, and [70, 110] GeV in order to account for the dependency of shape fit parameters on the mass window chosen. As summarized in Tab. 5.7, the background in the observed data is fit with the product of the exponential and the complementary error functions, or Bernstein polynomials of order 3, or the exponential function itself. We refer to these function forms as ‘RooCMSShape’, ‘Bernstein’, and ‘Exponential’, respectively, when abbreviation is needed. The latter two functions are used only when the [70, 110] GeV $m_{\ell\ell}$ window is considered because these functional forms cannot account for turn-on effects. Chebyshev (abbr. ‘Chebyshev’) polynomials up to order 3 are also considered for the background parametrization in the collection of fits performed if and only if the fits performed using the Bernstein parametrization fail.

Uncertainties The uncertainties on the lepton efficiencies and scale factors are categorized into four:

- **Statistical uncertainties:** This source of uncertainty arises purely from the number of events and uncertainties on the fit parametrization. Variations from the fit functions are included in this component. All p_T and η bins are treated as correlated in order to have a conservative, envelope-type variation, but the different data periods are treated as uncorrelated.
- **Systematic uncertainties:** This source of uncertainty arises from the variations on the tag lepton and the mass window used in the fits. All p_T and η bins are treated as correlated. Since the

specifics of the tag leptons change across the different data periods, this uncertainty is treated as uncorrelated across the data periods.

- Variations from alternative simulation generators: This source of uncertainty is observed to be anti-correlated between moderate and low or high p_T^ℓ ranges. The full shape effect is included in the uncertainties on efficiency scale factors. However, this is not included in the analysis when efficiencies themselves need to be used since these differences come from the physics process itself and how it is simulated. The uncertainties in different data periods are correlated.
- Pile-up variations: This source of uncertainty is correlated considering other variables such as p_T^{miss} . While the uncertainty on the minimum bias cross section is the same across different data periods, the pile-up distributions themselves are not. Therefore, the different data periods are treated as uncorrelated.

Fig. 5.14 shows tests of muon mass fit when choosing the best shape for the background. The mass region is extended to reach [70, 130] during the fit but it has little effects on the results since mass turn-on effects concentrate in the lower band.

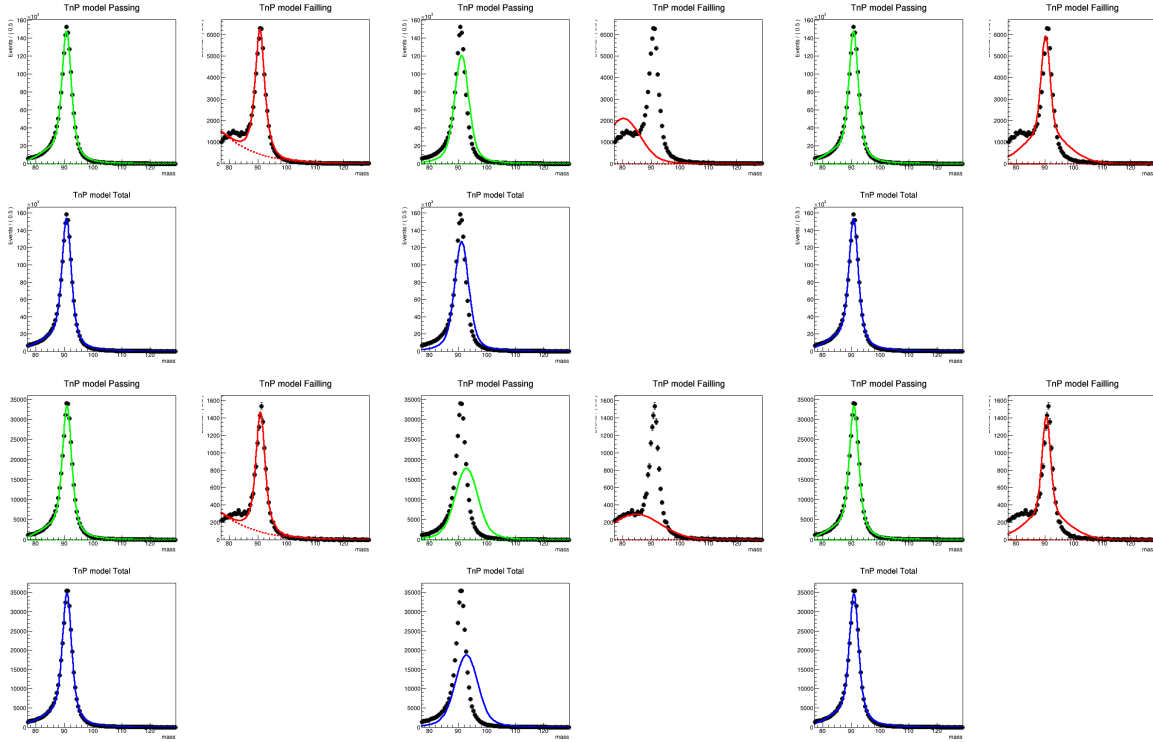


Figure 5.14: **Shown are the results of the muon mass fit for testing the medium isolation selection for 2016 as an example**, with top three figures for data and bottom three for Drell-Yan simulation. The functions used for fitting the shape of background are RooCMSShape, Chebyshev and Exponential from left to right respectively, in the bin of $|\eta| < 1.2$ and a combined p_T bin of $25 < p_T < 55$. Black dots represents for observed data, green line for the fit of the events passing iso. test, red for the failing and blue for the total (passing plus failing).

The final efficiencies measured from the observed data in periods 2016, 2017, and 2018 are shown in Fig. 5.15, 5.16, and 5.17 Likewise, the final efficiencies measured from the simulation for the 2016, 2017, and 2018 data periods are respectively shown in Figs. 5.18, 5.19, and 5.20

Table 5.5: **Summary of tag and probe selection requirements for the lepton efficiency measurements.** The requirements on the probe leptons for loose and tight isolation measurements add lepton identification or loose isolation as appropriate. The SR/CR triggers mentioned are listed in Sec. 5.1.

Muons	
Event requirements	Analysis MET filters, jet noise requirements, $p_T^{\text{miss}} < 70\text{GeV}$ No good iso. tracks, baseline photons with $p_T \geq 20\text{GeV}$, $ \eta < 2.5$, or loose electrons with $p_T \geq 5\text{GeV}$, $ \eta < 2.5$, separated by $\Delta R > 0.4$ from both leptons
Tag trigger reqs.	Single μ SR/CR triggers, SingleMuon data set $\Delta R < 0.2$ match with the firing HLT object $p_T \geq 27\text{GeV}$ in 2016 or 2018, $\geq 30\text{GeV}$ in 2017; $ \eta < 2.4$ +2GeV in p_T threshold for tighter trigger efficiency variation
Tag ID/iso. reqs.	Loose tag: Cut-based medium-prompt ID with $\mathcal{I}_{\text{rel}}^\mu < 0.15$ iso. (analysis tight selection req.) Tight tag: + Cut-based tight ID and best track $\delta p_T/p_T < 0.2$
Probe reqs.	$\Delta R > 0.4$ from the tag lepton ID: Tracker muon Loose iso.: Analysis ID requirement Tight iso.: + $\mathcal{I}_{\text{rel}}^\mu < 0.4$ (analysis loose iso. req.)

Electrons	
Event requirements	Analysis MET filters, jet noise requirements, $p_T^{\text{miss}} < 70\text{GeV}$ No good iso. tracks, baseline photons with $p_T \geq 20\text{GeV}$, $ \eta < 2.5$, or loose muons with $p_T \geq 5\text{GeV}$, $ \eta < 2.4$, separated by $\Delta R > 0.4$ from both leptons
Tag trigger reqs.	Single e/γ SR/CR triggers SingleElectron and SinglePhoton data sets (EGamma in 2018) $\Delta R < 0.2$ match with the firing HLT object $p_T \geq 28\text{GeV}$ in 2016, $\geq 38\text{GeV}$ in 2017, and $\geq 35\text{GeV}$ in 2018; $ \eta < 2.5$ +2GeV in p_T threshold for tighter trigger efficiency variation
Tag ID/iso. reqs.	Loose tag: Fall17 no-iso. MVA ‘WP90’ ID with $\mathcal{I}_{\text{rel}}^e < 0.1$ iso. (analysis tight selection req.) Tight tag: + ‘WP80’ and three-charge consistency
Probe reqs.	$\Delta R > 0.4$ from the tag lepton ID: $E_{\text{corr}}^{\text{ECAL}} \sin(\theta_{\text{SC}}^{\text{pos}}) \geq 5\text{GeV}$ Loose iso.: Analysis ID requirement Tight iso.: + $\mathcal{I}_{\text{rel}}^e < 0.4$ (analysis loose iso. req.)

Table 5.6: **Fit functions of dilepton resonance peak in the observed data and simulated Drell-Yan sample**

No mass peak shift	Account for mass peak shift
relativistic Breit-Wigner \otimes DCB	relativistic Breit-Wigner \otimes (DCB + another DCB or Gaussian)

Table 5.7: **Fit functions of the background in the observed data**

Mass range apart from turn-on effects $m_{ll} \in [70, 110]$ GeV	Accounting for turn-on effects $m_{ll} \in [60, 120]$ GeV, [65, 115] GeV
RooCMSShape Bernstein(Chebyshev) Exponential	RooCMSShape

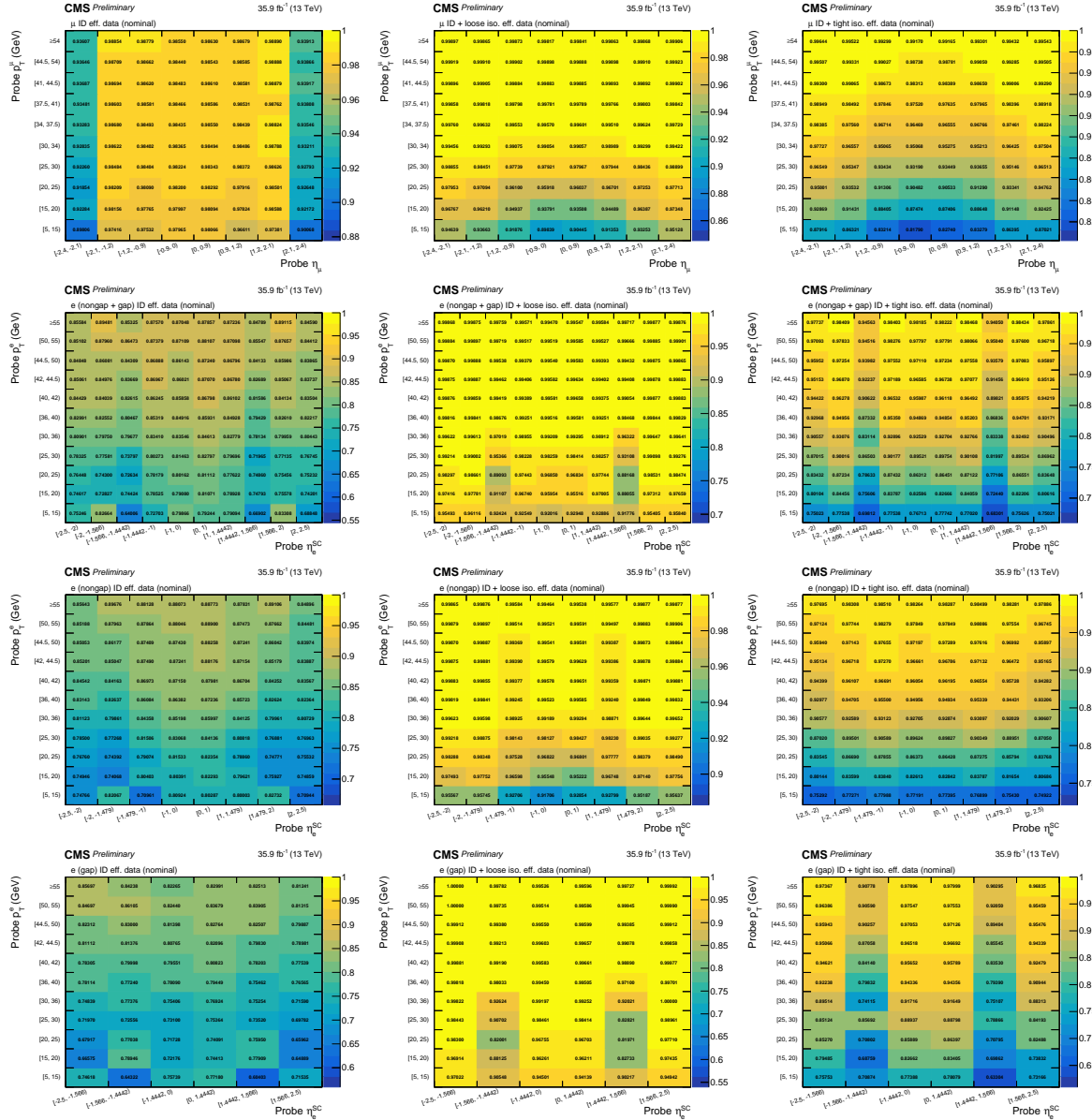


Figure 5.15: The lepton identification and isolation efficiencies measured from observed data in 2016 for muons (first row), non-gap and gap electrons combined (second row), non-gap electrons only (third row) and gap electrons only (fourth row). The panels show the nominal variations of the conditional efficiencies to pass lepton identification (first column), pass loose isolation for event veto (second column), and pass tight isolation for analysis (third column).

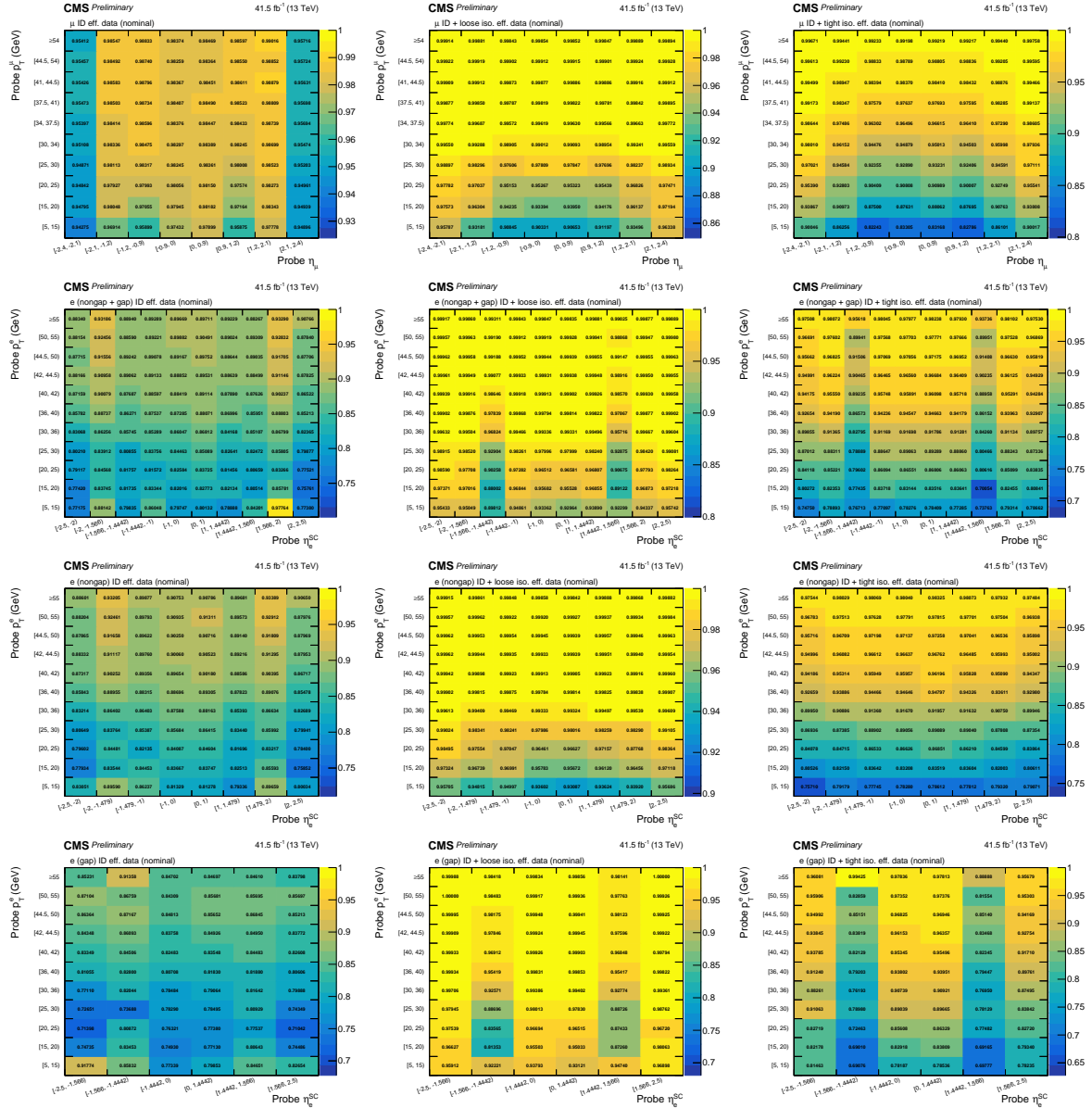


Figure 5.16: The lepton identification and isolation efficiencies measured from observed data in 2017 for muons (first row), non-gap and gap electrons combined (second row), non-gap electrons only (third row) and gap electrons only (fourth row). The panels show the nominal variations of the conditional efficiencies to pass lepton identification (first column), pass loose isolation for event veto (second column), and pass tight isolation for analysis (third column).

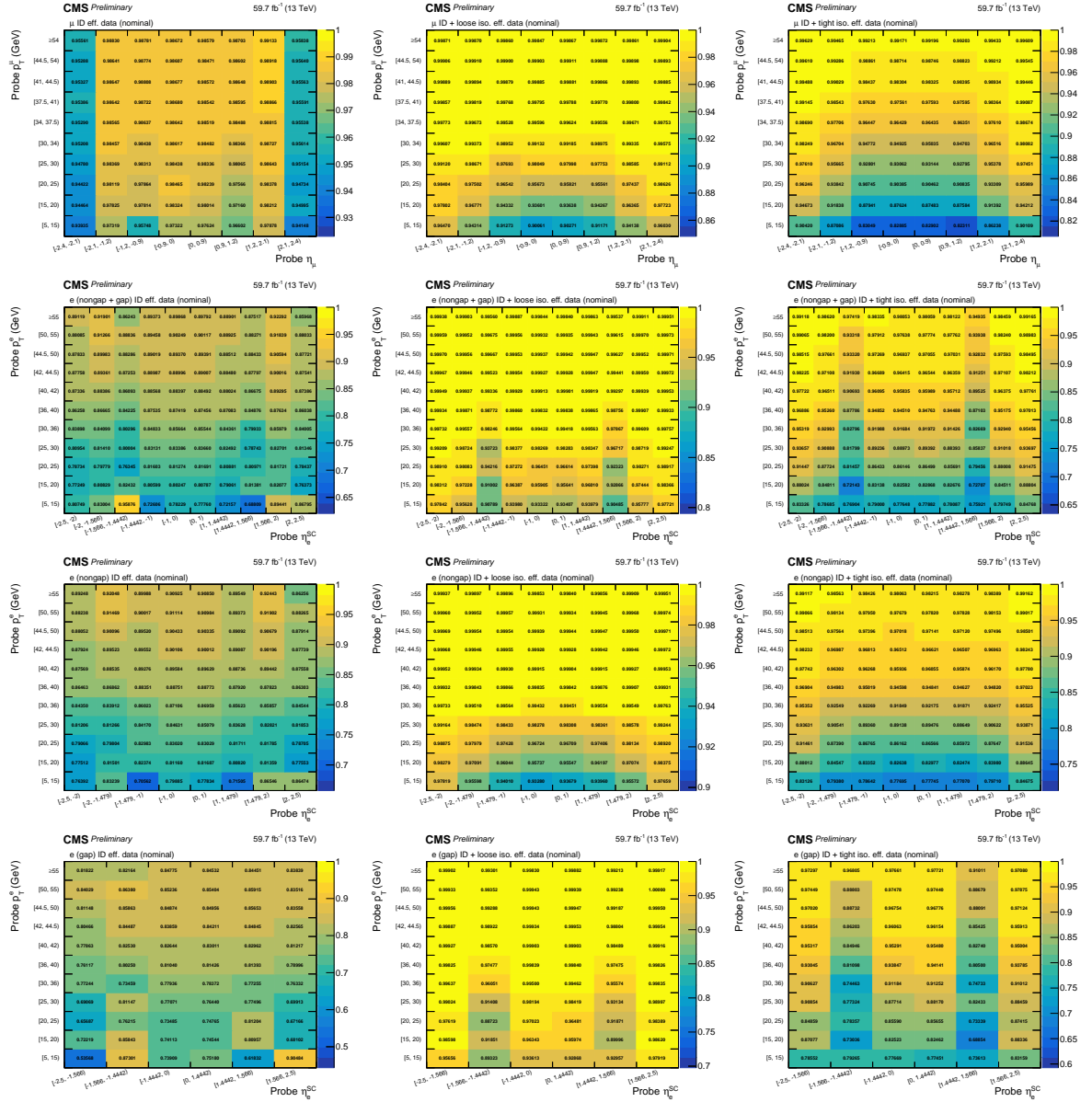


Figure 5.17: **The lepton identification and isolation efficiencies measured from observed data in 2018** for muons (first row), non-gap and gap electrons combined (second row), non-gap electrons only (third row) and gap electrons only (fourth row). The panels show the nominal variations of the conditional efficiencies to pass lepton identification (first column), pass loose isolation for event veto (second column), and pass tight isolation for analysis (third column).

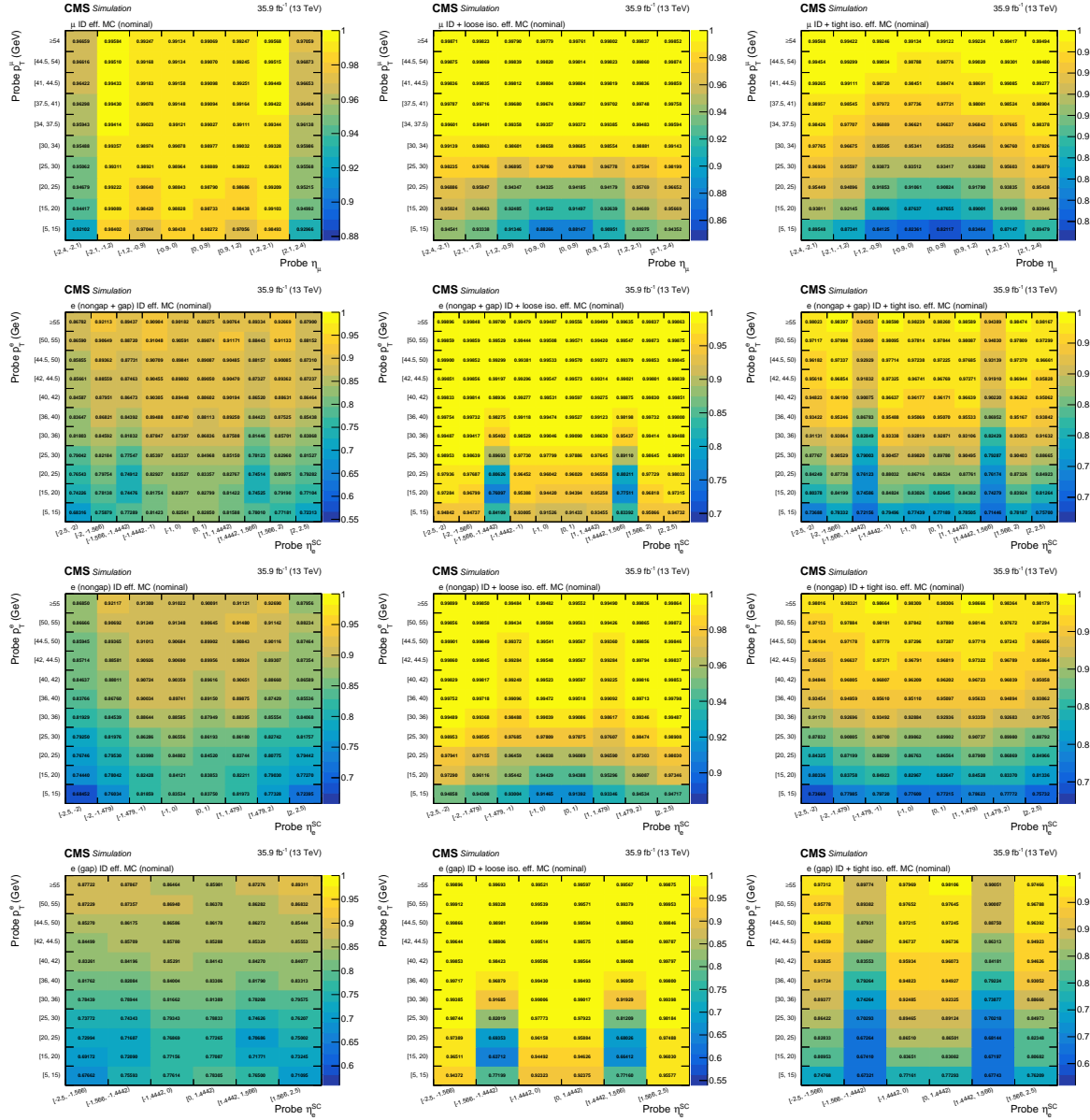


Figure 5.18: The lepton identification and isolation efficiencies measured from the simulation for the 2016 data period for muons (first row), non-gap and gap electrons combined (second row), non-gap electrons only (third row) and gap electrons only (fourth row). The panels show the nominal variations of the conditional efficiencies to pass lepton identification (first column), pass loose isolation for event veto (second column), and pass tight isolation for analysis (third column).

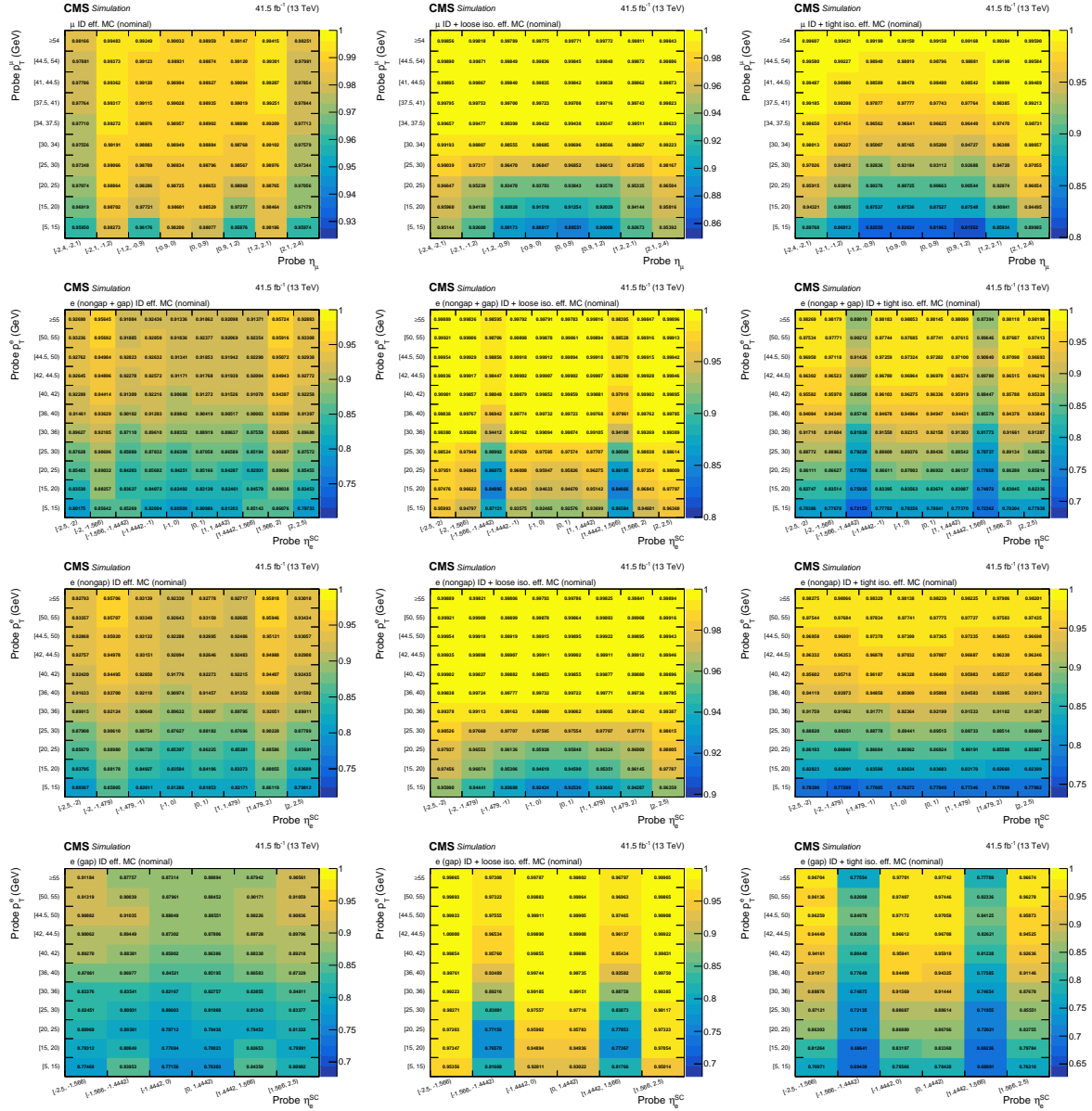


Figure 5.19: The lepton identification and isolation efficiencies measured from the simulation for the 2017 data period for muons (first row), non-gap and gap electrons combined (second row), non-gap electrons only (third row) and gap electrons only (fourth row). The panels show the nominal variations of the conditional efficiencies to pass lepton identification (first column), pass loose isolation for event veto (second column), and pass tight isolation for analysis (third column).

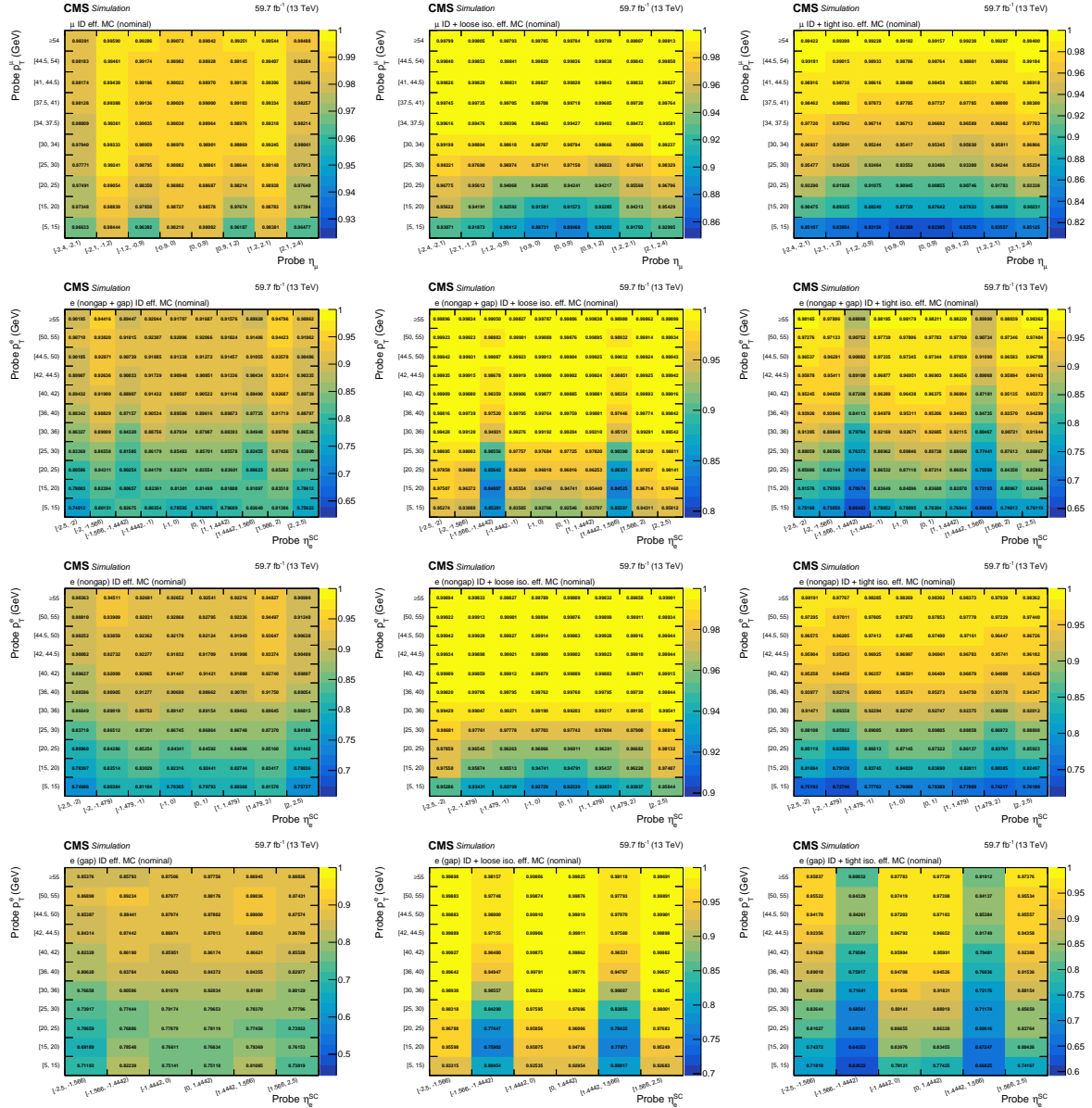


Figure 5.20: The lepton identification and isolation efficiencies measured from the simulation for the 2018 data period for muons (first row), non-gap and gap electrons combined (second row), non-gap electrons only (third row) and gap electrons only (fourth row). The panels show the nominal variations of the conditional efficiencies to pass lepton identification (first column), pass loose isolation for event veto (second column), and pass tight isolation for analysis (third column).

5.2.2 Investigations on the photon additional selections

By introducing additional requirements on the photon, loss of efficiencies may occur and further investigations on those effects are performed. The potential difference in the selection efficiency between data and MC are studied in the $ll\gamma$ CR, which is believed to be enriched with real, prompt photons. The results, which can be seen in Fig. 5.22, 5.23, show good agreement between data and simulation, and the left over 1–3% difference are applied as scale factors on the MC depending on p_T of the photon. These additional requirements are only considered when selecting for real, prompt photons in the single-photon CR. They are not applied when the photons are considered for event veto purposes, making the veto requirements slightly looser. Any photon with $p_T^\gamma \geq 20\text{GeV}$ and $|\eta| < 2.5$ is made subject to consideration for either purpose.

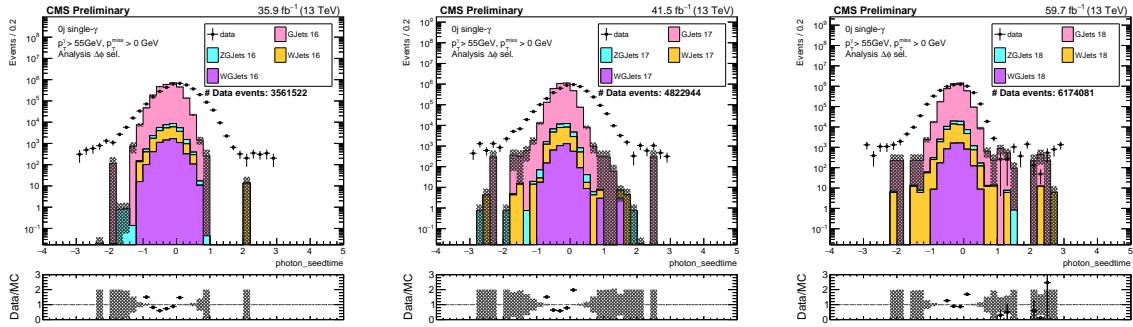


Figure 5.21: **Photon seedtime distributions** for 2016 (left), 2017 (middle) and 2018 (right), for a selection of 1 good photon, 0 jet, $p_T^\gamma \geq 55\text{GeV}$ and $\phi_{\text{miss}}^{\text{boson}} \geq 2.5$. Signs of non-gaussian tails can be seen in data after $|t_{\text{seed}}| > 2\text{ns}$, and in 2018, the tail starts at $t_{\text{seed}} > 1\text{ns}$.

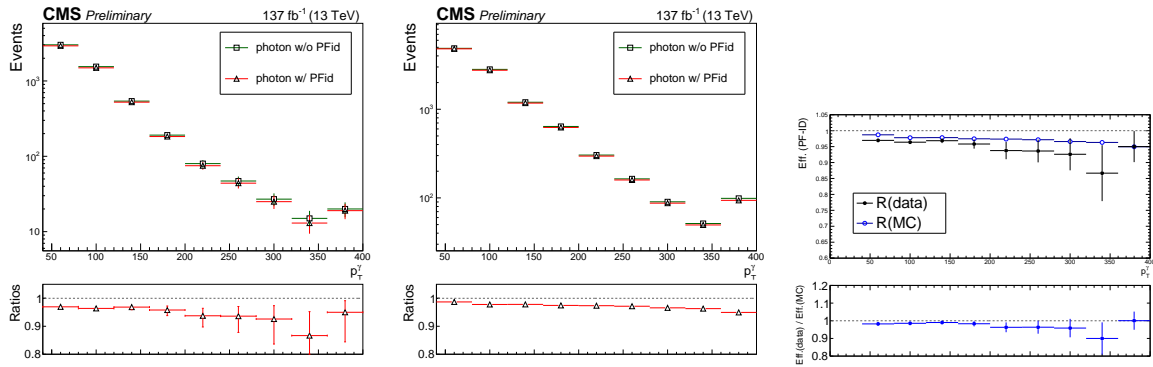


Figure 5.22: **Comparison of photon p_T distribution before and after applying the particle-flow ID on the photons**, in the $ll\gamma$ CR for data (left), MC (middle) and the comparison between their ratios (right). The $ll\gamma$ CR is believed to be enriched with real, prompt photons.

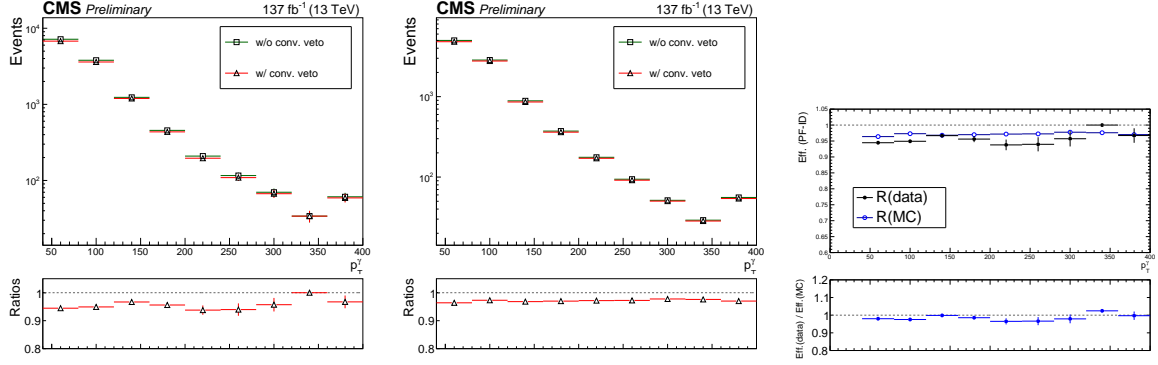


Figure 5.23: **Comparison of photon p_T distribution before and after applying the pixel seed veto and conversion safe ID on the photons**, in the $ll\gamma$ CR for data (left), MC (middle) and the comparison between their ratios (right). The $ll\gamma$ CR is believed to be enriched with real, prompt photons.

5.3 Event selection and categorization

The event selection requirements are setup on top of the physics objects selections that are described in Sec. 5.2. They are driven by the need to remove the instrumental p_T^{miss} background that comes mainly from the Drell-Yan process, and fully leptonic $t\bar{t}$ decay, which are major background sources in $2l2\nu$ final state. They can be summarized as

- having no b-tagged jets based on the loose working point defined for this analysis,
- $|m_{\ell\ell} - m_Z| \leq 15\text{GeV}$ where m_Z is taken to be 91.2 GeV,
- $p_T^{\text{boson}} \geq 55\text{GeV}$,
- $p_T^{\text{miss}} \geq 125\text{GeV}$ if $N_j < 2$, or $\geq 140\text{GeV}$ otherwise,
- $\Delta\phi_{\text{miss}}^{\text{boson+jets}} > 2.5$,
- $\Delta\phi_{\text{miss}}^{\text{boson}} > 1.0$,
- $\min\Delta\phi_{\text{miss}}^j > 0.25$ if $N_j = 1$, or > 0.5 if $N_j \geq 2$,

where the indicator ‘boson’ could stand for a dilepton pair or its proxy, which could be a photon in the single-photon or $ll\gamma$ control regions, or the lepton in the single-lepton control region. The quantity N_j denotes the multiplicity of any jet passing analysis criteria. The quantity $\Delta\phi_{\text{miss}}^{\text{boson}}$ denotes the unsigned difference between the ϕ of the boson and the missing transverse momentum; the quantity $\Delta\phi_{\text{miss}}^{\text{boson+jets}}$ denotes the unsigned difference between the ϕ of the total transverse momentum vector composed of the boson and jets, and the missing transverse momentum; and the quantity $\min\Delta\phi_{\text{miss}}^j$ denotes the minimum unsigned difference between the ϕ of any jet and the missing transverse momentum. These different $\Delta\phi$ requirements aim to reduce instrumental p_T^{miss} contribution from the Drell-Yan process by rejecting events with jets that have a large, misreconstructed energy, or events with large unclustered energy.

5.4 Observables and Discriminants

The analysis of off-shell H boson events is based on m_{ZZ} . This quantity is computed from the reconstructed momenta in the 4ℓ final state as the invariant mass of the 4ℓ system. However, in the $2l2\nu$ final state, we can only use the transverse mass m_{T}^{ZZ} , which provides an approximation by

assuming that the 3-vector $\mathbf{p}_T^{\text{miss}}$ is associated purely to the $Z \rightarrow 2\nu$ decay and that the decaying Z boson is produced on-shell. It is defined through relation

$$m_T^{\text{ZZ}^2} = \left[\sqrt{p_T^{\ell\ell^2} + m_{\ell\ell}^2} + \sqrt{p_T^{\text{miss}^2} + m_Z^2} \right]^2 - |\vec{p}_T^{\ell\ell} + \mathbf{p}_T^{\text{miss}}|^2, \quad (5.8)$$

where $\vec{p}_T^{\ell\ell}$ and $m_{\ell\ell}$ are transverse momentum and invariant mass of the the charged di-lepton system, respectively. m_Z is the Z boson resonance pole mass, taken to be 91.2GeV.

The distribution of p_T^{miss} itself is also sensitive to the couplings of the H and is used to discriminate processes with genuine, large p_T^{miss} against the Z+jets background. For events with at least two jets, we use matrix element (MELA [14–16, 18]) kinematic discriminants that distinguish the VBF process from the gg process or SM backgrounds. These discriminants are the $\mathcal{D}_{2\text{jet}}^{\text{VBF}}$ -type kinematic discriminants also used in previous analyses [13, 32], and are based on the four-momenta of the H boson and the two jets leading in p_T .

5.5 Likelihood parameterization

The results are extracted using binned extended maximum likelihood fits [114] performed on the events, split into the several categories. The details of the binning method in the fit are listed in Tab. 5.8 and observables used for each interpretation are summarized in Tab. 5.9.

Table 5.8: **The binning used in each of the observables examined in the analysis.** Binning for m_T^{ZZ} is identical in each N_j category, and the binning for p_T^{miss} is different between $N_j < \text{and } \geq 2$.

Observable	Bin boundaries
m_T^{ZZ} (GeV)	(300, 350, 400, 450, 500, 550, 600, 700, 850, 1000, 1250, 1500, 13000)
p_T^{miss} (GeV, $N_j < 2$)	(125, 150, 200, 300, 500, 1000, 13000)
p_T^{miss} (GeV, $N_j \geq 2$)	(140, 200, 13000)
$\mathcal{D}_{2\text{jet}}^{\text{VBF}}$ $\mathcal{D}_{2\text{jet},\Lambda_1}^{\text{VBF}}$	(0, 0.05, 0.1, 0.2, 0.8, 0.9, 0.95, 1)
$\mathcal{D}_{2\text{jet}}^{\text{VBF},a_2}$ $\mathcal{D}_{2\text{jet}}^{\text{VBF},a_3}$	(0, 0.1, 0.2, 0.4, 0.6, 0.8, 0.9, 1)

Table 5.9: **The set of observables used in each interpretation are summarized for the $2\ell 2\nu$ final state.** The interpretations are grouped by the parameters constrained. The observables for $N_j < 2$ are identical in any interpretation scenario, and the BSM $\mathcal{D}_{2\text{jet}}^{\text{VBF}}$ discriminant in the $N_j \geq 2$ category changes based on the anomalous HVV coupling constrained. The BSM discriminant $\mathcal{D}_{2\text{jet}}^{\text{VBF},a_2}$ is added to the SM-like HVV coupling scenarios as well in order to gain equivalent signal separation strength. Only two bins in p_T^{miss} , $<$ and $\geq 200\text{GeV}$, are considered for $N_j \geq 2$ as outlined in Tab. 5.8.

Interpretation parameters	$N_j < 2$	$N_j \geq 2$
$\mu^{\text{off-shell}}$	$m_T^{ZZ}, p_T^{\text{miss}}$	$m_T^{ZZ}, p_T^{\text{miss}}, \mathcal{D}_{2\text{jet}}^{\text{VBF}}, \mathcal{D}_{2\text{jet}}^{\text{VBF},a_2}$
$\Gamma_H (f_{ai} = 0)$	$m_T^{ZZ}, p_T^{\text{miss}}$	$m_T^{ZZ}, p_T^{\text{miss}}, \mathcal{D}_{2\text{jet}}^{\text{VBF}}, \mathcal{D}_{2\text{jet}}^{\text{VBF},a_2}$
Γ_H, \bar{f}_{a_2}	$m_T^{ZZ}, p_T^{\text{miss}}$	$m_T^{ZZ}, p_T^{\text{miss}}, \mathcal{D}_{2\text{jet}}^{\text{VBF}}, \mathcal{D}_{2\text{jet}}^{\text{VBF},a_2}$
Γ_H, \bar{f}_{a_3}	$m_T^{ZZ}, p_T^{\text{miss}}$	$m_T^{ZZ}, p_T^{\text{miss}}, \mathcal{D}_{2\text{jet}}^{\text{VBF}}, \mathcal{D}_{2\text{jet}}^{\text{VBF},a_3}$
$\Gamma_H, \bar{f}_{\Lambda_1}$	$m_T^{ZZ}, p_T^{\text{miss}}$	$m_T^{ZZ}, p_T^{\text{miss}}, \mathcal{D}_{2\text{jet}}^{\text{VBF}}, \mathcal{D}_{2\text{jet}}^{\text{VBF},\Lambda_1}$

As an approach suggested by Eq. 1.30 mentioned in previous Sec. 1.3.3, we can interpret the results in terms of off-shell signal strengths $\mu^{\text{off-shell}}$, with $\mu_F^{\text{off-shell}}$ for the ggF process, and $\mu_V^{\text{off-shell}}$ for the EW process, respectively. Simulations of the signal, background and the interference between the signal and the continuum background are already discussed in Sec. 4.2 and 4.2.2. The interpretations for $\mu_F^{\text{off-shell}}$ and $\mu_V^{\text{off-shell}}$ are considered during the likelihood scan with the other parameter kept unconstrained. This basis can be reparametrized for an overall off-shell signal strength parameter $\mu^{\text{off-shell}}$ as $\mu_F^{\text{off-shell}} \rightarrow \mu^{\text{off-shell}}$, $\mu_V^{\text{off-shell}} \rightarrow \mu^{\text{off-shell}} \times R_{V,F}^{\text{off-shell}}$, where $R_{V,F}^{\text{off-shell}}$ is a ratio parameter that can be either set to unity (i.e., $\mu_V^{\text{off-shell}} = \mu_F^{\text{off-shell}}$) or left unconstrained. This reparametrization is preferable over defining $\mu^{\text{off-shell}}$ strictly as an off-shell signal strength because the size and proportion of the gg and EW production mechanisms changes with different Higgs decay modes. The on-shell signal strength is left unconstrained in all cases. Independent joint fits are constructed in order to determine the total width of the Higgs boson under the SM-like assumption or in the presence of the three anomalous couplings a_2 , a_3 , and Λ_1 . These fits are also used to constrain the three corresponding anomalous coupling parameters \bar{f}_{ai} . When a certain anomalous coupling is tested, all

other anomalous couplings are assumed to be zero, and only real couplings in Eq. 1.32 are tested, that is with $a_1 \geq 0$ and $\cos(\phi_{ai}) = \pm 1$.

We can denote the generic probability density for any considered process in a way similar to that in Ref. [13]. It follows the relations in Eq. 1.30 and 1.31 closely with the additional potential contribution of interference between the signal and background amplitudes as

$$\mathcal{P}_{jk}(\vec{x}; \vec{\xi}_{jk}, \vec{\zeta}) = \tilde{\mu}_j \mathcal{P}_{jk}^{\text{sig}}(\vec{x}; \vec{\xi}_{jk}, f_{ai}, \phi_{ai}) + \sqrt{\tilde{\mu}_j} \mathcal{P}_{jk}^{\text{int}}(\vec{x}; \vec{\xi}_{jk}, f_{ai}, \phi_{ai}) + \mathcal{P}_{jk}^{\text{bkg}}(\vec{x}; \vec{\xi}_{jk}), \quad (5.9)$$

where different event categories are enumerated with an index k , $\vec{\zeta}$ are the unconstrained parameters of interest, which could be $(\mu_{\text{F}}^{\text{off-shell}}, \mu_{\text{V}}^{\text{off-shell}}, \Gamma_{\text{H}}, \vec{f}_{ai})$ or any other reparametrization based on the interpretation, and j is the index of the process, which could be gg (on-shell or off-shell); VBF, ZH, or WH (on-shell); EW (VBF, ZH, WH combined, off-shell); or any of the non-interfering backgrounds or those estimated directly from the data. The vector $\vec{\xi}_{jk}$ denotes the constrained nuisance parameters pertaining to the different processes in each category, and \vec{x} are the observables in each event category. The parameter $\tilde{\mu}_j$ equals either the on-shell signal strength μ_j for on-shell processes, or $\mu_j \cdot \Gamma_{\text{H}}/\Gamma_{\text{SM}}$ for the off-shell processes, with the SM reference value Γ_{SM} taken to be 4.07MeV. The signal strength parameter μ_j is defined in reference to Eq. 1.30 and 1.31 as either μ_{F} or μ_{V} according to the process type j . The EW H production mechanisms, or production via gluon fusion have different dependence on anomalous HVV couplings, equally in the on-shell or off-shell regions. There are two HVV vertices in the former production mechanism with the subsequent $\text{H} \rightarrow \text{VV} \rightarrow 2\ell 2\nu$ decay while there is only one HVV decay vertex in the latter case. In addition, there is interference with the background in the off-shell region. This leads to the following general expressions for the signal (sig) or interference (int) contributions appearing in Eq. 5.9 [13]:

$$\mathcal{P}_{jk}^{\text{sig/int}}(\vec{x}; \vec{\xi}_{jk}, f_{ai}, \phi_{ai}) = \sum_{m=0}^M \mathcal{P}_{jk,m}^{\text{sig/int}}(\vec{x}; \vec{\xi}_{jk}) f_{ai}^{\frac{m}{2}} (1 - f_{ai})^{\frac{M-m}{2}} \cos^m(\phi_{ai}), \quad (5.10)$$

where the sum over the index m runs up to $M = 4$ in the case of the EW signal process; $M = 2$ in the case of the gluon fusion, or any on-shell $t\bar{t}H$ and $b\bar{b}H$ signal processes, or the interference between the signal and background in the EW process; and $M = 1$ in the case of the interference between the signal and background in the gluon fusion process. The index m corresponds to the exponent of a_i in the squared scattering amplitude from Eq. 1.32, which may contain contributions from production and decay, and the factor $\cos(\phi_{ai}) = \pm 1$ affects only the sign of the terms that scale with an odd power of a_i .

Constraints on $\vec{\zeta}$ are placed using the profile likelihood method using the RooFit toolkit [115] within the ROOT [116] framework. The extended likelihood function is constructed using the probability densities as in Eq. 5.9 with each event characterized by the discrete category k and the set of observables \vec{x} . The likelihood \mathcal{L} is maximized with respect to the nuisance parameters $\vec{\xi}_{jk}$ describing the systematic uncertainties discussed below and the yield parameters μ_{F} and μ_{V} . The allowed 68% (95%) CL interval is defined using the profile likelihood function, $-2\Delta \ln \mathcal{L} = 1.00$ (3.84) for one-parameter constraints, and $-2\Delta \ln \mathcal{L} = 2.30$ (5.99) for two-parameter constraints, for which exact coverage is expected in the asymptotic limit [117].

5.6 Systematic uncertainties

Several systematic uncertainties are featured in the vectors of constrained parameters $\vec{\xi}_{jk}$. The template shapes describing the probability distributions in Eq. 5.9 and 5.10 are varied separately within theoretical, experimental, or statistical uncertainties. Most of the uncertainties affect both the shape of the observables and normalization of the different contributions. The following are the theoretical uncertainties considered:

Renormalization scale This source is considered separately for $q\bar{q} \rightarrow V_1 V_2$ ($V = W$ or Z), $q\bar{q} \rightarrow V\gamma$, processes with a t quark and a Z boson, and the QCD background sample used in the single-photon CR. $gg \rightarrow VV$, and the EW $VV + \text{jets}$ production mechanisms with H contributions are treated separately. The relative variations for the gg process obtained from the weight variations in the simulation are normalized to that for the inclusive k -factor variation prediction [59].

Factorization scale This source is considered to be uncorrelated in a way identical to the renormalization scale case, and the gg process is adjusted in the same way.

$\alpha_s(m_Z)$ A variation of $\alpha_s(m_Z) = 0.118 \pm 0.0015$ is considered. The correlation scheme with the different processes is as mentioned above, and the gg process is adjusted in the same way.

Parton distribution function variations This variation is taken as a conservative, envelope-type variation evaluated on a per-event basis. The correlation scheme with the different processes is as mentioned above, and the gg process is adjusted in the same way.

Simulation of the second jet in gg samples The uncertainty is evaluated as the difference of the nominal POWHEG samples for $m_H = 125\text{GeV}$ and $m_H = 300\text{GeV}$ from the simulation with the MINLO HJJ program [118] applied. The reweighting factors are extracted in three dimensions, in bins of m_{VV} below or above 150GeV , in bins of p_T^{VV}/m_{VV} , evaluated for the hard process, and in bins of N_j bins of 0, 1, and ≥ 2 with jets taken to be clustered using anti- k_T algorithm with a $\Delta R = 0.4$ parameter after hadronization.

Scale and tune variations of the hadronizer PYTHIA The scale variations are taken from the embedded variations of weights in the simulations for the 2017 and 2018 data periods, and when missing. They are taken from the dedicated samples generated at $m_H = 125\text{GeV}$ and $m_H = 300\text{GeV}$ in the signal simulation, or from the 2018 simulation in the other non-interfering background components. The tune variations are considered for the signal-related contributions and are extracted by comparing the differences of alternative simulation samples from the nominal samples at $m_H = 125\text{GeV}$ and $m_H = 300\text{GeV}$. Scale and tune variations are uncorrelated themselves, but simulation for the different data periods are correlated. The reweighting factors in the signal processes are extracted in three dimensions, in bins of m_{VV} below or above 150GeV , in bins of p_T^{VV}/m_{VV} , evaluated after hadronization, and in bins of N_j bins of 0, 1, and ≥ 2 with jets taken to be clustered using anti- k_T algorithm with a $\Delta R = 0.4$ parameter also after hadronization. The reweighting factors for the scale variations in the non-interfering backgrounds are extracted as a function of the p_T of the collected system of prompt leptons, neutrinos and photons after hadronization whenever necessary.

NLO EW correction on $q\bar{q} \rightarrow V_1 V_2$ This uncertainty is specific to the WZ and ZZ processes, and they are treated as correlated. The uncertainty on WZ accounts only for the virtual part, as the uncertainty on the photon-induced component is driven by the precision on the photon PDF, which is extremely precise thanks to the LUXqed PDF set [98], leading to a negligible contribution to the

uncertainty [100]. The uncertainty on the virtual component of the NLO EW correction is computed as follows. We distinguish two event categories according to the event recoil [119], defined as $\rho = \frac{|\sum_{i=1}^4 \vec{p}_T^i|}{\sum_{i=1}^4 |\vec{p}_T^i|}$, with i a lepton coming from one of the two bosons. If $\rho \geq 0.3$, we conservatively associate a full error of 100% of the electroweak correction. Else, the uncertainty is equal to the product of the electroweak and the QCD corrections. This is motivated by the fact that the uncertainties are coming from missing diagrams in $\alpha\alpha_S$, whose contribution is maximal if ρ is large. When $\rho < 0.3$, the uncertainty corresponds to the case where the EW and the QCD corrections go in the same direction.

The analysis also considers the following **instrumental uncertainties** on the simulation:

Luminosity This source is a normalization uncertainty applied only to the simulation and is uncorrelated across the three data periods. The values of these uncertainties are provided in Refs. [120–123] and summarized in Ref. [6]. The different sources of uncertainties are grouped into three classes, one class for the components that are uncorrelated between the different data periods, which results in three separate uncertainty sources for each of the 2016 (1.8%), 2017 (2.0%), and 2018 (1.5%) data periods (1.2% in 2015); another component that groups the components correlated across the 2016, 2017 and 2018 periods, which results in a single uncertainty source with variations magnitudes of 1.175%, 1.114%, and 2.020%, respectively; and a final component that only considers the components that are correlated between the 2015 and 2016 data periods, which produces another single uncertainty source with a variations magnitude of 1.249% (1.162% in 2015). This uncertainty is taken as a log-normal normalization uncertainty in all simulation-estimated components except in the estimate of the instrumental p_T^{miss} background, where they are taken as changing the shape as well because of the subtractions involved.

L1 prefire scale This source of uncertainty is applied only in 2016 and 2017, where the prefire weight need to be applied. They are treated as correlated.

Pile-up, JES, JER, and p_T^{miss} resolution correction These sources are uncorrelated across the years. The p_T^{miss} resolution is evaluated for each of the pile-up, JES and JER variation separately [124]. The jet energy scale and resolution [124] affect the counting of jets, as well as the reconstruction of the VBF discriminants.

Trigger, charged lepton, pile-up jet identification, and b-tagging efficiencies The prescription to apply and correlate the uncertainties on lepton efficiencies is discussed in Sec. 5.2. The others are uncorrelated across the three data periods.

In the estimation of instrumental p_T^{miss} background, the $\gamma \rightarrow \ell\ell$ transfer factors in the estimation of the contamination from genuine- p_T^{miss} contributions also account for the theoretical and instrumental uncertainties in the simulation in a correlated manner. In the estimation of the nonresonant background, the uncertainty on $f_{\text{corr}}^{\ell\ell}$ from the statistics of the sideband control region is also taken into account. All components that enter into the statistical analysis also take into account at least two uncertainties to account for the shape and normalization of the different histograms, the method of which is already described in Sec. 5.5.

Data-driven background estimations

Estimating the event yields and shape of different background processes is a central task for the analysis. By data-driven background estimate, we mean an estimate based on observed real collision events. In some cases, simulations cannot provide a reliable background estimate because of incorrect modeling and the inability to mimic instrumental effects, and in these cases, a data-driven background estimate is necessary.

A common ABCD method for data-driven background estimate is illustrated in Fig. 6.1 [12]. To estimate a background process in the signal region D, a separate control region C is defined. Region C is usually orthogonal to the signal region D, which means that it often uses inverted selections of one or more kinematic variables, or it is defined in a different scenario that is free of the signal. There are usually some differences in the selection efficiency for the background process between regions C and D. To account for these differences, so-called transfer factors (TFs) or scale factors (SFs) are used to correct the estimate obtained in region C. Those factors can be obtained from dividing region B by region A, or in some other particular ways.

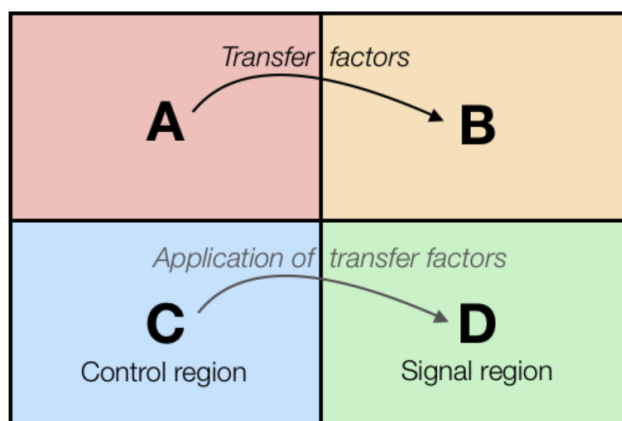


Figure 6.1: **Illustration of a common ABCD method** [12]

6.1 Non-resonant Backgrounds

We call all involved processes that do not contain a resonance decaying into two charged leptons, non-resonant. The main processes contributing to it are $t\bar{t} \rightarrow 2\ell 2\nu 2b$ and $WW \rightarrow 2\ell 2\nu$ with real, flavor-symmetric leptonic decay.

The procedure to estimate this component follows [112] closely and improves upon the method used in [53, 99]. Those two methods will be described in 6.1.1 and 6.1.2.

6.1.1 Estimation with reweighted $e\mu$ events

Non-resonant background in the e^+e^- and $\mu^+\mu^-$ channels is estimated by applying a weight $w_{e\mu}^{ij}$, where i and j are the leptons from the same-flavour dilepton sample that is modelled by the $e\mu$ sample

$$w_{e\mu}^{ij} = \frac{1}{2} \times \frac{\varepsilon_i \cdot \varepsilon_j}{\varepsilon_e \cdot \varepsilon_\mu} \times \frac{\varepsilon_{ij}^{\text{trigger}}}{\varepsilon_{e\mu}^{\text{trigger}}} \times f_{\text{corr}}^{\ell\ell}(p_T^{\text{miss}}) \quad (6.1)$$

where ε_i is the lepton identification and isolation efficiency of lepton i , and $\varepsilon_{ij}^{\text{trigger}}$ is the combined trigger efficiency on the ij lepton pair. It is worth emphasizing that both lepton selection efficiencies and trigger efficiencies depend on p_T and η and hence the weight is a function that relies on the lepton kinematics. This accounts for phase space where the ratio of different flavors is disturbed by the detector effects, especially in low p_T region and the barrel-endcap transition region in η , instead of using a uniform reweighting factor. Another reason is that, as it will be described in Sec. 6.1.2, a uniform α -value to reweight $e\mu$ events is calculated in an inclusive number of jet bin (combining $N_j = 0, 1$ and ≥ 2) and may somehow lose sensitivity in this way especially for the $\mathcal{D}_{2\text{jet}}^{\text{VBF}}$. The factor $1/2$ accounts for the SM ratio of ee or $\mu\mu$ events to $e\mu$ events. The last factor, $f_{\text{corr}}^{\ell\ell}$ is a correction factor on the spectrum of p_T^{miss} due to slightly different resolution of ee , $\mu\mu$, and $e\mu$ events and is derived from specially defined control regions.

The closure of this method is tested by examining the agreement in ee or $\mu\mu$ event distributions between those predicted from simulation by reweighting the $e\mu$ events in the signal region and the actual expectations.

Fig. 6.2 shows distributions of the VBF discriminants for nonresonant background. VBF discriminant in the 2-jet category is chosen as an example shown here because nonresonant contributions concentrate in this region.

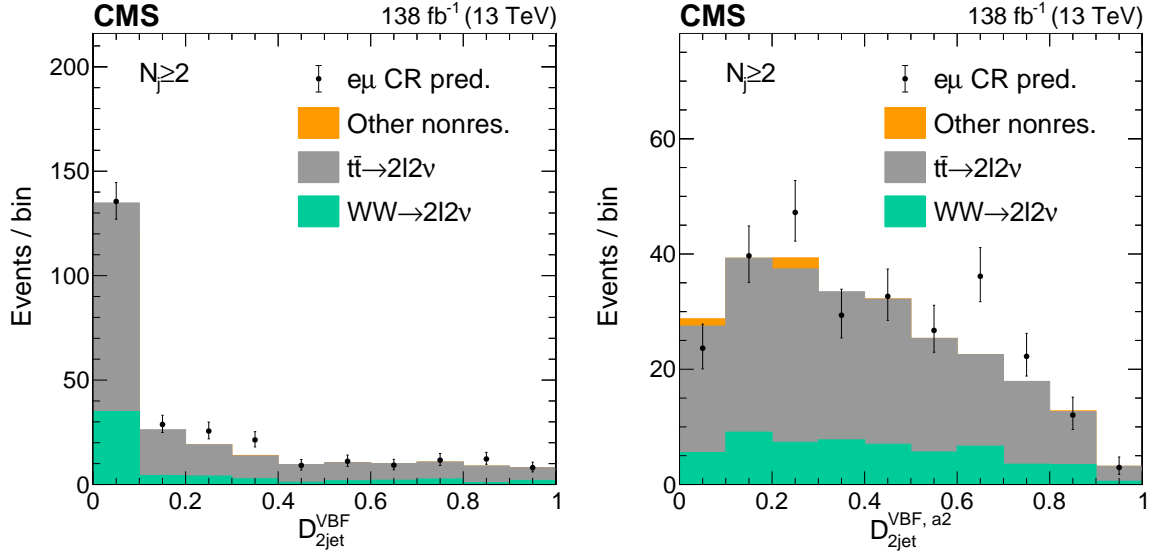


Figure 6.2: **Distributions of the VBF discriminants for nonresonant background.** The distributions of the SM $\mathcal{D}_{2\text{jet}}^{\text{VBF}}$ (left) and $\mathcal{D}_{2\text{jet}}^{\text{VBF}, a2}$ (right) kinematic VBF discriminants are shown in the $2\ell 2\nu$ signal region, $N_j \geq 2$ category. The stacked histogram shows the predictions from simulation, which consists of nonresonant contributions from WW (green) and $t\bar{t}$ (gray) production, or other small components (orange). The black points with error bars as uncertainties at 68% CL show the prediction from the $e\mu$ CR data. While only the data is used in the final estimate of the nonresonant background, we note that predictions from simulation already agree well with the data estimate.

6.1.2 Alpha method

The alpha method (α -method) is performed similarly as the method in Sec. 6.1.1 in re-scaling the number of $e\mu$ events by the formula to get an estimated number of non-resonant di-lepton events in the signal region $N_{\ell\ell}^{\text{SR}}$

$$N_{\ell\ell}^{\text{SR}} = \alpha_{\ell} \cdot N_{e\mu}^{\text{in}} \quad (6.2)$$

where $N_{e\mu}^{\text{in}}$ is number of $e\mu$ events selected passing all signal selection cuts but the same-flavour requirement for the two leptons (including $|M_{e\mu} - 91| < 15 \text{ GeV}$), α_{ℓ} with ℓ being e or μ is the correction factor which takes into account the difference in the lepton selection between the same flavor channel - $\ell\ell$ and the opposite flavor channel - $e\mu$. α_{ℓ} is computed directly from data using the events found in the dilepton invariant mass side bands. The events are counted in the $40 < m_{\ell\ell} < 70 \text{ GeV}$ (left side band) and $110 < m_{\ell\ell} < 200 \text{ GeV}$ (right side band). Fig. 6.3, 6.5, 6.7 shows $m_{\ell\ell}$ distributions of this control region for 2016, 2017 and 2018 separately, requiring each event to have at least one b-tagged jet, while Fig. 6.4, 6.6, 6.8 shows those distributions by rejecting events containing any b-tagged jets. In order to reduce the presence of Drell-Yan events in the control sample, as it is suggested in Fig. 6.9 and 6.10, we require $p_T^{\text{miss}} > 80 \text{ GeV}$ and a b-tagged jet. Then α_{ℓ} is computed from:

$$\alpha_{\ell} = N_{\ell\ell}^{\text{out}} / N_{e\mu}^{\text{out}} \quad (6.3)$$

Compared with Eq. 6.1, the α values are independent of variables like lepton and trigger efficiencies which are in bins of lepton p_T or η . The α value is more or less a uniform value in certain data-taking period and is only different in 2 lepton channels (ee and $\mu\mu$). In principle, α values are expected to have similar central value compared with the weights calculated with Eq. 6.1.

Tab. 6.1 shows the expected composition of the sidebands and the prediction obtained from it ("Predicted" column). The composition is shown incrementally for the two main processes expected to dominate the sidebands (Top and WW) and for using all the simulated processes. Each prediction

Table 6.1: α_ℓ with ℓ being e or μ computation from all side bands and only right side band

2016			
channel	process	btag, all side band	btag, up side band
ee	Data	0.389 ± 0.005	0.392 ± 0.006
	MC	0.402 ± 0.003	0.403 ± 0.003
$\mu\mu$	Data	0.636 ± 0.008	0.638 ± 0.009
	MC	0.639 ± 0.003	0.639 ± 0.004
2017			
channel	process	btag, all side band	btag, up side band
ee	Data	0.420 ± 0.005	0.421 ± 0.006
	MC	0.412 ± 0.002	0.414 ± 0.002
$\mu\mu$	Data	0.648 ± 0.007	0.643 ± 0.008
	MC	0.608 ± 0.002	0.603 ± 0.002
2018			
channel	process	btag, all side band	btag, up side band
ee	Data	0.420 ± 0.004	0.423 ± 0.005
	MC	0.413 ± 0.001	0.415 ± 0.002
$\mu\mu$	Data	0.638 ± 0.006	0.629 ± 0.007
	MC	0.612 ± 0.002	0.607 ± 0.002

obtained for each test is to be compared to the rightmost column ("Expected"). We find that after adding each process individually the method predicts correctly (within 5-10%) the contribution from the non-resonant background to our search. The usage of b-tags or not to build the sideband is expected not to yield significant differences except in the purity of the sidebands in terms of Top events. Because conditions vary over the LHC run period, as it is indicated by α -values with small but non-negligible differences, the results are presented separately of the three years.

We also perform extensive tests of the MC closure by comparing both, the b-vetoed and the b-tagged samples, as well as the inclusive and right-hand sidebands. The test is performed for each channel (ee and $\mu\mu$) inclusively. For each p_T^{miss} cut we compare the prediction of the method to the expectations from MC and evaluate the bias as:

$$\text{bias} = \left(\frac{N_{\text{predicted}}}{N_{\text{expected}}} - 1 \right) \quad (6.4)$$

Comparisons of the shape in p_T^{miss} and m_T^{ZZ} distributions between direct MC simulations, reweighted $e\mu$ events from data and reweighted $e\mu$ events from simulations are shown in Fig. 6.11, 6.12 for all the three years, based on the categorization by number of jets ($N_j = 0, 1$ or ≥ 2 as well as an inclusive one). It should be emphasized here that the α -values are derived as a uniform weight for a certain flavor of dilepton (ee or $\mu\mu$) from the inclusive N_j bin, but applied for different N_j categories. Bias is likely to increase in separated N_j bins compared with the inclusive one. The value of the bias (see Fig. 6.17) is considered to contribute to the systematic uncertainties of this α -method. In this estimation, events are counted combining p_T^{miss} bins into a single one but with a threshold, in a way that is similar as how we calculate the α -value with different MET cuts. Total uncertainty introduced by the α -method is estimated to be within a level of 10% and vary only a little for all three years.

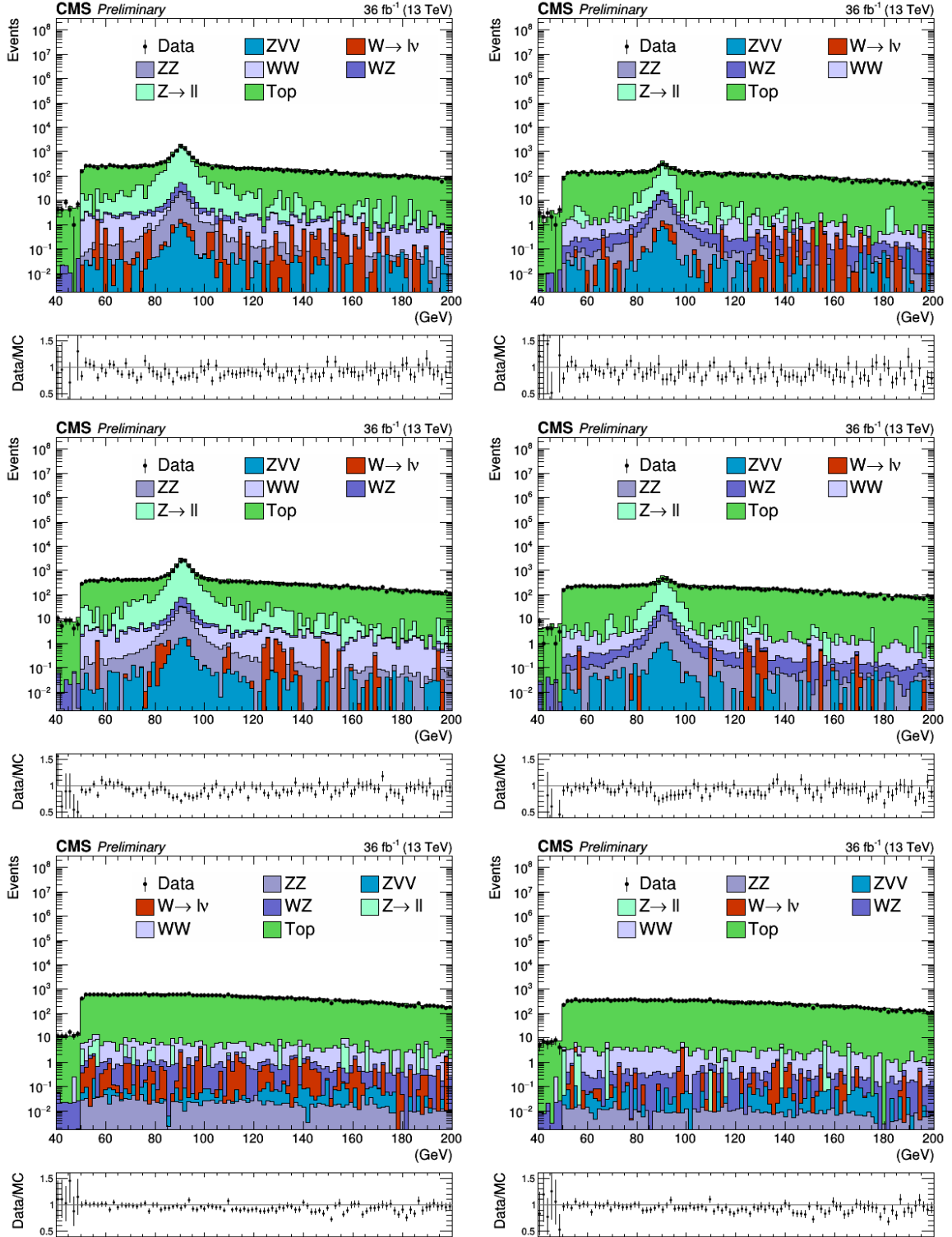


Figure 6.3: Distributions of $m_{\ell\ell}$ in NRB control region from data and all related MC simulation of 2016. At least one b-tagged jet with loose WP is required. From top to bottom are ee , $\mu\mu$ and $e\mu$ with $p_T^{\text{miss}} > 50 \text{ GeV}$ on the left and $p_T^{\text{miss}} > 80 \text{ GeV}$ on the right. A pre-selection of $m_{\ell\ell} \geq 50 \text{ GeV}$ is applied, which accounts for the cutoff around the threshold.

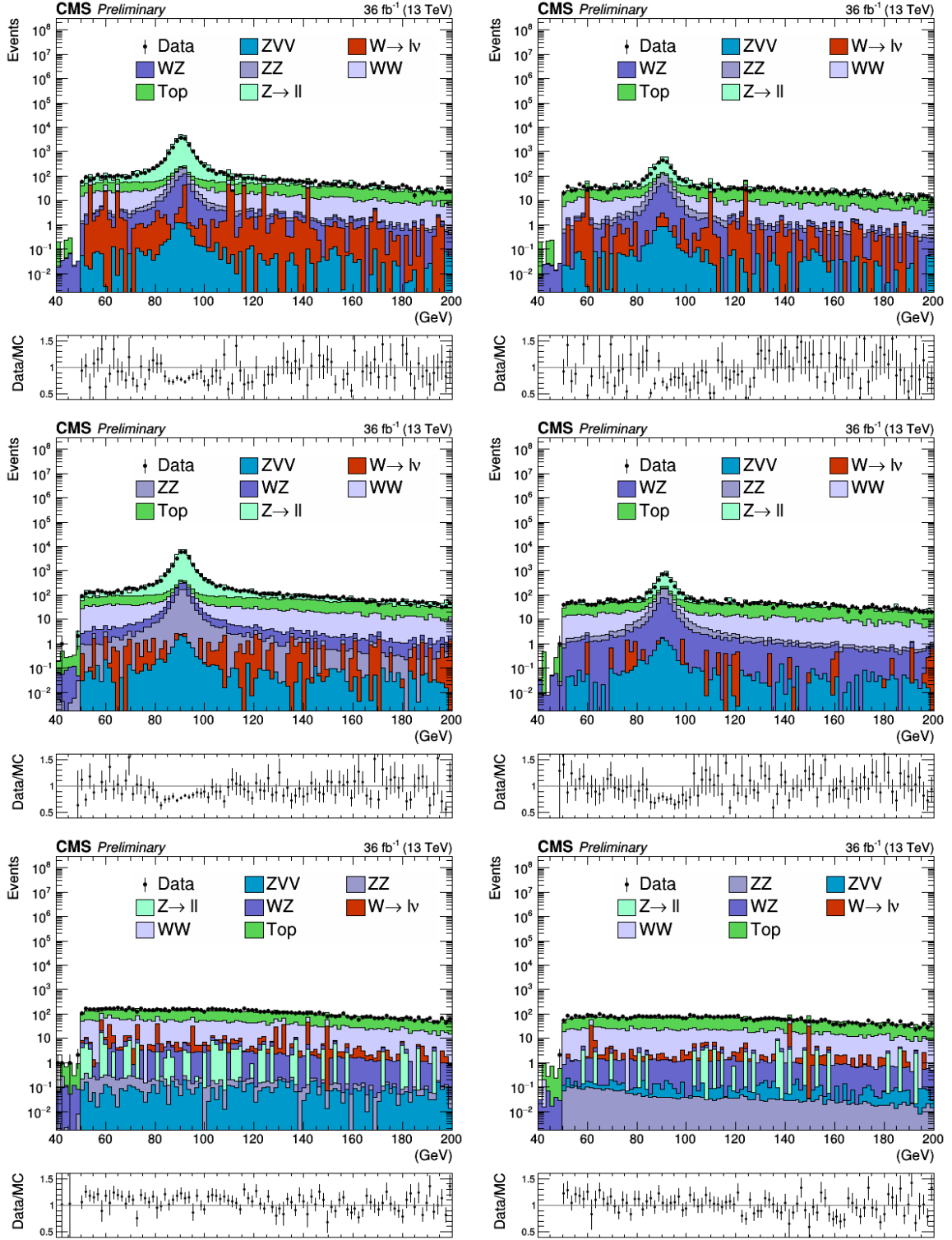


Figure 6.4: Distributions of $m_{\ell\ell}$ in NRB control region from data and all related MC simulation of 2016. Events containing one or more b-tagged jets with loose WP are rejected. From top to bottom are ee , $\mu\mu$ and $e\mu$ with $p_T^{\text{miss}} > 50$ GeV on the left and $p_T^{\text{miss}} > 80$ GeV on the right. A pre-selection of $m_{\ell\ell} \geq 50$ GeV is applied, which accounts for the cutoff around the threshold.

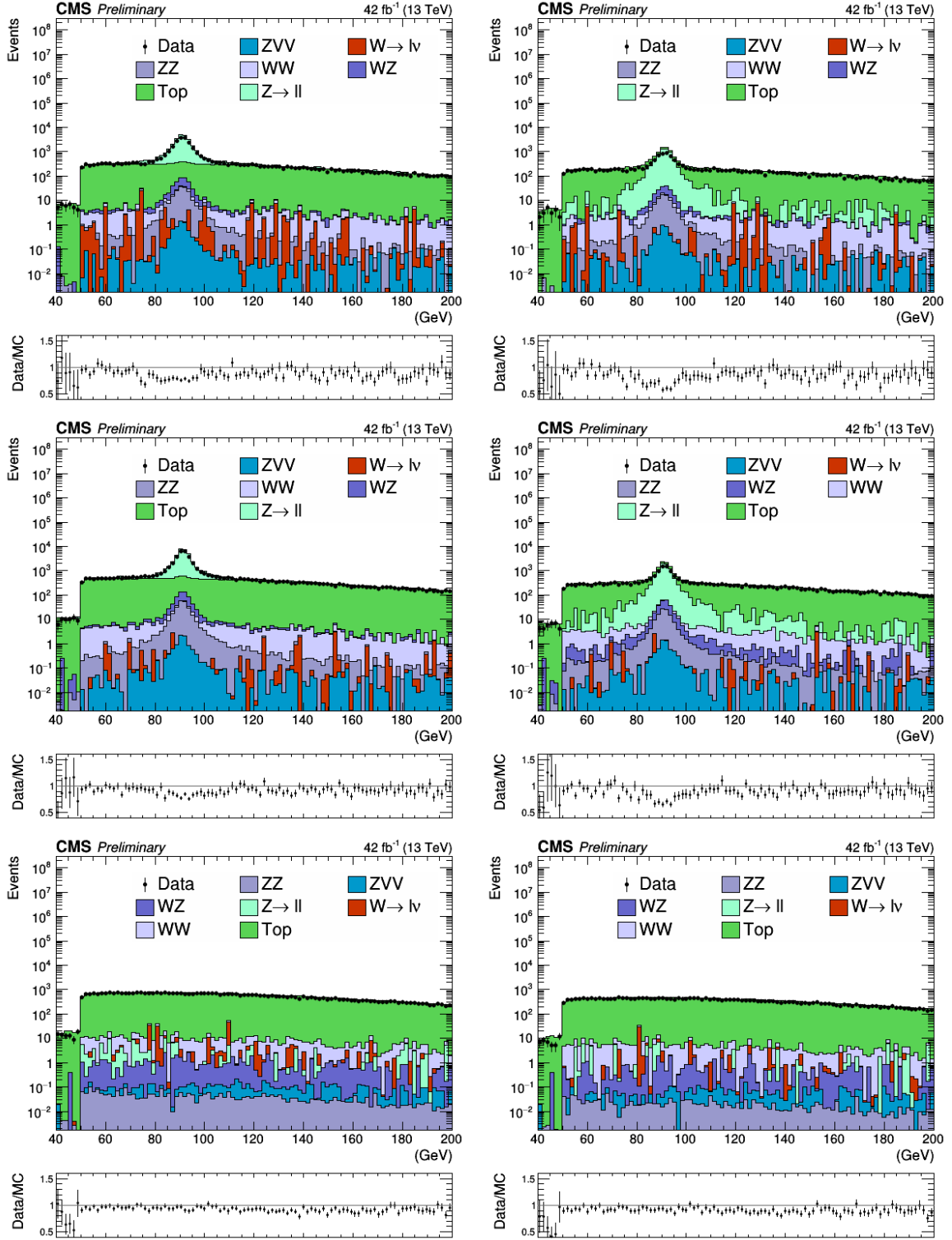


Figure 6.5: Distributions of $m_{\ell\ell}$ in NRB control region from data and all related MC simulation of 2017. At least one b-tagged jet with Loose WP is required. From top to bottom are ee , $\mu\mu$ and $e\mu$ with $p_T^{\text{miss}} > 50 \text{ GeV}$ on the left and $p_T^{\text{miss}} > 80 \text{ GeV}$ on the right. A pre-selection of $m_{\ell\ell} \geq 50 \text{ GeV}$ is applied, which accounts for the cutoff around the threshold.

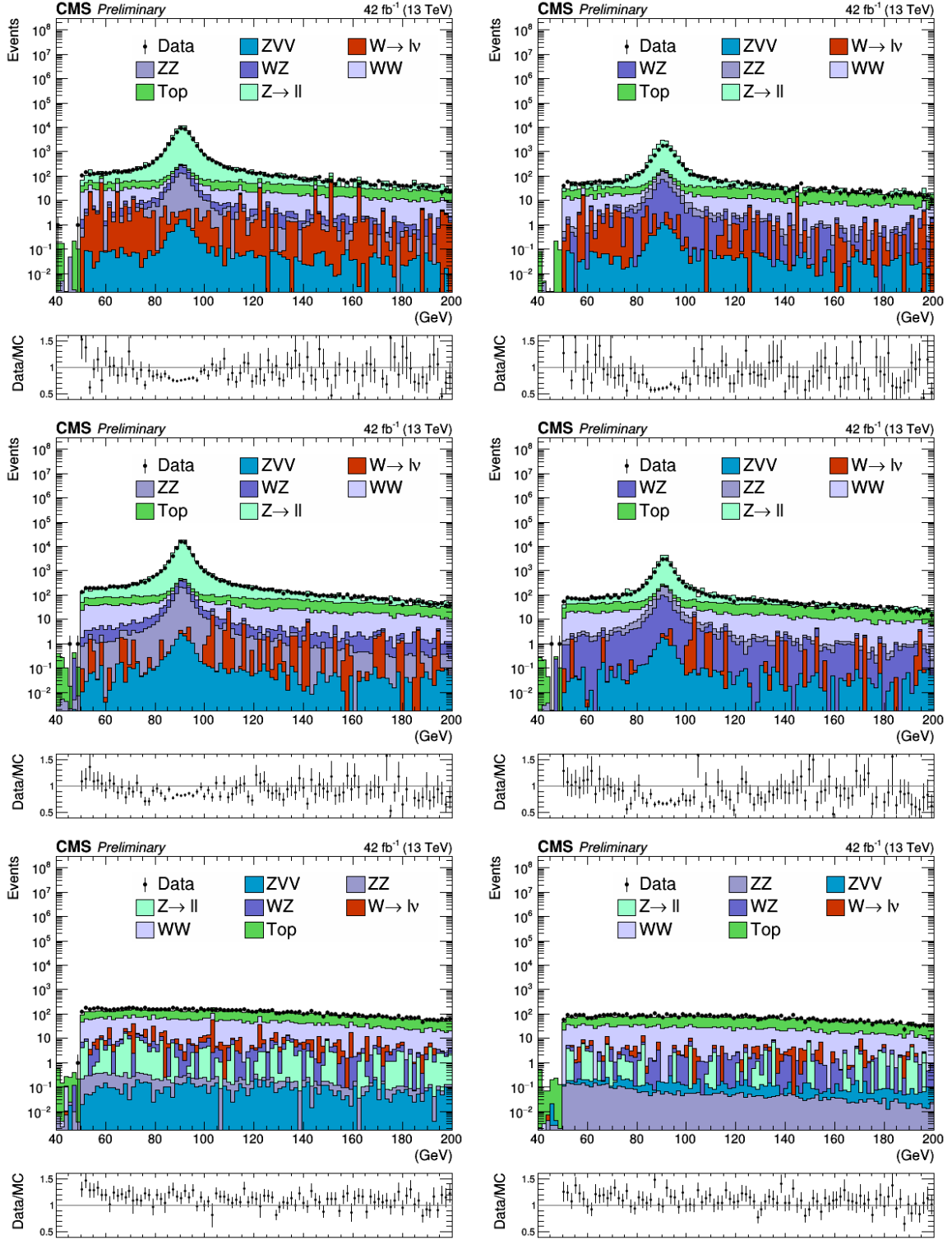


Figure 6.6: Distributions of $m_{\ell\ell}$ in NRB control region from data and all related MC simulation of 2017. Events containing one or more b-tagged jets with loose WP are rejected. From top to bottom are ee , $\mu\mu$ and $e\mu$ with $p_T^{\text{miss}} > 50$ GeV on the left and $p_T^{\text{miss}} > 80$ GeV on the right. A pre-selection of $m_{\ell\ell} \geq 50$ GeV is applied, which accounts for the cutoff around the threshold.

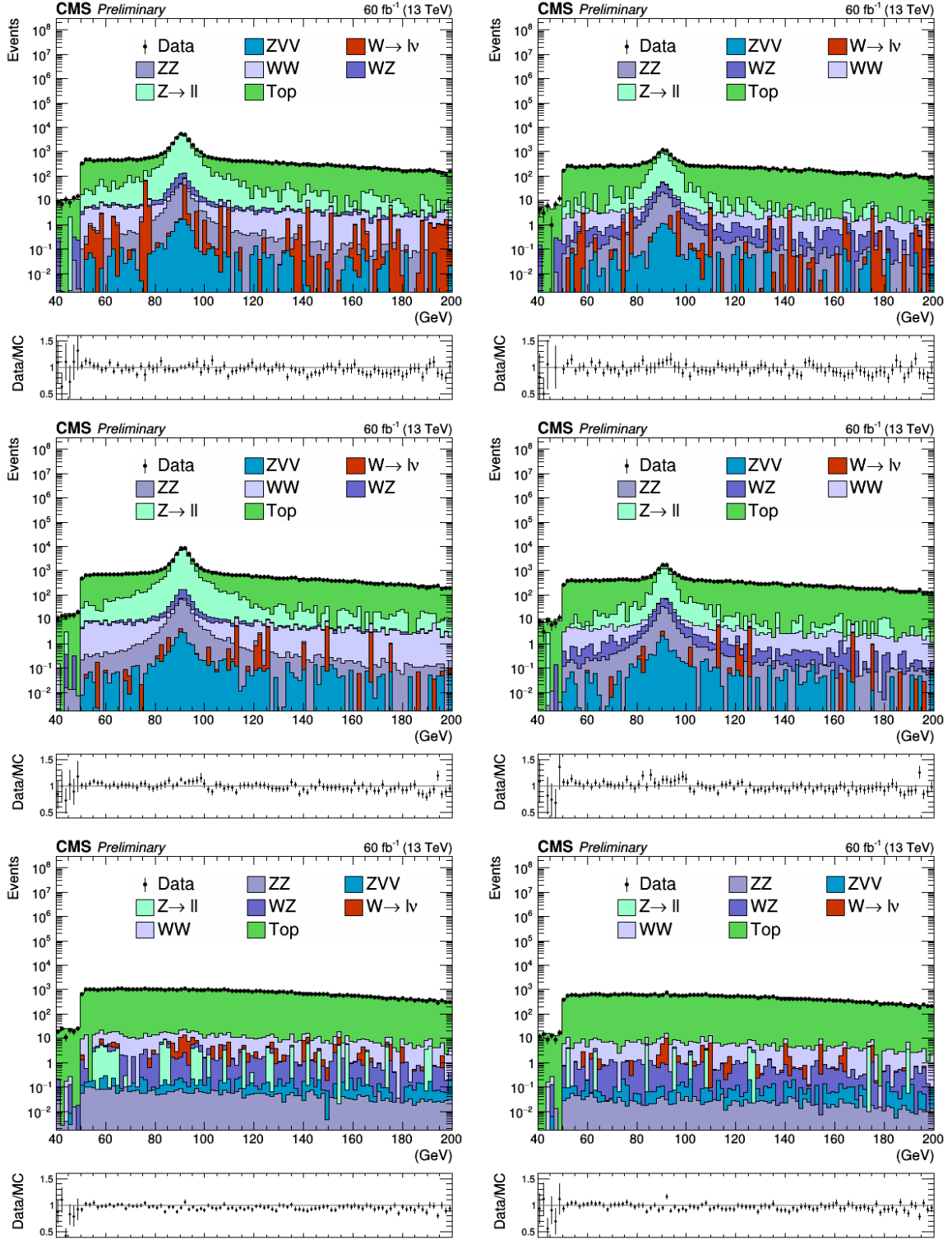


Figure 6.7: Distributions of $m_{\ell\ell}$ in NRB control region from data and all related MC simulation of 2018. At least one b-tagged jet with Loose WP is required. From top to bottom are ee , $\mu\mu$ and $e\mu$ with $p_T^{\text{miss}} > 50 \text{ GeV}$ on the left and $p_T^{\text{miss}} > 80 \text{ GeV}$ on the right. A pre-selection of $m_{\ell\ell} \geq 50 \text{ GeV}$ is applied, which accounts for the cutoff around the threshold.

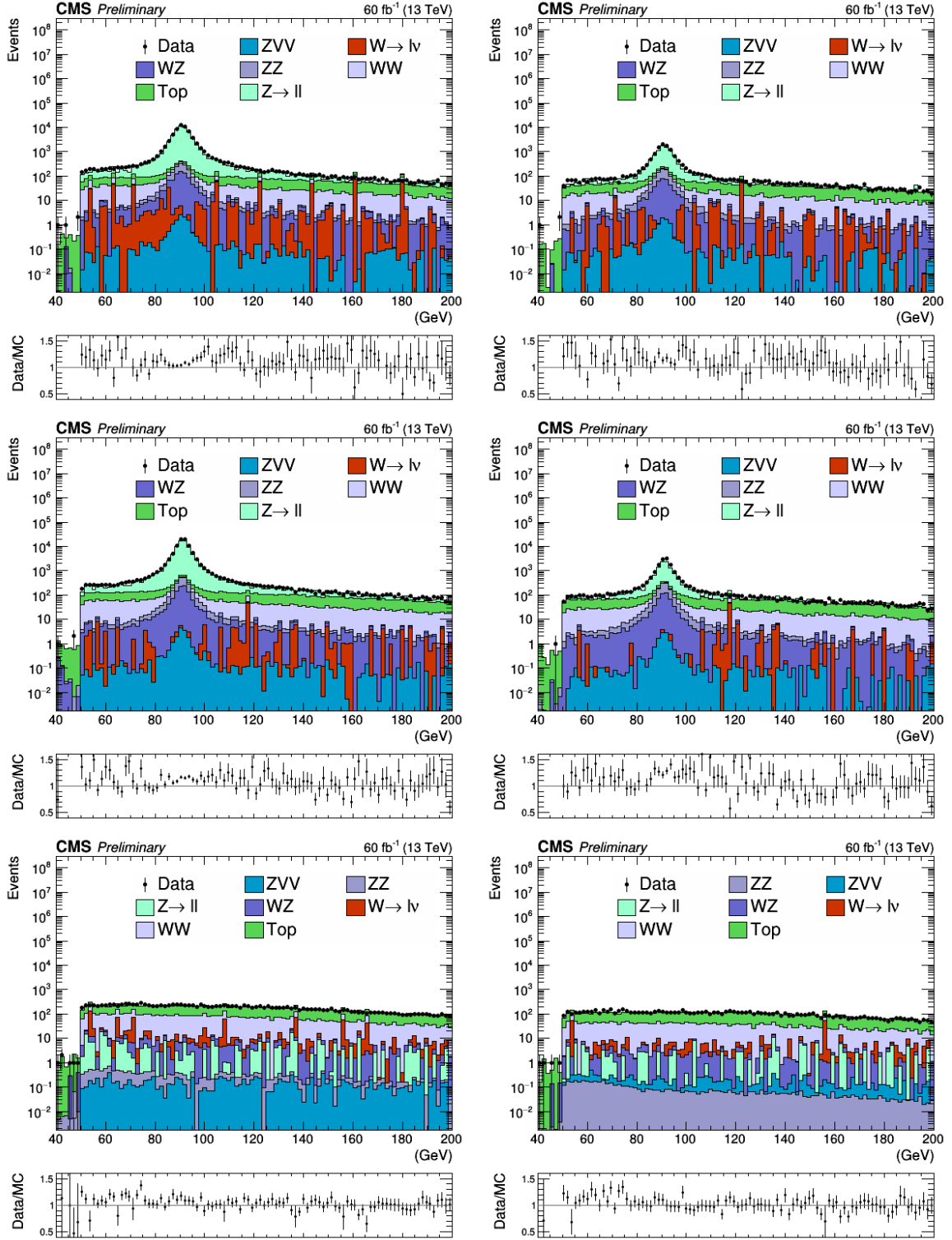


Figure 6.8: Distributions of $m_{\ell\ell}$ in NRB control region from data and all related MC simulation of 2018. Events containing one or more b-tagged jets with loose WP are rejected. From top to bottom are ee , $\mu\mu$ and $e\mu$ with $p_T^{\text{miss}} > 50$ GeV on the left and $p_T^{\text{miss}} > 80$ GeV on the right. A pre-selection of $m_{\ell\ell} \geq 50$ GeV is applied, which accounts for the cutoff around the threshold.

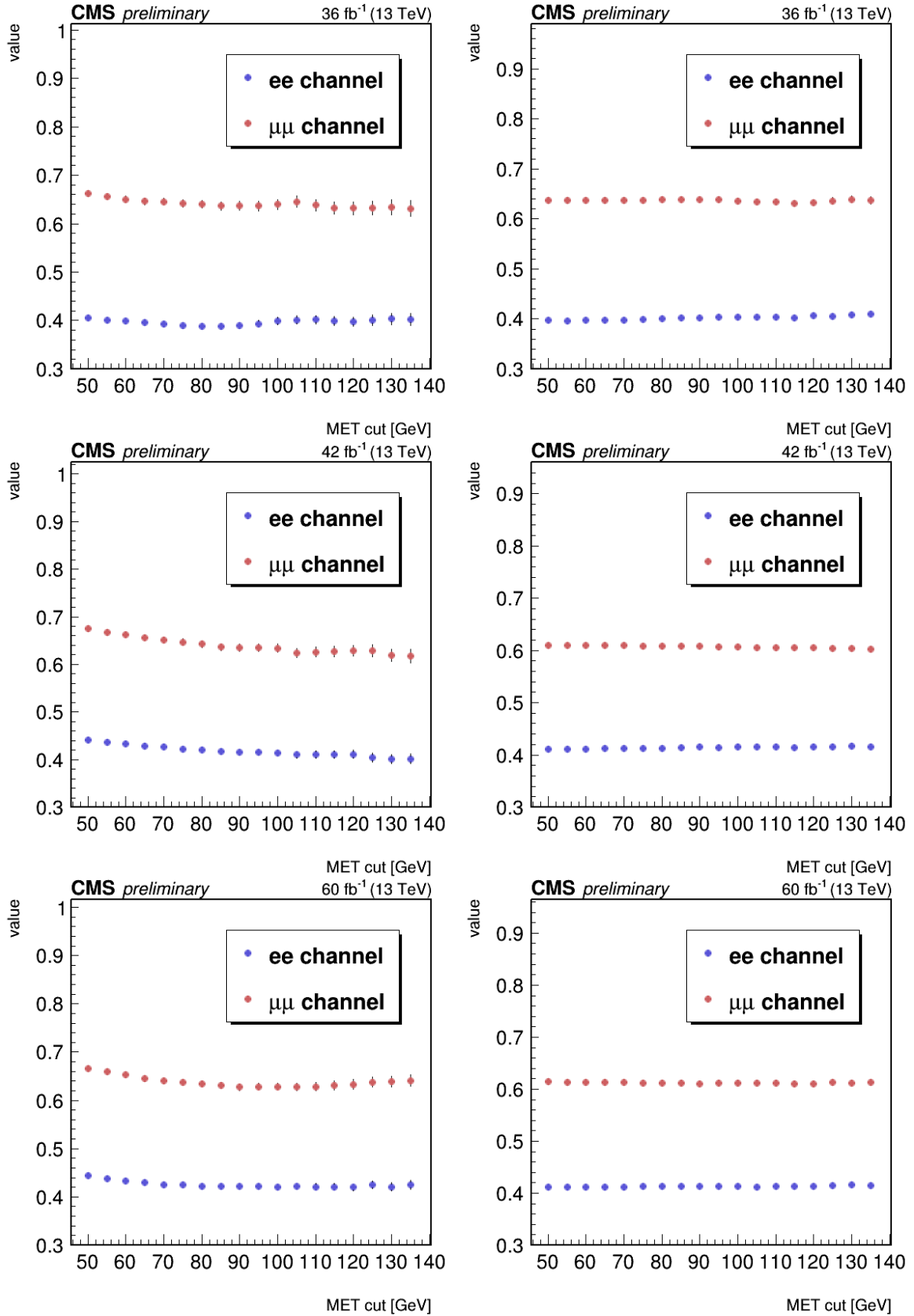


Figure 6.9: α value as a function of the met cut computed from all side bands ($40 < m_{\ell\ell} < 70$ GeV and $110 < m_{\ell\ell} < 200$ GeV) with b-tagged jet required in the events using both data (left) and MC simulations (right) in di-electron (red) and di-muon (blue) channel of year 2016 (top), 2017 (middle), 2018 (bottom).

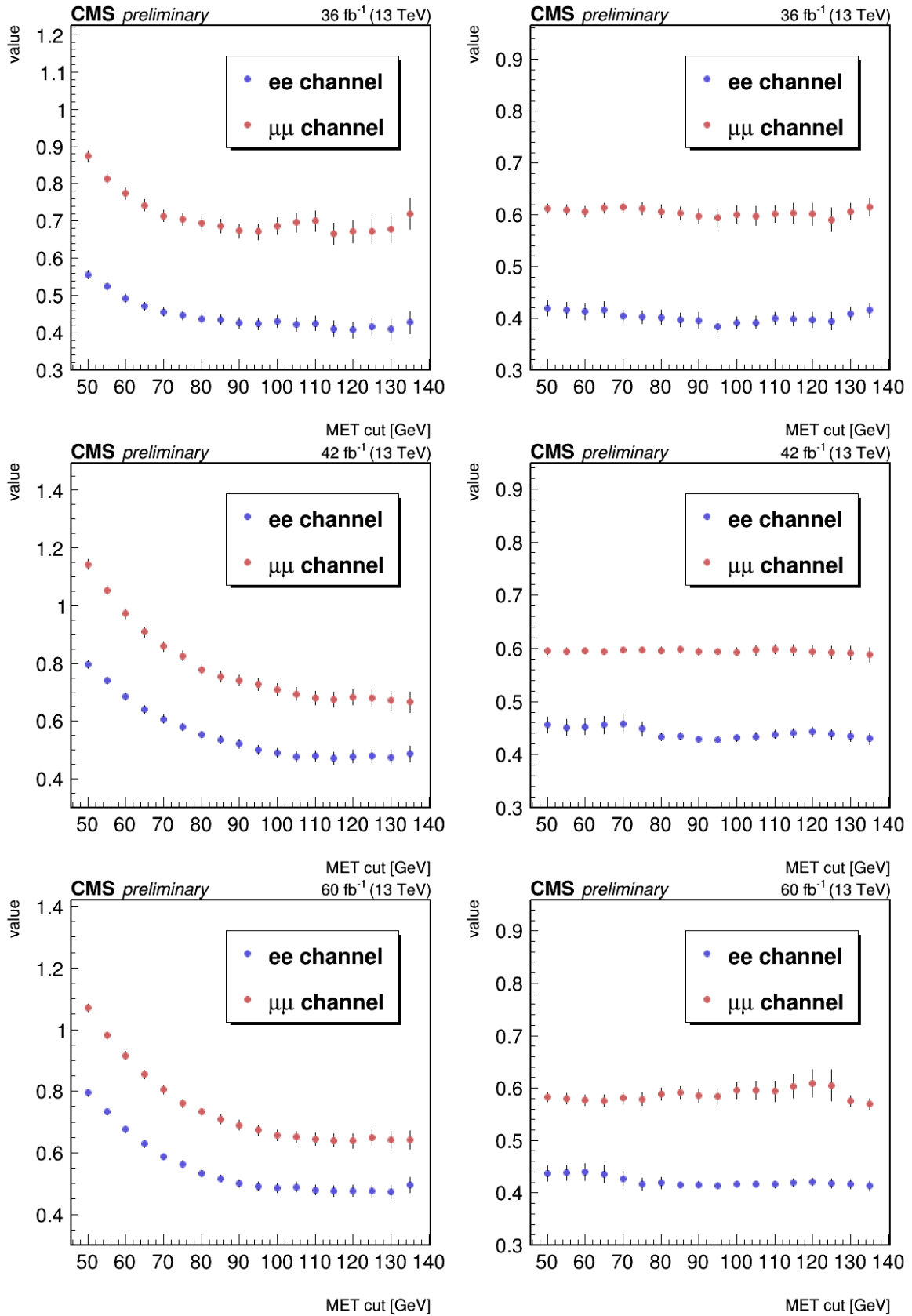


Figure 6.10: α value as a function of the met cut computed from all side bands ($40 < m_{\ell\ell} < 70$ GeV and $110 < m_{\ell\ell} < 200$ GeV) with events containing b-tagged jet rejected using both data (left) and MC simulations (right) in di-electron (red) and di-muon (blue) channel of year 2016 (top), 2017 (middle), 2018 (bottom).

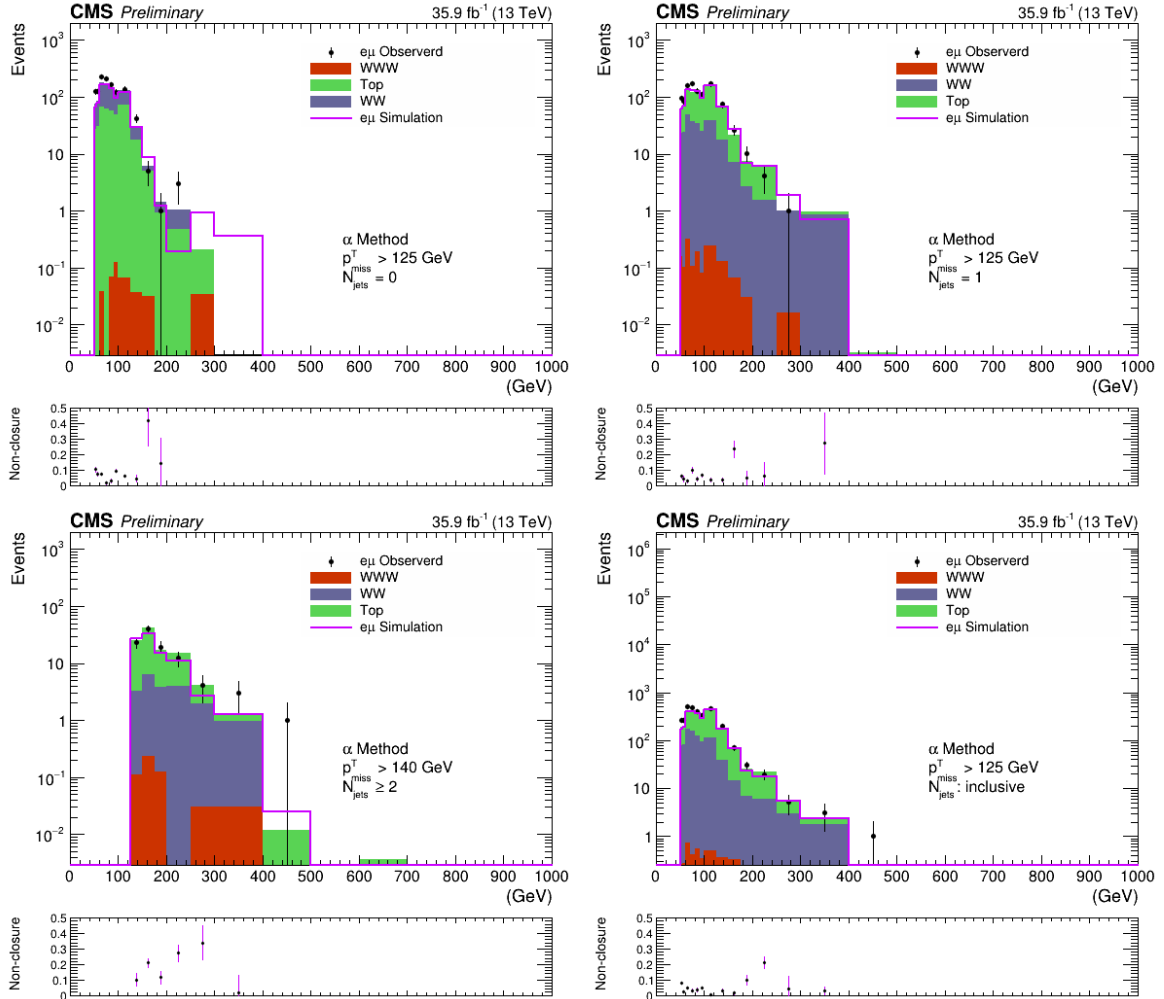


Figure 6.11: **Distributions of p_T^{miss} from non-resonant contribution in the signal region for 2016.** The stacked histograms are MC simulations of nonresonant contribution in the signal region and the color legend for them is given in the plots. Reweighted $e\mu$ events from data are shown as black points with error bars. The solid line in magenta shows the shape derived from reweighted $e\mu$ events of simulations. Bottom panels represent for the bias that is calculated in a similar way as Eq. 6.4 in each p_T^{miss} bin.

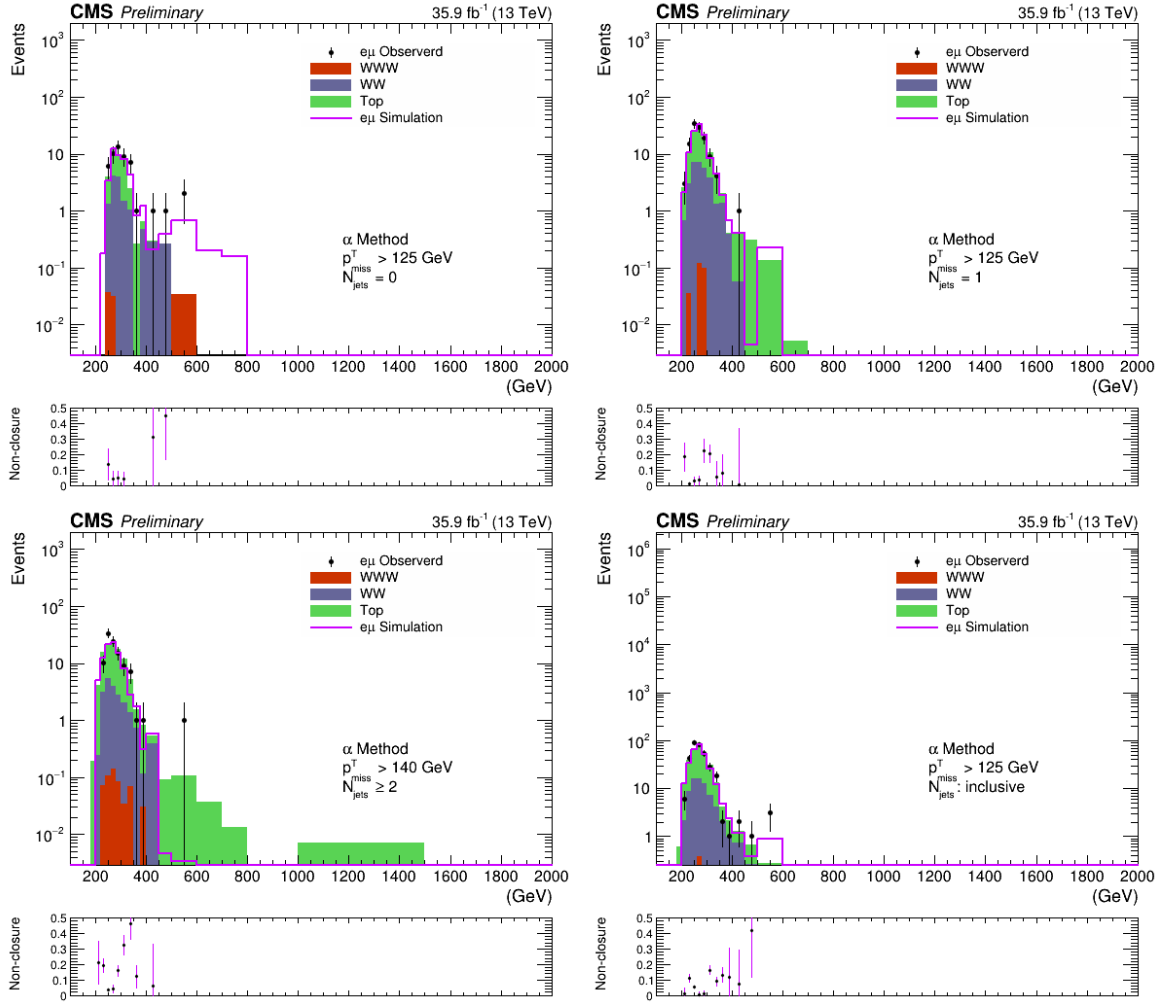


Figure 6.12: **Distributions of m_T^{ZZ} from non-resonant contribution in the signal region for 2016.** The stacked histograms are MC simulations of nonresonant contribution in the signal region and the color legend for them is given in the plots. Reweighted $e\mu$ events from data are shown as black points with error bars. The solid line in magenta shows the shape derived from reweighted $e\mu$ events of simulations. Bottom panels represent for the bias that is calculated in a similar way as Eq. 6.4 in each m_T^{ZZ} bin.

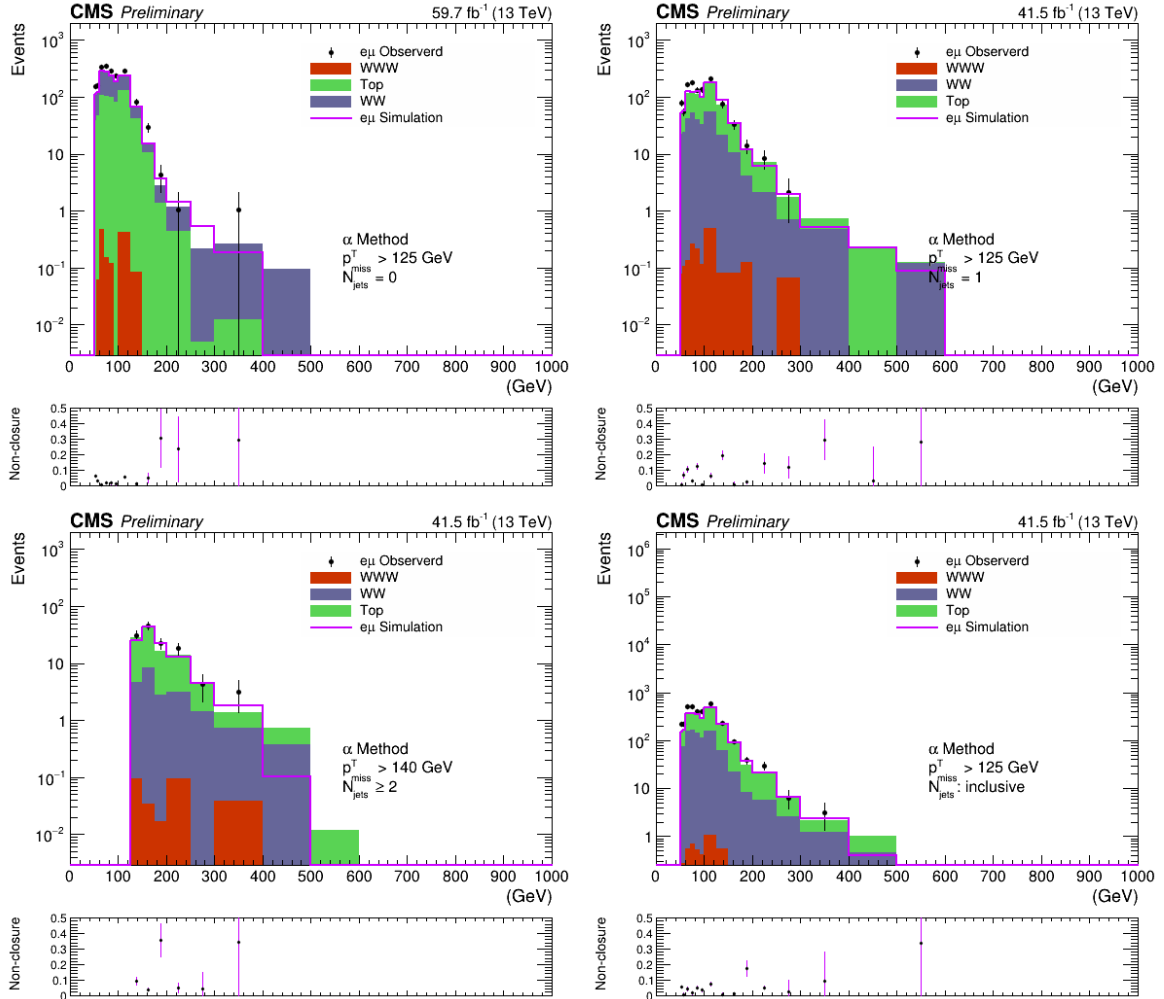


Figure 6.13: **Distributions of p_T^{miss} from non-resonant contribution in the signal region for 2017.** The stacked histograms are MC simulations of nonresonant contribution in the signal region and the color legend for them is given in the plots. Reweighted $e\mu$ events from data are shown as black points with error bars. The solid line in magenta shows the shape derived from reweighted $e\mu$ events of simulations. Bottom panels represent for the bias that is calculated in a similar way as Eq. 6.4 in each p_T^{miss} bin.

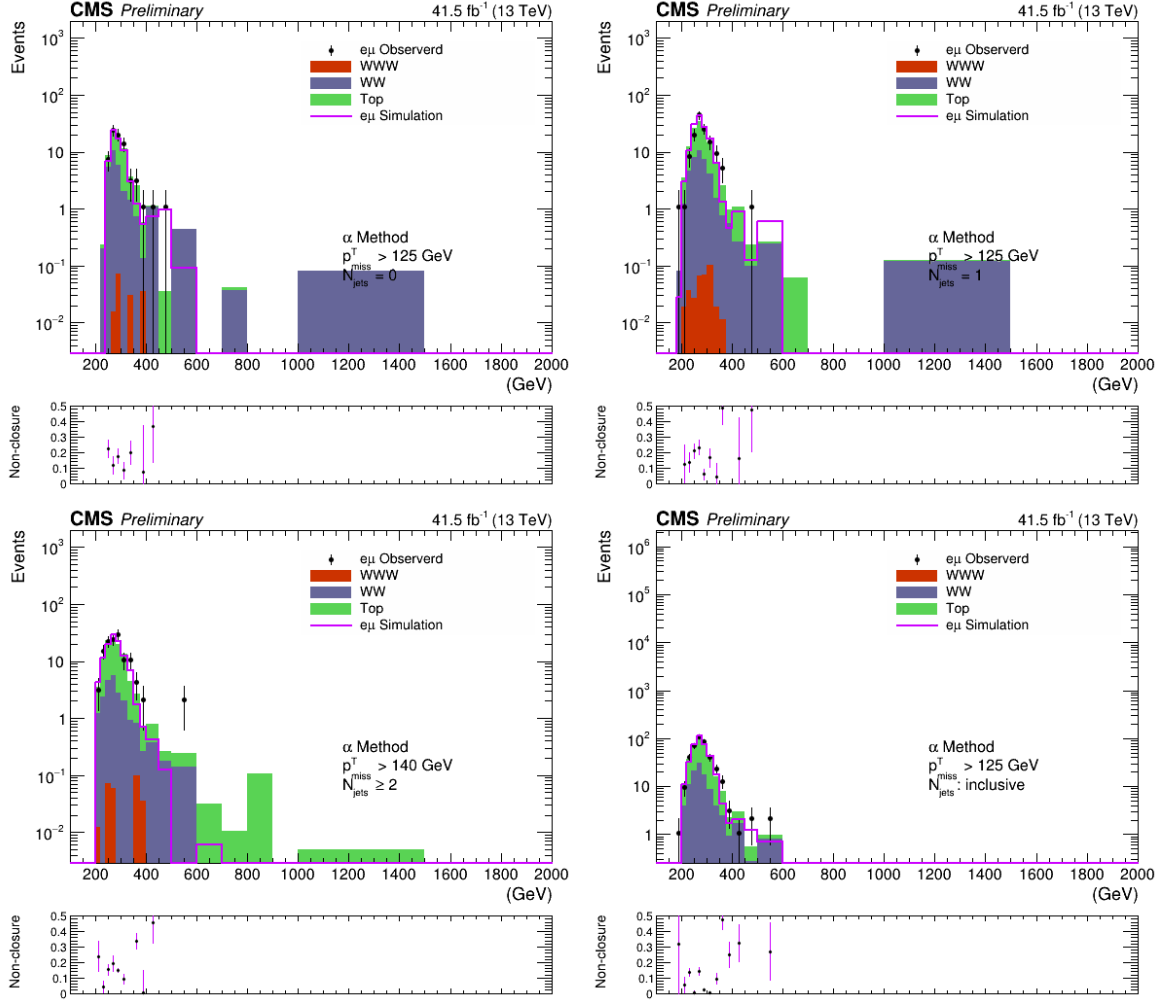


Figure 6.14: **Distributions of m_T^{ZZ} from non-resonant contribution in the signal region for 2017.** The stacked histograms are MC simulations of nonresonant contribution in the signal region and the color legend for them is given in the plots. Reweighted $e\mu$ events from data are shown as black points with error bars. The solid line in magenta shows the shape derived from reweighted $e\mu$ events of simulations. Bottom panels represent for the bias that is calculated in a similar way as Eq. 6.4 in each m_T^{ZZ} bin.

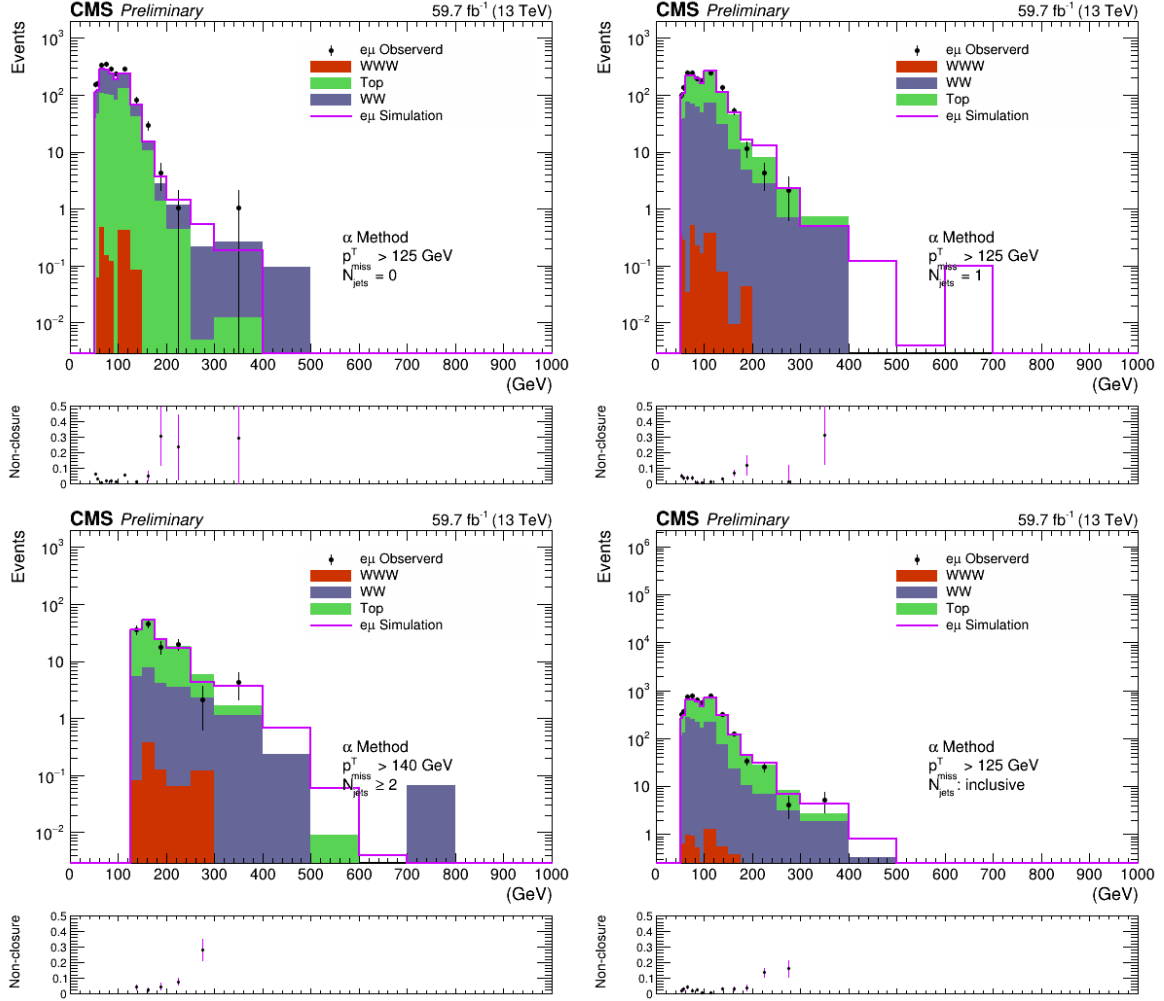


Figure 6.15: **Distributions of p_T^{miss} from non-resonant contribution in the signal region for 2018.** The stacked histograms are MC simulations of nonresonant contribution in the signal region and the color legend for them is given in the plots. Reweighted $e\mu$ events from data are shown as black points with error bars. The solid line in magenta shows the shape derived from reweighted $e\mu$ events of simulations. Bottom panels represent for the bias that is calculated in a similar way as Eq. 6.4 in each p_T^{miss} bin.

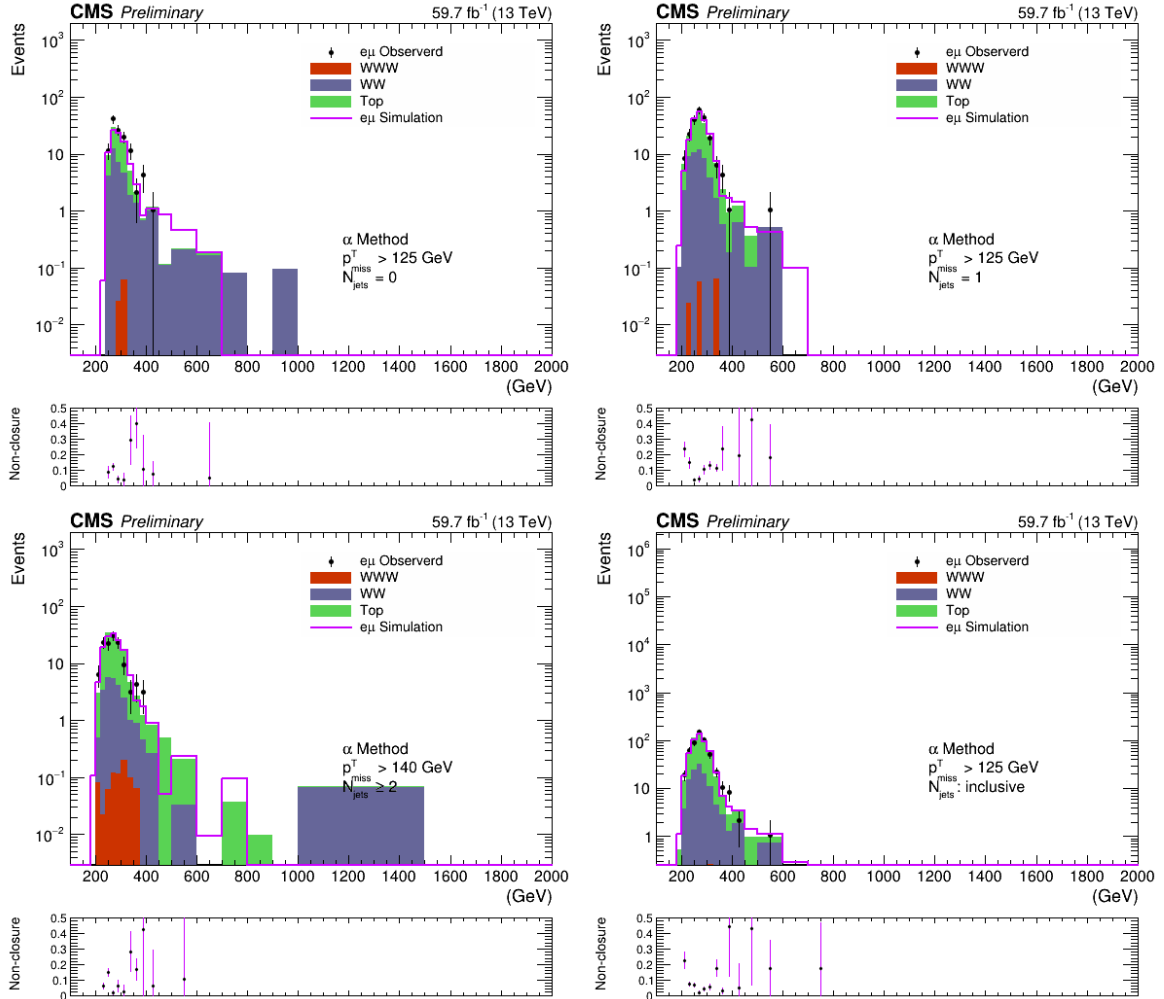


Figure 6.16: **Distributions of m_T^{ZZ} from non-resonant contribution in the signal region for 2018.** The stacked histograms are MC simulations of nonresonant contribution in the signal region and the color legend for them is given in the plots. Reweighted $e\mu$ events from data are shown as black points with error bars. The solid line in magenta shows the shape derived from reweighted $e\mu$ events of simulations. Bottom panels represent for the bias that is calculated in a similar way as Eq. 6.4 in each m_T^{ZZ} bin.

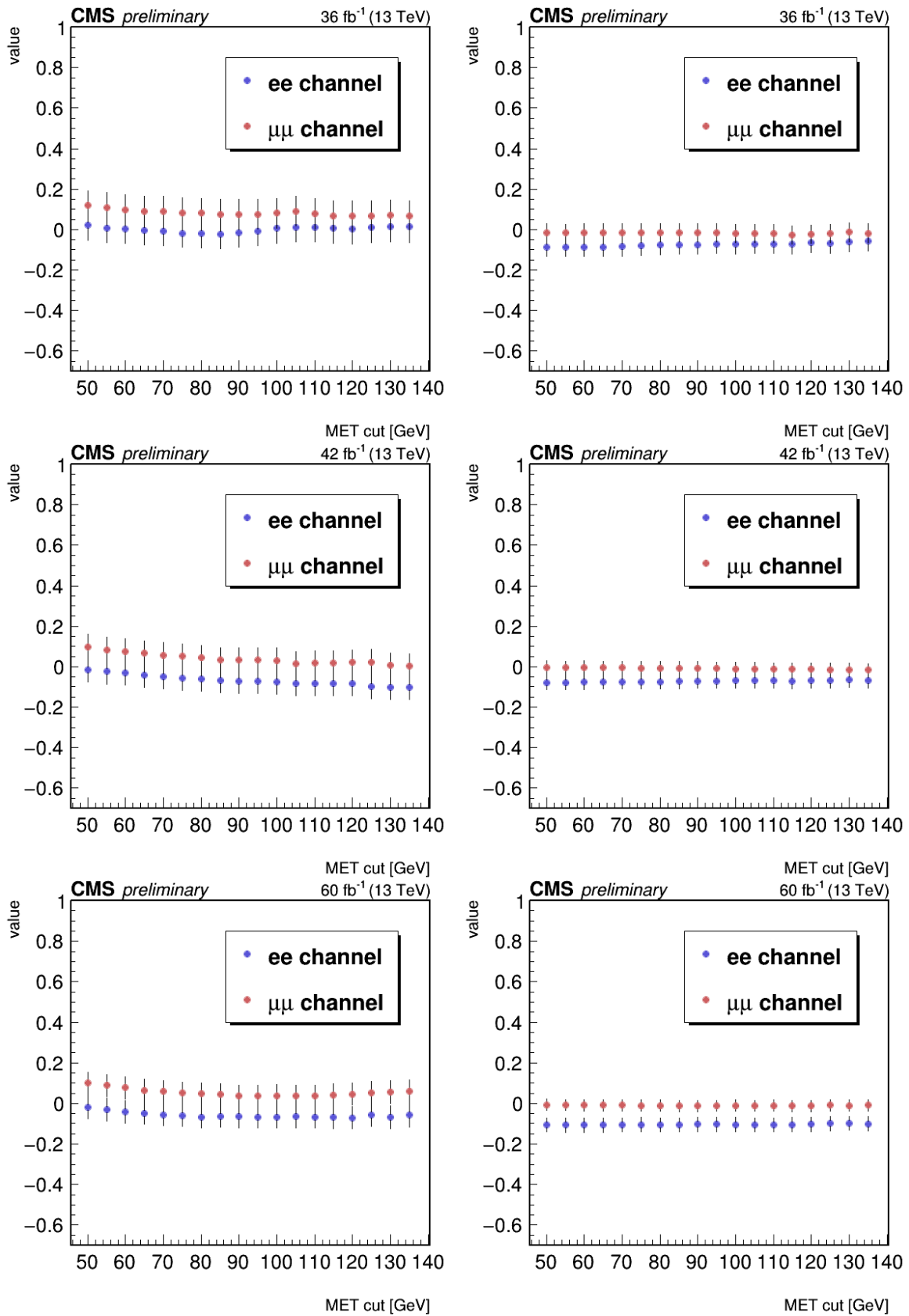


Figure 6.17: **Computed bias as a function of the met cut computed from all side bands ($40 < m_{\ell\ell} < 70$ GeV and $110 < m_{\ell\ell} < 200$ GeV) with b-tagged jet required in the events using both data (left) and MC simulations (right) in di-electron (red) and di-muon (blue) channel of year 2016 (top), 2017 (middle), 2018 (bottom).**

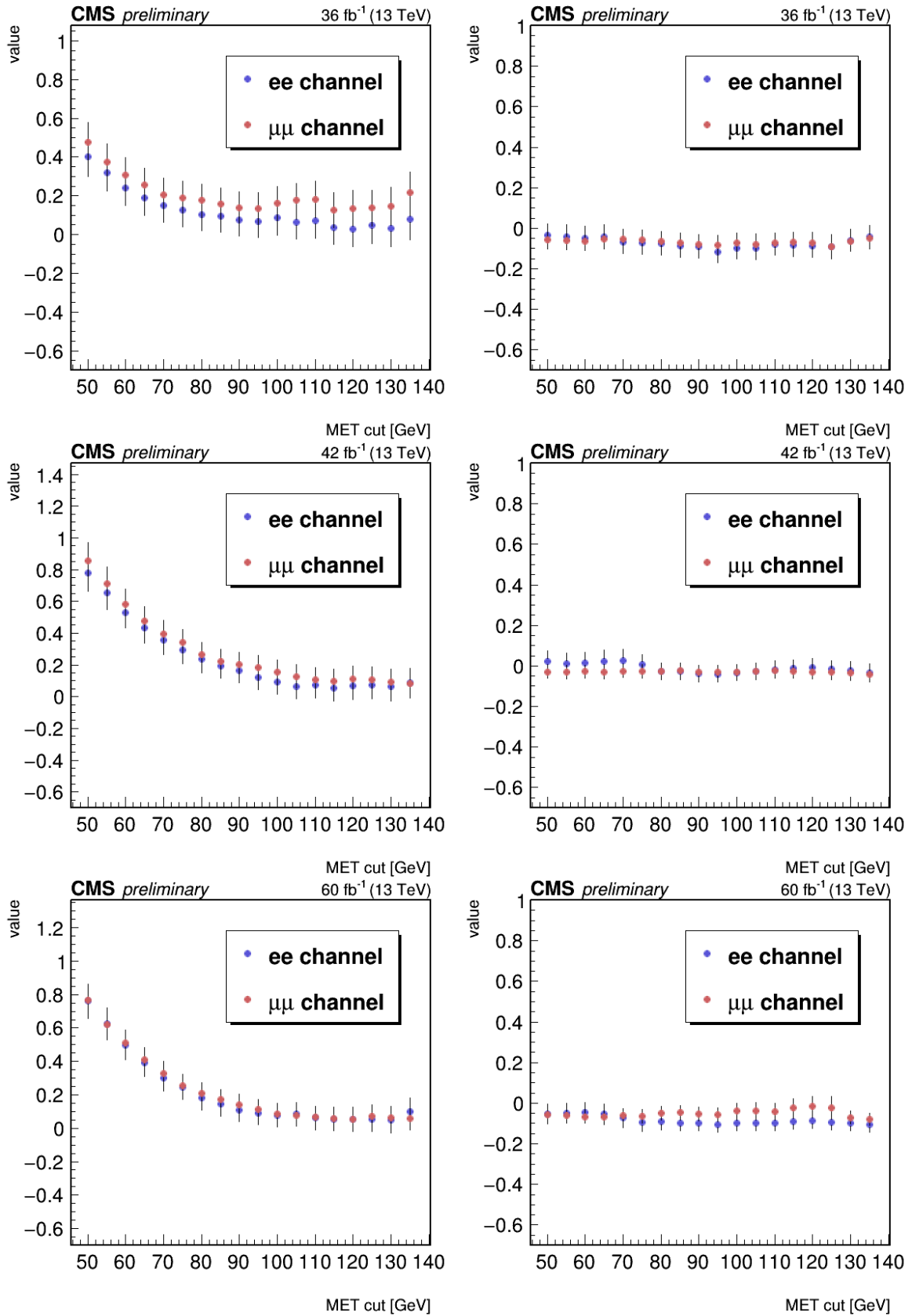


Figure 6.18: **Computed bias as a function of the met cut computed from all side bands ($40 < m_{\ell\ell} < 70$ GeV and $110 < m_{\ell\ell} < 200$ GeV) with events containing b-tagged jet rejected using both data (left) and MC simulations (right) in di-electron (red) and di-muon (blue) channel of year 2016 (top), 2017 (middle), 2018 (bottom).**

6.2 Single-photon control region

$Z(+\text{jets})$ process itself does not involve with genuine p_T^{miss} (see Fig. 6.19). After applying the final analysis selections, contribution from $Z(+\text{jets})$ should be small theoretically. However, due to instrumental effects, the $Z(+\text{jets})$ background cannot be well described by MC simulations (especially in the tails of the p_T^{miss} and m_{T}^{ZZ} distributions) for some sources of reasons: detector energy resolution, jet energy mismeasurement, fluctuations in the pileup energy, instrumental noise. The phase space with the final selections is so small that too few events are simulated, resulting in large statistical uncertainties from the simulation.

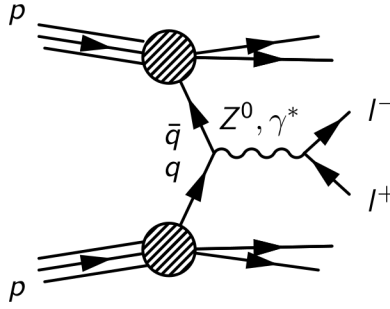


Figure 6.19: Feynman diagram of the Drell-Yan process

For this purpose, a single-photon CR is used, where exactly one photon is required to pass the identification criteria described in Sec. 5.2. The events are required to pass the CR- γ triggers described in Sec. 5.1 and are mostly prescaled. Prescales are applied per event, based on the run numbers and luminosity block.

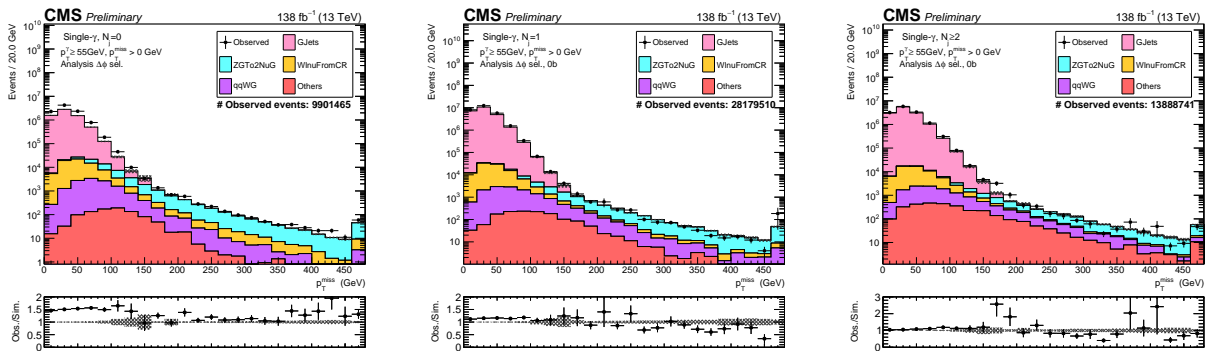


Figure 6.20: The data vs MC distributions of p_T^{miss} distribution in 0 jet (left), 1 jet (middle) and ≥ 2 jets (right) categories, collected over an data taking period correspond to an integrated luminosity of 138fb^{-1} . In these distributions, some discrepancy between data and MC are expected as the $\gamma+\text{jets}$ process come from simulations are not expected to be fully reliable. The gray error bands only correspond to the statistical uncertainty in the simulation.

$\gamma \rightarrow Z$ transfer factor calculation In order to use the information in the CR to estimate the $Z(+\text{jets})$ contribution in the SR, weights must be computed to account for the differences in the cross section, and in the spectra of boson p_T and of the number of good vertices. This reweighting procedure is done in two steps:

1. First, a weight in bins of the number of vertices is derived from photon and dilepton data. All jet and lepton categories are merged for this purpose. The weight spectrum is then fitted with a simple linear function, in order to avoid outlier values due to the lack of statistics.

2. Second, after applying weights in bins of the number of vertices to the photon data, a weight in bins of the boson $|\eta|$ is derived (only in the ≥ 2 -jet category). Both spectra for dilepton and photon are normalized to unity before dividing them.
3. Third, after applying two types of weights above to the photon data, a weight in bins of the boson p_T is derived. The procedure is the same as for the previous points, except that the spectra are not renormalized: this allows us to take into account the difference in normalization. These weights are computed and applied separately for the different jet categories.

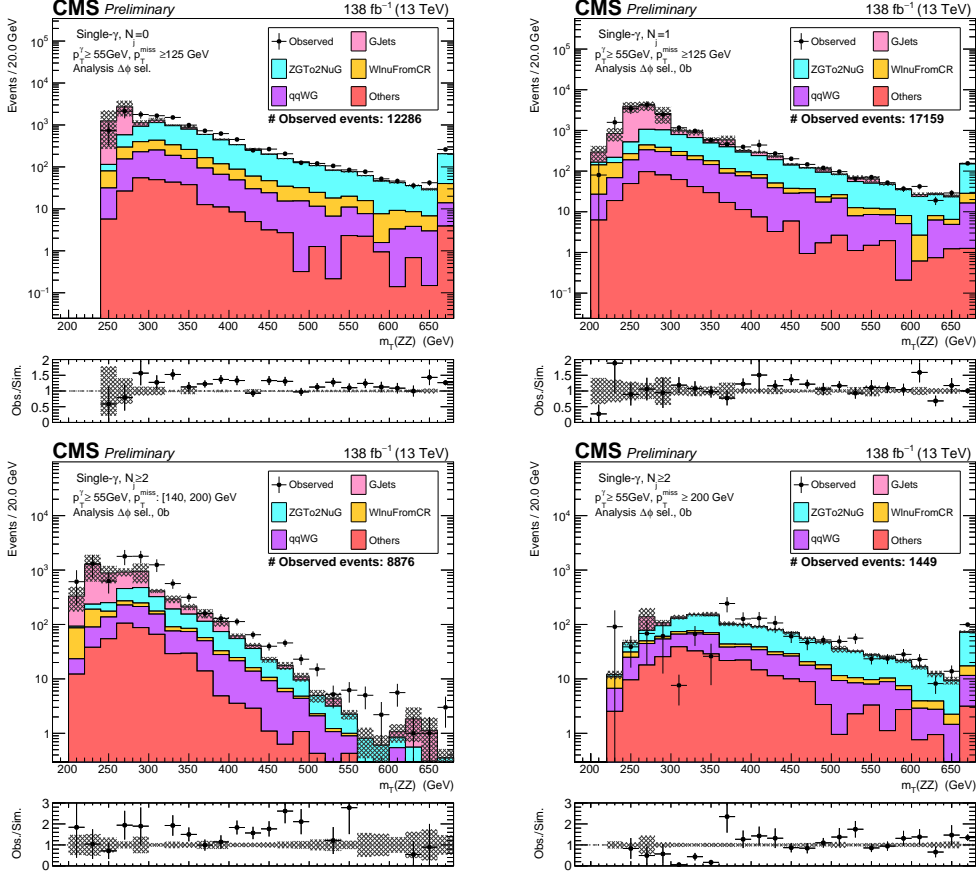


Figure 6.21: **The data vs MC distributions of $m_{\gamma\gamma}^{ZZ}$ distribution in 0 jet (top left), 1 jet (top right), ≥ 2 jets with $140 \leq p_T^{\text{miss}} < 200$ GeV (bottom left) and ≥ 2 jets with $p_T^{\text{miss}} \geq 200$ GeV (bottom right) categories, collected over an data taking period correspond to an integrated luminosity of 138fb^{-1} . In these distributions, some discrepancy between data and MC are expected as the γ +jets process come from simulations are not expected to be fully reliable.**

Processes with genuine p_T^{miss} The single photon CR consists of processes ($Z\gamma$, $W\gamma$, W +jets and $Z \rightarrow \nu\nu$) with genuine p_T^{miss} besides γ +jets. For this reason, a subtraction of these genuine p_T^{miss} contributions is needed. Those process are estimated as follows:

- $Z\gamma$ ($Z \rightarrow \nu\nu$) is estimated with a di-lepton plus photon ($\ell\ell\gamma$) CR. Due to lacking of statistics in this CR, a direct data-driven translation is replaced by a normalization factor applying to MC simulations, per jet category.
- W +jets is estimated with a single electron CR. The W +jets contribution estimated from the CR is represented by

$$N_{W+\text{jets}}^{\gamma-\text{CR}} = \epsilon^{e \rightarrow \gamma} \cdot N_{W+\text{jets}}^{e-\text{CR}} \cdot \frac{\eta^{\gamma-\text{trig.}}}{\eta^{e-\text{trig}}} \quad (6.5)$$

where $\epsilon^{e \rightarrow \gamma}$ is the conversion ratio from electron to photon measured from an $e\gamma$ sample of single electron data.

- Other processes are estimated with MC simulation, and several corrections are applied.

When performing the subtraction of contributions from those processes with genuine p_T^{miss} , we make consistent with the final likelihood construction described in Sec. 5.5. Histograms of each component are constructed for the nominal systematic variation and other variations separately. The variations of the final estimate are constructed by subtracting the different variations of the genuine- p_T^{miss} components from the nominal variation of the observed single-photon data, or the nominal variation of the genuine- p_T^{miss} components from the different variations of the observed single-photon data. Since each histogram encodes a separate probability density in this approach and, therefore, has to remain nonnegative, the bias on flooring is investigated and assigned with a systematic uncertainty.

6.3 WZ control region

The most important systematic uncertainties of the measurement are introduced by simulations of the $q\bar{q} \rightarrow ZZ$ and $q\bar{q} \rightarrow WZ$ backgrounds. To ensure the precision on the off-shell signal strength, it is necessary to control those systematic uncertainties within a reasonable level. A WZ control region is therefore developed for this purpose, constraining both the normalization and kinematic properties of $q\bar{q} \rightarrow ZZ$ and $q\bar{q} \rightarrow WZ$. This control region features a $Z \rightarrow \ell\ell$ decay, an additional lepton, and large enough p_T^{miss} . It should also be able to combine with the analysis signal region in the likelihood scan. Dedicated selection requirements can be applied to this CR, making an optimal use of statistics in the data by analyzing events in a way relevant for a WZ topology. In addition, the transverse momentum of the third lepton can be merged into p_T^{miss} in order to mimic a $Z + p_T^{\text{miss}}$ topology.

The control region is constructed by requiring that events should satisfy the following requirements:

- Events are rejected if any b-tagged jet found based on the loose working point,
- $p_T^{\text{miss}} \geq 20\text{GeV}$,
- $\min\Delta\phi_{\text{miss}}^j > 0.25$,
- $\min\Delta\phi_{\text{miss}}^j > 2.5$, where the unsigned difference is taken between the vector transverse momentum of the 3ℓ system and p_T^{miss} .
- $\Delta\phi_{\text{miss}}^{\text{boson}} > 1.0$, where the boson refers to the Z reconstructed from the opposite sign-same flavor (OSSF) pair with an invariant mass closest to $m_Z = 91.2\text{GeV}$,
- $|m_{\ell\ell} - m_Z| < 15\text{GeV}$ for the OSSF dilepton pair forming the Z candidate,
- $\min(m_{\ell\ell}) > 4\text{GeV}$ for any dilepton pair regardless of charge or flavor,
- $p_T^{\ell_{Z1}} \geq 30\text{GeV}$, $p_T^{\ell_{Z2}} \geq 20\text{GeV}$, where ℓ_{Z1} and ℓ_{Z2} are the leading and trailing lepton forming the Z candidate,
- The dilepton pair defined above fires the combination of single lepton and dilepton SR triggers outlined in Tab. 5.1,
- $p_T^{\ell_W} \geq 20\text{GeV}$ for the remaining lepton ℓ_W , tagged as the lepton from the $W \rightarrow \ell\nu$ decay,
- $A \times m_T^{\ell_W} + p_T^{\text{miss}} \geq 120\text{GeV}$, where $m_T^{\ell_W} = \sqrt{2 \left(p_T^{\ell_W} p_T^{\text{miss}} - \vec{p}_T^{\ell_W} \cdot \vec{p}_T^{\text{miss}} \right)}$ is the m_T of the system between p_T^{miss} and ℓ_W , and the values of A are 1.6 for $\ell_W = \mu$ and 4/3 for $\ell_W = e$,
- $m_T^{\ell_W} \geq 20\text{GeV}(10\text{GeV})$ for $\ell_W = \mu$ ($\ell_W = e$)

The second to last requirements are optimized from the simulation in order to keep high efficiency for WZ events while rejecting both the Drell-Yan and $Z\gamma$ contributions. The events of the control region are finally split into categories of the flavor of ℓ_W (μ or e) and jet multiplicity ($N_j = 0, 1, \geq 2$), and binned in m_T^{WZ} , defined using the W boson mass $m_W = 80.4\text{GeV}$ [125] as

$$\begin{aligned}
 (m_T^{\text{WZ}})^2 = & \left[\sqrt{p_T^{\ell\ell^2} + m_{\ell\ell}^2} \right. \\
 & \left. + \sqrt{|\mathbf{p}_T^{\text{miss}} + \vec{p}_T^{\ell_W}|^2 + m_W^2} \right]^2 \\
 & - \left| \vec{p}_T^{\ell\ell} + \mathbf{p}_T^{\text{miss}} + \vec{p}_T^{\ell_W} \right|^2.
 \end{aligned} \tag{6.6}$$

Event distributions of m_T^{WZ} from this CR are shown in Fig. 6.22

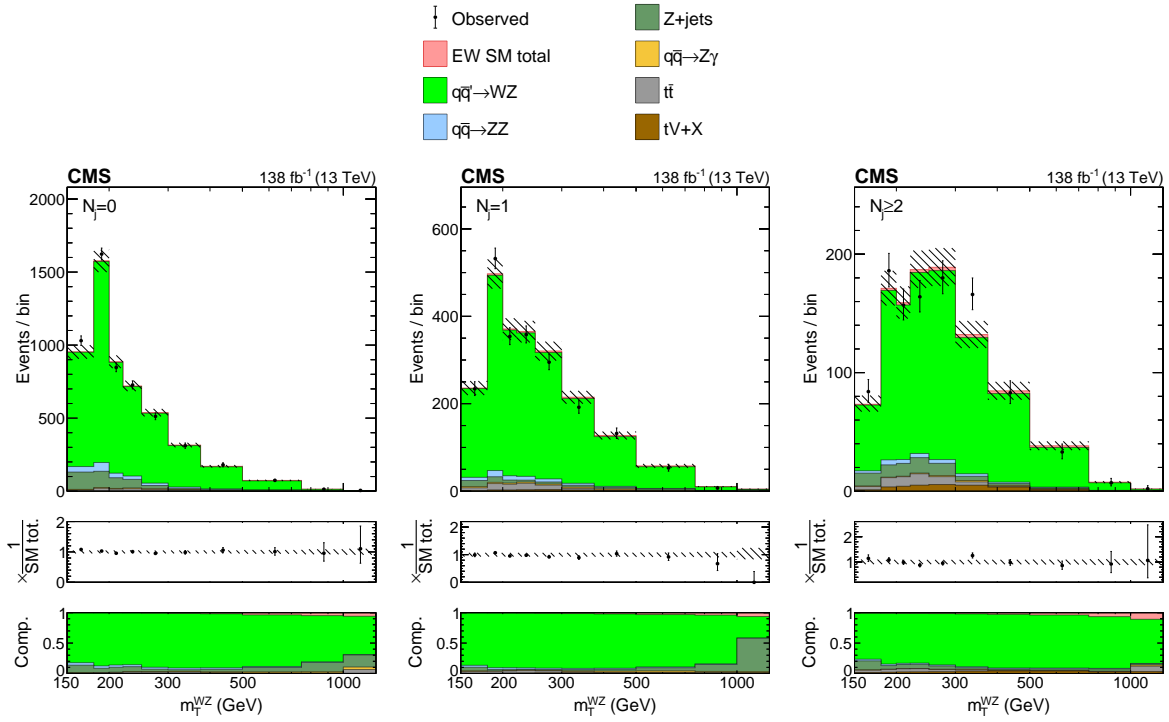


Figure 6.22: **Distributions of m_T^{WZ} in different N_j categories of the WZ control region.** The postfit distributions of the transverse WZ invariant mass are displayed for the $N_j = 0$, $N_j = 1$, and $N_j \geq 2$ jet multiplicity categories of the $WZ \rightarrow 3\ell 1\nu$ control region from left to right. Postfit refers to a combined $2\ell 2\nu + 4\ell$ fit, together with this control region, assuming SM H parameters. The stacked histogram is shown with the hashed band as the total postfit uncertainty at 68% CL. The color legend is given above the plots, with the different contributions referring to the WZ (light green), ZZ (blue), Z+jets (dark green), $Z\gamma$ (yellow), $t\bar{t}$ (gray), and $tV+X$ (brown, with X being any other particle) production processes, as well as the small EW ZZ production component (dark pink). The black points with error bars as uncertainties at 68% CL show the observed data. The middle panels along the vertical show the ratio of the data to the total prediction, and the lower panels show the predicted relative contributions of each process. The rightmost bins contain the overflow.

Results and Interpretations

In this chapter, final results of the measurement are presented and interpreted [22].

m_T^{ZZ} distribution As described in Sec. 5.4, the transverse mass m_T^{ZZ} is used as a major observable in the analysis. Fig. 7.1 shows distributions of m_T^{ZZ} in the different N_j categories of the $2\ell 2\nu$ signal region.

Systematic uncertainties Sources of the systematic uncertainties are already introduced by each component in Sec. 5.6. Final results show that theoretical uncertainties in the kinematic distributions include the simulation of extra jets (up to 20% depending on N_j), and the quantum chromodynamic (QCD) running scale and parton distribution function (PDF) uncertainties in the cross section calculation (up to 30% and 20%, respectively, depending on the process, and m_T^{ZZ} or $m_{4\ell}$). These are particularly important in the gg process since it cannot be constrained by the trilepton WZ CR. Theory uncertainties also include those associated with the EW corrections to the $q\bar{q} \rightarrow ZZ$ and WZ processes, which reach 20% at masses around 1TeV.

Experimental uncertainties include uncertainties in the lepton reconstruction and trigger efficiency (typically 1% per lepton), the integrated luminosity (between 1.2% and 2.5%, depending on the data-taking period [121–123]), and the jet energy scale and resolution [124], which affect the counting of jets, as well as the reconstruction of the VBF discriminants.

Figure 7.2 shows the expected impacts of the different systematics on $\mu^{\text{off-shell}}$ when $R_{V,F}^{\text{off-shell}}$ and on-shell μ_V are unconstrained, and Fig. 7.3 shows the case when $R_{V,F}^{\text{off-shell}} = \mu_V = 1$. The parameter for $R_{V,F}^{\text{off-shell}}$ is denoted with the label `rv_offshell` on the plot Fig. 7.2, and its upper bound, which is unbounded, is denoted with a large, placeholder value. The naming convention of the systematics includes the category, final state, or period labels whenever necessary, which also illustrates how different correlations are treated. Events from the $2\ell 2\nu$ SR and 3ℓ WZ CR are included in estimating these impacts. As can be seen from the impacts, the most dominant uncertainties are the NLO EW correction and parton distribution function uncertainties on the $q\bar{q} \rightarrow VV$ backgrounds in similar ways as the analysis of the off-shell H production from the 4ℓ final state [13].

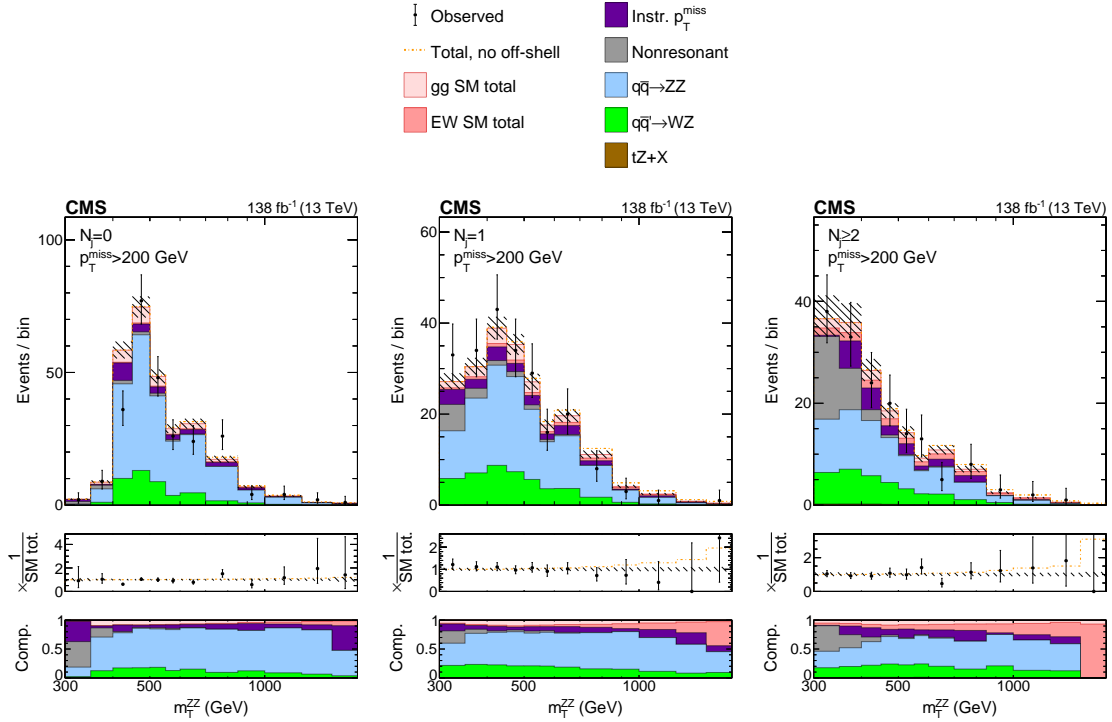


Figure 7.1: **Distributions of m_T^{ZZ} in the different N_j categories of the $2\ell 2\nu$ signal region.** Shown are the transverse ZZ invariant mass distributions in the jet multiplicity categories of $N_j=0$ (left), $=1$ (middle), and ≥ 2 (right) with a requirement of $p_T^{\text{miss}} > 200\text{GeV}$ to enrich H contributions. The color legend for the stacked or dot-dashed histograms is given above the plots. Observed data are shown as black points with error bars as uncertainties at 68% CL. SM backgrounds including the estimations from data-driven are shown in stacked histogram with the hashed band as the total postfit uncertainty at 68% CL. No off-shell H boson production after the fit is shown in dot-dashed gold line. The middle panels along the vertical show the ratio of the data or dashed histograms to the stacked histogram, and the lower panels show the predicted relative contributions of each process.

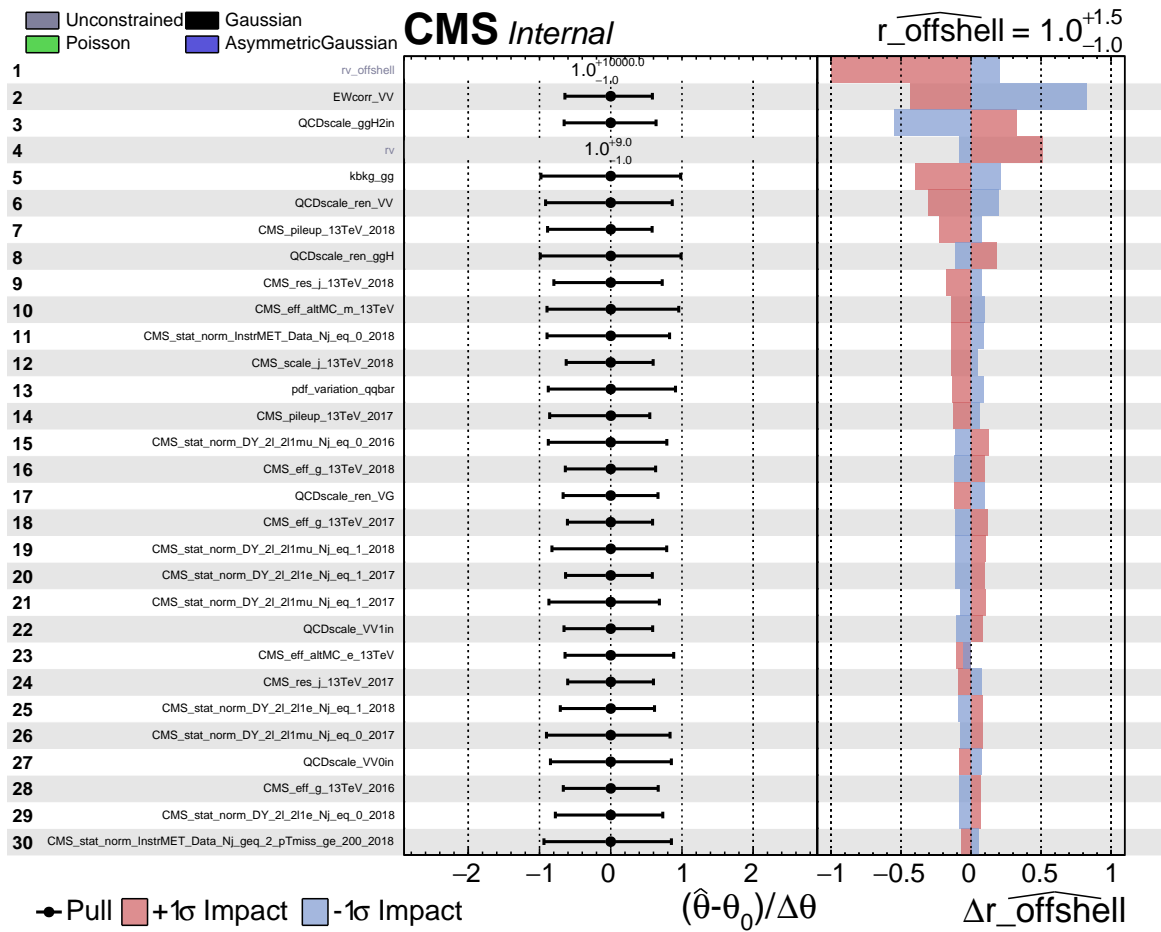


Figure 7.2: Shown are the top 30 nuisance parameters affecting the constraints on $\mu^{\text{off-shell}}$ when $R_{V,F}^{\text{off-shell}}$ and on-shell μ_V are unconstrained. The impacts are shown for the expected result only.

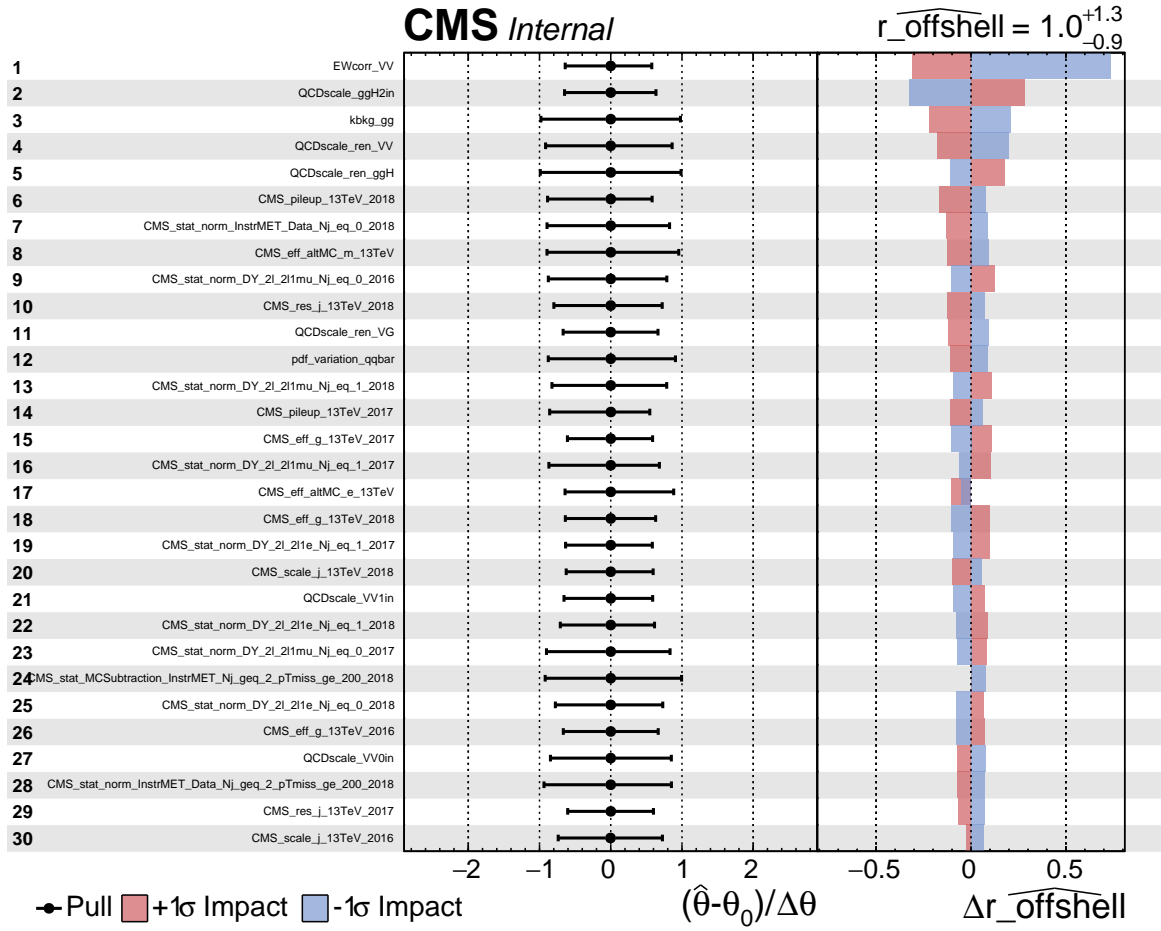


Figure 7.3: Shown are the top 30 nuisance parameters affecting the constraints on $\mu^{\text{off-shell}}$ when $R_{V,F}^{\text{off-shell}}$ and on-shell μ_V are fixed to the SM expectation. The impacts are shown for the expected result only.

Interpretation As well described in Sec. 5.5, we can interpret the results in terms of off-shell signal strengths $\mu^{\text{off-shell}}$, $\mu_{\text{F}}^{\text{off-shell}}$ for the ggF process, and $\mu_{\text{V}}^{\text{off-shell}}$ for the EW process.

For the 4ℓ samples, the binning is in $m_{4\ell}$ and MELA discriminants, which are sensitive to differences between the Higgs signal and continuum ZZ production, or the interfering amplitudes, or anomalous HVV couplings. These variables are listed in Ref. [13, 35] similarly as Tab. 5.8 and 5.9 in the previous Sec. 5.5. In the $2\ell 2\nu$ data sample, the value of m_{T}^{ZZ} is required to be greater than 300GeV. The $m_{4\ell}$ range is required to be within 105–140GeV for 4ℓ on-shell data, or above 220GeV for 4ℓ off-shell data. A representative distribution of m_{T}^{ZZ} , integrated over all N_j , is shown for $2\ell 2\nu$ events on the left panel of Fig. 7.4. On the right panel of Fig. 7.4 is a representative distribution of $m_{4\ell}$ from the combined off-shell 4ℓ events.

These constraints are summarized in Tab. 7.1 for the combination of $2\ell 2\nu$ and high-mass 4ℓ events, or using $2\ell 2\nu$ events alone, and Fig. 7.5 shows the corresponding observed and expected likelihood scans in these parameters. The two-parameter likelihood scan over $\mu_{\text{F}}^{\text{off-shell}}$ and $\mu_{\text{V}}^{\text{off-shell}}$ is also presented in this figure. The expected value of $-2\Delta \ln \mathcal{L}$ at $\mu^{\text{off-shell}} = 0$ exceeds the 95% CL threshold in both of the scenarios considered with events from the $2\ell 2\nu$ final state used alone, or when the events from the two final states are combined. The scenario with $\mu^{\text{off-shell}} = 0$ is excluded with more than 99.7% confidence in the observed result.

Table 7.1: Results on the off-shell signal strengths and Γ_{H} . The various fit conditions are indicated in the column labeled “Cond.”: Results on $\mu^{\text{off-shell}}$ are presented with $R_{\text{V,F}}^{\text{off-shell}} = \mu_{\text{V}}^{\text{off-shell}} / \mu_{\text{F}}^{\text{off-shell}}$ either unconstrained (u) or = 1, and constraints on $\mu_{\text{F}}^{\text{off-shell}}$ and $\mu_{\text{V}}^{\text{off-shell}}$ are shown with the other signal strength unconstrained. Results on Γ_{H} (in units of MeV) are obtained with the on-shell signal strengths unconstrained, and the different conditions listed for this quantity reflect which off-shell final states are combined with on-shell 4ℓ data. The expected central values, not quoted explicitly in this table, are either unity for $\mu^{\text{off-shell}}$, $\mu_{\text{F}}^{\text{off-shell}}$, and $\mu_{\text{V}}^{\text{off-shell}}$, or $\Gamma_{\text{H}} = 4.1\text{MeV}$.

Param.	Cond.	Observed		Expected	
		68% CL	95% CL	68% CL	95% CL
$\mu_{\text{F}}^{\text{off-shell}}$	$\mu_{\text{V}}^{\text{off-shell}}$ (u)	$0.62^{+0.68}_{-0.45}$	+1.38 -0.614	+1.1 -0.99998	< 3.0
$\mu_{\text{V}}^{\text{off-shell}}$	$\mu_{\text{F}}^{\text{off-shell}}$ (u)	$0.90^{+0.9}_{-0.59}$	+2.0 -0.849	+2.0 -0.89	< 4.5
$\mu^{\text{off-shell}}$	$R_{\text{V,F}}^{\text{off-shell}} = 1$	$0.74^{+0.56}_{-0.38}$	+1.06 -0.61	+1.0 -0.84	+1.7 -0.9914
	$R_{\text{V,F}}^{\text{off-shell}}$ (u)	$0.62^{+0.68}_{-0.45}$	+1.38 -0.6139	+1.1 -0.99996	+2.0 -0.99999
Γ_{H}	$2\ell 2\nu + 4\ell$	$3.2^{+2.4}_{-1.7}$	+5.3 -2.7	+4.0 -3.5	+7.2 -4.07
Γ_{H}	$2\ell 2\nu$	$3.1^{+3.4}_{-2.1}$	+7.3 -2.9	+5.1 -3.7	+9.1 -4.099
Γ_{H}	4ℓ	$3.8^{+3.8}_{-2.7}$	+8.0 -3.73	+5.1 -4.05	< 13.8

The different constraints on the Γ_{H} either under the SM-like assumption or with one of the three f_{a_i} parameters unconstrained are summarized in Tab. 7.2, and the corresponding likelihood scans are shown in Fig. 7.6. The constraints use slightly different observables in the analysis of $2\ell 2\nu$ or 4ℓ events, but the expected results show that they are close to each other within 0.1MeV. The observed results are similar between the SM-like scenario and with \bar{f}_{a_2} unconstrained, and between \bar{f}_{a_3} and \bar{f}_{Λ_1} unconstrained. Any of the constraint scenarios exclude $\Gamma_{\text{H}} = 0\text{MeV}$ with more than 99.7% confidence in the observed result. The range of postfit sensitivity on the $\Gamma_{\text{H}} = 0\text{MeV}$ hypothesis coming from each bin in the $2\ell 2\nu$ and 4ℓ off-shell signal regions is visualized in Fig. 7.7.

Table 7.2: **Results on Γ_H and the different anomalous HVV couplings.** The results on Γ_H are displayed in units of MeV, and those on the anomalous HVV couplings are summarized in terms of the corresponding on-shell cross section fractions f_{a2} , f_{a3} , and $f_{\Lambda 1}$ (\bar{f}_{ai} in short, and scaled by 10^5). For the results on Γ_H , the tests with the anomalous HVV couplings are distinguished by the denoted \bar{f}_{ai} , and the expected best-fit values, not quoted explicitly in the table, are always $\Gamma_H = 4.1\text{MeV}$. The SM-like result is the same as that from the combination of all 4ℓ and $2\ell 2\nu$ data sets in Tab. 7.1. For the results on \bar{f}_{ai} , the constraints are shown with either $\Gamma_H = \Gamma_H^{\text{SM}} = 4.1\text{MeV}$ required, or Γ_H left unconstrained, and the expected best-fit values, also not quoted explicitly, are always null. The various fit conditions are indicated in the column labeled “Condition”, where the abbreviation “(u)” indicates which parameter is unconstrained.

Parameter	Condition	Observed			Expected	
		Best fit	68% CL	95% CL	68% CL	95% CL
Γ_H (MeV)	SM-like	3.2	[1.5, 5.6]	[0.5, 8.5]	[0.6, 8.1]	[0.03, 11.3]
	\bar{f}_{a2} (u)	3.4	[1.6, 5.7]	[0.6, 8.4]	[0.5, 8.0]	[0.02, 11.3]
	\bar{f}_{a3} (u)	2.7	[1.3, 4.8]	[0.5, 7.3]	[0.5, 8.0]	[0.02, 11.3]
	$\bar{f}_{\Lambda 1}$ (u)	2.7	[1.3, 4.8]	[0.5, 7.3]	[0.6, 8.1]	[0.02, 11.3]
$\bar{f}_{a2} (\times 10^5)$	$\Gamma_H = \Gamma_H^{\text{SM}}$	79	[6.6, 225]	[-32, 514]	[-78, 70]	[-359, 311]
	Γ_H (u)	72	[2.7, 216]	[-38, 503]	[-82, 73]	[-413, 364]
$\bar{f}_{a3} (\times 10^5)$	$\Gamma_H = \Gamma_H^{\text{SM}}$	2.2	[-6.4, 32]	[-46, 107]	[-55, 55]	[-198, 198]
	Γ_H (u)	2.4	[-6.2, 33]	[-46, 110]	[-58, 58]	[-225, 225]
$\bar{f}_{\Lambda 1} (\times 10^5)$	$\Gamma_H = \Gamma_H^{\text{SM}}$	2.9	[-0.62, 17]	[-11, 46]	[-11, 20]	[-47, 68]
	Γ_H (u)	3.1	[-0.56, 18]	[-10, 47]	[-11, 21]	[-48, 75]

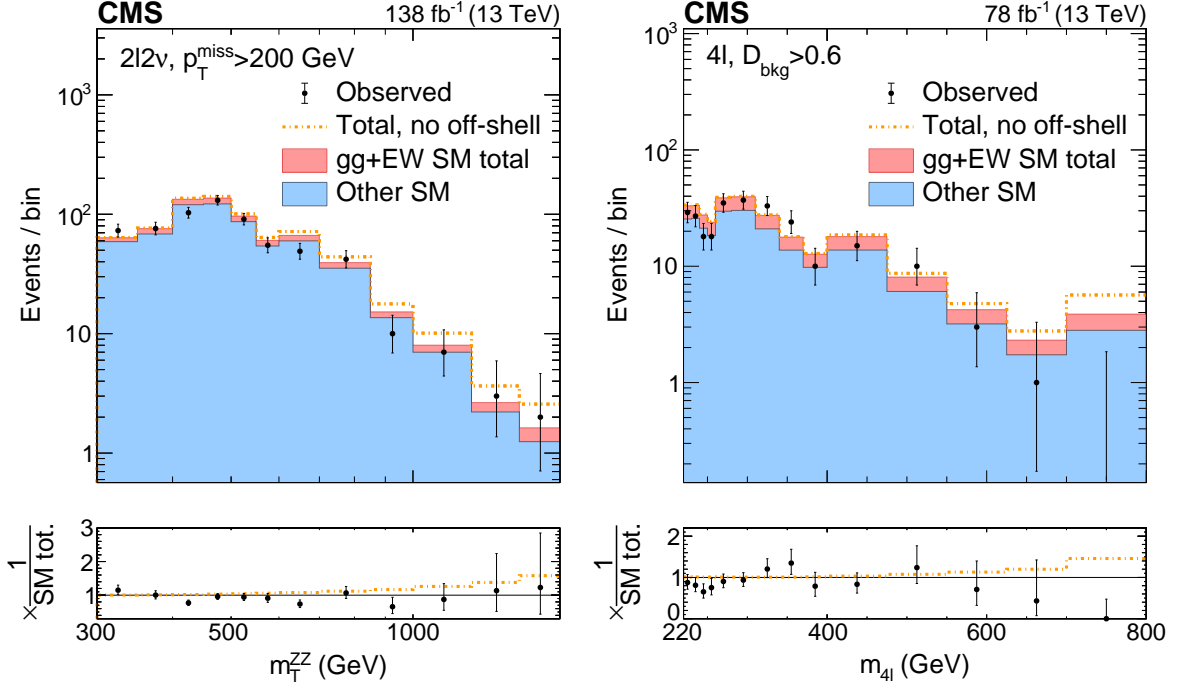


Figure 7.4: **Distributions of ZZ invariant mass observables in the off-shell signal regions.** The distributions of transverse ZZ invariant mass, m_T^{ZZ} from the $2\ell 2\nu$ off-shell signal region are displayed on the left panel, and those of the 4ℓ invariant mass, $m_{4\ell}$, from the 4ℓ off-shell signal region are displayed on the right. The stacked histogram displays the distribution after a fit to the data with SM couplings, with the blue filled area corresponding to the SM processes that do not include H interactions, and the pink filled area adding processes that include H and interference contributions. The gold dot-dashed line shows the fit to the no off-shell hypothesis. The black points with error bars as uncertainties at 68% CL show the observed data, which is consistent with the prediction with SM couplings within one standard deviation. The last bins contain the overflow. The requirements on the missing transverse momentum p_T^{miss} in $2\ell 2\nu$ events, and the \mathcal{D}_{bkg} -type kinematic background discriminants (see Table II of Ref. [13]) in 4ℓ events are applied in order to enhance the H signal contribution. The values of integrated luminosity displayed correspond to those included in the off-shell analyses of each final state. The bottom panels show the ratio of the data or dashed histograms to the SM prediction (stacked histogram). The black horizontal line in these panels marks unit ratio.

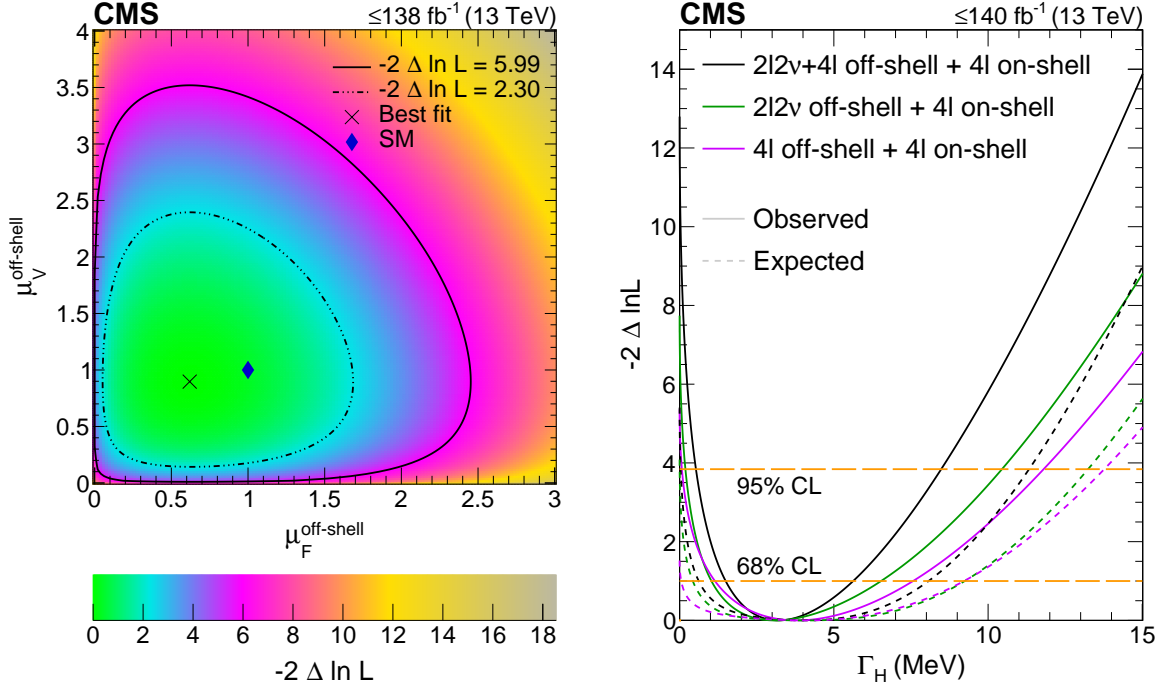


Figure 7.5: **Log-likelihood scans of $\mu_F^{\text{off-shell}}$ and $\mu_V^{\text{off-shell}}$, and Γ_H .** Left panel: Two-parameter likelihood scan of the off-shell gg and EW production signal strength parameters, $\mu_F^{\text{off-shell}}$ and $\mu_V^{\text{off-shell}}$, respectively. The dot-dashed and dashed contours enclose the 68% ($-\Delta \ln \mathcal{L}=2.30$) and 95% ($-\Delta \ln \mathcal{L}=5.99$) CL regions. The cross marks the minimum, and the blue diamond marks the SM expectation. The integrated luminosity reaches only up to 138 fb^{-1} as on-shell 4ℓ events are not included in performing this scan. Right panel: The observed (solid) and expected (dashed) one-parameter likelihood scans over Γ_H . Scans are shown for the combination of 4ℓ on-shell data with 4ℓ off-shell (magenta) or $2\ell 2\nu$ off-shell data (green) alone, or with both data sets (black). The horizontal lines indicate the 68% $-\Delta \ln \mathcal{L}=1.0$ and 95% ($-\Delta \ln \mathcal{L}=3.84$) CL regions. The integrated luminosity reaches up to 140 fb^{-1} as on-shell 4ℓ events are included in performing these scans. The exclusion of the no off-shell hypothesis is consistent with 3.6 standard deviations on both panels.

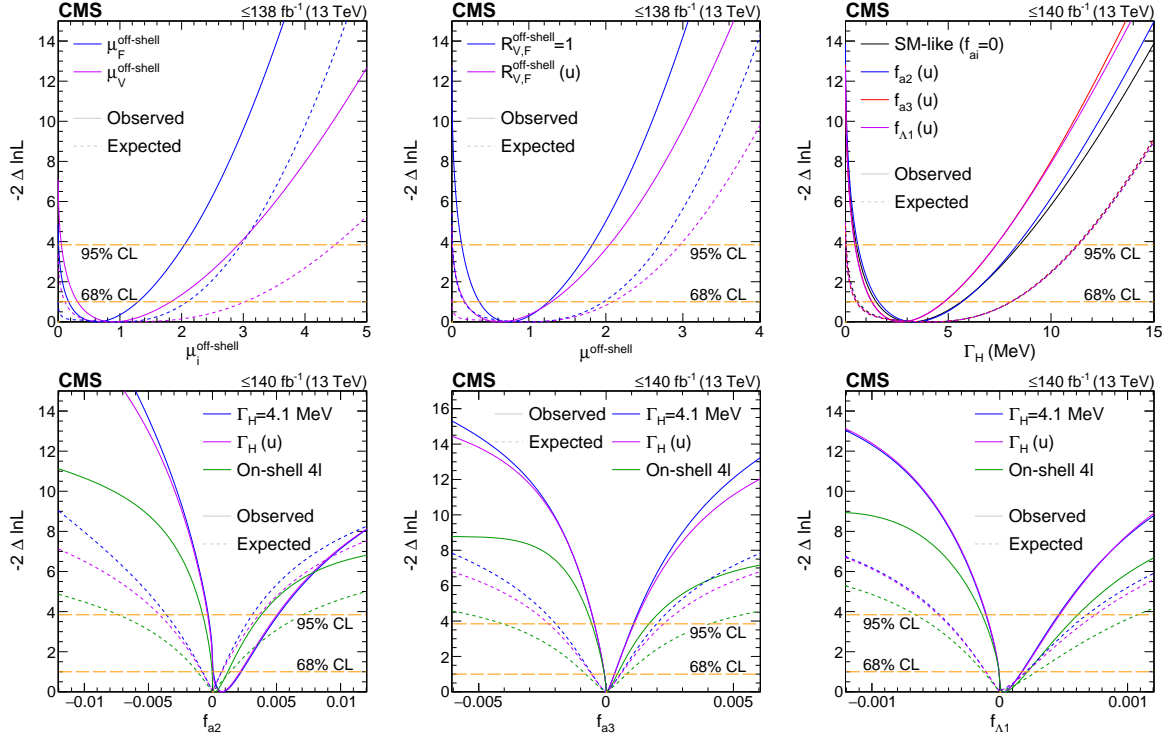


Figure 7.6: **Log-likelihood scans of the off-shell signal strengths, Γ_H , and \bar{f}_{ai} .** Top panels: The likelihood scans are shown for $\mu_F^{\text{off-shell}}$ or $\mu_V^{\text{off-shell}}$ (left), $\mu^{\text{off-shell}}$ (middle), and Γ_H (right). Scans for $\mu_F^{\text{off-shell}}$ (blue) and $\mu_V^{\text{off-shell}}$ (magenta) are obtained with the other parameter unconstrained. Those for $\mu^{\text{off-shell}}$ are shown with (blue) and without (magenta) the constraint $R_{V,F}^{\text{off-shell}} (= \mu_V^{\text{off-shell}}/\mu_F^{\text{off-shell}}) = 1$. Constraints on Γ_H are shown with and without anomalous HVV couplings. Bottom panels: The likelihood scans of the anomalous HVV coupling parameters \bar{f}_{a2} (left), \bar{f}_{a3} (middle), and $\bar{f}_{\Lambda 1}$ (right) are shown with the constraint $\Gamma_H = \Gamma_H^{\text{SM}} = 4.1\text{MeV}$ (blue), Γ_H unconstrained (magenta), or based on on-shell 4ℓ data only (green). Observed (expected) scans are shown with solid (dashed) curves. The horizontal lines indicate the 68% ($-\Delta \ln \mathcal{L}=1.0$) and 95% $-\Delta \ln \mathcal{L}=3.84$) CL regions. The integrated luminosity reaches up to 138fb^{-1} when only off-shell information is used, and up to 140fb^{-1} when on-shell 4ℓ events are included.

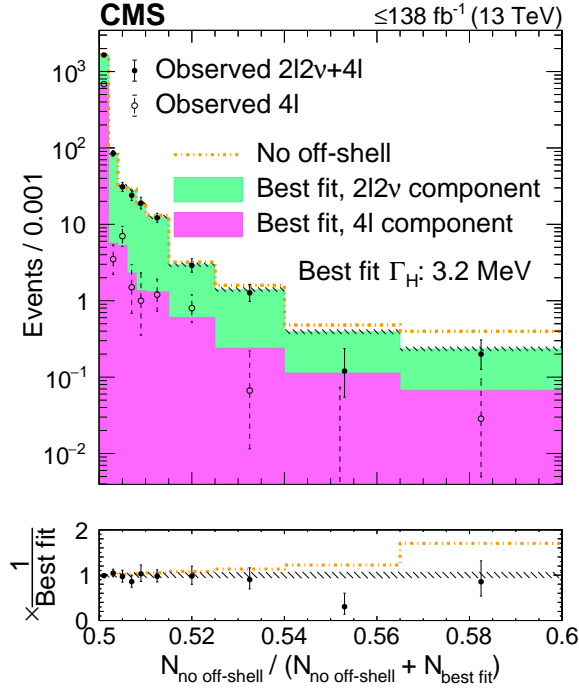


Figure 7.7: **Distributions of ratios of the numbers of events in each off-shell signal region bin.** The ratios are taken after separate fits to the no off-shell hypothesis ($N_{\text{no off-shell}}$) and the best overall fit ($N_{\text{best fit}}$) with the observed Γ_H value of 3.2 MeV in the SM-like HVV couplings scenario. The stacked histogram displays the predicted contributions (pink from the 4ℓ off-shell and green from the $2\ell 2\nu$ off-shell signal regions) after the best fit, with the hashed band representing the total postfit uncertainty at 68% CL, and the gold dot-dashed line shows the predicted distribution of these ratios for a fit to the no off-shell hypothesis. The black solid (hollow) points, with error bars as uncertainties at 68% CL, represent the observed $2\ell 2\nu$ and 4ℓ (4ℓ -only) data. The first and last bins contain the underflow and the overflow, respectively. The bottom panel displays the ratio of the various displayed hypotheses or observed data to the prediction from the best fit. The integrated luminosity reaches only up to 138 fb^{-1} since on-shell 4ℓ events are not displayed.

Conclusion

Presented are studies of off-shell Higgs production in the $ZZ \rightarrow 2\ell 2\nu$ final state, using data from the CMS experiment at the LHC that correspond to an integrated luminosity of 138fb^{-1} (140fb^{-1} with 4ℓ on-shell included) at a center-of-mass energy of 13TeV . Methods and selections used in this study are optimized iteratively by better and better understandings of the detector effects, signal simulations, event reconstructions, background estimations, etc. and finally the result reach the precision of $\Gamma_{\text{H}} = 3.2_{-1.7}^{+2.4}\text{MeV}$ at 68% confidence level (CL) and $\Gamma_{\text{H}} = 3.2_{-2.7}^{+5.3}\text{MeV}$ at 95% CL for the Higgs width measurement. Results are interpreted in terms of constraints on the Higgs off-shell signal production strengths. They are also interpreted in terms of its total width, and parameters that express its anomalous couplings to two electroweak vector bosons after events with a 4ℓ final state are included. Under the assumption of a coupling structure similar to that in the standard model, the constraints on an off-shell signal strength parameter is observed to be within the 95% confidence interval $[0.0061, 2.0]$ with an expectation of $[1 \cdot 10^{-5}, 3.0]$. Constraints interpreted in terms of the total H width become $[0.53, 8.5]\text{MeV}$ for the observation and $[0.035, 11.3]\text{MeV}$ for the expectation with small dependence on the tested anomalous HVV interactions, which are found to be consistent with the SM expectations. The no off-shell scenario with $\mu^{\text{off-shell}} = 0$, or $\Gamma_{\text{H}} = 0\text{MeV}$ is excluded at a p -value of 0.0003 (3.6 standard deviations).

The results presented in this study demonstrate significant progress in the measurement of off-shell Higgs production in the $ZZ \rightarrow 2\ell 2\nu$ final state, despite the numerous challenges encountered during the analysis.

- Improvements in the modeling of the signal, continuum background, and their interference have been achieved through the use of sophisticated simulations techniques and correction approaches. The signal is modeled at approximate NLO precision using a reweighting method based on the ratio of the matrix elements of the process to be modeled. It's the first time in the $ZZ \rightarrow 2\ell 2\nu$ analysis, the kinematic discriminant is used as an observable to improve the sensitivity to the vector-boson fusion channel.
- Physics object reconstructions and corrections have been carefully studied, and the efficiencies of the lepton offline selections and triggers have been measured in an elegant way. These efficiency measurements are crucial for reducing the systematic uncertainties associated with the lepton selection and trigger requirements. By carefully measuring these efficiencies and their uncertainties, the overall precision of the $ZZ \rightarrow 2\ell 2\nu$ analysis is improved. Those are also my major contributions to this analysis.
- Some data-driven methods have been employed to estimate major background contributions, which has enabled the characterization of their uncertainties as well. With the single photon control region, we translate the single photon events in the signal region into Z+jets events with instrumental effects after applying weights subtracted from dedicated control regions. It's a powerful method for estimating the contribution from the Z+jets with instrumental effects, which is difficult to simulate accurately. Another data-driven method is developed for the non-resonant processes, which allows us to estimate the non-resonant background in the ee and $\mu\mu$ channels by applying a weight to the $e\mu$ events. With data-driven estimated non-resonant, the total uncertainties drop from 30% (mainly theoretical uncertainties with simulations) to less than 10%. The measurements of the non-resonant background is also one of my main contributions to the analysis.
- To minimize systematic uncertainties arising from theoretical calculations and higher order corrections of $q\bar{q} \rightarrow ZZ$ and $q\bar{q} \rightarrow WZ$ processes, a data-driven approach called the WZ 3ℓ control region is employed. The WZ 3ℓ control region is defined by applying specific selection criteria that are optimized for events with a WZ topology. By analyzing events in this way, the available statistics in the data can be used optimally to constrain the systematic uncertainties associated

with these backgrounds, which are reckoned as the primary source of the uncertainties in this analysis.

While significant progress has been made in addressing these challenges, continued efforts to refine the analysis techniques and optimize the signal and background modeling are also critical for future studies. Overall, the techniques and results presented in this thesis provide valuable insights into the studies of the Higgs boson and have important implications for the standard model of particle physics.

In the meanwhile, recent results from the ATLAS collaboration also provide an independent confirmation of the evidence of off-shell Higgs. The results are consistent with the SM prediction, but still with limited precision. The precision is dominated by statistical uncertainties. The combination of our result with the recent result of the ATLAS experiment should therefore further improve the width measurement. For much better precision, if no improvement is introduced in the analysis strategy, the data of the full Run-3 would be needed. The two analyses are expected to be combined to provide a better measurement of the Higgs boson width. In the future, the upgraded HL-LHC will be accumulating statistics increased by approximately 20 times and it is expected to reduce the statistical uncertainties of the width measurement by around 5 times.

Bibliography

- [1] David Galbraith, “Standard Model of the Standard Model”, 2022.
<http://davidgalbraith.org/portfolio/ux-standard-model-of-the-standard-model>.
- [2] J. Woithe, G. J. Wiener, and F. F. V. der Veken, “Let’s have a coffee with the standard model of particle physics!”, *Physics Education* **52** (mar, 2017) 034001,
[doi:10.1088/1361-6552/aa5b25](https://doi.org/10.1088/1361-6552/aa5b25).
- [3] CMS Collaboration, “Evidence for higgs boson decay to a pair of muons”, *J. High Energ. Phys.* (sep, 2020) [doi:10.1007/JHEP01\(2021\)148](https://doi.org/10.1007/JHEP01(2021)148).
- [4] CMS Collaboration, “LHC Higgs Working Group”, 2019.
<https://twiki.cern.ch/twiki/bin/view/LHCPhysics/LHCHWG>.
- [5] F. Marcastel, “CERN’s Accelerator Complex. La chaîne des accélérateurs du CERN”, Oct, 2013. General Photo. <https://cds.cern.ch/record/1621583>.
- [6] CMS Collaboration, “Public CMS Luminosity Information”, 2022. <https://twiki.cern.ch/twiki/bin/view/CMSPublic/LumiPublicResults>.
- [7] CMS Collaboration, “Detector — CMS Experiment”, 2022.
<https://cms.cern/detector>.
- [8] CMS Collaboration, “The CMS experiment at the CERN LHC”, *JINST* **3** (2008) S08004,
[doi:10.1088/1748-0221/3/08/S08004](https://doi.org/10.1088/1748-0221/3/08/S08004).
- [9] CMS Collaboration, “Technical proposal for the upgrade of the CMS detector through 2020”, technical report, Jun, 2011.
- [10] M. Kim et al., “Web-based monitoring tools for resistive plate chambers in the CMS experiment at CERN”, *Journal of Instrumentation* **9** (oct, 2014) C10031–C10031,
[doi:10.1088/1748-0221/9/10/c10031](https://doi.org/10.1088/1748-0221/9/10/c10031).
- [11] A. Sirunyan et al., “Performance of the cms level-1 trigger in proton-proton collisions at $\sqrt{s} = 13$ tev”, *Journal of Instrumentation* **15** (oct, 2020) P10017–P10017,
[doi:10.1088/1748-0221/15/10/p10017](https://doi.org/10.1088/1748-0221/15/10/p10017).

- [12] CMS Collaboration, “Background estimation with the ABCD method”, 2022. <https://cms-opendata-workshop.github.io/workshop-lesson-abcd-method/01-introduction/index.html>.
- [13] CMS Collaboration, “Measurements of the Higgs boson width and anomalous HVV couplings from on-shell and off-shell production in the four-lepton final state”, *Phys. Rev. D* **99** (2019), no. 11, 112003, doi:10.1103/PhysRevD.99.112003, arXiv:1901.00174.
- [14] Y. Gao et al., “Spin determination of single-produced resonances at hadron colliders”, *Phys. Rev. D* **81** (2010) 075022, doi:10.1103/PhysRevD.81.075022, arXiv:1001.3396.
- [15] S. Bolognesi et al., “Spin and parity of a single-produced resonance at the LHC”, *Phys. Rev. D* **86** (2012) 095031, doi:10.1103/PhysRevD.86.095031, arXiv:1208.4018.
- [16] I. Anderson et al., “Constraining anomalous HVV interactions at proton and lepton colliders”, *Phys. Rev. D* **89** (2014) 035007, doi:10.1103/PhysRevD.89.035007, arXiv:1309.4819.
- [17] A. V. Gritsan, R. Röntsch, M. Schulze, and M. Xiao, “Constraining anomalous Higgs boson couplings to the heavy flavor fermions using matrix element techniques”, *Phys. Rev. D* **94** (2016) 055023, doi:10.1103/PhysRevD.94.055023, arXiv:1606.03107.
- [18] A. V. Gritsan et al., “New features in the JHU generator framework: constraining Higgs boson properties from on-shell and off-shell production”, *Phys. Rev. D* **102** (2020), no. 5, 056022, doi:10.1103/PhysRevD.102.056022, arXiv:2002.09888.
- [19] CMS Collaboration, “Luminosity recommendations for Run 2 analyses”, 2022. <https://twiki.cern.ch/twiki/bin/viewauth/CMS/LumiRecommendationsRun2>.
- [20] CERN, “The Large Hadron Collider”, 2022. <https://home.cern/science/accelerators/large-hadron-collider>.
- [21] CERN, “The CMS detector”, 2022. <https://cms.cern/detector>.
- [22] CMS Collaboration, “Measurement of the Higgs boson width and evidence of its off-shell contributions to ZZ production”, *Nature Phys.* **18** (2022), no. 11, 1329–1334, doi:10.1038/s41567-022-01682-0, arXiv:2202.06923.
- [23] C. Burgess and G. Moore, “The Standard Model, A Primer”. December, 2006. ISBN 978-0-521-86036-9.
- [24] T. Banks, “Modern Quantum Field Theory, A Concise Introduction”. September, 2008. ISBN 978-0-511-42899-9.
- [25] F. Englert and R. Brout, “Broken symmetry and the mass of gauge vector mesons”, *Phys. Rev. Lett.* **13** (1964) 321, doi:10.1103/PhysRevLett.13.321.
- [26] P. W. Higgs, “Broken symmetries and the masses of gauge bosons”, *Phys. Rev. Lett.* **13** (1964) 508, doi:10.1103/PhysRevLett.13.508.
- [27] CMS Collaboration, “Observation of a new boson at a mass of 125GeV with the CMS experiment at the LHC”, *Phys. Lett. B* **716** (2012) 30, doi:10.1016/j.physletb.2012.08.021, arXiv:1207.7235.

- [28] ATLAS Collaboration, “Observation of a new particle in the search for the Standard Model Higgs boson with the ATLAS detector at the LHC”, *Phys. Lett. B* **716** (2012) 1, [doi:10.1016/j.physletb.2012.08.020](https://doi.org/10.1016/j.physletb.2012.08.020), [arXiv:1207.7214](https://arxiv.org/abs/1207.7214).
- [29] CMS Collaboration, “On the mass and spin-parity of the Higgs boson candidate via its decays to Z boson pairs”, *Phys. Rev. Lett.* **110** (2013) 081803, [doi:10.1103/PhysRevLett.110.081803](https://doi.org/10.1103/PhysRevLett.110.081803), [arXiv:1212.6639](https://arxiv.org/abs/1212.6639).
- [30] CMS Collaboration, “Measurement of the properties of a Higgs boson in the four-lepton final state”, *Phys. Rev. D* **89** (2014) 092007, [doi:10.1103/PhysRevD.89.092007](https://doi.org/10.1103/PhysRevD.89.092007), [arXiv:1312.5353](https://arxiv.org/abs/1312.5353).
- [31] CMS Collaboration, “Constraints on the spin-parity and anomalous HVV couplings of the Higgs boson in proton collisions at 7 and 8TeV”, *Phys. Rev. D* **92** (2015) 012004, [doi:10.1103/PhysRevD.92.012004](https://doi.org/10.1103/PhysRevD.92.012004), [arXiv:1411.3441](https://arxiv.org/abs/1411.3441).
- [32] CMS Collaboration, “Limits on the Higgs boson lifetime and width from its decay to four charged leptons”, *Phys. Rev. D* **92** (2015) 072010, [doi:10.1103/PhysRevD.92.072010](https://doi.org/10.1103/PhysRevD.92.072010), [arXiv:1507.06656](https://arxiv.org/abs/1507.06656).
- [33] CMS Collaboration, “Combined search for anomalous pseudoscalar HVV couplings in VH ($H \rightarrow b\bar{b}$) production and $H \rightarrow VV$ decay”, *Phys. Lett. B* **759** (2016) 672, [doi:10.1016/j.physletb.2016.06.004](https://doi.org/10.1016/j.physletb.2016.06.004), [arXiv:1602.04305](https://arxiv.org/abs/1602.04305).
- [34] CMS Collaboration, “Constraints on anomalous Higgs boson couplings using production and decay information in the four-lepton final state”, *Phys. Lett. B* **775** (2017) 1, [doi:10.1016/j.physletb.2017.10.021](https://doi.org/10.1016/j.physletb.2017.10.021), [arXiv:1707.00541](https://arxiv.org/abs/1707.00541).
- [35] CMS Collaboration, “Constraints on anomalous higgs boson couplings to vector bosons and fermions in its production and decay using the four-lepton final state”, *Phys. Rev. D* **104** (Sep, 2021) 052004, [doi:10.1103/PhysRevD.104.052004](https://doi.org/10.1103/PhysRevD.104.052004).
- [36] ATLAS Collaboration, “Evidence for the spin-0 nature of the Higgs boson using ATLAS data”, *Phys. Lett. B* **726** (2013) 120, [doi:10.1016/j.physletb.2013.08.026](https://doi.org/10.1016/j.physletb.2013.08.026), [arXiv:1307.1432](https://arxiv.org/abs/1307.1432).
- [37] ATLAS Collaboration, “Study of the spin and parity of the Higgs boson in diboson decays with the ATLAS detector”, *Eur. Phys. J. C* **75** (2015) 476, [doi:10.1140/epjc/s10052-015-3685-1](https://doi.org/10.1140/epjc/s10052-015-3685-1), [arXiv:1506.05669](https://arxiv.org/abs/1506.05669).
- [38] ATLAS Collaboration, “Test of CP Invariance in vector-boson fusion production of the Higgs boson using the Optimal Observable method in the ditau decay channel with the ATLAS detector”, *Eur. Phys. J. C* **76** (2016) 658, [doi:10.1140/epjc/s10052-016-4499-5](https://doi.org/10.1140/epjc/s10052-016-4499-5), [arXiv:1602.04516](https://arxiv.org/abs/1602.04516).
- [39] ATLAS Collaboration, “Measurement of inclusive and differential cross sections in the $H \rightarrow ZZ^* \rightarrow 4l$ decay channel in pp collisions at $\sqrt{s} = 13\text{TeV}$ with the ATLAS detector”, *JHEP* **10** (2017) 132, [doi:10.1007/JHEP10\(2017\)132](https://doi.org/10.1007/JHEP10(2017)132), [arXiv:1708.02810](https://arxiv.org/abs/1708.02810).
- [40] ATLAS Collaboration, “Measurement of the Higgs boson coupling properties in the $H \rightarrow ZZ^* \rightarrow 4l$ decay channel at $\sqrt{s} = 13\text{ TeV}$ with the ATLAS detector”, *JHEP* **03** (2018) 095, [doi:10.1007/JHEP03\(2018\)095](https://doi.org/10.1007/JHEP03(2018)095), [arXiv:1712.02304](https://arxiv.org/abs/1712.02304).

- [41] ATLAS Collaboration, “Measurements of Higgs boson properties in the diphoton decay channel with 36 fb^{-1} of pp collision data at $\sqrt{s} = 13 \text{ TeV}$ with the ATLAS detector”, *Phys. Rev. D* **98** (2018) 052005, doi:[10.1103/PhysRevD.98.052005](https://doi.org/10.1103/PhysRevD.98.052005), arXiv:[1802.04146](https://arxiv.org/abs/1802.04146).
- [42] H. Georgi, S. Glashow, M. Machacek, and D. Nanopoulos, “Higgs bosons from two-gluon annihilation in proton-proton collisions”, in *The Standard Model Higgs Boson*, M. EINHORN, ed., volume 8 of *Current Physics—Sources and Comments*, pp. 113–115. Elsevier, 1991. doi:<https://doi.org/10.1016/B978-0-444-88807-5.50076-5>.
- [43] N. Kauer and G. Passarino, “Inadequacy of zero-width approximation for a light Higgs boson signal”, *JHEP* **08** (2012) 116, doi:[10.1007/JHEP08\(2012\)116](https://doi.org/10.1007/JHEP08(2012)116), arXiv:[1206.4803](https://arxiv.org/abs/1206.4803).
- [44] N. Kauer, “Inadequacy of zero-width approximation for a light Higgs boson signal”, *Mod. Phys. Lett. A* **28** (2013) 1330015, doi:[10.1142/S0217732313300152](https://doi.org/10.1142/S0217732313300152), arXiv:[1305.2092](https://arxiv.org/abs/1305.2092).
- [45] E. Glover and J. Van der Bij, “Z-boson pair production via gluon fusion”, *Nuclear Physics B* **321** (1989), no. 3, 561–590, doi:[https://doi.org/10.1016/0550-3213\(89\)90262-9](https://doi.org/10.1016/0550-3213(89)90262-9).
- [46] C. H. Llewellyn Smith, “High-Energy Behavior and Gauge Symmetry”, *Phys. Lett. B* **46** (1973) 233, doi:[10.1016/0370-2693\(73\)90692-8](https://doi.org/10.1016/0370-2693(73)90692-8).
- [47] J. M. Cornwall, D. N. Levin, and G. Tiktopoulos, “Derivation of gauge invariance from high-energy unitarity bounds on the s matrix”, *Phys. Rev. D* **10** (Aug, 1974) 1145–1167, doi:[10.1103/PhysRevD.10.1145](https://doi.org/10.1103/PhysRevD.10.1145).
- [48] F. Caola and K. Melnikov, “Constraining the Higgs boson width with ZZ production at the LHC”, *Phys. Rev. D* **88** (2013) 054024, doi:[10.1103/PhysRevD.88.054024](https://doi.org/10.1103/PhysRevD.88.054024), arXiv:[1307.4935](https://arxiv.org/abs/1307.4935).
- [49] J. M. Campbell, R. K. Ellis, and C. Williams, “Bounding the Higgs width at the LHC using full analytic results for $gg \rightarrow e^-e^+\mu^-\mu^+$ ”, *JHEP* **04** (2014) 060, doi:[10.1007/JHEP04\(2014\)060](https://doi.org/10.1007/JHEP04(2014)060), arXiv:[1311.3589](https://arxiv.org/abs/1311.3589).
- [50] CMS Collaboration, “Precise determination of the mass of the Higgs boson and tests of compatibility of its couplings with the standard model predictions using proton collisions at 7 and 8 TeV”, *Eur. Phys. J. C* **75** (2015) 212, doi:[10.1140/epjc/s10052-015-3351-7](https://doi.org/10.1140/epjc/s10052-015-3351-7), arXiv:[1412.8662](https://arxiv.org/abs/1412.8662).
- [51] ATLAS Collaboration, “Measurement of the Higgs boson mass from the $H \rightarrow \gamma\gamma$ and $H \rightarrow ZZ^* \rightarrow 4l$ channels with the ATLAS detector using 25fb^{-1} of pp collision data”, *Phys. Rev. D* **90** (2014) 052004, doi:[10.1103/PhysRevD.90.052004](https://doi.org/10.1103/PhysRevD.90.052004), arXiv:[1406.3827](https://arxiv.org/abs/1406.3827).
- [52] CMS Collaboration, “Measurements of properties of the Higgs boson decaying into the four-lepton final state in pp collisions at $\sqrt{s} = 13\text{TeV}$ ”, *JHEP* **11** (2017) 047, doi:[10.1007/JHEP11\(2017\)047](https://doi.org/10.1007/JHEP11(2017)047), arXiv:[1706.09936](https://arxiv.org/abs/1706.09936).
- [53] CMS Collaboration, “Constraints on the Higgs boson width from off-shell production and decay to Z-boson pairs”, *Phys. Lett. B* **736** (2014) 64, doi:[10.1016/j.physletb.2014.06.077](https://doi.org/10.1016/j.physletb.2014.06.077), arXiv:[1405.3455](https://arxiv.org/abs/1405.3455).

- [54] CMS Collaboration, “Search for Higgs boson off-shell production in proton-proton collisions at 7 and 8 TeV and derivation of constraints on its total decay width”, *JHEP* **09** (2016) 051, [doi:10.1007/JHEP09\(2016\)051](https://doi.org/10.1007/JHEP09(2016)051), [arXiv:1605.02329](https://arxiv.org/abs/1605.02329).
- [55] ATLAS Collaboration, “Constraints on off-shell Higgs boson production and the Higgs boson total width in $ZZ \rightarrow 4\ell$ and $ZZ \rightarrow 2l2\nu$ final states with the ATLAS detector”, *Phys. Lett. B* **786** (2018) 223, [doi:10.1016/j.physletb.2018.09.048](https://doi.org/10.1016/j.physletb.2018.09.048), [arXiv:1808.01191](https://arxiv.org/abs/1808.01191).
- [56] D. Gonçalves, T. Han, and S. Mukhopadhyay, “Higgs couplings at high scales”, *Phys. Rev. D* **98** (Jul, 2018) 015023, [doi:10.1103/PhysRevD.98.015023](https://doi.org/10.1103/PhysRevD.98.015023).
- [57] ATLAS Collaboration, “Constraints on the off-shell Higgs boson signal strength in the high-mass ZZ and WW final states with the ATLAS detector”, *Eur. Phys. J. C* **75** (2015) 335, [doi:10.1140/epjc/s10052-015-3542-2](https://doi.org/10.1140/epjc/s10052-015-3542-2), [arXiv:1503.01060](https://arxiv.org/abs/1503.01060).
- [58] ATLAS Collaboration, “Evidence of off-shell Higgs boson production and constraints on the total width of the Higgs boson in the the $ZZ \rightarrow 4\ell$ and $ZZ \rightarrow 2l2\nu$ decay channels with the ATLAS detector”.
- [59] LHC Higgs Cross Section Working Group Collaboration, “Handbook of LHC Higgs cross sections: 4. Deciphering the nature of the Higgs Sector”, [doi:10.23731/CYRM-2017-002](https://doi.org/10.23731/CYRM-2017-002), [arXiv:1610.07922](https://arxiv.org/abs/1610.07922).
- [60] CERN, “The Large Hadron Collider”, 2022. <https://home.cern/science/accelerators/large-hadron-collider>.
- [61] O. S. Brüning et al., “LHC Design Report”. CERN Yellow Reports: Monographs. CERN, Geneva, 2004. [doi:10.5170/CERN-2004-003-V-1](https://doi.org/10.5170/CERN-2004-003-V-1).
- [62] K. Klein, “The phase-1 upgrade of the cms pixel detector”, *Nuclear Instruments and Methods in Physics Research Section A: Accelerators, Spectrometers, Detectors and Associated Equipment* **845** (2017) 101–105, [doi:https://doi.org/10.1016/j.nima.2016.06.039](https://doi.org/10.1016/j.nima.2016.06.039). Proceedings of the Vienna Conference on Instrumentation 2016.
- [63] CMS Collaboration, “The CMS electromagnetic calorimeter project: Technical Design Report”. Technical design report. CMS. CERN, Geneva, 1997.
- [64] CMS Collaboration, “The CMS hadron calorimeter project: Technical Design Report”. Technical design report. CMS. CERN, Geneva, 1997.
- [65] CMS Collaboration, “Phase 1 upgrade of the CMS forward hadronic calorimeter”, *Journal of Instrumentation* **12** (feb, 2017) C02026–C02026, [doi:10.1088/1748-0221/12/02/c02026](https://doi.org/10.1088/1748-0221/12/02/c02026).
- [66] CMS Collaboration, “The CMS outer HCAL SiPM upgrade”, *Journal of Physics: Conference Series* **587** (feb, 2015) 012005, [doi:10.1088/1742-6596/587/1/012005](https://doi.org/10.1088/1742-6596/587/1/012005).
- [67] CMS Collaboration, “Hcal completes phase 1 upgrades on the cms detector”, 2022. <https://cms.cern/news/hcal-completes-phase-1-upgrades-cms-detector>.
- [68] CMS Collaboration, “Calibration of the CMS hadron calorimeters using proton-proton collision data at $\sqrt{s} = 13$ TeV”, *Journal of Instrumentation* **15** (may, 2020) P05002–P05002, [doi:10.1088/1748-0221/15/05/p05002](https://doi.org/10.1088/1748-0221/15/05/p05002).

- [69] CMS Collaboration, “Measurement of the Pion Energy Response and Resolution in the CMS HCAL Test Beam 2002 Experiment”, technical report, CERN, Geneva, Sep, 2004.
- [70] CMS Collaboration, “HGCAL: A High-Granularity Calorimeter for the endcaps of CMS at HL-LHC”, *J. Phys.: Conf. Ser.* **928** (2017) 012025. 4 p,
doi:10.1088/1742-6596/928/1/012025.
- [71] CMS Collaboration, S. Cittolin, A. Rácz, and P. Sphicas, “CMS The TriDAS Project: Technical Design Report, Volume2: Data Acquisition and High-Level Trigger. CMS trigger and data-acquisition project”. Technical design report. CMS. CERN, Geneva, 2002.
- [72] CMS Collaboration, “CMS Technical Design Report for the Level-1 Trigger Upgrade”, technical report, Jun, 2013. Additional contacts: Jeffrey Spalding, Fermilab, Jeffrey.Spalding@cern.ch Didier Contardo, Universite Claude Bernard-Lyon I, didier.claude.contardo@cern.ch.
- [73] CMS Collaboration, J. G. Layter, “The CMS muon project: Technical Design Report”. Technical design report. CMS. CERN, Geneva, 1997.
- [74] CMS Collaboration, “primary-vertex reconstruction with the cms tracker”, *Journal of Instrumentation* **9** (oct, 2014) P10009, doi:10.1088/1748-0221/9/10/P10009.
- [75] M. REGLER, R. FRÜHWIRTH, and W. MITAROFF, “Filter methods in track and vertex reconstruction”, *International Journal of Modern Physics C* **07** (1996), no. 04, 521–542, doi:10.1142/S0129183196000454,
arXiv:https://doi.org/10.1142/S0129183196000454.
- [76] R. Mankel, “Pattern recognition and event reconstruction in particle physics experiments”, *Reports on Progress in Physics* **67** (mar, 2004) 553–622,
doi:10.1088/0034-4885/67/4/r03.
- [77] A. Strandlie and R. Frühwirth, “Track and vertex reconstruction: From classical to adaptive methods”, *Rev. Mod. Phys.* **82** (May, 2010) 1419–1458,
doi:10.1103/RevModPhys.82.1419.
- [78] CMS Collaboration, “Tracking and Primary Vertex Results in First 7 TeV Collisions”, technical report, CERN, Geneva, 2010.
- [79] K. Rose, “Deterministic annealing for clustering, compression, classification, regression, and related optimization problems”, *Proceedings of the IEEE* **86** (1998), no. 11, 2210–2239,
doi:10.1109/5.726788.
- [80] A. Sirunyan et al., “Performance of the cms muon detector and muon reconstruction with proton-proton collisions at $\sqrt{s}=13$ tev”, *Journal of Instrumentation* **13** (jun, 2018) P06015–P06015, doi:10.1088/1748-0221/13/06/p06015.
- [81] CMS Collaboration, “The performance of the cms muon detector in proton-proton collisions at $\sqrt{s}=7$ tev at the lhc”, *Journal of Instrumentation* **8** (nov, 2013) P11002–P11002,
doi:10.1088/1748-0221/8/11/p11002.
- [82] R. Frühwirth, “Application of kalman filtering to track and vertex fitting”, *Nuclear Instruments and Methods in Physics Research Section A: Accelerators, Spectrometers, Detectors and Associated Equipment* **262** (1987), no. 2, 444–450,
doi:https://doi.org/10.1016/0168-9002(87)90887-4.

- [83] A. Bodek et al., “Extracting Muon Momentum Scale Corrections for Hadron Collider Experiments”, *Eur. Phys. J. C* **72** (2012) 2194, [doi:10.1140/epjc/s10052-012-2194-8](https://doi.org/10.1140/epjc/s10052-012-2194-8), [arXiv:1208.3710](https://arxiv.org/abs/1208.3710).
- [84] CMS Collaboration, “Electron and photon reconstruction and identification with the cms experiment at the cern lh”, *Journal of Instrumentation* **16** (may, 2021) P05014, [doi:10.1088/1748-0221/16/05/P05014](https://doi.org/10.1088/1748-0221/16/05/P05014).
- [85] T. Chen and C. Guestrin, “XGBoost: A scalable tree boosting system”, in *Proceedings of the 22nd ACM SIGKDD International Conference on Knowledge Discovery and Data Mining, KDD '16*, pp. 785–794. ACM, New York, NY, USA, 2016. [doi:10.1145/2939672.2939785](https://doi.org/10.1145/2939672.2939785).
- [86] M. Cacciari, G. P. Salam, and G. Soyez, “The anti- k_t jet clustering algorithm”, *JHEP* **04** (2008) 063, [doi:10.1088/1126-6708/2008/04/063](https://doi.org/10.1088/1126-6708/2008/04/063), [arXiv:0802.1189](https://arxiv.org/abs/0802.1189).
- [87] CMS Collaboration, “Pileup mitigation at CMS in 13 TeV data”, *Journal of Instrumentation* **15** (sep, 2020) P09018–P09018, [doi:10.1088/1748-0221/15/09/p09018](https://doi.org/10.1088/1748-0221/15/09/p09018).
- [88] CMS Collaboration, “Determination of Jet Energy Calibration and Transverse Momentum Resolution in CMS”, *JINST* **6** (2011) P11002, [doi:10.1088/1748-0221/6/11/P11002](https://doi.org/10.1088/1748-0221/6/11/P11002), [arXiv:1107.4277](https://arxiv.org/abs/1107.4277).
- [89] E. Bols et al., “Jet Flavour Classification Using DeepJet”, [arXiv:2008.10519](https://arxiv.org/abs/2008.10519).
- [90] CMS Collaboration, “Identification of b -quark jets with the CMS experiment”, *JINST* **8** (2013) P04013, [doi:10.1088/1748-0221/8/04/P04013](https://doi.org/10.1088/1748-0221/8/04/P04013), [arXiv:1211.4462](https://arxiv.org/abs/1211.4462).
- [91] CMS Collaboration, “Identification of heavy-flavour jets with the CMS detector in pp collisions at 13 TeV”, *JINST* **13** (2018) P05011, [doi:10.1088/1748-0221/13/05/P05011](https://doi.org/10.1088/1748-0221/13/05/P05011), [arXiv:1712.07158](https://arxiv.org/abs/1712.07158).
- [92] A. Buckley et al., “General-purpose event generators for lhc physics”, *Physics Reports* **504** (2011), no. 5, 145–233, [doi:https://doi.org/10.1016/j.physrep.2011.03.005](https://doi.org/10.1016/j.physrep.2011.03.005).
- [93] S. Agostinelli et al., “Geant4—a simulation toolkit”, *Nuclear Instruments and Methods in Physics Research Section A: Accelerators, Spectrometers, Detectors and Associated Equipment* **506** (2003), no. 3, 250–303, [doi:https://doi.org/10.1016/S0168-9002\(03\)01368-8](https://doi.org/10.1016/S0168-9002(03)01368-8).
- [94] NNPDF Collaboration, “Unbiased global determination of parton distributions and their uncertainties at NNLO and at LO”, *Nucl. Phys. B* **855** (2012) 153, [doi:10.1016/j.nuclphysb.2011.09.024](https://doi.org/10.1016/j.nuclphysb.2011.09.024), [arXiv:1107.2652](https://arxiv.org/abs/1107.2652).
- [95] NNPDF Collaboration, “Parton distributions for the LHC Run II”, *JHEP* **04** (2015) 040, [doi:10.1007/JHEP04\(2015\)040](https://doi.org/10.1007/JHEP04(2015)040), [arXiv:1410.8849](https://arxiv.org/abs/1410.8849).
- [96] NNPDF Collaboration, “Parton distributions from high-precision collider data”, *Eur. Phys. J. C* **77** (2017), no. 10, 663, [doi:10.1140/epjc/s10052-017-5199-5](https://doi.org/10.1140/epjc/s10052-017-5199-5), [arXiv:1706.00428](https://arxiv.org/abs/1706.00428).
- [97] A. Bierweiler, T. Kasprzik, and J. H. Kühn, “Vector-boson pair production at the LHC to $\mathcal{O}(\alpha^3)$ accuracy”, *JHEP* **12** (2013) 071, [doi:10.1007/JHEP12\(2013\)071](https://doi.org/10.1007/JHEP12(2013)071), [arXiv:1305.5402](https://arxiv.org/abs/1305.5402).

- [98] A. Manohar, P. Nason, G. P. Salam, and G. Zanderighi, “How bright is the proton? A precise determination of the photon parton distribution function”, *Phys. Rev. Lett.* **117** (2016) 242002, doi:10.1103/PhysRevLett.117.242002, arXiv:1607.04266.
- [99] CMS Collaboration, “Search for a new scalar resonance decaying to a pair of Z bosons in proton-proton collisions at $\sqrt{s} = 13\text{TeV}$ ”, *JHEP* **06** (2018) 127, doi:10.1007/JHEP06(2018)127, arXiv:1804.01939.
- [100] CMS Collaboration, “Photon-induced electroweak corrections to the $pp \rightarrow W^\pm Z + X$ process at $\sqrt{s} = 13\text{ TeV}$, and associated uncertainties”, CMS Note 2016/431, 2016.
- [101] M. Grazzini, S. Kallweit, and D. Rathlev, “ZZ production at the LHC: fiducial cross sections and distributions in NNLO QCD”, *Phys. Lett. B* **750** (2015) 407, doi:10.1016/j.physletb.2015.09.055, arXiv:1507.06257.
- [102] M. Grazzini, S. Kallweit, and M. Wiesemann, “Fully differential NNLO computations with MATRIX”, *Eur. Phys. J. C* **78** (2018), no. 7, 537, doi:10.1140/epjc/s10052-018-5771-7, arXiv:1711.06631.
- [103] S. Frixione, P. Nason, and C. Oleari, “Matching NLO QCD computations with parton shower simulations: the POWHEG method”, *JHEP* **11** (2007) 070, doi:10.1088/1126-6708/2007/11/070, arXiv:0709.2092.
- [104] P. Nason and C. Oleari, “NLO Higgs boson production via vector-boson fusion matched with shower in POWHEG”, *JHEP* **02** (2010) 037, doi:10.1007/JHEP02(2010)037, arXiv:0911.5299.
- [105] E. Bagnaschi, G. Degrossi, P. Slavich, and A. Vicini, “Higgs production via gluon fusion in the POWHEG approach in the SM and in the MSSM”, *JHEP* **02** (2012) 088, doi:10.1007/JHEP02(2012)088, arXiv:1111.2854.
- [106] G. Luisoni, P. Nason, C. Oleari, and F. Tramontano, “ $HW^\pm/HZ + 0$ and 1 jet at NLO with the POWHEG BOX interfaced to GoSam and their merging within MiNLO”, *JHEP* **10** (2013) 083, doi:10.1007/JHEP10(2013)083, arXiv:1306.2542.
- [107] H. B. Hartanto, B. Jager, L. Reina, and D. Wackerroth, “Higgs boson production in association with top quarks in the POWHEG BOX”, *Phys. Rev. D* **91** (2015) 094003, doi:10.1103/PhysRevD.91.094003, arXiv:1501.04498.
- [108] G. Ferrera, M. Grazzini, and F. Tramontano, “Associated WH production at hadron colliders: a fully exclusive QCD calculation at NNLO”, *Phys. Rev. Lett.* **107** (2011) 152003, doi:10.1103/PhysRevLett.107.152003, arXiv:1107.1164.
- [109] K. Hamilton, P. Nason, C. Oleari, and G. Zanderighi, “Merging H/W/Z + 0 and 1 jet at NLO with no merging scale: a path to parton shower + NNLO matching”, *JHEP* **05** (2013) 082, doi:10.1007/JHEP05(2013)082, arXiv:1212.4504.
- [110] S. Gorla, G. Passarino, and D. Rosco, “The Higgs Boson Lineshape”, *Nucl. Phys. B* **864** (2012) 530, doi:10.1016/j.nuclphysb.2012.07.006, arXiv:1112.5517.
- [111] CMS Collaboration, “High mass off-shell hnnlo v2 13 tev”, 2017. <https://twiki.cern.ch/twiki/bin/view/LHCPhysics/HighMassOffshellHNNLOv213TeV>.

- [112] A. M. Sirunyan and Tumasyan, “Search for supersymmetry in final states with two oppositely charged same-flavor leptons and missing transverse momentum in proton-proton collisions at $\sqrt{s}=13$ TeV”, *Journal of High Energy Physics* **2021** (2021) 123, [doi:10.1007/JHEP04\(2021\)123](https://doi.org/10.1007/JHEP04(2021)123).
- [113] E. Bols et al., “Jet flavour classification using deepjet”, *Journal of Instrumentation* **15** (dec, 2020) P12012, [doi:10.1088/1748-0221/15/12/P12012](https://doi.org/10.1088/1748-0221/15/12/P12012).
- [114] R. J. Barlow, “Extended maximum likelihood”, *Nucl. Instrum. Meth. A* **297** (1990) 496, [doi:10.1016/0168-9002\(90\)91334-8](https://doi.org/10.1016/0168-9002(90)91334-8).
- [115] W. Verkerke and D. P. Kirkby, “The RooFit toolkit for data modeling”, in *13th International Conference for Computing in High-Energy and Nuclear Physics (CHEP03)*. 2003. [arXiv:physics/0306116](https://arxiv.org/abs/physics/0306116). CHEP-2003-MOLT007.
- [116] R. Brun and F. Rademakers, “ROOT: An object oriented data analysis framework”, *Nucl. Instrum. Meth. A* **389** (1997) 81, [doi:10.1016/S0168-9002\(97\)00048-X](https://doi.org/10.1016/S0168-9002(97)00048-X).
- [117] S. S. Wilks, “The large-sample distribution of the likelihood ratio for testing composite hypotheses”, *Annals Math. Statist.* **9** (1938) 60, [doi:10.1214/aoms/1177732360](https://doi.org/10.1214/aoms/1177732360).
- [118] K. Hamilton, P. Nason, and G. Zanderighi, “MINLO: multi-scale improved NLO”, *JHEP* **10** (2012) 155, [doi:10.1007/JHEP10\(2012\)155](https://doi.org/10.1007/JHEP10(2012)155), [arXiv:1206.3572](https://arxiv.org/abs/1206.3572).
- [119] S. Gieseke, T. Kasprzik, and J. H. Kuehn, “Vector-boson pair production and electroweak corrections in HERWIG++”, *Eur. Phys. J. C* **74** (2014) 2988, [doi:10.1140/epjc/s10052-014-2988-y](https://doi.org/10.1140/epjc/s10052-014-2988-y), [arXiv:1401.3964](https://arxiv.org/abs/1401.3964).
- [120] **CMS Collaboration**, “CMS luminosity measurements for the 2016 data taking period”, CMS Physics Analysis Summary CMS-PAS-LUM-17-001, 2017.
- [121] CMS Collaboration, “Precision luminosity measurement in proton-proton collisions at $\sqrt{s}=13$ TeV in 2015 and 2016 at CMS”, *Eur. Phys. J. C* **81** (2021), no. 9, 800, [doi:10.1140/epjc/s10052-021-09538-2](https://doi.org/10.1140/epjc/s10052-021-09538-2), [arXiv:2104.01927](https://arxiv.org/abs/2104.01927). Replaced with the published version. Added the journal reference and the DOI. All the figures and tables can be found at <http://cms-results.web.cern.ch/cms-results/public-results/publications/LUM-17-003> (CMS Public Pages).
- [122] **CMS Collaboration**, “CMS luminosity measurement for the 2017 data taking period at $\sqrt{s}=13$ TeV”, CMS Physics Analysis Summary CMS-PAS-LUM-17-004, 2018.
- [123] **CMS Collaboration**, “CMS luminosity measurement for the 2018 data-taking period at $\sqrt{s}=13$ TeV”, technical report, CERN, Geneva, 2019.
- [124] V. Khachatryan et al., “Jet energy scale and resolution in the cms experiment in pp collisions at 8 tev”, *Journal of Instrumentation* **12** (feb, 2017) P02014, [doi:10.1088/1748-0221/12/02/P02014](https://doi.org/10.1088/1748-0221/12/02/P02014).
- [125] P. D. Group, “Review of Particle Physics”, *Progress of Theoretical and Experimental Physics* **2022** (08, 2022) [doi:10.1093/ptep/ptac097](https://doi.org/10.1093/ptep/ptac097). 083C01.